

Alma Mater Studiorum - Università di Bologna

DOTTORATO DI RICERCA IN
MECCANICA E SCIENZE AVANZATE DELL'INGEGNERIA

Ciclo 34

Settore concorsuale: 09/C2 - FISICA TECNICA E INGEGNERIA NUCLEARE

Settore scientifico-disciplinare: ING-IND/19 - IMPIANTI NUCLEARI

MODELLING AND UNCERTAINTY QUANTIFICATION
APPLICATION TO SA SIMULATION CODES
IN ADVANCED SMR

Presentata da: PIETRO MACCARI

Coordinatore Dottorato

MARCO CARRICATO

Supervisore

SANDRO MANSERVISI

Co-supervisore

FEDERICO ROCCHI

Esame finale anno 2022

Abstract

In the framework of a global transition to a low-carbon energy mix, the interest in advanced nuclear Small Modular Reactors (SMRs) has been growing at the international level. Due to the high level of maturity reached by Severe Accident Codes for currently operating reactors, their applicability to advanced SMRs is starting to be studied. Within the present work of thesis and in the framework of a collaboration between ENEA, UNIBO and IRSN, an ASTEC code model of a generic IRIS reactor has been developed. The simulation of a DBA sequence involving the operation of all the passive safety systems of the generic IRIS has been carried out to investigate the code model capability in the prediction of the thermal-hydraulics characterizing an integral SMR adopting a passive mitigation strategy. The following simulation of 4 BDBAs sequences explores the applicability of Severe Accident Codes to advanced SMRs in beyond-design and core-degradation conditions.

The uncertainty affecting a code simulation can be estimated by using the method of Input Uncertainty Propagation, whose application has been realized through the RAVEN-ASTEC coupling and implementation on an HPC platform. This probabilistic methodology has been employed in a study of the uncertainty affecting the passive safety system operation in the DBA simulation of ASTEC, providing a further characterization of the thermal-hydraulics of this sequence. The application of the Uncertainty Quantification method to early core-melt phenomena has been investigated in the framework of a BEPU analysis of the ASTEC simulation of the QUENCH test-6 experiment. A possible solution to the encountered challenges has been proposed through the application of a Limit Surface search algorithm.

Acknowledgments

The present work of thesis has been developed in collaboration with the FSN-SICNUC division of the ENEA research center of Bologna. Many of the works described have been carried out in the framework of international research projects and activities in which the ENEA division has been involved.

The realization of the generic IRIS model with the ASTEC code has been developed in the NUGENIA TA-2 ASCOM project in the framework of a collaboration between UNIBO, ENEA and IRSN. The activity of the ASTEC simulation of QUENCH test-6 experiment has been supported by the IAEA and has been conducted under the Coordinated Research Project award I31033 on *Advancing the State-of-Practice in Uncertainty and Sensitivity Methodologies for Severe Accident Analysis in Water Cooled Reactors*, launched in 2019.

Another international project whose work contributed to the development of the present work of thesis is the EU - Management and Uncertainties of Severe Accidents (MUSA). This project has received funding from the Euratom research and training programme 2014-2018 under grant agreement No 847441.

A special thanks to the FSN-SICNUC team of ENEA and to the IRSN developers of ASTEC for the support provided in the realization of this work of thesis.

An acknowledge to the KIT institute that provided the experimental data of the QUENCH test-6 experiment.

Finally, a special thanks to IAEA for the involvement in the Coordinated Research Project - I31033.

List of Figures

2.1	Temperatures evolution and main phenomena in early core degradation [1].	18
2.2	Stratification configurations of corium materials in LP with focusing effect.	19
3.1	Scheme of ASTEC modules and structure [4].	30
3.2	ICARE representation of degrading core in a PWR 900-like reactor.	32
3.3	ASTEC-CESAR nodalizations of the primary circuit (left) and of the secondary circuit (right) of a the generic PWR 900 MWe [37] (only one line is represented for each circuit).	37
3.4	ASTEC nodalization of vessel (left) and of containment (right) of a the generic PWR 900 MWe [37]	38
3.5	MELCOR overall nodalization of the generic PWR 900 MWe developed by using SNAP (left) and core representation (right) [37]	39
3.6	ASTEC - MELCOR calculated pressure in PRZ, SG1 and SG2 (left), primary to secondary SG heat and FP decay heat (right).	41
3.7	ASTEC - MELCOR total H_2 mass produced (left) and cladding temperature in rings 1, 3, 5 (right).	42
4.1	Scheme of SMR modules installed in a plant (left) and generic design of an integral SMR (right).	52
4.2	Schematic view of PERSEO safety system in operation [16].	55
4.3	Experimental data versus code calculations for the average value of the SG outlet temperature [22].	56
4.4	IRIS integral RPV layout [26].	60
4.5	3D scheme of a generic IRIS reactor.	61
4.6	Scheme of safety systems for a generic IRIS reactor (for redundant systems only one line is reported) [9].	63

4.7	Scheme of main reactor phases during the DBA transient sequence.	65
4.8	CESAR nodalization scheme of the generic IRIS reactor [9].	67
4.9	Radial discretization (Left) and ASTEC visualization (right), of the of ICARE model of the generic IRIS.	69
4.10	CPA containment nodalization scheme of the generic IRIS reactor [9].	70
4.11	Mass flow rate through the break from the RPV.	74
4.12	Pressure evolution in PRZ, secondary system and drywell.	75
4.13	Pressure evolution in PRZ, drywell, LGMS and PSS.	75
4.14	FP decay heat, SGs power from RPV to EHRS loops, power from EHRS loops to RWRT.	76
4.15	Temperature of cladding, EHRS hot leg, EHRS cold leg, outlet of core and RWST.	77
4.16	Total primary mass flow-rate from the core to the riser.	78
4.17	Mass flow rate through the broken DVI (to the RC) and the intact DVI (to the RPV).	79
4.18	Normalized collapsed level inside the core channels (between upper and lower core plates elevations).	80
4.19	Normalized water level inside the tanks of PSS (1 and 2), LGMS (1 and 2), EBT (1 and 2), the RC and Break relative level in RC. . . .	81
4.20	Normalized value of the average collapsed level in the core (upper and lower core plates elevations taken as reference).	86
4.21	Normalized value of the water level in the RC, with respect to the RC total elevation.	87
4.22	Mass flow rate through the brake (positive value is from RPV to containment).	88
4.23	Primary system pressure (PRZ).	88
4.24	Containment pressure.	89
4.25	Core outlet temperature.	89
4.26	Total hydrogen mass produced.	90
4.27	ASTEC - ICARE mask of core degradation evolution for the <i>ADS</i> <i>st-1</i> and <i>EHRS failure</i> scenario.	92
4.28	ASTEC - ICARE mask of core degradation evolution for the <i>EBTs</i> , <i>LGMS</i> , <i>EHRS</i> and <i>ADS st-1 failure</i> scenario.	93
5.1	Scheme of ASTEC – RAVEN coupling workflow for UQ analysis. . .	114
5.2	Schematic view of the QUENCH facility (Left); Section of the QUENCH- 06 bundle (Right) [23]	117

5.3	Radial view of the QUENCH model in ASTEC (left); Translation of the QUENCH model into the ASTEC computational together with the distribution of materials (right).	119
5.4	Mass flow rate of fluids injections (left) and electric power generated in the heated rods (right), considered as boundary conditions to the ASTEC simulation.	120
5.5	Central un-heated rod center temperature evolution from experimental data and from code simulation, at 950 mm of elevation.	121
5.6	Outer-ring heated rod cladding temperature evolution from experimental data (north and south-west oriented thermocouples) and from code simulation, at 950 mm of elevation.	122
5.7	Shroud internal temperature evolution from experimental data and from code simulation, at 950 mm of elevation.	123
5.8	Hydrogen cumulated mass produced from experimental data and from code calculation.	123
5.9	Hydrogen mass production rate from experimental data and from code calculation.	124
5.10	ZrO_2 outer layer thickness axial profile for the extracted corner rod at 6620 s.	125
5.11	Materials in unheated rod and inner-ring heated rod (left); materials in outer-ring heated rod and corned-rods (right), at 7179 s of ASTEC simulation.	125
5.12	Materials in shrouds at 7179 s of ASTEC simulation.	126
5.13	Axial profile of ZrO_2 thickness, averaged on not-extracted corner rods (left), and of shroud (right), at 9000 s.	127
5.14	Dispersion band of instantaneous H_2 production, against experimental data.	130
5.15	Mean value and STD of H_2 production rate against experimental data, from 7000 to 7300 s.	130
5.16	Final components materials in cases of lowest (left) and highest (right) heating-up.	131
5.17	Dispersion band of ZrO_2 profile in the ASTEC representative corner rod against experimental ZrO_2 profile in the extracted corner rod, at 6620 s.	132
5.18	Dispersion band of internal temperature of central rod simulator, at the elevation of 950 mm, against experimental data.	133
5.19	Mean value and STD of internal temperature of central rod simulator against experimental data, from 6500 to 8500 s.	133

5.20 Spearman correlation coefficients related to H_2 production rate (geometric and boundary conditions parameters).	134
5.21 Spearman correlation coefficients related to H_2 production rate (cladding integrity criteria and physical models parameters).	135
5.22 Coefficients of Lasso regression related to H_2 production rate (geometric and boundary conditions parameters).	135
5.23 Coefficients of Lasso regression related to H_2 production rate (cladding integrity criteria and physical models parameters).	136
5.24 Spearman correlation coefficients related to the corner rod ZrO_2 thickens, at 6620 s, for geometric and boundary conditions parameters(left), and for cladding integrity criteria and physical models parameters (right).	137
5.25 Coefficients of Lasso regression related to the corner rod ZrO_2 thickens, at 6620 s, for geometric and boundary conditions parameters (left), and for cladding integrity criteria and physical models parameters (right).	138
5.26 Spearman correlation coefficients related to central temperature of central rod at 950 mm (geometric and boundary conditions parameters).	139
5.27 Spearman correlation coefficients related to central temperature of central rod at 950 mm (cladding integrity criteria and physical models parameters).	139
5.28 Coefficients of Lasso regression related to central temperature of central rod at 950 mm (geometric and boundary conditions parameters).	140
5.29 Coefficients of Lasso regression related to central temperature of central rod at 950 mm (cladding integrity criteria and physical models parameters).	140
5.30 Dispersion band of ZrO_2 profile in the cladding of internal-ring heated-rod (left) and of external-ring heated-rod (right) at calculation end, against experimental data.	144
5.31 Cs-137 % mass fraction emitted from degrading fuel of a Spent Fuel Pool, in 36 calculations for a preliminary UQ analysis.	147
5.32 Dispersion band of DW pressure, against reference value data and upper bound.	150
5.33 Dispersion band of maximum cladding temperature, against reference value and upper bound.	150
5.34 Spearman coefficients related to DW pressure, against maximum calculated DW pressure.	151

5.35	Lasso coefficients related to DW pressure, against maximum calculated DW pressure.	152
5.36	Spearman coefficients related to cladding maximum temperature, against maximum calculated DW pressure.	153
5.37	Lasso coefficients related to cladding maximum temperature, against maximum calculated DW pressure.	153
5.38	Transition of the goal function C on a 2-D Cartesian grid in the input domain [12].	157
5.39	Iterative scheme of the LS Search algorithm of RAVEN.	158
5.40	Spearman coefficients between the goal function C and the 23 input parameters to the UQ analysis.	160
5.41	Calculations executed in the LS search in terms of input values (normalized) and corresponding goal function value (yellow for intact and purple for failed cladding).	161
5.42	Calculations executed in the LS search in terms of input values (normalized) and corresponding order of execution in a color scale.	162
5.43	Maximum values of DW pressure dispersion obtained in the UQ analysis, and new safety limit of 11 bar.	164
5.44	Calculations executed in the LS search in terms of input values (normalized) and corresponding value of output P_{max} in a color scale.	165
5.45	Calculations executed in the LS search in terms of submission index and output P_{max}	166

List of Tables

2.1	SA scenarios and core melt frequency for a PWR 900 MWe, according to the PSA level-1 of IRSN [1]	14
3.1	MELCOR versus ASTEC steady-state conditions before the SOT.	39
3.2	SBO transient in PWR 900-like, sequence of Main events ASTEC – MELCOR.	40
4.1	Steady-state calculation values against IRIS reference values.	71
4.2	Sequence of main events and systems actuation in the DBA simulation.	72
4.3	Main phenomena qualitatively predicted by the code along the transient, per reactor system.	73
4.4	Timings (s) of main events in the 4 BDBA sequences.	85
5.1	Timings of main events characterizing the test and relative PhW [22].	118
5.2	Uncertain parameters of type: Geometry of the bundle; Initial and boundary conditions.	128
5.3	Uncertain parameters of type: Integrity criteria of cladding; Radiative H.T.; Convection H.T.; Material relocation parameters [24].	129
5.4	list of input uncertain parameters, rage of variation and PDF type for UQ analysis.	149

List of Acronyms

[A](#) | [B](#) | [C](#) | [D](#) | [E](#) | [F](#) | [H](#) | [I](#) | [L](#) | [M](#) | [N](#) | [P](#) | [Q](#) | [R](#) | [S](#) | [U](#)

A

ACC ACCumulator.

ADS Automatic Depressurization System.

AI Artificial Intelligence.

ASCOM ASTEC COMmunity.

B

BDBA Beyond Design Basis Accidents.

BEPU Best-Estimate Plus Uncertainty.

BWR Boiling Water Reactor.

C

CL Cold Leg.

CRDM Control Rod Drive Mechanism.

CRP Coordinated Research Projects.

D

DBA Design Basis Accident.

DP-signal low RPV - Containment Differential Pressure - signal.

DVI Direct Vessel Injection.

DW DryWell.

E

EBT Emergency Boration Tank.

EHRS Emergency Heat Removal System.

F

FFTBM Fast Fourier Transform Based Method.

FL Feed Line.

FOM Figures Of Merit.

FP Fission product.

H

HL Hot Leg.

HPC High Performance Computing.

I

IAEA International Atomic Energy Agency.

ICSP International Collaborative Standard Problem.

IRIS Reactor Innovative and Secure.

ISP International Standard Problem.

IVMR In Vessel Melt Retention.

L

LB-LOCA Large Break - LOCA.

LGMS Long-term Gravity Make-up System.

LH Lower Head.

LM-signal LOCA Mitigation - signal.

LP Lower Plenum.

LS Limit Surface.

LWR Light Water Reactor.

M

MCCI Molten Core - Concrete Interaction.

ML Machine Learning.

N

NPP Nuclear Power Plant.

P

PDF Probability Density Function.

PERSEO in-Pool Energy Removal System for Emergency Operation.

PhW Phenomenological Window.

PRZ Pressurizer.

PSA Probabilistic Safety Assessment.

PSS Pressure Suppression System.

PWR Pressurized Water Reactor.

Q

QT Quench Tank.

R

RC Reactor Cavity.

RCS Reactor Coolant System.

RI-DC Riser-Downcomer.

ROM Reduced Order Model.

RPV Reactor Pressure Vessel.

RWST Refueling Water Storage Tank.

S

SA Severe Accident.

SB-LOCA Small Break - LOCA.

SBO Station Black-Out.

SEBIM Safety Valves of Pressure Compensator.

SG Steam Generator.

SIS Safety Injection Systems.

SL Steam Line.

SMR Small Modular Reactor.

SNAP Symbolic Nuclear Analysis Package.

SOT Start Of the Transient.

SRV Steam Relief Valve.

STD STandard Deviation.

SVM Support Vector Machine.

U

UQ Uncertainty Quantification.

Contents

1	Introduction	1
1.1	Motivation	1
1.2	Structure of the thesis	3
1.3	Objectives of the thesis	4
2	Nuclear Safety and Severe Accidents in LWR	9
2.1	Nuclear Safety principles in LWR	9
2.1.1	Concept of Defence-in-dept	10
2.1.2	Deterministic and probabilistic safety assessments	12
2.2	Severe Accident (SA) Concept	13
2.2.1	Accident scenarios that may lead to core melt	14
2.2.2	Phenomenology characterizing core melt accidents in LWR	15
3	Core melt accident simulation codes	25
3.1	Introduction to Integral codes for SA simulation	26
3.1.1	Integral and Mechanistic codes for SA simulation in LWR	26
3.1.2	Development and validation of Integral codes	27
3.2	The ASTEC code	29
3.2.1	Modules of ASTEC code	29
3.2.2	Validation of ASTEC code	35
3.3	Example of code-to-code application for SA integral codes: ASTEC – MELCOR simulation of SBO in a generic French PWR-900	35
3.3.1	Brief introduction to MELCOR code	36
3.3.2	Codes models of the generic PWR 900 MWe	37
3.3.3	Steady-state calculations comparison	38
3.3.4	SBO transient calculations comparison	40
3.3.5	Conclusions of the analysis	43

4	ASTEC modelling and simulation of advanced passive SMR	51
4.1	Introduction and code modelling of advanced water-cooled SMR . . .	51
4.1.1	Potential advantages of water-cooled advanced SMR	52
4.1.2	Considerations about thermal-hydraulic phenomena characterizing advanced SMR	53
4.1.3	Considerations and research activities regarding code modelling of advanced SMR	55
4.2	ASTEC code modelling of a generic IRIS design	58
4.2.1	Motivations	58
4.2.2	IRIS reactor	59
4.2.3	IRIS passive mitigation strategy for a DVI line double-ended break	63
4.2.4	Description of ASTEC nodalization of the generic IRIS reactor	66
4.3	ASTEC simulation of DBA sequence on the generic IRIS model . . .	70
4.3.1	Steady-State conditions	70
4.3.2	Simulation of DBA sequence	71
4.3.3	Conclusions and remarks	81
4.4	ASTEC simulation of BDBA sequences on the generic IRIS model . .	83
4.4.1	Assumptions of BDBA sequences	84
4.4.2	Results of BDBA simulations	84
4.4.3	Conclusions and remarks	93
5	Uncertainty Quantification analyses	101
5.1	Uncertainty Quantification in deterministic code simulations	102
5.1.1	Introduction to Uncertainty Quantification methodology . . .	102
5.1.2	The propagation of input uncertainty probabilistic method . .	105
5.1.3	Sensitivity analysis	110
5.1.4	Implementation of RAVEN – ASTEC coupling for UQ	113
5.2	BEPU analysis of the ASTEC simulation of QUENCH test-6	115
5.2.1	The QUENCH-6 experiment	116
5.2.2	ASTEC model of QUENCH-6	117
5.2.3	Results of reference simulation	120
5.2.4	Uncertainty Quantification analysis	126
5.2.5	Conclusions	137
5.3	Discussion on the applicability of the UQ method to SA	143
5.3.1	Considerations on core degradation phenomena and UQ . . .	143
5.3.2	Challenges of UQ analysis to SA in plant applications	145
5.3.3	Conclusions ad remarks	147

5.4	UQ analysis of ASTEC simulation of DBA sequence in a generic IRIS reactor	148
5.4.1	Uncertainty Quantification analysis	148
5.4.2	Conclusions	154
5.5	Application of the automatic Limit Surface Search Method	155
5.5.1	Limit Surface Search	155
5.5.2	LS search of change in SA degradation phenomenology	159
5.5.3	LS Search of safety conditions	163
6	Conclusions	171

CHAPTER 1

Introduction

1.1 Motivation

Nowadays, energy production plays a key role in the world's economic growth and sustainability, as well as in the progression of social, health and environmental conditions. Accordingly, this sector is the major contributor to greenhouse gases emissions and, therefore to global warming and climate change [1]. Considering the current trend of energy demand increase of developed and developing countries, a big effort has to be done soon to reform the world energy mix and its policy to satisfy the scientific community call for a more sustainable and secure energy future.

In the framework of a transition from conventional energy mix to low carbon energy sources, advanced Nuclear Power Plant (NPP) have the needed features to play a central role. The international nuclear community has been developing new advanced reactor designs for the last 20 years to satisfy the people's demand for improved safety of nuclear power, still taking into account the needs of industries to improve economic efficiency and reduce capital costs of this technology [2]. In this framework, the interest in advanced Small Modular Reactors (SMRs) [3] has been growing in the past decade because of the valuable economic and safety potential advantages of this technology concerning conventional size reactors [4]. In addition, Light Water SMRs can also benefit from the consolidated knowledge developed in the past 60 years in water-cooled large size NPP, e.g. large-scale Pressurized Water Reactor (PWR) and Boiling Water Reactor (BWR).

Every aspect of NPP technology, from design and development to construction and operation, is heavily regulated and has to respect strict standards and to be supported by safety studies and analyses [5]. The objective of safety analysis is to

study, through adequate tools, the safety basis of a specific part of the NPP; or to evaluate the behavior of the plant in operational states under specific accidental scenarios [6].

The accident in 1979 of Three Mile Island and the Fukushima-Daiichi accident in 2011, showed that an external hazard not considered in the plant design, combined with multiple failures of safety systems, could lead to the melt of the nuclear fuel whether inadequately mitigated [5]. These unfortunate events provided a call to nuclear regulatory authorities and to the international nuclear research community: in the last 40 years, intensive research programs, finalized to acquire the knowledge on core-melt accidents and necessary to increase the safety level of NPP, have been carried out in the international framework.

The huge advancement in computer science and the growth of massive calculation power promoted the development of Severe Accident (SA) simulation codes: deterministic tools that incorporate all the knowledge of the past years of research and experimental campaigns in the SA field [7]. Integral SA codes are aimed at providing exhaustive coverage of all the main phenomena taking place in a core melt accident; thus, a major effort is currently underway by the international research community to improve their accuracy and reliability and to extend their applicability to further NPP designs.

In the framework of the NUGENIA TA-2 ASTEC COMmunity (ASCOM) collaborative project [8][9], coordinated by IRSN, a generic SMR design based on the International Reactor Innovative and Secure (IRIS) [10], has been the object for the development of an ASTEC code [11] model. The work has been carried out in a collaboration between ENEA-IRSN and it is aimed at providing a new ASTEC input-deck able to simulate the main features of an advanced integral SMR. Accordingly, the passive mitigation strategy adopted by IRIS involves several passive safety systems and, therefore, relies on most of the main natural-driven thermal-hydraulic phenomena of interest for the ASTEC assessment [12]. This work represents one of the central Ph.D. research activity and it has opened to the further studies that have been developed and presented in the present work of this thesis.

Despite the high level of maturity and accuracy reached today by SA and thermal-hydraulic codes, it should be always considered that the result of a deterministic calculation is inevitably affected by a certain uncertainty deriving, for example, from the uncertain knowledge of the input data. Uncertainty Quantification (UQ) methods have been developed in the past to characterize the uncertainty affecting a simulation and to find the main sources of uncertainty to be reduced, thus increasing the confidence in code results. In this thesis, the probabilistic *method of input uncertainty propagation* for UQ studies has been presented and applied [13].

These studies involve the UQ analysis of the ASTEC simulation of early core-melt phenomena and of the thermal-hydraulics in a passive mitigation strategy of the generic IRIS.

Considering the large number of calculations required, the large amount of data produced and the complex relationship between input and output variations in a UQ application, the recent development of large High Performance Computing (HPC), along with the development of Machine Learning (ML) [14], is introducing new opportunities for nuclear safety. In this framework, the ASTEC coupling with the statistical platform RAVEN [15] has been crucial for the development of UQ studies on a multi-nodes cluster. In addition, the coupling of the code has been used in the application of new methods based on active learning algorithms as support to the safety studies performed.

1.2 Structure of the thesis

By starting from an overview of the main concepts of nuclear safety, the 2nd Chapter of the present work of thesis proposes an introduction to core-melt accidents in NPP and the main phenomenology involved in this kind of sequences.

The 3rd Chapter of the thesis deals with SA simulation codes and, in particular, it is aimed at introducing the ASTEC code and its features. As an example of SA code simulation, the chapter concludes with the description of an ASTEC - MELCOR code-to-code analysis of an unmitigated Station Black-Out (SBO) accident in a French PWR 900 MWe and evolving to a SA.

Chapter 4 deals with the central topic of SMR and code modeling of their advanced design features. The approach adopted in the ASTEC code modeling of the generic IRIS design is described in this chapter, and it follows with the development of accidental transient simulations performed with the SMR model. The ASTEC simulation of a Design Basis Accident (DBA) is first described, and this study has the purpose of assessing the code model capability to simulate the thermal-hydraulic phenomena involved in the passively mitigated sequence of an integral SMR. It follows the description of four Beyond Design Basis Accidents (BDBA) simulations, from whose results it is possible to draw some first outcomes regarding the behaviors of SMRs and passive safety systems under beyond design and SA conditions.

Chapter 5 starts by introducing the concept of uncertainty affecting a deterministic code calculation. The central topic of UQ analysis to code simulations [13] is then introduced, and the methodology that will be used in the following UQ studies is presented. The first UQ study described concerns a comprehensive

Best-Estimate Plus Uncertainty (BEPU) analysis on the ASTEC simulation of the QUENCH test-6 experiment [16]. This work has been developed in the framework of the International Atomic Energy Agency (IAEA) Coordinated Research Projects (CRP) - I31033 [17], and covers a UQ application to the simulation of early core-melt phenomena. This analysis provides the basis to discuss the applicability of the UQ method to SA simulations and to identify the related challenges. The following study is a UQ application to the DBA sequence of the generic IRIS reactor, by considering the main input uncertainties affecting the operation of passive safety systems. To conclude the chapter, a Limit Surface (LS) search algorithm is described and proposed as support to the UQ analyses treated in the present work of the thesis.

1.3 Objectives of the thesis

Considering the thesis structure described in the above Section, Chapters 2 and 3 of the present work of thesis have an introductory purpose. These 2 chapters are aimed at providing to the reader the basis on which the main works treated in the following chapters have been developed.

The work described in Chapter 4, deals with the modeling and simulation of an advanced integral SMR with the SA code ASTEC. In particular, the code nodalization realized for the generic IRIS design aims at providing some code-user guidelines to be followed for the modeling of passive safety systems and facing with integral SMR, with a modular code. The simulation and analysis of the DBA sequence are important to point out the code needs, to identify which specific code models need to be further validated, and to find useful development areas. Accordingly, this analysis is aimed to be the first step of qualitative assessment for the thermal-hydraulic modules of ASTEC against integral design and passive safety systems.

The purpose of the 4 BDBA simulations, described in the same Chapter, is to test the ASTEC-IRIS model capability to simulate beyond-design and SA conditions. In addition, the comparison of the 4 simulations provides useful insights on the passive safety systems operation in beyond-design and challenging conditions, underlines possible SMR drawbacks, and opens to the study and development of better management mitigation action and more efficient passive safety systems for advanced SMRs and to be considered in SA conditions.

The last Chapter of the thesis explores the use of the probabilistic method of *input uncertainty propagation* to the ASTEC code simulations of advanced SMR designs and of eventual SA conditions. At first, Chapter 5 introduces the reader to the concept of code uncertainty and provides a description of the UQ methodology

and of the technical implementation adopted in the following studies.

The BEPU analysis of the ASTEC simulation of QUENCH-6 has the purpose to validate the code models for the main early core-degradation phenomena governing the experiment. In the framework of the present thesis, the study wants also to provide remarks and guidelines regarding the UQ methodology used. Indeed, this analysis offers a simplified case to explore the applicability of the described UQ methodology to the simulation of SA phenomena. The challenges encountered and identified in UQ applications to SA are here discussed.

The following UQ study is aimed at assessing an additional characterization of the ASTEC simulation of the thermal-hydraulics characterizing the passive mitigation strategy of the generic IRIS. The analysis investigates the uncertainty propagation of selected input uncertainties affecting the operation of passive safety systems and tests the response of the SMR code model.

An advanced and innovative method to be used as support to UQ and safety analyses is the LS search algorithm presented in the last Section of Chapter 5. The examples provided show as this method can be very useful for the determination of the safety condition of a system. In addition, the method is proposed to be used as a solution in the case of phenomenological bifurcation in a UQ application to SA.

Bibliography

- [1] “Energy and air pollution: World energy outlook special report 2016,” OECD - International Energy Agency (IEA), Paris, France, 2016.
- [2] F. Mascari, G. Vella, B. G. Woods, K. Welter, and F. D’Auria, “Analysis of primary/containment coupling phenomena characterizing the MASLWR design during a SBLOCA scenario,” in *Nuclear Power Plants*, InTech, 2012, pp. 203–233.
- [3] H. Subki, *Advances in Small Modular Reactor Technology Developments*. International Atomic Energy Agency (IAEA), 2020.
- [4] R. J. Budnitz, H.-H. Rogner, and A. Shihab-Eldin, “Expansion of nuclear power technology to new countries—SMRs, safety culture issues, and the need for an improved international safety regime,” *Energy policy*, vol. 119, pp. 535–544, 2018.
- [5] B. R. Sehgal, Ed., *Nuclear safety in light water reactors: severe accident phenomenology*. Academic Press, 2012. DOI: <https://doi.org/10.1016/C2010-0-67817-5>.
- [6] G. Petrangeli, *Nuclear safety*. Elsevier, 2006. DOI: <https://doi.org/10.1016/B978-0-7506-6723-4.X5000-1>.
- [7] A. Bentaïb, H. Bonneville, and G. Cénérino, *Nuclear Power Reactor Core Melt Accidents: Current State of Knowledge*. EDP Sciences, 2021, ISBN: 9782759819300. DOI: [doi:10.1051/978-2-7598-1930-0](https://doi.org/10.1051/978-2-7598-1930-0). <https://doi.org/10.1051/978-2-7598-1930-0>.
- [8] P. Chatelard, “ASCOM project overview and description of work,” SARNET-ASCOM-COORDI-P1, 2018.
- [9] *NUGENIA TA-2 : ASCOM project (2018-2022)*. <https://snetp.eu/portfolio-items/ascom/>.

-
- [10] “IRIS International Reactor Innovative and Secure, IRIS Plant Overview,” October 17, 2002. <https://www.nrc.gov/docs/ML0336/ML033600086.pdf>.
- [11] P Chatelard, S Belon, L Bosland, *et al.*, “Main modelling features of the ASTEC V2.1 major version,” *Annals of Nuclear Energy*, vol. 93, pp. 83–93, 2016. DOI: <https://doi.org/10.1016/j.anucene.2015.12.026>.
- [12] P. Maccari, F. Mascari, S. Ederli, P. Meloni, and S. Manservigi, “ASTEC code DBA analysis of a passive mitigation strategy on a generic IRIS SMR,” *Annals of Nuclear Energy*, vol. 156, p. 108 194, 2021.
- [13] F. S. D’Auria, H Glaeser, S Lee, J Miák, M Modro, and R. Schultz, *Best Estimate Safety Analysis for Nuclear Power Plants: Uncertainty Evaluation. IAEA Safety Report Series*. International Atomic Energy Agency (IAEA), 2008, vol. 52.
- [14] I. Goodfellow, Y. Bengio, and A. Courville, *Deep learning*. MIT press, 2016.
- [15] A. Alfonsi, C. Rabiti, D. Mandelli, *et al.*, “RAVEN theory manual,” Idaho National Lab.(INL), Idaho Falls, ID (United States), INL/EXT-16-38178, April 2020.
- [16] L. Sepold, W Hering, C Homann, *et al.*, “Experimental and computational results of the QUENCH-06 test (OECD ISP-45),” Forschungszentrum Karlsruhe GmbH Technik und Umwelt (Germany), FZKA-6664, 2004.
- [17] <https://www.iaea.org/projects/crp/i31033>.

CHAPTER 2

Nuclear Safety and Severe Accidents in LWR

To introduce the present work of the thesis, this Chapter deals with an overview of the Nuclear Safety principle, by describing measures and studies developed to guarantee the best level of safety of current and new generations of NPP. The second part of the chapter introduces the reader to the concept of core melt accident and provides a description of the main phenomenology characterizing such severe sequences. This last section wants to provide the basis needed for the development of the following works.

2.1 Nuclear Safety principles in LWR

NPP, and in particular Light Water Reactors ([LWRs](#)), feature specific health and environmental risks related to significant quantities of radioactive material deriving from the nuclear fission reactions. Radioactive Fission Products ([FPs](#)) trapped in the nuclear fuel, can potentially cause individuals, population and environment to be exposed to dangerous ionizing radiations. Nuclear safety purpose is to study and set up a series of physical barriers, as well as technical and organizational measures to be taken during all phases of a facility life, to protect workers, population and environment from exposure to this radioactive substance. In particular, this can include [\[1\]](#):

- Ensuring normal operation of the reactor, keeping the worker's exposure and the releases of radioactivity to the environment below the limits of low;
- Preventing accidents and the consequent release of radioactivity;

- Mitigating the consequences of hypothetical accidents that would occur despite the implemented prevention measures.

Since NPP safety aims to protect the public and environment at large, it is strictly regulated. Each country employing nuclear power as an energy source (and even some without NPPs) has regulatory commissions (bodies) that regulate every aspect of a NPP from design and construction to operation and any modifications. They require very extensive analyses, documentation, quality control and impose the reactor safety design to follow strict rules and regulations [2].

2.1.1 Concept of Defence-in-dept

The defense-in-depth concept was introduced in the nuclear safety field at the beginning of the 1970s [1][2]. Its objective is to ensure the basic safety requirements of the reactor (reactions regulation, fuel cooling, containment of radioactivity, etc) and, if prevention fails, to limit and mitigate any accident consequences. In NPP defense-in-depth is achieved by implementing several levels of defense between the radioactive materials and the environment, such as intrinsic features of the facility, equipment and safety systems or new measures and procedures.

Defence-in-depth covers all stages of life of a facility (e.g. design, construction, operation, decommissioning and dismantling). The specific safety measures and how these are implemented have evolved over time to take into account operational experience from facilities (including accidents that have occurred) to build an ever higher safety margin. For reactors currently in operation, defense-in-depth is based on five levels which apply in the various states of the facility, from normal operation to core melt accident [3].

Level-1: prevention of operating anomalies and system failures

This level corresponds to the normal domain of operation for the plant unit with general rules and operating procedures designed to maintain the systems within their normal operating conditions. The reactor design, components, equipment and systems have to be manufactured and operated to the highest quality standards.

Level-2: failure detection and management of operating malfunctions

It includes resources designed for the detection and the control of operating malfunctions; automatic control systems that can correct an abnormal change in facility parameters and return it to the normal operating conditions through an operational transient. Their typical frequency of occurrence is within the order of 10^{-2} year⁻¹).

Level-3: accident management, including Design Basis Accidents (DBA)

The objective of the first two levels of defense-in-depth is to reduce the risks of system failure. Nevertheless, it is assumed the possibility of an accident during reactor operation. The DBA results from a single accidental initiating event, such as the rupture of a component essential for basic safety and function of the reactor (s.a. break of a pipe of the reactor coolant system; stop of the primary coolant pumps); and have a much lower frequency of occurrence than operational transients, typically in the range 10^{-2} - 10^{-5} year⁻¹. Hence, these kinds of events are not expected to occur during the lifetime of the plant; however, they are considered in the plant design at level-3 of defense-in-depth. This level consists in the implementation of safety systems able to ensure the integrity of the core structure and limit releases into the environment, in the event of a DBA. Level-3 also includes defining emergency operating procedures.

Level-4: management of Beyond-Design-Basis-Accident (BDBA) and Severe Accidents (SA)

After the accidents of TMI and Fukushima, the concept of defense-in-depth was enlarged to include accidents that had not been explicitly considered at facility design; namely BDBA. In particular, accidents result from multiple systems failures and those leading to the melt of the core. The objective of level-4 of defense-in-depth is to prevent accidents from resulting in core melt and, in the event core melt nevertheless would occur, to limit radioactivity releases outside the site by ensuring the containment of FPs. This level includes emergency procedures, associated equipment resources, severe accident operating guidelines and the facility's on-site emergency plan.

For Generation-III and following reactor generations, serious failures and core melt accidents are considered in the initial design of the reactors, which means a further step in the range of accident situations for which measures are planned from the design, therefore extending the concept of DBA. Example of these measures are: In-Vessel Melt Retention (IVMR) strategy [4], core catcher [5], catalytic hydrogen recombiners [6], etc.

Level-5: limiting consequences of radiation in the event of radioactive releases

Despite all the measures taken in the previous levels, it is considered the possibility that a radioactive release may occur. Additional measures taken by public authorities are then implemented to protect the people and on-site staff from the conse-

quences of these releases. Public authorities implement the off-site emergency plan, which organizes emergency operations to limit public radiation exposure. Measures include controlled evacuation, shelter in hard-wall accommodation, administration of potassium iodide pills and restrictions on the consumption of foodstuffs.

2.1.2 Deterministic and probabilistic safety assessments

Deterministic safety assessment

The objective of safety analysis is to study, through adequate analysis tools, the safety basis of a specific part of the plant or to evaluate the behavior of the plant in operational states under specific accidental scenarios [7]. Often, deterministic analyses are performed using conservative assumptions for initial and boundary conditions and for the various elements of the evaluation. Consequently, the behavior of the plant as evaluated could be rather different from the most likely one, even if in a sense beneficial to safety (conservative analyses). Thermal-hydraulic deterministic analyses are based on a well-consolidated basis since they have been used for a longer time; while SA has more recently become part of deterministic analyses. However, because of the very low probability of SA occurrence, and also depending on the aim of the study, the conservative assumptions used for DBAs may also not be used, and a "best estimate" treatment of the phenomena may be preferred.

Probabilistic safety assessments

Probabilistic Safety Assessment (PSA) for nuclear power plants supports the traditional deterministic analyses by investigating the several possibilities of accidental events combinations and sequences that constitute accident scenarios. PSAs are a set of technical probabilistic analyses for assessing the risks at a facility in terms of accident frequency, and their consequences of selected scenarios. It provides an overall view of reactor safety, including both equipment resistance and operator behavior.

There are three major types of PSAs based on consequences under examination [1]:

level-1 PSA, aimed to identify sequences leading to core melt and quantifying their frequency; level-2 PSA, used to assess and characterize the nature, significance and frequency of radioactive releases; level-3 PSA, used to assess the probabilities of consequences on the public in terms of dose, contamination and health damages.

Despite PSA will not be an argument of this work of thesis, a short introduction

of this topic is important to have a correct overview of nuclear safety. The deterministic and probabilistic approaches to nuclear safety constitute an ensemble that contributes to the prevention and mitigation of accidents consequences and to the development of new and more reliable levels of safety for the current and new reactor designs. The approaches continue to evolve and it is important not to discount the reciprocal action between the level of safety at facilities and the current state of knowledge available from research on core melt accidents, on operating experience, and on incident and accident analysis.

2.2 Severe Accident (SA) Concept

Despite the several levels of safety measures taken in current NPP designs, the very unlikely scenario of multiple failures of the safety systems, for example, due to an external hazard not considered in the reactor design, can possibly lead to what is called a SA. In the case of a BDBA in which it is not possible to guarantee the cooling of the reactor core, the decay heat produced by the nuclear fuel can lead to its damage and to the release of FPs, with more or less extensive melting of core structures. If the core degradation is not stopped through sufficient cooling, the sequence can end up to the loss of integrity of the primary system and of the external containment, with an ultimate release of radioactive FPs [1]. According to the definition provided by IAEA, accident conditions more severe than a design basis accident and involving significant core degradation are termed “Severe Accident” [8].

The unfortunate event of the Fukushima-Daiichi accident in 2011 provided a call to the nuclear industry and regulatory authorities. It was clear that despite very improbable such accidents had to be prevented and mitigated, and with this purpose, it was crucial that a knowledge base on those accidents would be developed and acquired [2].

In the last 40 years, the international research nuclear community has carried out intensive programs of research finalized to acquire the knowledge necessary to increase the safety level of current and advanced NPP and to avoid and mitigate the occurrence of new SAs. Examples of European and international research projects in the field of nuclear severe accidents are EU-CESAM [9], EU-FASTNET [10][11], EU-IVMR [12][13], EU-MUSA [14].

2.2.1 Accident scenarios that may lead to core melt

An NPP accident leading to core degradation can be initiated by a different series of equipment or human failures (initiator events). Accordingly, in the previous section has been presented level 1 of PSA, aimed at evaluating the occurrence probability (frequency) of the main accidental scenarios for a specific reactor. As an example, in the PSA level-1 study developed by IRSN on the PWR 900 MWe, it has been estimated a total core melt frequency to be around 7.5×10^{-6} year⁻¹ per reactor, for all reactor operational states. With respect to this study, the different accidental scenarios concerning core melt and expected in a PWR 900 MWe have been reported in Table 2.1, with the respective occurrence frequencies [1].

Scenario type	Core melt frequency (per year/reactor)	% of total core melt frequency
Loss-of-coolant	1.2×10^{-6}	16%
Loss-of-coolant with containment bypass	2.2×10^{-7}	2.9%
Steam line break	5×10^{-8}	0.7%
Steam generator tube rupture	1.1×10^{-8}	0.1%
Total loss of heat sink	1.3×10^{-6}	17%
Total loss of the SG feedwater supply	1×10^{-6}	14%
Station Black-Out (SBO)	2.9×10^{-6}	38%
Loss of onsite power	5.1×10^{-7}	6.8%
Transients involving automatic shutdown failure	3.3×10^{-8}	0.4%
Coolant System transients	3×10^{-7}	4%
Total core melt frequency	7.5×10^{-6}	100%

Table 2.1: SA scenarios and core melt frequency for a PWR 900 MWe, according to the PSA level-1 of IRSN [1]

From this example, it results clear that a large variety of initiator events may lead to a SA on the same reactor design. Despite the evolution of a core melt sequence deepening on both the type of sequence and the reactor design, in the following part of this chapter we will try to generalize with some simplifications, and describe the SA phenomenology characterizing a conventional LWR.

2.2.2 Phenomenology characterizing core melt accidents in LWR

As it has been mentioned in the previous section, a wide variety of accidental scenarios in a specific LWR design are liable to lead to a core melt accident. Despite each scenario being triggered by different initiator events, it can be expected a similar phenomenological evolution of the SA sequence and, hence, similarities make it possible to describe and discuss the main phenomena that play a key role during a "generic SA". In this section, an overview of these main generic SA phenomena is presented. The section content does not aim to be an exhaustive and detailed description of the various and complex phenomenology involved in a core melt nuclear accident, but only to summarize the main base concepts needed for the development of the following chapters of the thesis.

Thermal-hydraulics of the reactor systems

In any kind of SA scenario, the sequential series of events that lead the state of the reactor from the nominal working conditions to the start of core degradation are of thermal-hydraulic nature. The pre-degradation thermal-hydraulics scenarios can widely vary depending on the type of initiator event; the state of the safety system; and the initial and boundary condition of the reactor. It will influence the whole evolution of the accident as, for instance, it can lead to a strong delay or an anticipation of the starting of the fuel uncovering and degradation. Moreover, the thermal-hydraulic state of the reactor during the fuel melting phenomena strongly affects the evolution of the degradation and of its consequences: it drives the oxidation kinetic and hence the hydrogen production; determines the fuel cooling condition; affects the pressure evolution of the Reactor Pressure Vessel (RPV) and of the containment (which could cause anticipated failures); drives the FPs transport; etc. In general, thermal-hydraulic phenomena and core degradation phenomena are strongly related and influence each other during all the evolution of a SA.

Core uncovering

The accident evolves to the point where fuel rods are no longer completely covered by coolant as a consequence of a leakage (loss of coolant), or as a consequence of the boiling and evaporation of the coolant (loss of cooling conditions). It can be reached within a matter of minutes, hours, or days from the initiator event, depending on the thermal-hydraulics evolution of the sequence. For example, in case of a 10 cm

break in the Reactor Coolant System (RCS) of a PWR, if water is not injected into the primary system by the Safety Injection Systems (SIS), the complete uncovering of the fuel rods is reached in around 30 minutes [1]. If a sufficient level of cooling cannot be restored, the uncovering leads to the starting of core structures degradation. Progression and consequences of the accident can vary also depending on the vessel pressure at the time of uncovering. A "high-pressure core melt accident" is considered to take place if the vessel pressure is higher than 15 - 20 bar.

In-vessel fuel degradation: Failure of fuel-rod cladding (first containment barrier)

Following the uncovering of part of the active fuel, the residual heat produced in the nuclear fuel is no longer completely removed from the core by the coolant and, as a consequence, the uncovered parts of the active fuel rods start to heat up. The Zircaloy cladding of fuel rods, enclosing the nuclear fuel pellets (generally made of UO_2), is at normal operation at a maximum temperature of $350\text{ }^\circ\text{C}$. The degradation of the Zr mechanical properties, at about $700 - 900\text{ }^\circ\text{C}$, leads to the starting of deformation of the cladding.

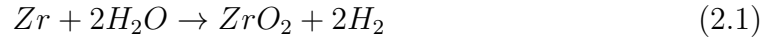
At this point it is important to make a distinction: the vessel pressure may be greater or lower than the rods gap pressure (pressure of the inert gases, usually helium, filling the gap between the fuel pellets and the cladding):

- if the pressure of the gap is higher than vessel pressure, the cladding will swell until it bursts;
- if the pressure of the gap is lower than vessel pressure, the cladding will push and get in touch with the fuel pellets, promoting the formation of $UO_2 - Zr$ eutectic with a melting point of $1200 - 1400\text{ }^\circ\text{C}$, which is much lower than the Uranium dioxide fusion points.

The loss of cladding integrity determines the loss of the first barrier containing the radioactive materials. The first FPs released out of the fuel are the most volatile materials and noble gases.

In-vessel fuel degradation: Zr oxidation, Hydrogen risks and FPs release

One of the main phenomena, playing a key role in aggravating the degradation of the core, is the oxidation of the rods cladding made of zirconium (but also of the other Zr core structures) in contact with superheated steam. The chemical equation of this oxidation is:



The reaction starts at about 1200 °C and it is an exothermic chemical reaction with the energy released between 600 and 700 kJ/mole of reacting Zr. At a temperature around 1500 °C, the heat supplied to the cladding cannot be removed by convection with the steam, and it leads the reaction to accelerate determining a rapid escalation of the core temperature. This phenomenology is known as "reaction runaway". The heat released can reach peaks higher than the residual heat power during this phase. As can be stated by the chemical equation, there is also a production of molecular hydrogen, released into the core and carried through the RCS to the containment. Here, the presence of the air can cause ignitions producing deflagration that, under certain conditions, leads to a detonation and hence to the probable failure of the containment (as appended in some units in the Fukushima accident). During the reaction, the cladding Zr is gradually substituted by a ZrO₂ layer, which is more brittle but has a higher melting point than Zr.

In this part of the degradation volatile FPs are released by the fuel pellet, and the rate of release can be considered to increase with the escalation in the temperature of fuel pellets. A scheme of the early core degradation evolution of phenomena at the different core temperatures is reported in Fig. 2.1.

In-vessel fuel degradation: Melting and relocation of core materials

The melting of control rods components starts below 1200 °C, depending on the control rods type and the formation of eutectic mixtures dissolve the steel structural components before the steel melting temperature is reached. When the Zircaloy melting point is reached (about 1760 °C), also the fuel UO₂ starts to be partially dissolved by the liquid metal in contact with it (formation of UO₂ - Zr eutectic). Above 1800 °C, the still solid core components (mainly oxides) begin to melt. This degradation process results in the local loss of mechanical integrity of the fuel rods (loss of core geometry) and in the production of partially solid "debris" (fragments of core materials) and of molten "Corium". It is called Corium the molten mixture of fuel and materials of the core structures, which is heated up and kept molten by the decay heat of the FPs in the mixture. The loss of core geometry and accumulation of degraded materials may also be responsible for the blockage and obstruction of core zones in case a coolant flow is reestablished.

The ultimate melting point of the UO₂ is reached at approximately 2800 °C. At these temperatures, all the volatile and semi-volatile FPs entirely escaped from the fuel. The corium mass advances through its relocation and solidification in colder

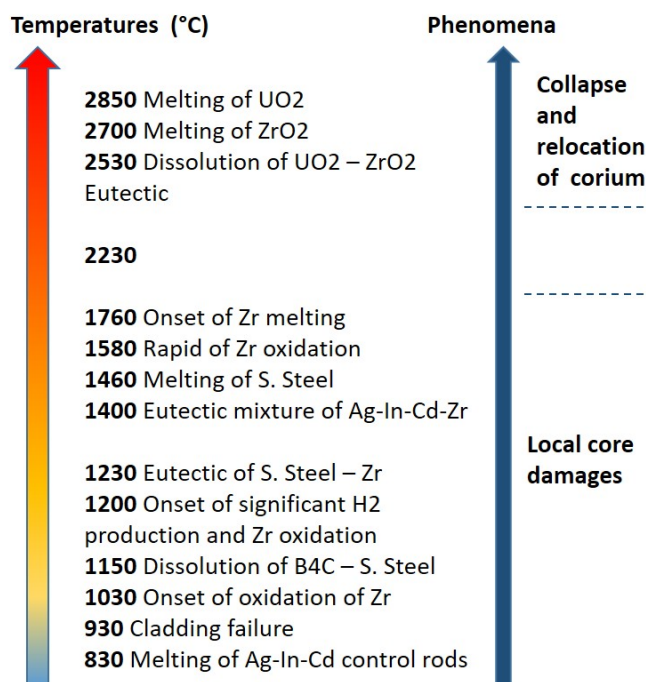


Figure 2.1: Temperatures evolution and main phenomena in early core degradation [1].

and still solid areas, until the liquefaction and collapse of this area are reached. In this way, the molten pool expands axially and radially until it reaches the core support plate.

In-vessel fuel degradation: LP retention

Reached the failure of the core support plate, part of the corium mass relocates in the Lower Plenum (LP) of the vessel, which in most cases contains water. The interaction of corium with the coolant leads to instantaneous production of a large quantity of steam (or even a “steam explosion”) which causes very fast pressurization of the RCS and could challenge its integrity. The same explosive interaction leads to the fragmentation (and fast oxidation) of part of the hot corium into solid particles, which accumulate in the LP bottom creating a “debris bed”. In some time, the corium evaporates the water eventually left in the LP, the temperature reaches the melting temperature of steel and the corium embodies the LP structures. At this point, depending on the previous accident evolution, the pool of molten materials in the LP may contain a different concentration of oxides and metals, and may or may not lay on solid debris bed or on a solid crust separating

it from the Lower Head (LH) structure.

Several tests proved the formation of immiscible liquid phases in the pool, metallic and oxides phases. Depending on the oxidation degree of the materials (mainly Uranium, Zircaloy, Steel and their oxides) and, consequently, on their density, the stratification may feature a bottom metallic layer under an oxide top layer or vice versa. In a classic configuration, a thin metallic lighter top layer (Zr , Fe , U) lays over a bottom oxides pool (ZrO_2 , FeO_2 , UO_2). Such configuration, shown in Fig. 2.2, results in the heat flux to the LH structure being concentrated in the more conductive top metallic layer. This phenomenon, which is one of the main threats to vessel integrity, is known as the “focusing effect”. The erosion of the vessel may take place in any case also due to the erosion of the $Fe - U - Zr$ eutectic mixture, dissolving the steel structures at a temperature of about $1100\text{ }^\circ\text{C}$.

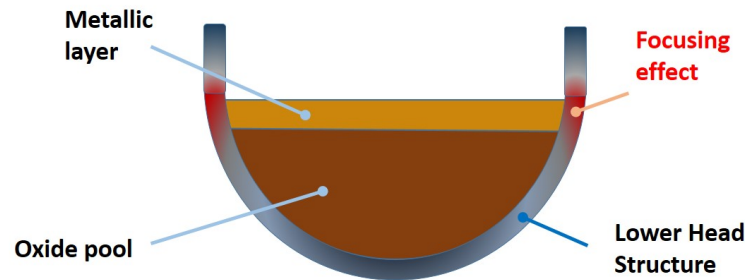


Figure 2.2: Stratification configurations of corium materials in LP with focusing effect.

The possibility of containing the molten pool in an LP sufficiently cooled by external water is called IVMR strategy, and its feasibility has been investigated for different reactors designs, pool configurations and external cooling regimes [12][13].

Ex-vessel fuel degradation: LH failure and Molten Core - Concrete Interaction (MCCI)

The LH of the vessel may be breached by the corium within a matter of minutes or hours and, after that, the core would drop in to the pit of the Reactor Cavity (RC). Also, in this case, the presence of water in the RC could cause a steam explosion, threatening the containment integrity. The following long-time interaction between corium and concrete of the basement is called Molten Core - Concrete Interaction (MCCI). This scenario is characterized by the gradual erosion (ablation) of the pitted concrete by the corium mass, driven by the residual heat that is continuously produced.

More in details, the MCCI erosion features the decomposition of concrete (made mainly of SiO_2 , $CaCO_3$, H_2O), which causes the dissolution of material in to the corium pool (SiO_2 , CaO) and the release of gases into the above containment atmosphere (H_2O , CO_2 , CO , SiO , H_2), contributing also to increase its pressure and changing its composition. It is estimated that the penetration time for the concrete basement can be from one to several days, depending on the type of concrete and on the corium features (e.g. composition, residual heat).

Some of the most recent types of the reactor (s.e. EPR) include the adoption of a “Core catcher” which aims to protect the containment basement from MCCI by creating a sufficiently large and thin layer of corium on an appropriate material surface (corium spreader) so that the corium can be flooded and cooled by water from the containment.

Phenomena that may threaten the integrity of containment barrier

The main phenomena that might threaten the integrity of containment barrier during the evolution of a generic SA are listed below.

- Induced Steam Generator (SG) tube rupture: if the RCS is pressurized during in-vessel core melting, its SGs structures may yield and break. The induced rupture of the SG tubes would cause fission products to be transferred to the secondary system loops and then released directly to the outside atmosphere via the secondary safety valves, therefore bypassing the reactor containment barrier.
- Direct heating of gases in the containment: if the RCS is pressurized when the vessel fails, corium may be ejected outside at high velocity and be dispersed into the containment causing a fast rise in pressure because of the rapid heat-transfer from the molten corium to the containment atmosphere. This phenomenon is called “direct containment heating” and may cause the failure of the containment. (High-pressure core melt should be always avoided by mitigation management action).
- Hydrogen risk: as previously mentioned in this chapter, it is the possibility of a loss of containment integrity due to hydrogen deflagration in an oxidizing atmosphere (air). H_2 is produced by the oxidation of core materials and by MCCI. Catalytic recombiners able to reduce the mass of H_2 are located in the containment of several reactors. Other advanced reactors adopt an inert containment atmosphere (e.g. N_2).
- Steam explosion: The corium may come into contact with a large quantity of water after the relocation in the LP or in the RC. This contact can cause

a high energetic interaction, the corium may be highly fragmented and cause massive, instantaneous water vaporization, known as a “steam explosion”, with a consequent dangerous increase of the containment pressure.

Release, transport and chemistry of FPs

FPs are produced during the fission reactions due to the effect of neutron interaction with fuel. Their inventory and their quantity depend on the type and on the story of the nuclear fuel inside the reactor (burnup) and outside (in fuel spent pool). At the onset of the cladding failure, the gaseous (Kr , Xe) and the most volatile FPs (I , Ce , Br , Ru , Te , Sb , etc.), that have accumulated in the fuel rods gap, are released into the vessel and the primary system. The same happens for part of FPs initially trapped in the fuel pellets: volatile FPs are progressively released by the pellets as temperature increases and core degradation advances. Nearly all volatile and semi-volatile FPs will have escaped from the fuel by the time it starts to melt.

The transport of FPs to the containment and eventually to the environment depends on their physical and chemical evolution in the facility. The transport of each volatile FP is mainly determined by its phase (gas or aerosol), by its chemical form, and by the thermal-hydraulic and chemical conditions encountered in the reactor. The mass of aerosols FP (which can be considered also aerosol deriving from core structures and control rods) released into the containment may be high: it is estimated to be around 1500 kg for a 900 MWe PWR. However, in a short time and static conditions, the aerosols agglomerate and sediment in the containment, which means a very high reduction of the suspended. Yet, the deposited aerosol may also resuspend because of dynamic phenomena taking place in the containment (s.a. steam explosions, H_2 deflagrations).

Particular attention is dedicated to the study of the Iodine behavior due to its complexity and to the potential short-term radiological consequences whether released in the environment. The main chemical and physical forms that can be found in the containment atmosphere are gaseous molecular iodine (I_2), particulate iodine (in aerosol form, s.a. cesium iodide [CsI]) and gaseous organic iodine (e.g., methyl iodide [CH_3I]). Organic iodine is the most dangerous as it is the hardest to be trapped for the existing filtration systems. Strongly simplifying, during a SA, iodine is released in the form of aerosol particles and gas (molecular iodine) into the RCS and then to the containment. Here, the gaseous molecular iodine may undergo several phenomena: it is adsorbed by the paint on the containment walls, with which it reacts to release gaseous organic iodine; in case containment spray system is actuated, a portion of gaseous iodine mixes with water in the containment sumps; in addition, part of the gaseous iodine is also released outside the containment

by direct or filtered leaks paths. The iodine in form of aerosol is deposited (for thermophoresis, sedimentation, etc.) on the containment walls and floors and can be transported to sumps by condensed water. Iodine in sumps, on the base of the physical and chemical conditions of the water and under the effect of radiations, may feature complex chemical reactions ending to the formation of gas molecular iodine (I_2), that evaporates again into the containment atmosphere. Organic iodine in gas form (as well as FPs gases, s.a. Xe , Kr) does not deposit, but it may be released outside the containment through direct, indirect, or filtered leaks; and part of it is also converted by radiation into iodine oxides (very fine aerosols).

Bibliography

- [1] A. Bentaïb, H. Bonneville, and G. Cénérino, *Nuclear Power Reactor Core Melt Accidents: Current State of Knowledge*. EDP Sciences, 2021, ISBN: 9782759819300. DOI: [doi:10.1051/978-2-7598-1930-0](https://doi.org/10.1051/978-2-7598-1930-0). <https://doi.org/10.1051/978-2-7598-1930-0>.
- [2] B. R. Sehgal, Ed., *Nuclear safety in light water reactors: severe accident phenomenology*. Academic Press, 2012. DOI: <https://doi.org/10.1016/C2010-0-67817-5>.
- [3] *Defence in Depth in Nuclear Safety*, ser. INSAG 10. Vienna: International Atomic Energy Agency (IAEA), 1996, ISBN: 92-0-102596-3. <https://www.iaea.org/publications/4716/defence-in-depth-in-nuclear-safety>.
- [4] *In-vessel Melt Retention and Ex-vessel Corium Cooling*, ser. IAEA-TECDOC 1906. Vienna: International Atomic Energy Agency (IAEA), 2020, ISBN: 978-92-0-106320-5. <https://www.iaea.org/publications/13576/in-vessel-melt-retention-and-ex-vessel-corium-cooling>.
- [5] M. Fischer, O. Herbst, and H. Schmidt, “Demonstration of the heat removing capabilities of the epr core catcher,” *Nuclear Engineering and Design*, vol. 235, no. 10, pp. 1189–1200, 2005, Festschrift Edition Celebrating the 65th Birthday of Prof. Richard T. Lahey, Jr., ISSN: 0029-5493. DOI: <https://doi.org/10.1016/j.nucengdes.2005.02.022>.
- [6] E.-A. Reinecke, I. M. Tragsdorf, and K. Gierling, “Studies on innovative hydrogen recombiners as safety devices in the containments of light water reactors,” *Nuclear Engineering and Design*, vol. 230, no. 1, pp. 49–59, 2004, 11th International Conference on Nuclear Energy, ISSN: 0029-5493. DOI: <https://doi.org/10.1016/j.nucengdes.2003.10.009>. <https://www.sciencedirect.com/science/article/pii/S0029549303003832>.

-
- [7] G. Petrangeli, *Nuclear safety*. Elsevier, 2006. DOI: <https://doi.org/10.1016/B978-0-7506-6723-4.X5000-1>.
- [8] *IAEA Safety Glossary: 2018 Edition*. Vienna: INTERNATIONAL ATOMIC ENERGY AGENCY, 2019, ISBN: 978-92-0-104718-2. <https://www.iaea.org/publications/11098/iaea-safety-glossary-2018-edition>.
- [9] H Nowack, P Chatelard, L Chailan, V Sanchez, L Herranz, *et al.*, “Cesam-code for european severe accident management, euratom project on astec improvement,” *Annals of Nuclear Energy*, vol. 116, pp. 128–136, 2018.
- [10] <https://www.fastnet-h2020.eu/>.
- [11] F Mascari, F Carny, F Rocchi, *et al.*, “FASTNET scenarios database development and status,” *Proceedings of ERMSAR2019*, 2019.
- [12] <https://cordis.europa.eu/project/id/662157>.
- [13] F. Fichot, L. Carenini, M. Sangiorgi, *et al.*, “Status of the IVMR project: First steps towards a new methodology to assess In-Vessel Retention Strategy for high-power reactors,” in *ERMSAR Conference, The 8th European Review Meeting on Severe Accident Research, 16-18 May 2017, Warsaw, Poland, ERMSAR Conference, The 8th European Review Meeting on Severe Accident Research, 2017, JRC106398..*
- [14] <https://musa-h2020.eu/>.

CHAPTER 3

Core melt accident simulation codes

Nowadays, thanks to the huge advancement in computer science and the development of a massive calculation power, nuclear safety studies are carried out and supported by numerical calculations performed with everyday more accurate and powerful computer codes. Numerical codes aimed at the simulation of NPP core melt accidents started to be developed in the 1970s in the US; in Europe and Japan, it started only in the late 1980s, in parallel with PSA studies. In the following years, SA codes become of more popular use in nuclear safety research for studying and developing reliable mitigation management actions; but also for training of reactor operators [1].

After a general overview of SA integral codes, the present chapter of the thesis is aimed at introducing the ASTEC code and its features. As an example of code application, the chapter concludes with a code-to-code benchmark, in which the two SA codes ASTEC and MELCOR have been compared in the simulations of the same core melt accident, postulated to take place in a generic French PWR 900 MWe.

3.1 Introduction to Integral codes for SA simulation

3.1.1 Integral and Mechanistic codes for SA simulation in LWR

Core melt simulation codes can be generically divided into two categories:

- Integral codes: aimed to simulate the entire SA, from the initiating event up to the estimation of the radioactive release in the environment;
- Detailed or mechanistic codes: to simulate in detail more specific phenomena involved in a particular accident phase (s.a. early cladding failure, core degradation, steam explosions, FPs transport, etc.)

Integral codes and mechanistic codes adopt different approaches: the first usually use correlations derived from experiments, which implies that they can only be used within the scope of the correlations in question and within the limits given by the experimental knowledge. With a different approach, mechanistic codes calculate numerical solutions of differential equations describing the phenomenon /set of phenomena of interest [1].

Integral Codes

US started to develop two integral codes during the 1980s, after the TMI accident: MELCOR [2], for the regulatory authorities, and MAAP [3], intended for the nuclear industry. France and Japan began to develop their integral SA codes at the end of the 1980s: THALES, developed by JAERI and ASTEC [4], developed in collaboration by the French IRSN and the German GRS. In the early 2000s, also the Russians began to develop their own SA integral code, SOCRAT.

A core melt integral code should provide exhaustive coverage of all the (main) physical phenomena involved in a core melt accident (described in chapter 1) and, also, to be able to couple all these phenomena which come into play on different spatial and temporal scales. They should also provide the possibility to simulate the behavior of reactor control logic and of the main safety systems. Usually, the adoption of a modular/packages structure provides the possibility to independently model the different phenomena to be coupled and allow the validation against experimental results for the single phenomenon. SA integral codes for LWR are in general based on the more consolidated thermal-hydraulic integral codes. Accordingly, they usually employ a module (or a package) based on the 5 or 6 balance

equations approach for the two-phases fluid. A great effort is now being conducted by the international research community to improve knowledge and reliability of the modules (or a package) dedicated to the complex and less consolidated SA phenomena. These codes incorporate in their models and correlations all the knowledge of the past 30 years of research and experimental campaigns in the SA field; as well as the knowledge deriving from various scientific disciplines (s.a. thermo-dynamics, thermal-hydraulics, structural mechanics and chemistry). Integral codes do not generally cover steam explosion or containment mechanical strength, which are covered by specific mechanistic codes.

Nowadays, three SA integral codes are mainly used within the word nuclear-safety community: ASTEC, developed by IRSN; MELCOR, developed for the US Nuclear Regulatory Commission (US NRC) by Sandia National Laboratories; and MAAP, developed by the American Fauske & Associates. These are used in reactor safety studies and in particular to estimate the radioactive releases to the environment of a SA sequence and in level-2 PSA analyses. They are also employed in the characterization of management mitigation strategies for core melt accidents to define or improve severe accident operating guidelines, mitigation procedures and reactor safety systems.

Mechanistic codes

Despite the growth in the accuracy of models included in integral codes, mechanistic codes often serve as references to determine the validity of integral code results. Generally speaking, these codes are used to simulate specific phenomenology in the specific area of the reactor and their main goal is to provide a more detailed understanding of physical phenomena and to reduce uncertainties. For this reason, they include detailed, state-of-the-art models known as “best-estimate” models. Computing time is generally long, it can take several weeks to perform calculations for one day of accident [1].

3.1.2 Development and validation of Integral codes

Integral simulation codes are aimed to reproduce the behavior of the considered physical phenomena involved in steady, DBA and BDBA of a full-scale plant. In this framework, the aim of code validation is to evaluate the code accuracy in the simulation of overall system dynamics, reactor components interactions and local component phenomena [5]. Due to the difficulties and huge costs of performing the thermal-hydraulic test at full scale, the code has usually to be validated against scaled-down experiments which are characterized by well-known scaling distortions.

Regarding core-melt phenomena, we have to add the impossibility to use real nuclear fuel materials in experimental tests; yet simulant materials with similar properties have to be used. Plant data (mainly thermal-hydraulic transient data, start-up test, etc), are not affected by scaling and materials issues. However, only a few parameters are available from the full-scale plant in comparison to experimental tests and, regarding SA data, very limited information are available (s.a. from Three Mile Island - 2 and Fukushima Daiichi).

Levels of SA code validation

In general, code validation can be carried out at the following 3 different levels [1]:

- Validation of a physical model implemented in the code against results of separate-effect tests (often carried out on a small scale and, eventually, by using simulant materials);
- Validation against integral tests usually at large scale (for example on rod clusters of actual height) and using real materials;
- Validation by applying the code to real reactor accident scenarios. In particular, through sensitivity studies on model parameters, by comparison with other validated codes, or by simulation against data available from real reactor accident (s.a. Three Mile Island - 2 and Fukushima Daiichi).

Phases of code development and validation

According to [5], the Code Internal Development can be considered the first step of code validation, in which the modules implemented in the code and the global code architecture are qualified (e.g. verification of code design and source code, identification and fixing of errors). After this phase, the code has to be subjected to the Code Independent Qualification, whose objective is to evaluate code accuracy. This evaluation is carried out by an independent user by a qualitative and a quantitative assessment, through the comparison of calculated transient against the measured data developed in a scaled test facility. The evaluation of qualitative code accuracy includes the following steps: qualitative comparison between experimental and calculated trends; qualitative comparison of main quantities characterizing the sequence; qualitative evaluation of accuracy based on phenomena included in the CSNI matrix (e.g. [6], [7], [8]); qualitative evaluation of accuracy based on the “sequence relevant aspects” (aspects of events related to the main physical process).

The positive conclusion of the qualitative accuracy evaluation is followed by the quantitative accuracy evaluation, to be carried out through a quantitative accu-

racy evaluation methodology, such as the Fast Fourier Based Transform Method (FFTBM) [9][10].

Another component of the Code Independent Qualification is the Assessment of the Scaling-up Code Capability. Since the main objective of a code is to simulate full-scale reactors, it is used in the simulations of tests at different scales with the same (or similar) initial and boundary conditions. This kind of test is called Similar/Counterpart test [11]. In conclusion, one of the most important element of the Code Independent Qualification, is the international common consensus, to be matured in the framework of international research activities. Examples are the International Standard Problem (ISP) of the OECD-NEA [12], the International Collaborative Standard Problem (ICSP) of the IAEA (e.g. [13], [14]) and the international recognized Code Validation Matrix (e.g. [6], [7], [8]).

3.2 The ASTEC code

ASTEC (Accident Source Term Evaluation Code) [4][15] is developed by the French “Institut de Radioprotection et de Sûreté Nucléaire” (IRSN). It aims at simulating an entire SA sequence in nuclear water-cooled reactors from the initiating event through the release of radioactive elements out of the containment. ASTEC has progressively become the European reference code for the analyses of SA progressions in LWR thanks to the intensification of joint research activities mainly carried out in the framework of the SARNET European Network [16]. ASTEC covers most of the physical phenomena involved in SA, except steam explosion and mechanical response of the containment. Its main applications are source term evaluation studies, PSA-2 studies, accident management studies and physical analyses against experiments to improve the phenomenology understanding.

3.2.1 Modules of ASTEC code

ASTEC features a modular structure (Fig. 3.1) where each module is aimed to simulate a specific set of physical phenomena or related to a specific part of the reactor. A module of ASTEC is itself a code and can be used either stand-alone (for module validation and separate-effect tests) or in coupled mode with the other modules. An introduction of all the code modules will be covered in this section, focusing the attention on those involved in thermal-hydraulic and in-vessel core degradation phases which are of main interest for the present work of thesis.

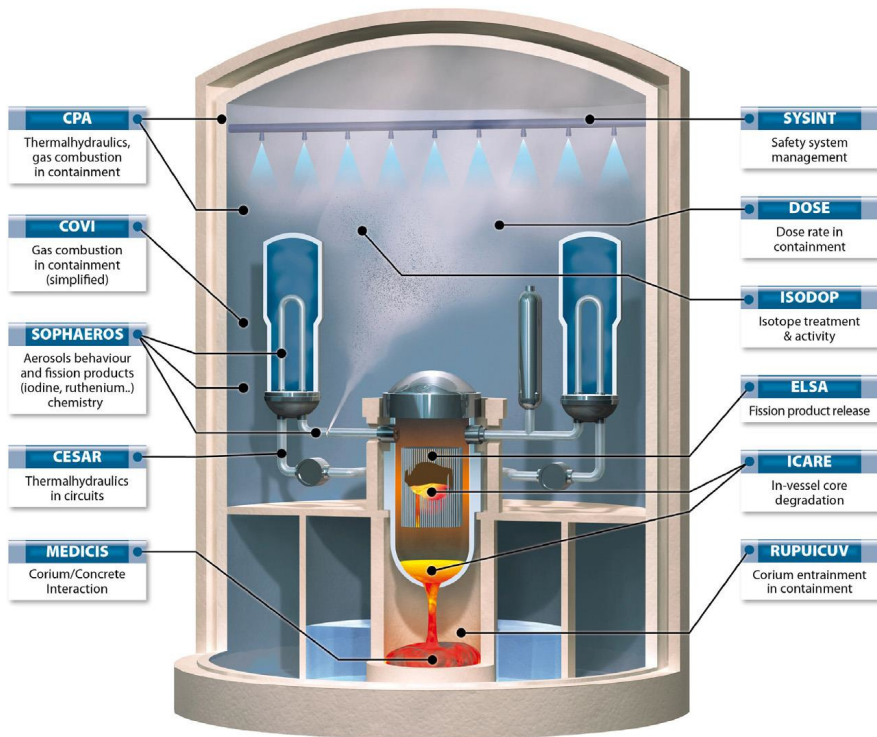


Figure 3.1: Scheme of ASTEC modules and structure [4].

CESAR module: thermal-hydraulics in primary and secondary system

CESAR [17][18] is the module of ASTEC dedicated to the simulation of the RPV, primary and secondary systems thermal-hydraulics. It is a one-dimensional two-phase thermal-hydraulic system code, based on a 5 or 6-equations two-phase flow model: two mass balance equations, two energy balance equations, and two momentum balance equations (one mean momentum equation in case of 5-equations, with the addition of phase-slip model). In the current version of ASTEC (V2.2) the two-fluids 6-equations model is used as default. Up to five non-condensable gases can be considered in the CESAR gas phase. As a result, the total number of differential equations to solve is 6, plus an equation for each incondensable gas:

- $2 + nI$ mass balance equations ($nI < 5$ is the number of non-condensable gasses): one mass balance equation for the gas mixture, nI mass balance equations for nI non-condensable gases, and one mass balance equation for the liquid;
- 2 energy balance equations: one for the gas mixture (vapor and non-condensable are considered to be in thermal equilibrium), and one for the liquid phase. 1 mean momentum balance equation with the mean velocity as a state variable;

- 2 momentum balance equation (1 mean momentum equation and 1 drift algebraic equation in case of 5-equations model).

CESAR adopts a finite volumes discretization approach using a staggered grid, where the velocity solution of the momentum balance equations is calculated on the junctions of the grid; all the other scalar variables such as pressure, void fraction and temperature, associated with the scalar equations of mass and energy conservation, are integrated on the volumes. To simulate fluids heat transfer with the solid structures of the reactor, solid walls can be defined in CESAR. The walls are connected to the thermal-hydraulic volumes and the heat transfer coefficient is evaluated on the base of a boiling curve [17][19], depending on void fraction, fluids velocities, and pressure in the volume and wall temperature. The time discretization of the basic equations is applied to adopt a first-order backward difference scheme. The system of discretized equations is solved using the Newton-Raphson method.

ICARE module: in-vessel fuel degradation

ICARE [20] is the ASTEC module dedicated to the modeling of the reactor vessel and core components. It employs 2D geometrical objects (MACRO-COMPONENTS) able to reproduce most of the internals of the core. The core is discretized in cylindrical rings and axial meshes and only one representative component fuel, control rods and other components are considered in each radial ring, weighted by the true number of components. The fluid channel paths are represented by objects named “CHANNEL” which complete the meshing allowing the two-dimensional axial-symmetric computation of the thermal-hydraulics inside the vessel by CESAR module. ICARE implements mechanical models, processes several chemical reactions, incorporates fission product release and describes core thermal behavior, degradation and relocation in the LP, until the rupture of the LH. More in detail, ICARE implements the following physical models in ASTEC V2:

- Heat transfer: axial and radial conduction between walls, gap exchanges between rod and cladding, convection between fluid and wall as well as radiation. The heat transfers is calculated during the evolution of core geometry degradation with specific models.
- Rod mechanics: ballooning, creep and the burst of *Zr* fuel rod claddings, creep of control rod steel claddings, loss of integrity of fuel rods (using user-defined criteria).
- Chemistry: oxidation of *Zr* and stainless steel by steam; dissolution of UO_2 by *Zr*; dissolution of *Zr* by liquid *Ag – In – Cd* and by solid steel; oxidation/dissolution of relocated magma; oxidation of solid debris.

- Reflooding of intact or slightly degraded cores: based on a special tracking of the quench front evolution.
- Material melting and relocation (both in early and late degradation phases): formation of debris and magma, 2D movement of magmas and corium slump into the lower plenum.
- Corium behavior in lower plenum: the 2D meshing of the vessel LH combined with a 0D approach for the LP thermal-hydraulics; stratification of corium in 3 possible layers (light metallic layer, oxide pool, heavy metallic layer) and 2 possible debris layers.
- Vessel lower head rupture: melt-through or mechanical failure (either instantaneous plastic rupture or creep rupture) accounting for the corium and water loading on the LH and on other user-defined criteria.

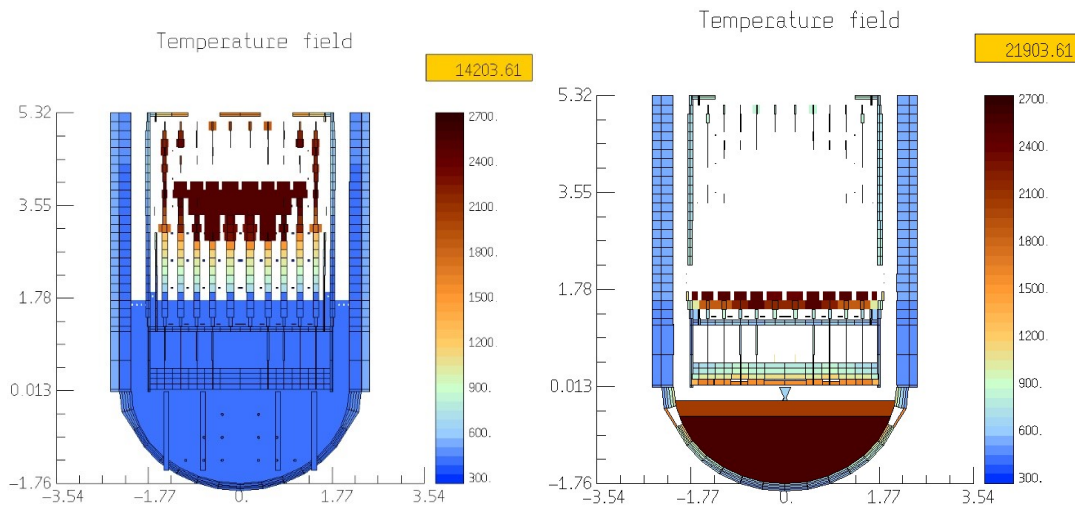


Figure 3.2: ICARE representation of degrading core in a PWR 900-like reactor.

An example of core degradation evolution simulated with ICARE module is reported in Fig. 3.2. The picture derives from the simulation of a SA in a generic French PWR 900 MWe.

ELSA module: FPs release from core

ELSA module [21] is aimed to simulate the release of fission products and structural materials in the RCS during the in-vessel core degradation; therefore, ELSA is tightly coupled with the ICARE module. The ELSA modeling allows describing the release from fuel rods and control rods, followed by the release from debris and the release from the in-core molten pool. The modeling employs a semi-empirical

approach and the physical phenomena taken into account are the main governing the release.

ISODOP and DOSE: decay heat and dose calculation

The ISODOP [22] module simulates the decay of FPs and actinide isotopes and it allows to estimate the decay heat and the isotopes inventory in the different zones of the reactor. The calculation is started by using an initial isotopes inventory for the fuel, which can be externally generated by a dedicated code calculation (s.a. ORIGEN calculation). During the SA transient, ISODOP considers a different isotopes inventory for each reactor “domain” and it updates the different inventories on the base of the isotopes decay and of the FPs transport calculated by SOPHAEROS. ISODOP relies on a database provided by CEA and contains the nuclear data of about 3800 isotopes. The DOSE module allows the calculation of the dose rate in the bulk gas phase, in the liquid phase and to the walls structures of each zone of the containment. The dose rates include beta and gamma radiation contributions relative to each isotope.

SOPHAEROS: FPs and aerosol transport in the RC

The module SOPHAEROS [23] is in charge of simulating the transport of vapors and aerosols FPs in the RCS and in the containment, accounting for the chemical reactions and speciation. The mass balance equation resulting from the intra-volume phenomena combined with inter-volume transport produce a non-linear system solved by the Newton-Raphson method. The code considers 6 states for the FPs: suspended vapor, suspended aerosol, vapor condensed on walls, deposited aerosol, sorbed vapor and species in water. And further 6 states specific for iodine chemistry: Species on dry-wet painted surfaces, species on dry-wet steel surfaces, species on dry-wet concrete. The phenomena that SOPHAEROS can model can be classified in the following points:

- Chemical interactions of all gas and vapor species;
- Transport of suspended vapors and aerosols by the carrier-gas; transport of species in water;
- Coagulation (or agglomeration) of suspended aerosols;
- Deposition of aerosols on structure surfaces;
- Mechanical resuspension of deposited aerosol on structure surfaces;
- Homogeneous nucleation of vapors and condensation/evaporation on/from suspended aerosols;
- Vapour condensation/evaporation related to structure surfaces;

- Vapour evaporation from deposited aerosols;
- Vapour sorption on structure surfaces (an irreversible process);
- Specific chemical interactions of iodine.

CPA: thermal-hydraulics in the containment

CPA [24] provides a tool based on mechanistic models aimed at simulating all the relevant thermal-hydraulic processes and plant states taking place in the containment compartments of an LWR (i.e., gas distribution, pressure build-up, condensation, etc.). The discretization model adopted is lumped-parameter, where the compartments are divided into control volumes whose status is defined by temperature and mass of each component. The thermal-hydraulics state of a CPA zone can be described in two approaches: Equilibrium model: by assuming water and atmosphere homogeneously mixed for saturated and superheated conditions (i.e. water and gases assumed at the same temperature); and non-equilibrium model, where deposited and airborne water is separated (separate temperatures, mass and energy balances for atmosphere and water).

Mass transfer between zones is described separately for gas and liquid flows by momentum equations accounting for the height differences. For a realistic description of the accident, models are available for the behavior of engineered safety systems such as catalytic hydrogen combiners, containment sprays and pressure suppression systems.

SYSINT: reactor safety systems management

The SYSINT module allows the user to easily simulate the management of the reactor safety systems features, s.a. reactor SCRAM, safety injection systems, pressurizer spray and heaters, management of SG and of pumps, the opening of valves, containment spray, etc.

MEDICIS and RUPUICUV: MCCI and direct containment heating

MEDICIS is the ASTEC module aimed at simulating the MCCI by using a lumped-parameter 0-D approach. And RUPUICUV is the module in charge of simulating the direct containment heating which may potentially develop after a vessel lower head rupture taking place under relatively high pressure. The application of these two modules regards the ex-vessel phenomena of a core melt accident and the framework of the present work of thesis this application will not be covered.

3.2.2 Validation of ASTEC code

The ASTEC V2 validation is supported by a large set of French, German and international experiments that cover most aspects and phenomenology of SA sequences [15]. Regarding the current validation of its thermal-hydraulic modules (CESAR, CPA), it includes comparisons against accidental scenarios and natural circulation phenomena in conventional LWR scaled facilities [18][25][26][27][28].

In particular, the CESAR module has been successfully validated vs. several well-known integral experiments, such as BETHSY 9.1b and 5.2e experiments; PACTEL ISP-33 and T2.1 experiments; PMK2-SBLOCA experiment. However, considering the scopes of this work of thesis, it is important to underline that specific validation of ASTEC modules against experimental activities for advanced integral SMR designs and passive safety systems have not been performed yet [29], but such validation studies are currently planned to be realized. Regarding thermal-hydraulic codes validation for advanced SMR, more details will be assessed in the next chapter of the thesis. The CPA module was validated in transients conditions against systems of different scales, s.a. the Phébus containment, the KAEVER vessel, the Battelle Model Containment [30].

Some examples of core degradation experiment used to validate the ICARE module are: Phébus FPT-4 experiment; CORA-13 and CORA-W2 experiments; QUENCH-11 and QUENCH-13 experiments; FARO L14 and L28 experiments; etc. [25].

For the ELSA and SOPHAEROS modules has been used a validation strategy based on both separate-effect experiments and integral experiments, as described in [31].

3.3 Example of code-to-code application for SA integral codes: ASTEC – MELCOR simulation of SBO in a generic French PWR-900

To provide a classical example of SA integral codes application, this section deals with a code-to-code comparison between the two codes ASTEC (V2.1.1.6) and MELCOR (version 2.2) on a SA sequence. Code-to-code exercises are performed in the framework of several nuclear safety research projects. These studies are useful to underline codes predictions discrepancies to evaluate models uncertainty and characterize the code state of the art. In addition, applications involving code-users give some insights about codes modeling differences and characterize the influence

of the user. Examples are reported in [32][33].

The present ASTEC - MELCOR codes comparison concern an SBO accident in a French PWR 900 MWe. The generic models (input-deck) of the reactor have been realized with the two codes by starting from the same plant data. The simulations have been carried out only within the in-vessel phase of the transient and the Figures Of Merit (FOMs) chosen for the comparison are related to main thermal-hydraulics and core degradation phenomena. The activity has been carried out in the framework of the NUGENIA TA-2 ASCOM collaborative project [34][35] coordinated by IRSN.

3.3.1 Brief introduction to MELCOR code

MELCOR (version 2.2) [2] is a fully integrated SA code aimed at simulating the thermal-hydraulics and the main severe accident phenomena characterizing an LWR during a SA and estimating the source term released in the environment. MELCOR is being developed at Sandia National Laboratories for the US NRC.

The code has a structure based on many integrated packages where each package simulates a different transient phenomenology. In particular, the Control Volume Hydrodynamics and Flow Paths packages simulate the mass and energy transfer between control volumes; the Heat Structure package simulates the thermal response of the heat structure; the Core package evaluates the behavior of the fuel, core and LP structures including the degradation phenomena; the Cavity package models the core-concrete interactions; the Radionuclide package characterizes the aerosol behavior, transport, dynamics and deposition, and removal by engineering safety features. It is to underline the role of the Volume Hydrodynamics/Flow Paths packages that provide the boundary condition for other packages.

The code is based on a “control volume” approach. MELCOR can be used with the Symbolic Nuclear Analysis Package (SNAP) [36] for the development of the nodalization and for post-processing, by using its animation model capabilities.

The validation of the MELCOR code is based mainly on comparison with analytical results; code to code benchmark with other validated computer codes; validation against experimental data; and comparison to published real accident/events [32].

3.3.2 Codes models of the generic PWR 900 MWe

PWR-900 ASTEC model description

The reactor model used for the ASTEC calculation is the generic PWR 900 MWe input-deck provided by IRSN with the release of ASTEC, and it has been used as a reference model to develop the MELCOR input-deck. The primary and secondary system nodalization is realized with CESAR module and a scheme is shown in Fig. 3.3. The primary circuit features 3 independent loops (Hot Leg (HL), Pressurizer (PRZ), SG tubes, main pump and Cold Leg (CL)) and it includes the top parts of the vessel (upper plenum, collector, etc). The secondary circuit includes the secondary side SGs and the Steam Lines (SLs). The ICARE model of the reactor core is discretized with 5 radial regions and 16 axial segments plus the LP volume; and it considers all the main core internal structures (vessel, barrel, fuel rods, control rods, grids, plates, etc.), as Fig. 3.4 - left. The containment is realized with CPA module (Fig. 3.4 - right).

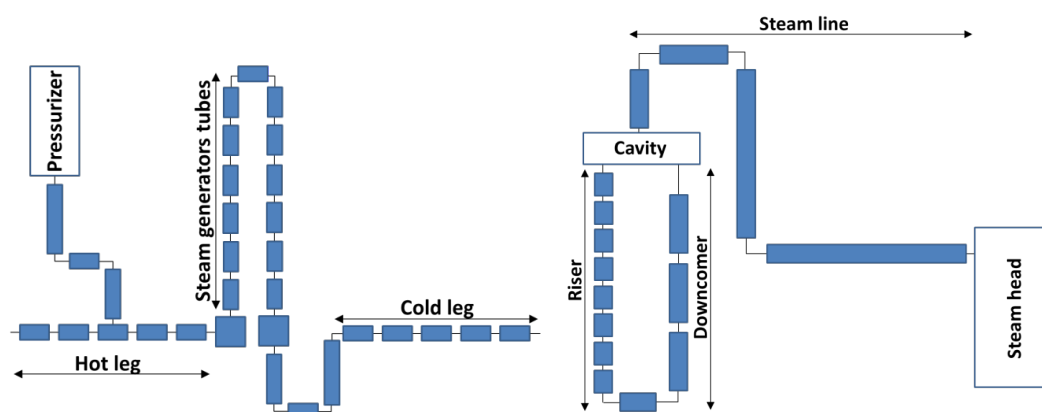


Figure 3.3: ASTEC-CESAR nodalizations of the primary circuit (left) and of the secondary circuit (right) of a the generic PWR 900 MWe [37] (only one line is represented for each circuit).

PWR-900 MELCOR model description

The nodalization realized with MELCOR [32][38] has been developed considering the plant information reported in the 2013 Foucher reports [39][40], and the ASTEC input files provided by IRSN during the EU-CESAM project [41]. It has been revised along the EU-FASTNET [42][43] and EU-IVMR [44][45][46] projects. Like the ASTEC model, the three cooling loops are modeled separately and the PRZ is modeled with one equivalent volume. The U tubes of each SG, are modeled

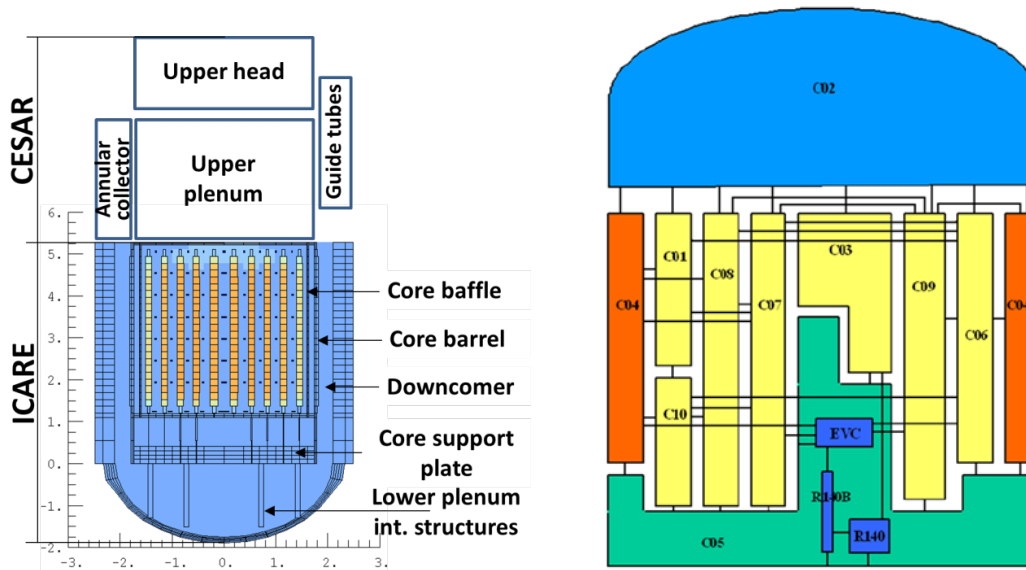


Figure 3.4: ASTEC nodalization of vessel (left) and of containment (right) of a the generic PWR 900 MWe [37]

with two equivalent regions and the SG secondary side is made of three different volumes (SG downcomer, riser and cavity). Fig. 3.5 - left shows the overall RCS thermal-hydraulic nodalization. The core thermal-hydraulics is modeled by a single Hydrodynamic Volume coupled with the Core package model, in which the core is discretized with 17 axial regions. 5 radial regions are used for the active core in agreement with the ASTEC model. The containment features a simple nodalization made of one hydraulic volume coupled with several heat structures having the same surfaces and thermal inertia of the ASTEC input; while a separate volume models the cavity. The model parameters used in the early SOARCA project [47] or the code default values are selected. The value of 2500 K is used for the melting temperature of Uranium-dioxide and Zirconium-oxide [48].

3.3.3 Steady-state calculations comparison

Close nominal operation conditions have been reached by the two codes in the respective steady-state simulation. Table 3.1 shows that the two codes are in general characterized by matching and stable initial conditions. The ASTEC operational values have been assumed as a reference for the comparison.

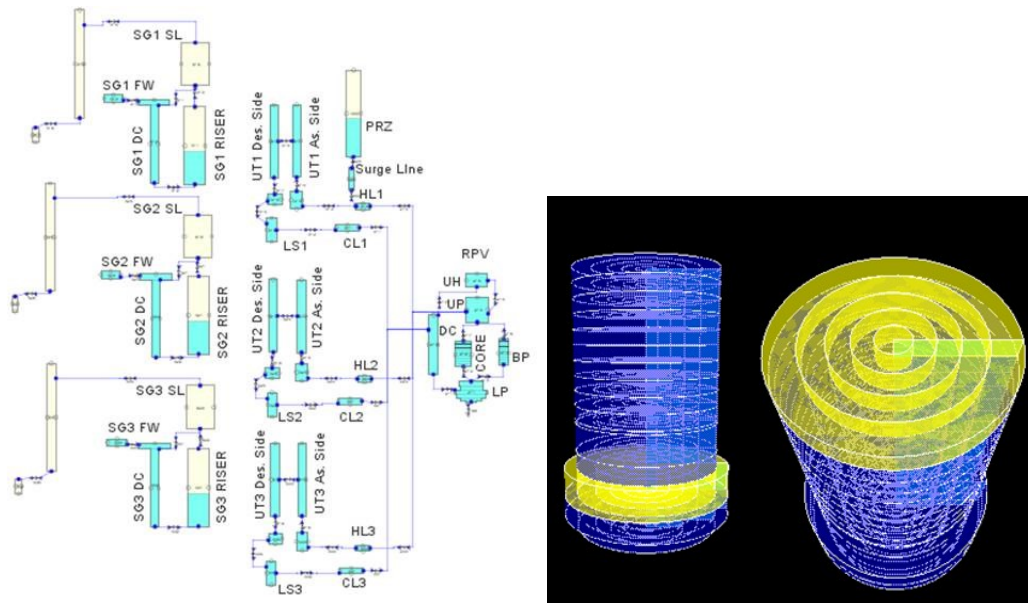


Figure 3.5: MELCOR overall nodalization of the generic PWR 900 MWe developed by using SNAP (left) and core representation (right) [37]

Parameters	ASTEC value	MELCOR Value	Discr. %
PRZ Pressure (bar)	155.	155.	0.00
PRZ Level(%)	50.	50.	0.00
CL 1,2,3 Flow Rate (kg/s)	4735.3, 4736.87, 4730.54	4735.8, 4736.0, 4736.5	0.01, 0.02, 0.13
Core Flow Rate (kg/s)	13660.59	13650.52	0.07
Bypass Flow Rate (kg/s)	267.15	282.3	5.67
Primary Mass (kg)	204150	197296.22	3.36
Inlet Core Temperature (K)	559.72	559.8	0.01
Outlet Core Temperature (K)	595.33	594.6	0.12
SG-1,2,3 Pressure (bar)	57.86	57.7	0.28
SG-1,2,3 Liquid Mass (kg)	47210.0, 47210.0, 47210.0	44312.0, 44334.0, 44336.0	6.8, 6.1, 6.1
SG-1,2,3 MFWS Flow Rate (kg/s)	511.89, 510.79, 510.81	512., 511.7, 512.	0.02, 0.18, 0.23
SG-1,2,3 Recirc. Ratio	4.24, 4.25, 4.25	4.14, 4.15, 4.14	2.36, 2.35, 2.59

Table 3.1: MELCOR versus ASTEC steady-state conditions before the SOT.

3.3.4 SBO transient calculations comparison

The postulated SA scenario taking place in the generic French PWR 900 MWe is an unmitigated SBO, where the accident initiator event is the loss of offsite Alternating Current power with the failure of all diesel generators. The plant operational point before the Start Of the Transient (SOT) is the nominal working point, reported in Table 3.2. All the reactor safety systems have been assumed unavailable, except for the ACCumulators (ACCs) passive injection. The only SA management action assumed to take place is the opening of the Safety Valves of Pressure Compensator (SEBIM) upon reaching the core outlet temperature set-point of 650°C. The automatic opening of the primary and secondary sides Steam Relief Valves (SRVs) at the respective design pressures is also considered. The sequence has been analyzed until the LH failure and can be divided into 4 main Phenomenological Windows (PhWs), according to [37]. The timing of the main events of the sequence is reported in Table 3.2 for the two simulations.

Event (s)	ASTEC	MELCOR
SG-1,2,3 Cycling Inception	8	20
SEBIM Cycling Inception	3880	4013
Two-Phase Inception in the HL	6000	6100
Top of Active Fuel (TAF) uncovered	7950	7240
Start of H_2 production	9000	8280
SEBIM stuck open	9270	9315
First Bottom of Active Fuel (BAF) uncovered	9350	9465
ACC injection start	9870	10515
Cladding T > 1300K	10080	8655
Cladding T > 1855K	12790	9215
Second BAF uncovered	12900	16905
Massive slumping inception	19070	21565
Vessel failure	21970	22350

Table 3.2: SBO transient in PWR 900-like, sequence of Main events ASTEC – MELCOR.

PhW-1: SOT and primary side quasi – steady-state phase

The transient is initiated at $t = 0$ s, within the reactor SCRAM and secondary-system isolation. Along the first PhW of the sequence, the three isolated SGs operate as the only heat sink to dispose of the residual decay-heat: power is transferred

from SG primary-side to the secondary-side, whose pressure rapidly increases. Following the overcome of the secondary-side SRV set-points pressure (at 8 s in ASTEC and 20 s in MELCOR), the three SRVs start to release steam from SGs to the atmosphere and, hence, the SGs secondary mass inventory begins to decrease. As can be observed in Fig. 3.6 - left, at SOT the primary pressure rapidly drops to around 140 bar, reaching a quasi-steady-state regime during the cycling of SGs; both the codes show a consistent prediction of this first phase of the transient. During the quasi-steady state phase, the primary to secondary heat-flux balances the FP decay heat produced in the core. The total heat transferred from the primary to secondary side is reported in Fig. 3.6 - right.

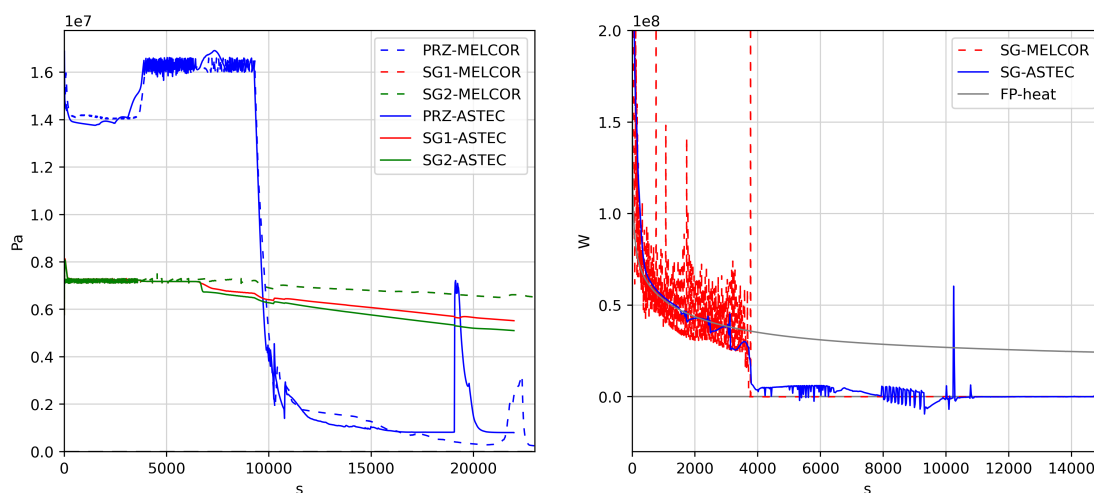


Figure 3.6: ASTEC - MELCOR calculated pressure in PRZ, SG1 and SG2 (left), primary to secondary SG heat and FP decay heat (right).

PhW-2: Primary coolant loss and first oxidation

The primary-side quasi-steady-state phase lasts until the heat removal capability of SGs is reduced due to secondary water depletion. It follows a primary pressure increase, as can be observed in Figure Fig. 3.6 - left. When the primary pressure set-point of SEBIM valves is reached, also these valves begin to cycle and steam is released from the PRZ head to the reactor containment. The loss of the primary coolant is followed by the decrease of water level in the RPV. Timings of SEBIM cycling inception and of the Top of Active Fuel (TAF) uncover are reported in Table 3.2 for the two codes simulations. The first core oxidation phase features higher temperature and H_2 production in MELCOR simulation than in ASTEC,

as reported in Fig. 3.7 - left, and much lower oxidation is predicted by ASTEC in this phase.

PhW-3: Core refill

Following the fast primary depressurization due to the opening of the SEBIM valves, the primary system quickly reaches a pressure below 40 bar. At this point check-valves of ACCs passively open, leading to the injection of cold water in the three CLs (Table 3.2). As a consequence, the core is quenched (Fig. 3.7 - right) and the RPV gets again almost completely filled. As more accurately discussed in [37], from a quantitative point of view the ASTEC core refill is faster and the water inside the core reaches a higher level; the MELCOR injection takes place more gradually, reaching a lower water level in the core but injecting water for a longer time.

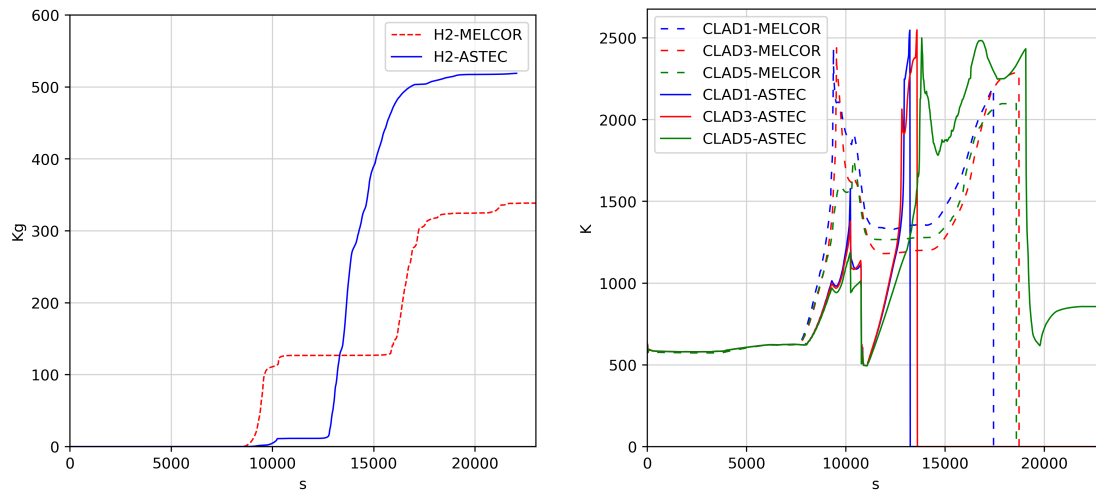


Figure 3.7: ASTEC - MELCOR total H_2 mass produced (left) and cladding temperature in rings 1, 3, 5 (right).

PhW-4: Core degradation evolution and retention in the LP

After the ACCs intervention and core refill, the RPV water level begins to decrease again and the second core BAF uncovering is reached at 12900 s in ASTEC and in 16905 s in MELCOR, as reported in Table 3.2. In this phase, the core degradation features more rapid progress in ASTEC: higher temperatures and onset of hydrogen production are reached earlier than in MELCOR. Looking at Fig. 3.7 - left, can also be observed the much higher total hydrogen mass-produced in ASTEC simulation: more than 500 kg in ASTEC and less than 350 kg in MELCOR. The corium

relocation in the LP takes place at 19070 s in ASTEC and at 21565 s in MELCOR. In Fig. 3.6 - left can be observed the pressure peaks calculated by the two codes due to the interaction of the hot corium relocation in LP. The RPV failure arrives at 21970 s in ASTEC and at 22350 s in MELCOR.

3.3.5 Conclusions of the analysis

The work described is a code-to-code benchmark exercise between two state-of-the-art SA codes, focusing attention on the thermal-hydraulics and the in-vessel core degradation phenomena. By the analysis of analogies and discrepancies between the two codes calculations, the following main outcomes and conclusions can be made.

The first PhW of the transient is dominated by thermal-hydraulic phenomena, and the two codes show a good agreement in the qualitative and quantitative prediction of the FOMs. Starting from the onset of cladding oxidation, during the core degradation the same qualitative phenomenological evolution is observed; yet, major quantitative discrepancies in FOMs values and events timing are predicted. In particular, both the calculations feature a first degradation phase (before the ACCs injection) without a loss of core geometry; however, this first core oxidation features a different quantitative evolution: in MELCOR a larger quantity of hydrogen is produced and higher temperatures are reached than in ASTEC. In the second degradation phase (after the ACCs injection), on the contrary, the degradation advances more rapidly in ASTEC and, at the end of the transient, a much higher total hydrogen mass is produced in this simulation.

The work described confirms previous studies [32] and shows that, in general, the phase dominated by the thermal-hydraulics phenomena is predicted with a reasonable agreement and minor discrepancies; while major quantitative differences are observed along with the evolution of the core degradation. These discrepancies can be attributed to the different approaches adopted in the modeling of the core degradation phenomena by the two codes. But can also be attributed to other factors, such as the user effect on the modeling of the reactor and the choice of models parameter.

This section wants to provide a classical example of SA codes applied to the simulation of a plant core melt accident. However, the study described also opens to the concept of uncertainty affecting the result of a code simulation. Chapter 4 of the present work of the thesis will deal with some methodology developed to characterize the simulation uncertainty deriving from specific input uncertainty sources. In particular, the probabilistic method of propagation of the input uncertainty will be introduced and applied to assess and characterize the uncertainty affecting the

results of the simulations under investigation.

Bibliography

- [1] A. Bentaïb, H. Bonneville, and G. Cénérino, *Nuclear Power Reactor Core Melt Accidents: Current State of Knowledge*. EDP Sciences, 2021, ISBN: 9782759819300. DOI: [doi:10.1051/978-2-7598-1930-0](https://doi.org/10.1051/978-2-7598-1930-0). <https://doi.org/10.1051/978-2-7598-1930-0>.
- [2] L. L. Humphries, V. G. Figueroa, M. F. Young, D. Louie, and J. T. Reynolds, “MELCOR Computer Code Manuals,” Sandia National Lab.(SNL-NM), Albuquerque, NM (United States), SAND-2015-6692R, 2015. DOI: [10.2172/1433918](https://www.osti.gov/biblio/1433918). <https://www.osti.gov/biblio/1433918>.
- [3] “LLC, Transmittal Document for MAAP5 Code Revision MAAP 5.02,” Fauske & Associates, FAI/13-0801, 2013.
- [4] P Chatelard, S Belon, L Bosland, *et al.*, “Main modelling features of the ASTEC V2.1 major version,” *Annals of Nuclear Energy*, vol. 93, pp. 83–93, 2016. DOI: <https://doi.org/10.1016/j.anucene.2015.12.026>.
- [5] F Mascari, F De Rosa, H Nakamura, K Umminger, and F. S. D’Auria, “Scaling issues for the experimental characterization of reactor coolant system in integral test facilities and role of system code as extrapolation tool,” in *Proceedings of 16th International Topical Meeting on Nuclear Reactor Thermal-Hydraulics (NURETH-16)*, American Nuclear Society, 2015, pp. 4921–4934.
- [6] K Wolfert, H Glaeser, and N Aksanm, “CSNI Validation Matrix for PWR and BWR Codes,” Nuclear Energy Agency of the OECD (NEA), NEA/CSNI/R(92)12, 1992.
- [7] A. Nusret, R. Pochard, H. Glaeser, F. D’Auria, A. Sjoberg, and C. Richards, “Separate Effects Test Matrix for Thermal-Hydraulic Code Validation,” Nuclear Energy Agency of the OECD (NEA), NEA/CSNI/R(93)14, 1993.

-
- [8] A. Annunziato, H. Glaeser, J. Lillington, P. Marsili, p. Renault, and A. Sjoberg, “CSNI integral test facility validation matrix for the assessment of thermal-hydraulic codes for LWR LOCA and transients,” Nuclear Energy Agency of the OECD (NEA), NEA/CSNI/R(96)17, 1996.
- [9] A. Prošek, M. Leskovar, and B. Mavko, “Quantitative assessment with improved fast fourier transform based method by signal mirroring,” *Nuclear engineering and design*, vol. 238, no. 10, pp. 2668–2677, 2008.
- [10] A. Prošek and M. Leskovar, “Use of FFTBM by signal mirroring for sensitivity study,” *Annals of Nuclear Energy*, vol. 76, pp. 253–262, 2015.
- [11] H. Karwat, “Elaboration of a guideline for counterpart testing of integral loop systems,” Commission of the European Communities, EUR-6540, 1988. https://inis.iaea.org/search/search.aspx?orig_q=RN:20006350.
- [12] “CSNI International Standard Problems (ISP) Brief descriptions (1975-1999),” Nuclear Energy Agency of the OECD (NEA), NEA/CSNI/R(2000)5.
- [13] *Evaluation of Advanced Thermohydraulic System Codes for Design and Safety Analysis of Integral Type Reactors*, ser. IAEA-TECDOC 1733. Vienna: International Atomic Energy Agency (IAEA), 2014, ISBN: 978-92-0-100314-0.
- [14] F. Mascari and G. Vella, “IAEA International Collaborative Standard Problem on Integral PWR Design Natural Circulation Flow Stability and Thermohydraulic Coupling of Containment and Primary System during Accidents. OPEN Calculation Results,” 2011.
- [15] P Chatelard, N Reinke, S Arndt, *et al.*, “ASTEC V2 severe accident integral code main features, current V2.0 modelling status, perspectives,” *Nuclear Engineering and Design*, vol. 272, pp. 119–135, 2014.
- [16] T. Albiol, J. Van Dorsselaere, B Chaumont, *et al.*, “SARNET: Severe accident research network of excellence,” *Progress in Nuclear Energy*, vol. 52, no. 1, pp. 2–10, 2010.
- [17] J.-A. Zambaux, “ASTEC: CESAR physical and numerical modelling,” IRSN/2021-00184, 2021.
- [18] I. Gomez and L. Laborde, “Validation of selected cesar friction models of the astecv21 code based on moby dick experiments,” *Journal of Nuclear Engineering and Radiation Science*, vol. 5, no. 2, 2019.
- [19] S. Manservigi and R. Scardovelli, *Termoidraulica dei flussi bifase*. Società Editrice Esculapio, 2012.

-
- [20] V. Topin, L. Carenini, O. Coindreau, and L. Laborde, “ASTEC V2.2: Physical modelling of the ICARE module,” IRSN/2021-00185, 2021.
- [21] K. Chevalier, “ASTEC V2.2 ELSA module : fission products and structural elements release from intact and degraded cores theoretical manual,” IRSN/PSN-RES/SAG/2015-00110, 2021.
- [22] F. Cousin and F. Jacq, “ASTEC v2.2 ISODOP module theoretical manual,” IRSN/2015-00366, 2021.
- [23] L. Bosland and F. Kremer, “ASTEC SOPHAEROS module theoretical manual,” IRSN/2021-00244, 2021.
- [24] N. Reinke, W. Klein-Hessling, and B. Schwinges, “CPA Module of ASTEC Programme Reference Manual,” ASTEC-V2/DOC/15-03, 2015.
- [25] G Bandini, M Buck, W Hering, *et al.*, “Recent advances in ASTEC validation on circuit thermal-hydraulic and core degradation,” *Progress in Nuclear Energy*, vol. 52, no. 1, pp. 148–157, 2010.
- [26] I. Gomez, L. Laborde, and J.-A. Zambaux, “Overview of the CESAR thermohydraulic module of ASTEC V2. 1 and selected validation studies,” in *Proceedings of 18th International Youth Nuclear Congress (IYNCWiN18), Bariloche, Argentina, Mar, 2018*, pp. 11–17.
- [27] J. Van Dorsselaere, P Chatelard, M Cranga, *et al.*, “Validation status of the ASTEC integral code for severe accident simulation,” *Nuclear Technology*, vol. 170, no. 3, pp. 397–415, 2010.
- [28] P. Chatelard, S. Arndt, B. Atanasova, *et al.*, “Overview of the independent ASTEC V2. 0 validation by SARNET partners,” *Nuclear Engineering and Design*, vol. 272, pp. 136–151, 2014.
- [29] P. Maccari, F. Mascari, S. Ederli, P. Meloni, and S. Manservisi, “ASTEC code DBA analysis of a passive mitigation strategy on a generic IRIS SMR,” *Annals of Nuclear Energy*, vol. 156, p. 108 194, 2021.
- [30] I Kljenak, M Dapper, J Dienstbier, *et al.*, “Recent activities on validation of modeling of thermal-hydraulic and aerosol phenomena in ASTEC CPA,” *ERMSAR-2007*, 2007.
- [31] L Cantrel, F Cousin, L Bosland, K Chevalier-Jabet, and C Marchetto, “ASTEC V2 severe accident integral code: Fission product modelling and validation,” *Nuclear Engineering and Design*, vol. 272, pp. 195–206, 2014.

- [32] F. Mascari, F. De Rosa, M. Sangiorgi, and G. Bandini, “Analyses of an Unmitigated Station Blackout Transient in a Generic PWR-900 with ASTEC , MAAP and MELCOR Codes,” NUREG/IA-0515, 2019.
- [33] J. C. de la Rosa Blul, S. Brumm, F. Mascari, S. Lee, and L. Carenini, “ASTEC–MAAP Comparison of a 2 Inch Cold Leg LOCA until RPV Failure,” *Science and Technology of Nuclear Installations*, vol. 2018, 2018.
- [34] P. Chatelard, “ASCOM project overview and description of work,” SARNET-ASCOM-COORDI-P1, 2018.
- [35] *NUGENIA TA-2 : ASCOM project (2018-2022)*. <https://snetp.eu/portfolio-items/ascom/>.
- [36] “Applied Programming Technology, Inc., Symbolic Nuclear Analysis Package (SNAP) User’s Manual,” 2021.
- [37] P. Maccari, F. Mascari, S. Ederli, and S. Manservigi, “SBO analysis of a generic PWR-900 with ASTEC and MELCOR codes,” in *Journal of Physics: Conference Series*, IOP Publishing, vol. 1868, 2021, p. 012 019.
- [38] *Status and Evaluation of Severe Accident Simulation Codes for Water Cooled Reactors*, ser. IAEA-TECDOC 1872. Vienna: International Atomic Energy Agency (IAEA), 2019, ISBN: 978-92-0-102919-5.
- [39] L. Foucher, “ASTEC V20R3 PWR900 Like ASTEC Input Deck,” Rapport n IRSN/PSN-RES/SAG/2013-451.
- [40] L. Foucher, “ASTEC V20R3, PWR900 Like ASTEC Steady State Calculation,” Rapport n IRSN/PSN-RES/SAG/2013-466.
- [41] H Nowack, P Chatelard, L Chailan, V Sanchez, L Herranz, *et al.*, “Cesam–code for european severe accident management, euratom project on astec improvement,” *Annals of Nuclear Energy*, vol. 116, pp. 128–136, 2018.
- [42] <https://www.fastnet-h2020.eu/>.
- [43] F Mascari, F Carny, F Rocchi, *et al.*, “FASTNET scenarios database development and status,” *Proceedings of ERMSAR2019*, 2019.
- [44] F Fichot, L Carénini, M Sangiorgi, *et al.*, “Some considerations to improve the methodology to assess in-vessel retention strategy for high-power reactors,” *Annals of Nuclear Energy*, vol. 119, pp. 36–45, 2018.
- [45] <https://cordis.europa.eu/project/id/662157>.

-
- [46] F. Fichot, L. Carenini, M. Sangiorgi, *et al.*, “Status of the IVMR project: First steps towards a new methodology to assess In-Vessel Retention Strategy for high-power reactors,” in *ERMSAR Conference, The 8th European Review Meeting on Severe Accident Research, 16-18 May 2017, Warsaw, Poland, ERMSAR Conference, The 8th European Review Meeting on Severe Accident Research, 2017, JRC106398.*
- [47] K. W. Ross, J. Phillips, R. O. Gauntt, and K. C. Wagner, “MELCOR Best Practices as Applied in the State-of-the-Art Reactor Consequence Analyses (SOARCA) Project,” NUREG/CR-7008, 2014.
- [48] F Mascari and S Ederli, “Analyses with MELCOR code of an unmitigated SBO scenario with in vessel retention strategy applied to a generic PWR 900 MWe,” in *18th International Topical Meeting on Nuclear Reactor Thermal Hydraulics, NURETH 2019*, pp. 2497–2510.

CHAPTER 4

ASTEC modelling and simulation of advanced passive SMR

The present chapter deals with the central topic of advanced passive SMR, and it starts by introducing the challenges to be overcome in thermal-hydraulic and SA codes modelling of their advanced features. In this framework, the approach adopted in the ASTEC code modelling of a generic IRIS reactor is described. The chapter follows with the description of the ASTEC simulation of a DBA sequence in the generic IRIS design, and it concludes with the comparison between four BDBA simulations.

4.1 Introduction and code modelling of advanced water-cooled SMR

The increasing energy demand of developing and developed countries; the industries needs to improve efficiency and reduce capital costs; and the call for a more sustainable energy future, imply a big effort to be achieved in the near future in the transformation of the world energy mix. In this framework, the interest in advanced SMRs has been growing in the past decade in virtue of their recognized advantages with respect to conventional size NPP, in terms of capital costs, safety, flexibility, etc [1].

According to the classification adopted by IAEA [2], small reactors are characterized by an equivalent electric power of up to 300 MWe; and medium sized reactors are characterized by an equivalent electric power between 300 and 700 MWe [3]. In general, the acronym SMR is used to refer to a reactor whose size is adequate to

be built and assembled in a factory, and then shipped to the plant location for the installation of the module. Due to the large and consolidated experience with conventional LWR, light water SMR (and in particular light water PWR) is the most consolidated and promising technology being developed [4]. Fig. 4.1 represents a schematic view of a generic SMR and of three SMR modules installed in a plant.

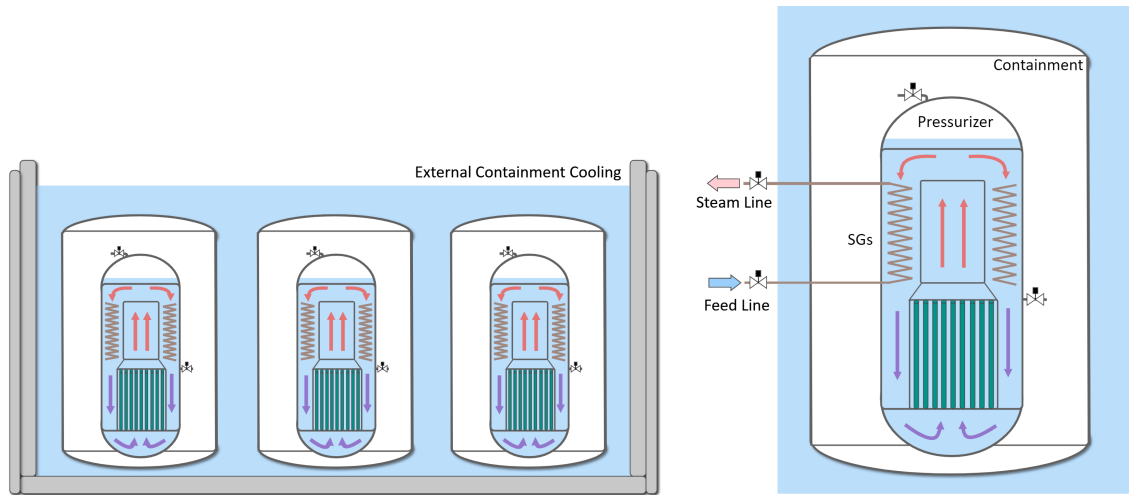


Figure 4.1: Scheme of SMR modules installed in a plant (left) and generic design of an integral SMR (right).

4.1.1 Potential advantages of water-cooled advanced SMR

Economic competitiveness

Lower capital costs of SMRs may provide an attractive and affordable nuclear power option, especially for developing countries with limited investment capability. The drawbacks of scale economy (operation of larger size reactor makes the return on investment faster) is compensated by offering the economy of mass production of multiple prefabricated modules, a simplified and standardized design, shorter construction time, less operation and maintenance cost. In addition, modules can be added as needed to guarantee the possibility to increase the total power capacity. Also, the possibility of implementing cogeneration makes this technology suitable to be economically competitive [5].

Flexibility in energy production and other applications

In view of the transition to an electric power production based on renewable intermittent sources, it is becoming popular the idea of a shift from a localized electric

power production to a more distributed, smart and decentralized electric power supply strategy (microgrids) [6]. Thanks to the size of each reactor and to the modularity of the site, SMR technology offers both flexible and stable energy production features; and the integration in this new electric distribution concept may provide a solution to overcome most of the microgrids limitations [7].

The integral configuration results in a light weighted transportable and compact units and in a significant reduction in the size of the nuclear island. This feature makes the technology suitable to be installed in remote area of the Earth where SMRs can be applied not only to supply electricity but also for process as water desalination. Moreover, high-temperature reactors can produce high temperature steam that could be used in industrial applications, hydrogen production, cogeneration and that can be even combined with off-shore wind farms [5][8].

Safety and reliability advantages

Enhanced safety and reliability are key aspects of the SMR concept, which is said to adopt *inherent safety features*. With regard to conventional size reactors, SMRs feature a smaller power density which means a smaller ratio between the heat needed to be removed and the reactor surfaces area. In terms of safety, this is an advantage in accidental conditions and it allows the reactor design to be simpler and suitable for the adoption of passive mitigation strategies. Passive safety systems are aimed to be more reliable than conventional active safety systems since they do not need an active source of power (s.a. diesel generator, electric emergency batteries, etc.) to operate; yet, they only rely on natural-driven phenomena (s.a. natural circulation, gravitational injection, pressure difference, etc.). Another advantage in terms of safety is given by the integral configuration adopted by most of SMRs. This design eliminates large pressurized pipes outside the vessel, hence reducing the number of possible LOCA and totally eliminating the possibility of Large Break LOCA (LB-LOCA) [9].

4.1.2 Considerations about thermal-hydraulic phenomena characterizing advanced SMR

Many of the thermal-hydraulic features characterizing passive SMR designs (and in general advanced LWR) are in common with the current generation of LWR (e.g. large-scale PWR and BWR); while other thermal-hydraulic features are specific of only SMRs design [10][11]. In relation to features in common with conventional reactors, advanced designs may be characterized by a different ranking of some phenomena; concerning features characterizing only advanced SMR designs, as as-

sessed in [4][10][11], new kinds of phenomena and accident scenarios can be grouped in:

- a) Containment process and interactions with the RCS;
- b) Low pressure phenomena (atmospheric pressure);
- c) Phenomena related specifically to new system components or reactor configurations.

Regarding point a: In safety analysis involving current reactor designs it is possible to study the containment behavior separately from the RCS, which can be considered as a boundary condition for the containment and vice versa. For an advanced passive SMR it is not possible to make this approximation, but it is necessary to consider the thermal-hydraulic coupling between containment and RCS and to characterize the integrated RCS-containment system behavior during the transient evolution. This is due to the strong coupling and feedback effects between primary and containment systems. In relation to low-pressure phenomena (point b), we can mention natural circulation phenomena; influence of non-condensable gases; steam-liquid interaction phenomena (e.g. direct condensation); gravity driven reflooding phenomena; liquid temperature stratification phenomena. More information about low pressure phenomena can be found in [10][12][13][2].

As an example of phenomena related to new system components (point c), it can be mentioned: natural circulation in integral type configuration (in transient and steady operation); behavior of compact SG, such as helical coiled SGs; passive residual heat removal systems.

The in-Pool Energy Removal System for Emergency Operation (PERSEO) in Fig. 4.2, is an example of a new passive heat exchanger for decay-heat removal, based on natural-circulation. The facility, built to characterize the PERSEO thermal-hydraulics [14][15][16], is made of two separated pools: the overall pool and the heat-exchanger pool containing the emergency heat-exchanger. The two pools are connected at the bottom by a pipe line with an activation valve. When the passive system has to be activated the valve is opened, the heat-exchanger pool is flooded with water and heat transfer starts from the heat-exchanger to the pool. The system works in two natural circulation loops to passively remove heat from the vessel.

Considering that advanced SMR designs are characterized by new types of phenomena, different accidental scenarios and different ranking of phenomena, further experimental investigations in *separated test facilities* and *integral test facilities* are necessary to extend the “assessment database”. For this purpose, some experimental facilities have been designed and experimental campaigns have been performed in the last decade [11].

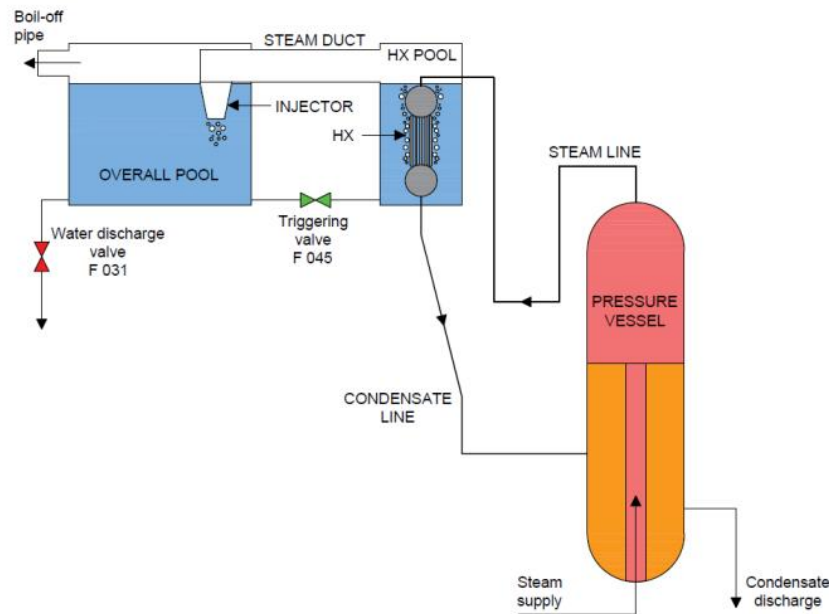


Figure 4.2: Schematic view of PERSEO safety system in operation [16].

4.1.3 Considerations and research activities regarding code modelling of advanced SMR

Thermal-hydraulic modelling of advanced SMR

As described in the previous section, advanced reactors using passive safety systems are characterized by specific thermal-hydraulic phenomena and features. For this reason, thermal-hydraulic system codes and thermal-hydraulic modules/packages of SA codes need to be proven able to accurately predict the thermal-hydraulics of such advanced designs. With this purpose, national and international code application activities have been carried out or are currently in progress. Examples of such activities are the IAEA ICSP on “Integral PWR Design Natural Circulation Flow Stability and Thermo-hydraulic Coupling of Primary System and Containment During Accidents” [17] and the ongoing activity on the accuracy evaluation of the TRACE code [18] against the OSU-MASLWR DOE tests [19][20][21]. From these activities, some remarks can be done regarding thermal-hydraulic code modelling of SMR in terms of:

- a) Modelling of heat transfer from primary to secondary side by helical-coils SG;
- b) Modelling of primary side natural circulation at different core power levels and feedwater flow rates;
- c) Modelling of primary/containment coupling;

d) Modelling of containment behavior.

In relation to point a), one of the outcomes of the IAEA ICSP activity is that the modelling of the heat-transfer from primary to secondary side by helical coils SG requires the implementation in the codes of a dedicated helical-coil heat-transfer model. Fig. 4.3 shows the average value of the SG outlet temperature of the experimental OSU-MASLWR-002 data against TRACE code calculations. The main phenomena typical of a superheating helical-coil SG have been simulated by the code by using the specific helical-coil SG new model called “Curved pipe”.

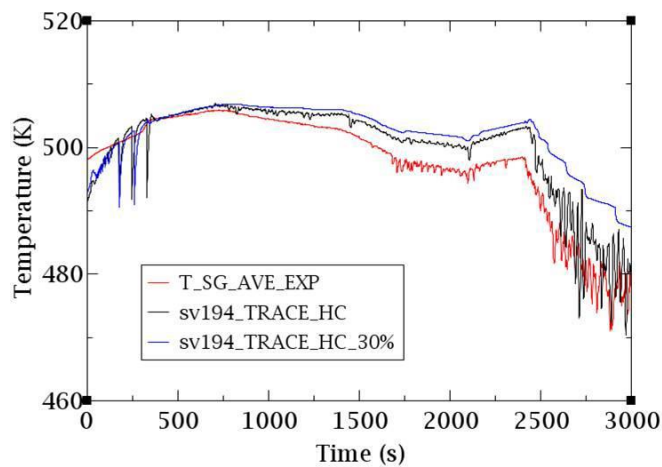


Figure 4.3: Experimental data versus code calculations for the average value of the SG outlet temperature [22].

Regarding point b), another outcomes of the IAEA ICSP activity was that an accurate simulation of the form pressure losses along the integral RPV shall constitute a key modelling aspect. The use of Reynolds number dependent form losses has been suggested to be investigated for the prediction of the primary natural circulation flows rates.

In relation to point c), Integral passive SMRs are characterized by a high level of interaction between the reactor systems and in particular of the RPV – containment coupling. This requires a detailed code modelling of the system which is beyond common code application for conventional LWR and active mitigation strategies (e.g. the containment could be considered as a boundary condition for the primary system). Examples of activities aimed at investigating the code prediction of single/two-phase natural circulation and primary-to-containment coupling phenomena in DBA and BDBA are the IAEA ICSP test 2 and in the ongoing analyses of the TRACE capability to simulate the DOE blowdown, tests (001 and 003B).

Concerning point d), the results of the IAEA ICSP show that different codes applications produce similar results for the high pressure containment simulation. Though, some discrepancies with the experimental data are observed probably due to uncertainty in the location of instrumentation, but also due to the presence of multidimensional phenomena. The ongoing analyses of the TRACE capability to simulate the DOE blowdown tests (001 and 003B) shows that by adopting a 3D vessel model the code is able to reproduce the mixing phenomena in the lower part of containment and a general better prediction of the experimental temperature is achieved.

The analyses developed along the OECD/NEA/CSNI/WGAMA PERSEO benchmark [15][16] highlighted another central point related to scaling: most of the codes used in the benchmark have shown an underestimation of the heat-transfer prediction with respect to the experimental data and general limitations in simulating the full-scale experiment. It was concluded that an accurate evaluation of the validation domain and of the related scaling issues is necessary to apply thermal-hydraulic codes in the simulation of full-scale passive safety systems.

SA codes simulation of advanced SMR

AS highlighted in the previous Chapters of this thesis, the simulation of a SA sequence involves many complex phenomena strongly related to the thermal-hydraulics of the system. For this reason, also SA codes (e.g. ASTEC, MELCOR) need sufficient accurate modeling of the thermal-hydraulics characterizing advanced SMR in order to be applied for accurate simulations of core melt sequences in these reactors. Therefore, when dealing with advanced SMRs, it is necessary to validate the SA code's modules/packages for thermal-hydraulic simulation against experimental activities dedicated to the main thermal-hydraulic phenomena specific to integral configurations and passive safety systems.

Regarding core degradation phenomena and core degradation modules/packages, similar considerations can be done. Despite the reactor core of SMRs usually presents similar design and materials with respect to conventional size NPP, we can expect that SMR designs might present some specific core-degradation features which have not been considered in conventional SA. Whereas, in relation to SA features in common with conventional reactors, SMR designs may be characterized by a different ranking of core-degradation phenomena. For this reason, we can expect that the validation studies performed for conventional SA conditions might not be enough to ensure accurate modelling in case of SMR design. E.g. the physical conditions obtained may not remain within the limits of validity of the validated SA model. Or, in other cases, new accidental scenarios and configurations that had

not been considered for conventional SA could have to be accounted.

Due to the growing interest in SMRs and the consolidated knowledge in the use of SA codes, the international safety research community is currently starting new research activities to investigate the applicability of SA integral codes to SA sequences in SMR, by starting from the identification of the new features characterizing SA in this advanced reactors. The next chapters of the present work of thesis will cover some first analyses developed with the ASTEC code and aimed at simulating thermal-hydraulic and core degradation phenomena in an advanced SMR. The studies can be considered a first step in the SA code assessment of SMRs and provide important information in this direction. Further code validation and development activity are necessary to assess with accuracy the accident scenarios of interest.

4.2 ASTEC code modelling of a generic IRIS design

4.2.1 Motivations

In the previous sections it has been highlighted as advanced passive SMR are characterized by new thermal-hydraulic phenomena and by a different ranking of these, with respect to conventional LWR. And that, for this reason, thermal-hydraulic codes as well as SA codes need to be proven capable of predicting the thermal-hydraulics characterizing advanced passive SMRs.

In the framework of the NUGENIA TA-2 ASCOM collaborative project [23][24] coordinated by IRSN, a first application of ASTEC code to advanced passive SMR has been developed. It concerns the development of an ASTEC model of an integral PWR facing with passive safety systems, aimed at studying the code capability to simulate SMR designs in challenging conditions. The reactor chosen is a generic design based on the “International Reactor Innovative and Secure” (IRIS). This advanced SMR adopts a mitigation strategy involving a large number of passive safety systems and, thus, relying on the natural-driven phenomena of interest. In addition, the passive mitigation strategy of IRIS involves a high level of interaction between the reactor systems (containment compartments, primary system, safety systems), and this requires a complex phenomenological coupling between the ASTEC modules that is beyond the common code use for conventional LWR applications (in which the modules coupling has much simpler features).

The generic IRIS model developed with ASTEC V2 has to be able to assess the specific natural-driven thermal-hydraulic phenomena of advanced integral SMR

and of their passive safety systems. In addition, the model should contain all the ASTEC features needed to simulate the development of a core-melt accident. Yet, the reactor model developed is considered “generic” since only open-data (e.g. reactor geometry, logics, boundary conditions, materials, etc.) have been used for the realization of the input-deck (e.g. excluding IRIS proprietary-data).

Due to the generic design and to the lack of experimental data, the activity does not pretend to be an exhaustive code assessment, but a first step in this direction. The work is important to point out the code needs, to find useful development areas and to identify which specific code models need to be validated against experimental data. The description of the ASTEC nodalization approach is aimed to underline the limitations found in the code modules, to describe the solution adopted, and it provides some code-user guidelines to be followed for the modelling of passive systems and facing with SMR. The results of the DBA simulation provide useful information on the ASTEC code capability to be applied in the prediction of the thermal-hydraulic phenomena of interest and it can be considered a first step of qualitative assessment for the thermal-hydraulic modules of ASTEC.

The following simulations of the 4 BDBAs explore the applicability of SA codes to SMR in beyond design conditions. The study represents an example of SA code application to address the behavior of the passive safety systems in severe challenging conditions. In addition, the work can provide important insights regarding possible SMR drawbacks, as well as insights on the development of better management mitigation action and more efficient passive safety systems, by considering the eventuality of SA scenario.

4.2.2 IRIS reactor

RPV and integrated primary system

The reactor IRIS is an integral PWR of 300 MWe (1000 MWt), developed by an international consortium led by Westinghouse and involving several Universities, industries and organizations from different countries [25][26]. The reactor design features a RPV hosting all the reactor coolant primary system components: Reactor core, PRZ, Control Rod Drive Mechanism (CRDM), SGs, spool-type primary coolant pumps, etc. The integral arrangement of the primary circuit, reported in Fig. 3.4, is part of the “safety by design” concept: it avoids high pressure components outside the RPV and large primary vessel penetration [27][28][29]. The reactor core is located at the bottom of the RPV and the PRZ is integrated in the RPV upper head. The heated water coming from the core outlet, flows upward through the inner riser channel and reaches the top part of the circuit. Here, the

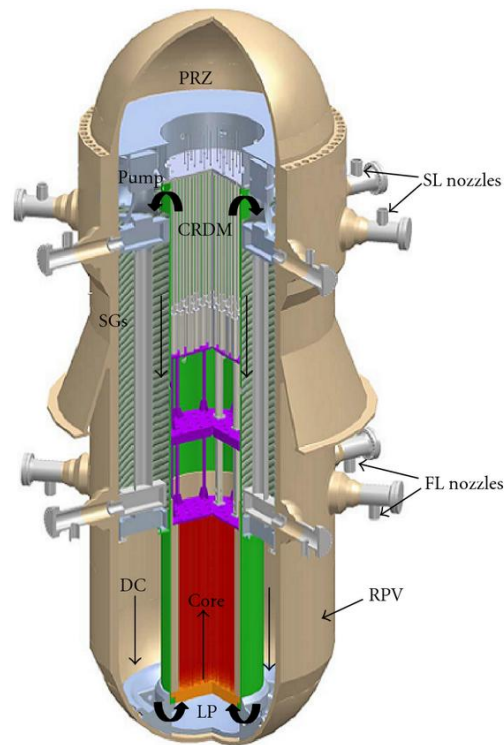


Figure 4.4: IRIS integral RPV layout [26].

water flow path reverses moving from the inner region to the outer annulus where the pumps suction plenum are located. The coolant is pushed downward by the 8 immersed pumps through the 8 primary-side SGs downcomer tubes. Flowing out from the bottom of SG pipes, the cooled primary water descends along the annular downcomer to the LP and again up inside the core.

Secondary system

In each of the 8 SG primary-side tubes is located a bundle of secondary-side helical-coils in countercurrent flow. This integrated design offers a large heat-transfer surface effectively in both nominal and transient conditions. Outside containment, the 8 Feed Lines (FLs) and the 8 Steam Lines (SLs) are grouped (by pairs) to 4 parallel lines which constitute the secondary system loop, as it can be observed in Fig. 4.5 reporting a 3D scheme of the IRIS reactor.

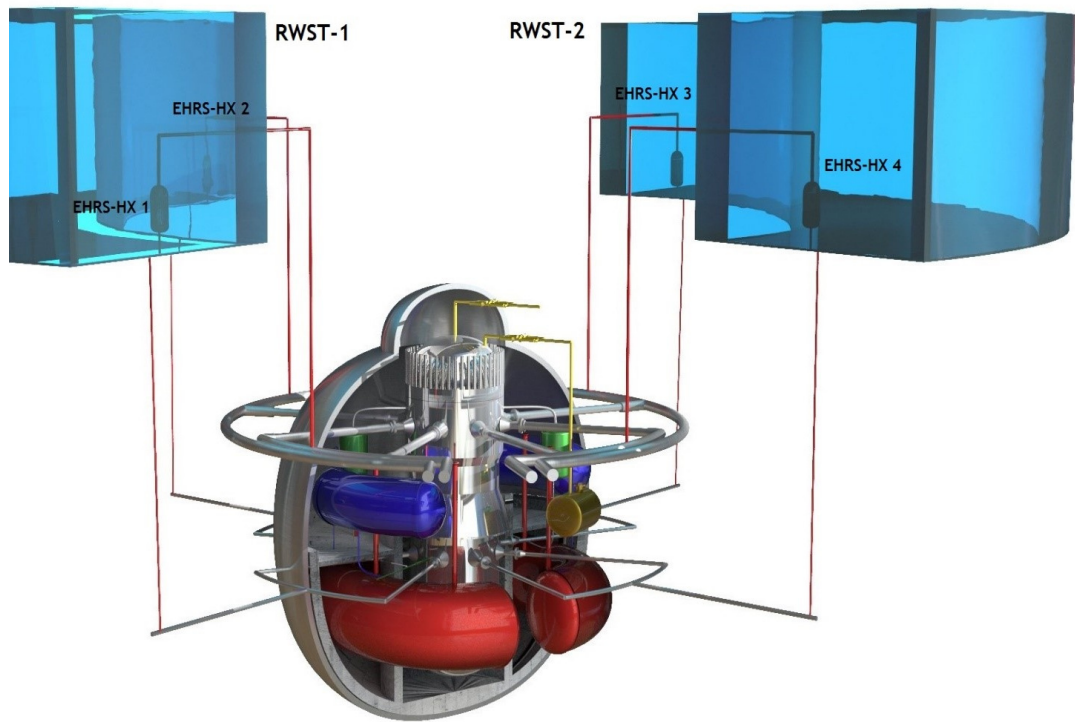


Figure 4.5: 3D scheme of a generic IRIS reactor.

Containment

The RPV is placed in a spherical containment of stainless steel which can be considered made of 2 main zones: the RC is a narrow chamber with concrete walls in which the bottom half of the RPV is placed; the DryWell (DW) is the top chamber with steel walls for water condensation and a larger internal volume in which most of passive safety systems are placed (Figure 4.5). The containment is filled with Nitrogen and, in the case of a LOCA, it is directly involved in the mitigation strategy: the dynamic thermal-hydraulic coupling with the primary system and the passive safety systems allows the leak mitigation and the refill of the core in the most challenging condition [30].

Passive safety systems

A scheme of the IRIS passive safety systems is reported in Fig. 4.6 (the scheme shows only one line for each of the redundant line systems) and a realistic representation of their location in the reactor can be found in Fig. 4.5 The safety systems of IRIS include:

- Emergency Heat Removal System (EHRS): 4 independent loops working in

natural circulation once the system is activated. Each train is connected to a pair of the 8 secondary-side SGs and removes energy in natural circulation by using the large water mass of two Refueling Water Storage Tanks (RWSTs) located outside the containment as heat sink;

- Automatic Depressurization System stage-1 (ADS st-1): made of 3 trains connected to the head of the PRZ by check-valves. The opening of ADS st-1 valves is aimed to the RPV depressurization as a results of steam dumping into the pool of a Quench Tank (QT) located in the DW;
- Automatic Depressurization System stage-2 (ADS st-2): allows the pressure equalization between containment and RPV atmospheres through the opening of a larger connection located on the PRZ head.
- 2 Emergency Boration Tanks (EBTs): located in the DW, able to inject borated water for gravity in the RPV through the Direct Vessel Injection (DVI) lines;
- 2 Long-term Gravity Make-up System (LGMS): bigger tanks, also located in the DW and connected to the DVI lines;
- 2 Pressure Suppression System (PSS) tanks: located outside the DW volume and connected to the DW atmosphere through large vent-pipes. The PSS features the largest tanks and are designed to work in two ways in the passive mitigation strategy: limiting the containment pressurization whether the DW pressure is higher than the pressure in the PSS atmosphere; helping to fill the RC with a water reverse flow if the PSS atmospheric pressure becomes lower than the DW pressure.
- 2 DVI lines: each EBT, LGMS, and PSS tanks belongs to one of the 2 independent system lines (as the one reported in Fig. 4.6) connected to the RPV through a DVI line. The 2 DVI lines are connected to the vessel above the elevation of the top core plate.
- Riser-Downcomer (RI-DC) valves: 8 connections between the riser and the downcomer SGs, designed to allow the primary water to flow through a shorter path, bypassing the pumps suction plenum and allowing natural circulation at a lower RPV water level. These connections are kept closed in nominal reactor conditions by the primary pumps delivery pressure and are able to automatically open once the pumps are turned off.

The atmospheric parts of PSS tank LGMS tank belonging to the same line are connected by an open vent-pipe, as it is shown in Fig. 4.6 The gas is free to flow through the vent-pipe keeping LGMS and PSS tanks (on the same line) line at the same pressure during transient. EBTs, LGMS, ADS and EHRS systems can be activated by opening safety valves activated by specific safety signals during the

mitigation strategy. After the safety valve is opened the system works thanks only to natural-driven (passive) phenomena.

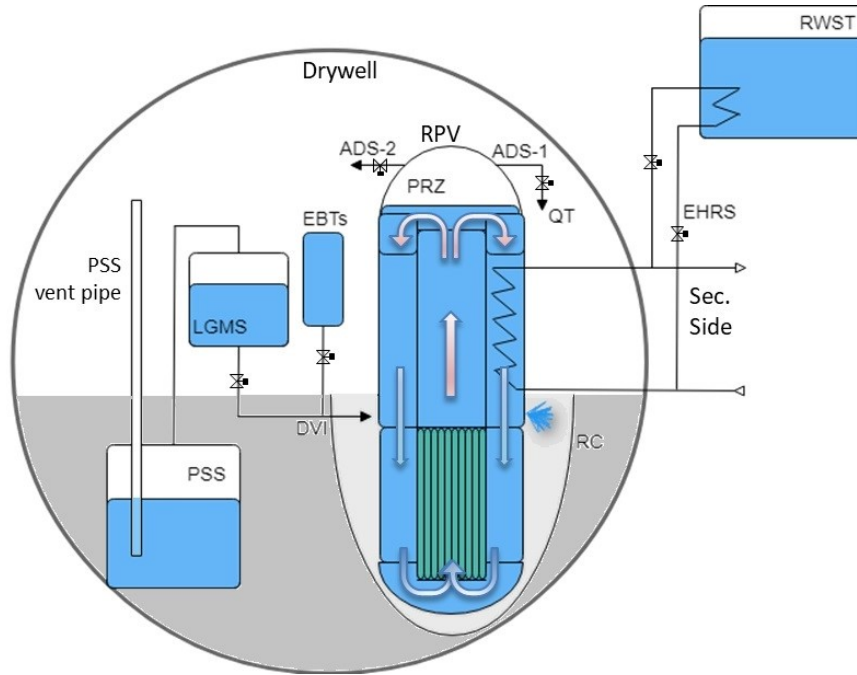


Figure 4.6: Scheme of safety systems for a generic IRIS reactor (for redundant systems only one line is reported) [9].

4.2.3 IRIS passive mitigation strategy for a DVI line double-ended break

Among the DBA scenarios studied in the past on IRIS, the Small Break LOCA (**SB-LOCA**) concerning the double-ended break of one of the two DVI lines is the lowest elevation LOCA and, hence, the most challenging accidental scenario in terms of safety. The DBA transient progression of reference assumes the availability of all the emergency passive safety systems of the IRIS design. The passive mitigation strategy relies on the opening of specific safety valves activating specific safety systems, consequently to the triggering of set-point signals and the phases of the sequence can be considered driven by the triggering of such signals.

According to [26][30][29], the DBA sequence can be divided into 6 PhWs (from PhW-a to PhW-f). Considering the DVI line-A as the broken line and the DVI line-B as intact, the expected phenomenological sequence and the related main phenomena/processes are summarized in the following. Fig. 4.7 shows a scheme of

the main reactor configurations during the DBA transient.

- a) The opening of the guillotine break of DVI line-A starts the RPV depressurization and the decreasing of PRZ level. At the same time, containment pressure and temperature start to increase and the pressurization causes the transfer of hot steam-gas mixture from DW to PSS tanks, through the PSS vent-pipes. Steam and non-condensable gas are pushed inside PSS pool, forcing steam condensation underwater and limiting containment pressurization. The PSS and LGMS tanks pressures increase following the containment trend during the pressurization phase. Primary water flowing from the break and steam condensation on DW metal walls start to slowly fill the RC.
- b) Once reached the “high containment pressure set-point”, the Safety-signal (S-signal) triggers the reactor SCRAM, the secondary-side lines isolation and the activation of 2 of the 4 EHRS loops. Following the secondary system isolation, natural circulation starts in the EHRS open loops allowing power transfer to the RWST water and, hence, contributing to RPV cooling and depressurization.
- c) The primary pumps coastdown is triggered by the “low PRZ level signal” and the stop of pump delivery pressure makes the RI-DC check valves to automatically open. From this moment on, the core cooling is driven only by natural circulation both in RPV (primary loop) and in EHRS (secondary loop).
- d) The “LOCA Mitigation-signal” (LM-signal) occurs when “low PRZ pressure set-point” is reached. This actuates ADS stage-1, EBTs and the 2 EHRS remaining loops. As a consequence, EBTs cold water starts to be injected by gravity through the two DVI lines: the broken DVI loop (line-A) drops water inside RC; the intact DVI loop (line-B) injects water in the RPV. ADS st-1 opening leads to steam dumping from PRZ head inside QT water and enhances the PRZ depressurization, hence accelerating the equalization between primary and containment pressures. The actuation of all the EHRS loops increases the energy removal from primary system.
- e) At the RPV - DW pressures equalization ($\Delta P < 0.5$ bar), the “low RPV-Containment Differential Pressure - signal” (DP-signal) triggers the opening of the valves connecting LGMS line-B to RPV (through the intact DVI) and LGMS line-A to RC (through the broken DVI). The containment pressure reaches its maximum value and then it starts to decrease following the RPV trend. The depressurization of the systems is driven both by steam condensation on the containment walls and by EHRS heat removal from RPV. As a consequence, the DW pressure decreases below the pressure of PSS atmo-

sphere (and LGMS), pushing the PSS water inside the vent-pipes up to the top end. It results in a large water flow which is dropped out of PSS vent-pipes and rapidly fills the RC. During the depressurization phase, the water head inside PSS vent-pipe keeps a differential pressure between LGMS (PSS) and RPV (DW), enhancing LGMS water injection.

- f) Reached the “LGMS low water mass signal”, the ADS stage-2 valves are opened allowing the complete pressure equalization and steam circulation between RPV and DW. During the long-term cooling phase, the core is kept filled by the water available from RC filled above the break level; the reactor slowly cools down thanks to the power removed by the EHRS system and the heat losses to the environment through the large DW metal surfaces.

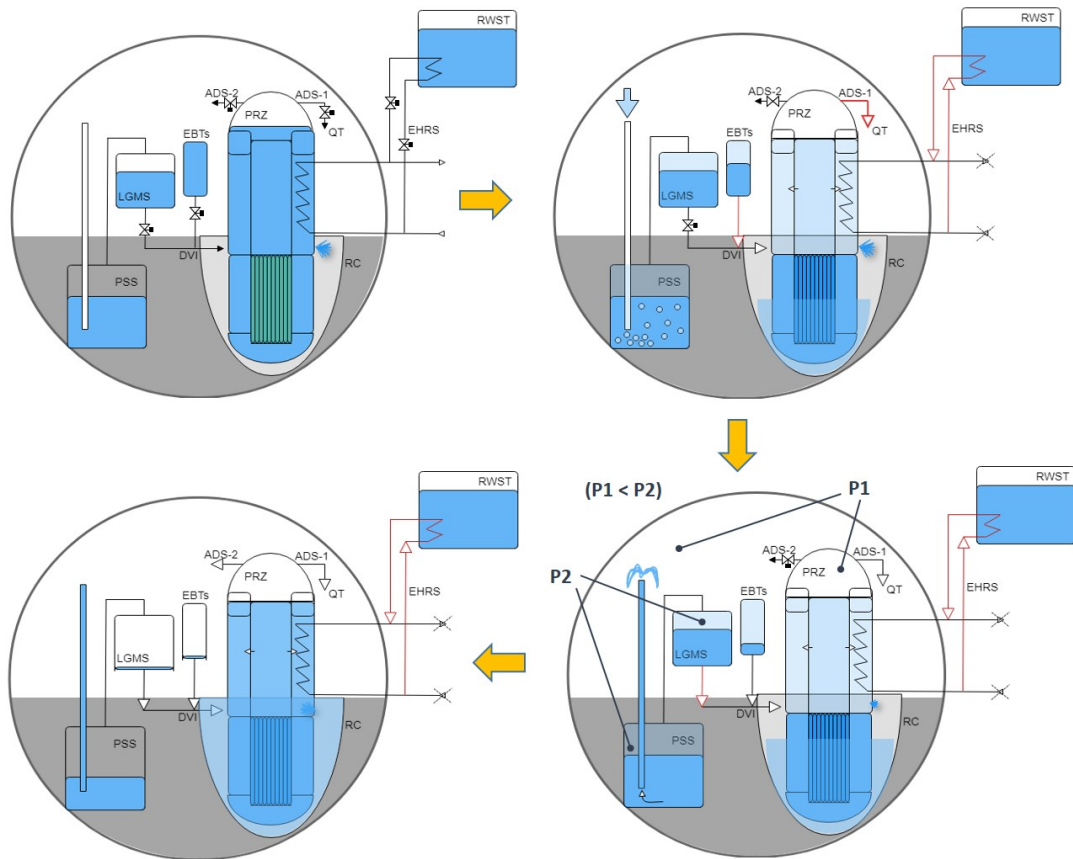


Figure 4.7: Scheme of main reactor phases during the DBA transient sequence.

4.2.4 Description of ASTEC nodalization of the generic IRIS reactor

The model of the generic IRIS SMR reactor has been developed by using the modules CESAR, CPA, ICARE, SOPHAEROS and ISODOP of the ASTEC code version V2. In order to develop the nodalization of the “generic” IRIS design, aimed to reproduce the qualitative behavior of a SMR having the same generic feature of IRIS, no proprietary-data have been used. The main information on the SMR (geometry, control logics, boundary conditions, etc.) has been determined by scaling the open-data available from the SPES-3 facility [27][26][31], from public general data available on IRIS [25][32] and by engineering evaluation. In addition, more details on the reactor nodalization adopted can be found in [9].

CESAR model of top-RPV

The top-RPV nodalization has been realized with CESAR following the scheme reported in Fig. 4.8. The main internal metal structures (CRDM, metallic liner, downcomer SG pipes, pumps, upper plenum, plates, etc..) have been considered in the model and coupled with the thermal-hydraulic volumes. The external vessel metal structure has been coupled with the CPA zones in order to consider the heat losses to the containment. The 8 primary-side SGs tubes have been nodalized as an equivalent one (defining a weight equal to 8 for the corresponding volumes), by assuming as a first approximation that the behavior of the 8 parallel lines is the same. This approximation is necessary in order to be able to use the SMR model for SA analysis and still preserving acceptable computation timings. The same approach and assumption has been used for the secondary system modelling (FL and SL). Due to the lack of specific heat-transfer models for helical-coil SG in CESAR, in agreement with previous studies [33], the secondary side SGs of the generic IRIS have been modelled by increasing the total heat-transfer surface of 30%. In this way, the steady-state conditions can be established, and the same assumption has been preserved also for transient simulations. Thermal structures have been taken into account also for the secondary-system pipes. The behavior of reactor components such as pumps, valves and the PRZ heater, which are necessary for the steady-state calculation, have been simulated with the dedicated structures of ASTEC. CESAR volumes modelling the top-RPV are coupled to the ICARE nodalization of the bottom-RPV within 3 flow connections (core channels, bypass, downcomer), as in Fig. 4.8.

CESAR model of PSS, LGMS, EBTs, DVI lines and EHRS systems

In order to assess the natural-driven phenomena characterizing a passive mitigation strategy, a detailed nodalization of the passive system is needed. For this reason, CESAR volumes have been employed for modelling the 2 lines of passive systems connected to the RPV by DVI lines (DVI, EBT, LGMS, PSS). The nodalization is summarized in Fig. 4.8. The 2 lines of safety systems, despite being identical, have been modelled separately since a very different behavior is expected between the two during the DVI-break sequences. PSS vent-pipes are coupled to the DW zones of CPA with “BREAK” types connection. And LGMS and EBTs are thermally coupled to the respective zones of DW in which the tanks are placed. The 3 ADS stage-1 lines on the head of RPV are modelled as one equivalent pipe and are connected to the quench-pipe zone of CPA. Following the secondary-system assumption, the 4 EHRS loops are modelled as one equivalent loop and connected to the secondary circuit (Fig. 4.8); the RWST equivalent tank is coupled to the EHRS circuit. Boundary conditions are applied to the RWST in order to consider the heat and mass losses to the environment and keep its pressure at atmospheric value. Modelling the 4 parallel lines of EHRS system as an equivalent one by using weights implies the assumption that the behavior of the lines is the same during the transient evolution.

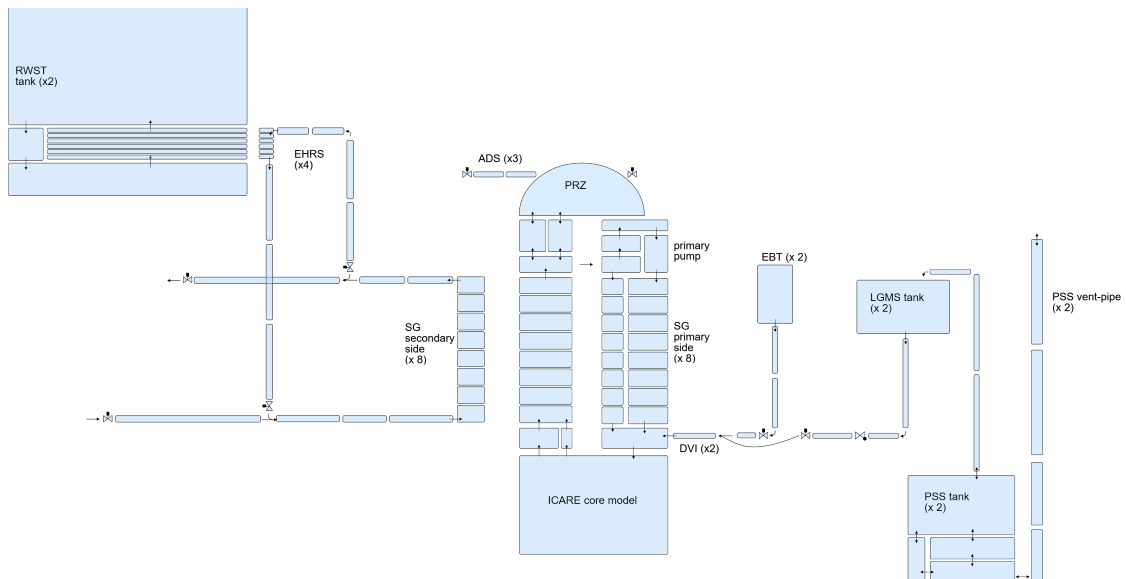


Figure 4.8: CESAR nodalization scheme of the generic IRIS reactor [9].

ICARE model of bottom-RPV and core

Aiming at using the reactor model for SA analyses, the bottom part of the RPV (core, lower downcomer, LP) has been modeled using a 2D geometry by employing the 2D cylindrical axial-symmetric vessel structures of ICARE, and the related 2D fluid channels (Fig. 4.9). In the nodalization, 5 fluid coaxial core channels model the radial nodalization of core region, in which the cylindrical structures of core internals (fuel rods, control rods, nozzles, spacer grids, upper and lower support plates) are placed. The core structures have been modelled as cylindrical 2D elements or by employing ASTEC vessel dedicated structures. Fuel and control rods elements are located inside the 5 core channels and are weighted considering the average number of assemblies in each channel. Wrapping the core channels there are a core bypass channel and a downcomer channel, for a total of 7 fluid channels. Reflector, barrel and vessel are concentric cylindrical structures bounding core, bypass and downcomer, respectively (Fig. 4.9). Fluid channels are discretized in 16 axial regions for a total of 112 control volumes where the thermal-hydraulic is calculated by CESAR. Convection, conduction and radiative heat models have been activated to calculate the heat exchange between the core structures. The ICARE physical models for the core mechanical behavior, degradation and chemistry have been activated to allow the simulation of the in-vessel core degradation. Some of core modelling data (e.g. radial and axial power distribution in the core, distribution of material composition of grids) and structures integrity criteria (s.a. creep, burst and dislocation of cladding, LH failure criteria, etc.) have been taken from the data of the PWR 900-like input-deck delivered with the ASTEC code.

The external structures bounding the ICARE model (LH; bottom part of vessel) are thermally coupled to the RC zone (of CPA module) in order to consider the heat exchange to the cavity. Different values of heat transfer coefficient are applied to the external surface of these structures depending on the water level inside the RC zones, in order to consider the possible external cooling conditions for dry, partially filled and filled RC. In ASTEC the value of the heat transfer coefficient for the heat transfer between CPA and ICARE structures has to be assumed by the user and is not calculated by the code depending on the external fluid regime.

CPA model of containment

CPA has been used in the realization of the spherical DW, RC, QT and quench-pipe following the scheme in Fig. 4.10. The metallic structure of DW has been modeled and coupled to the environment external zone, as well as the concrete walls of the cavity and of other containment structures. The “INSERTION” model

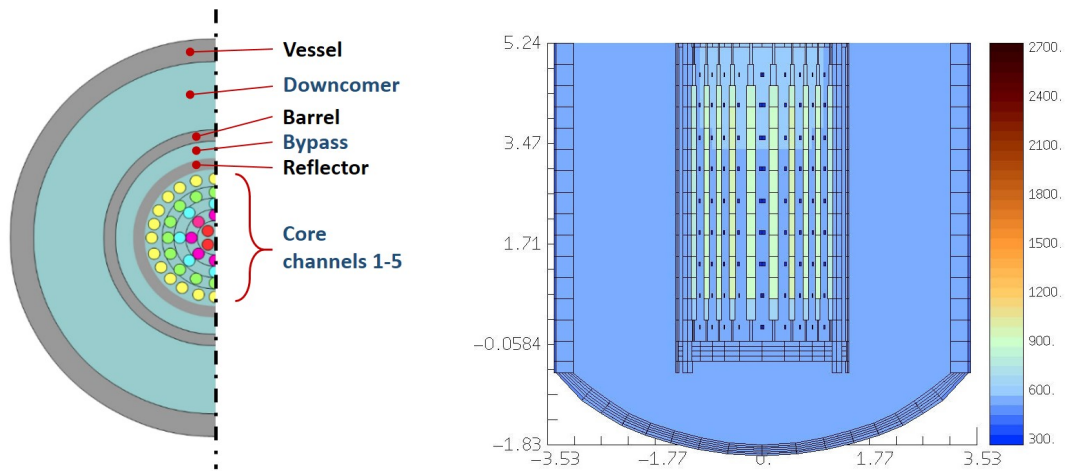


Figure 4.9: Radial discretization (Left) and ASTEC visualization (right), of the ICARE model of the generic IRIS.

of CPA is used for modeling the QT as a suppression pool, receiving steam from the ADS (CESAR) through the quench-pipe zone. The RC is nodalized with one zone connected to the bottom of DW zones. The CPA zones are coupled with “HEAT” type connections to the CESAR RPV for the estimation of the heat losses of the Vessel, as previously mentioned. CPA and CESAR modules are also coupled by several “BREAK” connections for fluid transfer: one for ADS stage-1 valves, one for ADS-stage-2 valves, one for the postulated DVI break, and two for the connections between the two PSS vent pipes and the DW atmosphere.

SOPHAEROS and ISODOP modelling of FPs behavior

SOPHAEROS module has been added to the model for the simulation of FPs transport and chemistry. The reactor meshing considered by SOPHAEROS includes the RPV volumes and all the zones of the containment. The FPs initial inventory provided to ISODOP for the calculation of decay heat and of isotopes transmutation has been estimated with an ORIGEN-ARP code [34] calculation, by assuming a four-year fuel cycle lifetime with a burnup of 40000 MWd/tU.

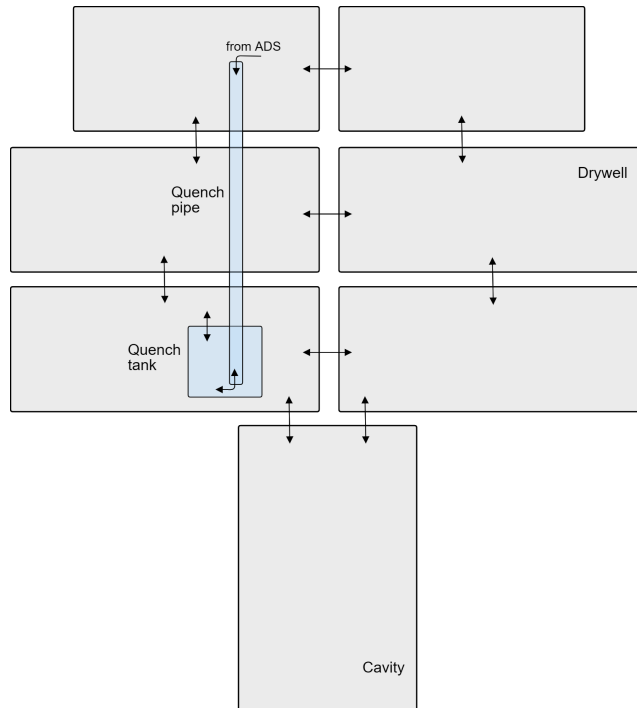


Figure 4.10: CPA containment nodalization scheme of the generic IRIS reactor [9].

4.3 ASTEC simulation of DBA sequence on the generic IRIS model

4.3.1 Steady-State conditions

Reproducing the correct nominal steady-state conditions is a crucial starting point for any further transient analysis on a NPP. In order to match the working conditions of reference for the generic IRIS, the initial set-up of some systems is necessary, e.g. for the 8 immersed primary pumps and the heaters inside PRZ regulating the primary pressure. Boundary conditions applied to the FL are the nominal feed flow-rate, temperature and pressure. Boundary condition to the SL outlet is the SL nominal pressure. 1 GWth is applied to the fuel structures inside the core model during the steady-state calculation (decay heat is calculated by ISODOP in transient condition). As mentioned in the previous section, the equivalent exchange surface of the helical-coil SGs has been increased in order to reach the steady reference power removed from primary. The steady-state conditions are summarized in Table 4.1 against the reference values obtained by the steady-state calculation on SPES-3 facility, presented in [26] and [27] (volumetric flow rate and total volumes

have been scaled considering the facility scaling factor, i.e. 1/100). The simulation was performed for 2000 s and, at the end of the calculation, the nominal conditions have been reached by the code with good agreement to the reference values.

Parameters	Reference Value	ASTEC value	Discr. %
Pressurizer P (bar)	155.0	154.9	0.06
Primary flow rate (kg/s)	4800.0	4857	1.19
Inlet Core T (K)	565.2	572	1.20
Outlet Core T (K)	603.6	606	0.40
Primary pumps head (bar)	1.5	1.5	0.00
Reactor coolant Vol. (m ³)	455.0	460.4	1.19
Core power (MW)	1000.0	1000	0.00
SG outlet pressure (bar)	58.3	58	0.51
SG inlet temperature (K)	497.0	493	0.80
SG outlet temperature (K)	594.0	595	0.17
SG mass flow rate (kg/s)	62.9	62.9	0.00

Table 4.1: Steady-state calculation values against IRIS reference values.

4.3.2 Simulation of DBA sequence

DBA assumptions

The ASTEC code simulation of the DBA sequence has been carried out for 70000 s in order to include all the main thermal-hydraulic phenomenologies characterizing the sequence. The SOT, considered at $t = 0$ s, is initiated with the opening of the 2-in double-ended break of DVI line-A.

Results of DBA simulation

The computational time for running the transient was around 40 hours. The results of the ASTEC calculation are reported in this section and the phenomenology is described and discussed according to the sequence PhWs summarized in Section 4.2.3. The sequence of main events characterizing the DBA simulation are summarized in Table 4.2; the main thermal-hydraulic phenomena predicted by the code along the transient are reported in Table 4.3, according to [12][10][35].

Event	Signal	Time (s)	Systems actuation
Break	-	0	-
High Containment P set-point	S-Signal	29	SCRAM; S.S. isolation; EHRS
Secondary pressure peak	-	42	-
Low PRZ level set-point	Low-PRZ	106	RCP coastdown; RIDC valves
Low PRZ pressure set-point	LM-Signal	134	ADS stage-1; EBTs
EBT-B emptying	-	1650	-
EBT-A emptying	-	320	-
Low ΔP (RPV-Containment) set-point	DP-signal	1330	LGMS
DW-PSS pressure inversion	-	1500	-
Start of flow from PSS to DW	-	1720	-
RC level at DVI level	-	4100	-
Low LGMS mass set-point	Low LGMS	17800	ADS stage-2
LGMS-B emptying	-	25500	-
LGMS-A emptying	-	20600	-
RWST boiling	-	48000	-

Table 4.2: Sequence of main events and systems actuation in the DBA simulation.

PhW-a

In the first 29 seconds of transient, before the activation of S-signal, the simulation is characterized by a RPV pressure decreasing and containment pressure increasing due to the opening of the DVI break; at the same time, secondary system and reactor core keep working at nominal reference power. The calculated water flow rate through the break from RPV (Fig. 4.11) shows the maximum value of 219 Kg/s at the SOT, rapidly decreasing to about 10 kg/s in the first 1000 seconds of transient, thanks to the RPV rapid depressurization and containment pressurization. In Fig. 4.12 it is reported the calculated pressure trend of PRZ, DW and secondary system. In Fig. 4.13 can be observed the PSS and LGMS systems pressure increasing, following the DW trend (from 0 s to about 1500 s). During the containment compartments pressurization, steam and non-condensable gases located in DW are pushed underwater through the PSS vent pipe in the PSS tanks. The code is able to predict the expected phenomenology of direct interaction of the steam-gas mixture injected in the PSS pool cold water. Accordingly, it is observed a temperature and water level slight increase in PSS, following the steam direct condensation in the pool. Inside the DW zones of CPA, gas mixture natural convection and thermal

System	Component	Predicted Phenomena
Primary	RPV	Break Flow
		Single and two phase natural circulation
		Heat transfer in SG primary side
		Heat transfer in covered and partially uncovered core
Secondary	SG	Heat transfer in SG secondary side
		Liquid boiling in SG helical coils
		Steam superheated on secondary side
EHR	EHR loops	Steam condensation in heat exchanger (heat transfer in tubes side)
		High and low pressure heat exchange in exchangers
		Two phases natural circulation
RWST	Large pool (RWST)	Thermal stratification
		Natural convection in the pool
		Heat and mass transfers at the interface
		Heat transfer pool-side
EBT	EBT tanks	Gravity driven injection
LGMS	LGMS tanks	Gravity and differential pressure driven injection
PSS	PSS pools	Direct condensation for liquid-steam interaction
		Thermal stratification
		Distribution of pressure drop
		Influence of non-condensable gas on condensation heat-transfer
Containment	Drywell	Thermal stratification
		Condensation on containment structures
		Heat losses to the environment
		Effect of non-condensable gases on condensation heat transfer
		Natural convection of gas
		Primary - Containment coupling
	Reactor Cavity	Gravity driven injection
Quench system	Quench tank	Direct Condensation for Liquid-Steam interaction

Table 4.3: Main phenomena qualitatively predicted by the code along the transient, per reactor system.

stratification phenomena are predicted in the code simulation. Steam condensation

on the colder DW metal structures makes the condensed water to flow in the RC and slowly increase its level. During the containment pressurization phase (0 – 1524 s), the pressure of PSS (and LGMS) follows the containment trend (Figure 8). The main predicted phenomena related to containment, PSS and primary side are summarized in Table 4.3.

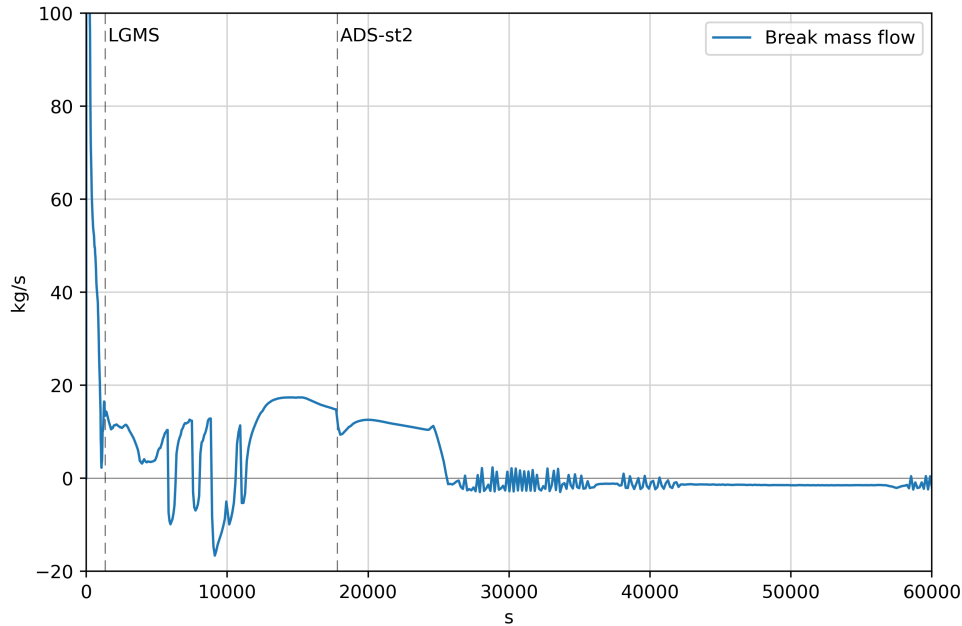


Figure 4.11: Mass flow rate through the break from the RPV.

PhW-b

The high containment pressure set-point triggers the Safety-signal at 29 s of simulation. Reactor SCRAM, secondary system isolation and EHRS actuation take place with the respective delay times. The secondary system isolation drives the SG pressure to saturation, reaching a temporary maximum value of 122 bar at 42 seconds. After the peak, the secondary pressure rapidly decreases due to the heat removed by the RWST actuation (Fig. 4.12). In the present analysis, since the EHRS system has been modeled as one equivalent loop, as a first approximation the 4 loops of the system are considered to be actuated all at the same time. The total power removed from the primary system through SGs is shown in Fig. 4.14, together with the core decay heat and the power transferred from EHRS to the RWST. The power removed from RPV, thanks to the operation of EHRS in natural circulation, is greater than the decay heat during the first part of transient

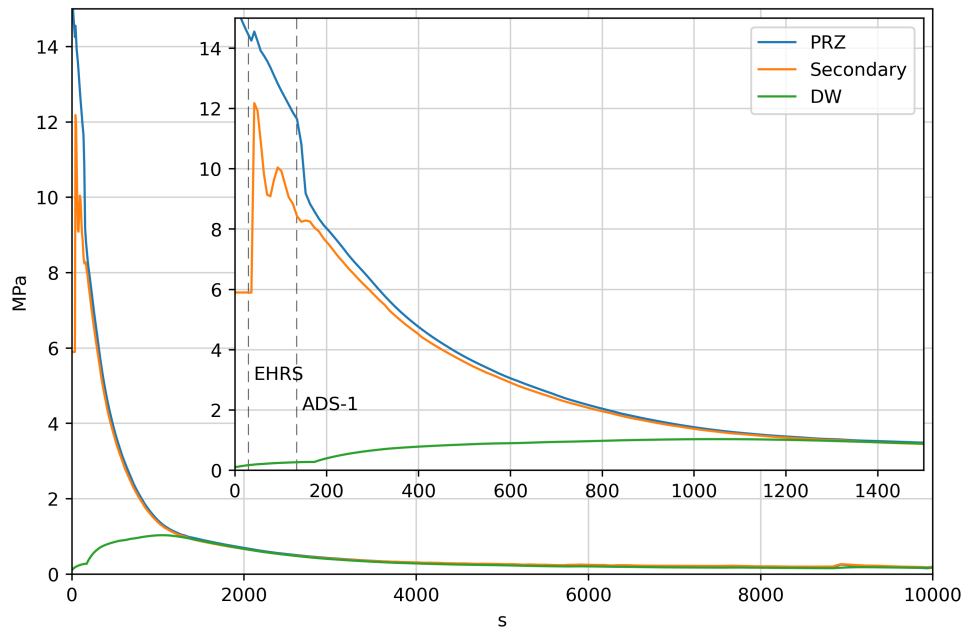


Figure 4.12: Pressure evolution in PRZ, secondary system and drywell.

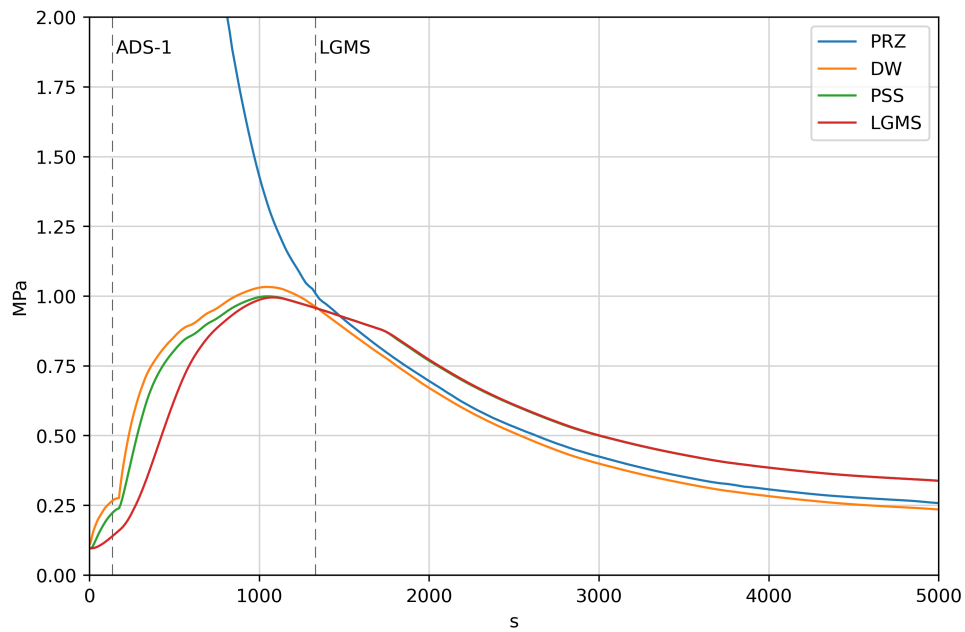


Figure 4.13: Pressure evolution in PRZ, drywell, LGMS and PSS.

(up to around 10000 s). Temperatures of EHRs and RWST during the transient are reported in Figure 10. Natural circulation is predicted by the code also inside

RWST tank due to the nodalization adopted. Natural circulation in the RWST pool enhances the steam condensation inside EHRS condenser tubes. The main predicted phenomena related to secondary side, EHRS and RWST are summarized in Table 4.3.

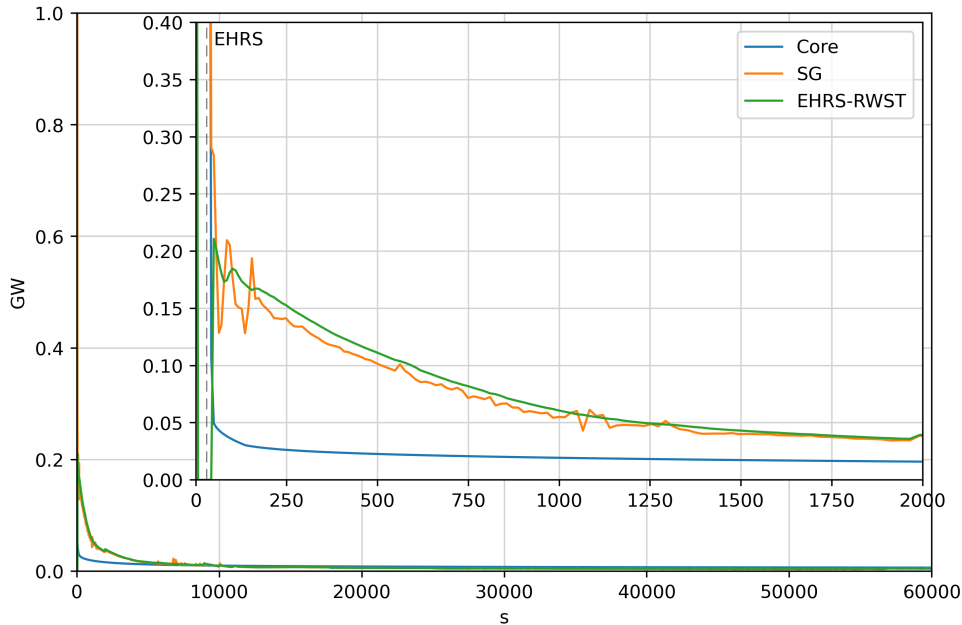


Figure 4.14: FP decay heat, SGs power from RPV to EHRS loops, power from EHRS loops to RWRT.

PhW-c

At 106 s the Low PRZ level signal is triggered and, following the plant logics, primary pump coast-down and RI-DC check valves opening take place. Natural circulation regime starts at this point inside the RPV. Till the water level covers the pump suction, two different natural circulation paths are predicted: In the first, the fluid heated in the core ascends along the riser until the pumps suction plenum, then it moves along the downcomer transferring energy to the secondary system through SGs. In the second path the heated fluid from core passes at middle-riser height through the RI-DC check valves, moving along half of SGs length and transferring energy to the secondary side. The opening of RI-DC check valves allows natural circulation to take place in RPV also for water level lower than the pumps suction plenum elevation, extending the duration of the natural circulation regime in RPV until the liquid level becomes lower than the RI-DC connections (at about

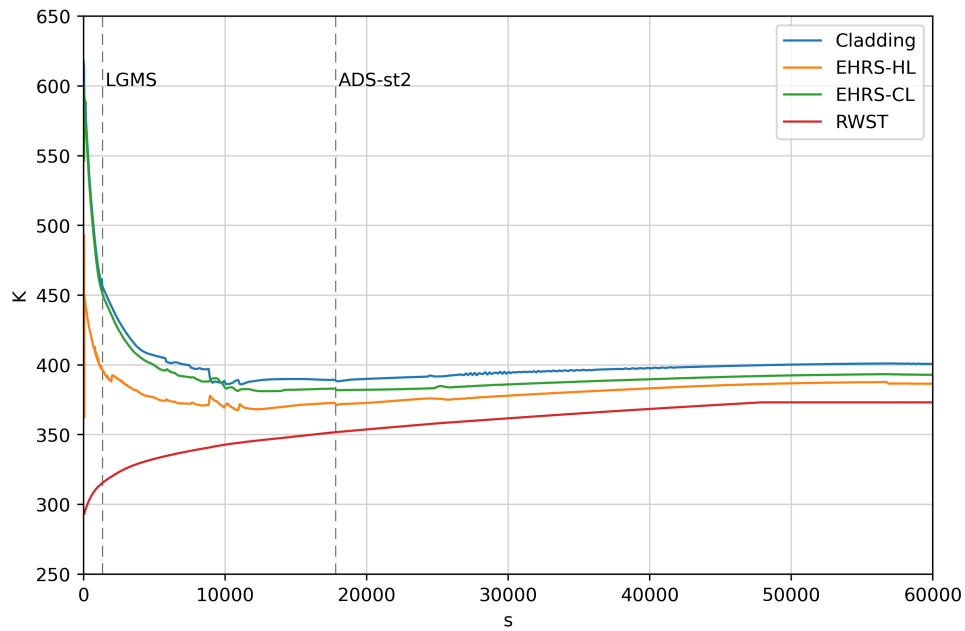


Figure 4.15: Temperature of cladding, EHRH hot leg, EHRH cold leg, outlet of core and RWST.

800 s). In Fig. 4.16 it is reported the total primary water flow rate calculated in reactor riser. The main predicted phenomena related to secondary and primary systems are summarized in Table 4.3.

PhW-d

The low PRZ pressure set-point is reached at 134 s, triggering the LM-signal. At this point, the PRZ is almost empty. Following the ADS st-1 actuation, water is pushed upwards inside PRZ whose water level quickly rises. Due to the high mass flow-rate of steam transferred through ADS stage-1 to the water of QT, both the trends of containment pressurization and primary depressurization increase, as can be observed in Fig. 4.12 and 4.13. The consequent reduction of pressures gap between the two systems is important to mitigate the primary leak. As soon as the valves of EBTs are opened, cold borated water starts to be injected for gravity through the two DVI lines. At this point, as expected, the calculated EBT injection rate through the broken DVI line-A is much higher than the calculated injection flow rate through the intact line-B. The mass flow-rate through the intact line-B (to RPV) and through the broken line-A (to RC) is reported in Fig. 4.17. The collapsed water level inside RPV decreases below the TAF level at about 300 s;

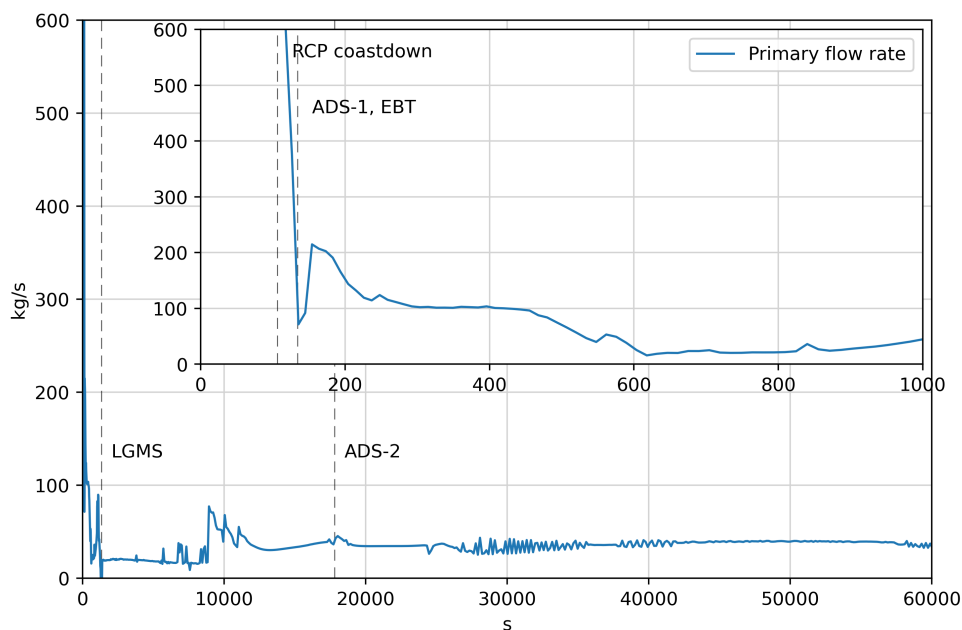


Figure 4.16: Total primary mass flow-rate from the core to the riser.

but the water injected and power removal is sufficient to prevent any fuel heat up. The normalized values of the collapsed level inside core channels is reported in Fig. 4.18. The main predicted phenomena related to EBTs, QT and primary side are summarized in Table 4.3.

PhW-e

The low RPV - DW differential pressure set-point (below 0.5 bar) is reached at 1330 s (Figure 8) thus, the valves that connect the two tanks of LGMS to the DVI lines are actuated, and it follows the starting of the LGMS water injection into RPV (intact line) and into RC (broken line). From this moment the containment depressurization phase starts, as can be observed in Fig. 4.12 and 4.13. Around 20 s later, DW pressure decreases below PSS (and LGMS) pressure. Pushed by the depressurization of DW, the code captures the water level of PSS vent pipes rising up, until the pipes top head and, hence, dropping water outside the PSS vent pipe into the containment. This phenomenon gives the major contribution to the filling of RC. During the containment depressurization phase, LGMS and PSS tanks are kept at higher pressure with respect to DW by the hydrostatic pressure of the water head inside the PSS vent-pipes (Fig. 4.13). The PSS (and LGMS) higher pressure (with respect to DW and RPV) is responsible of the enhancement

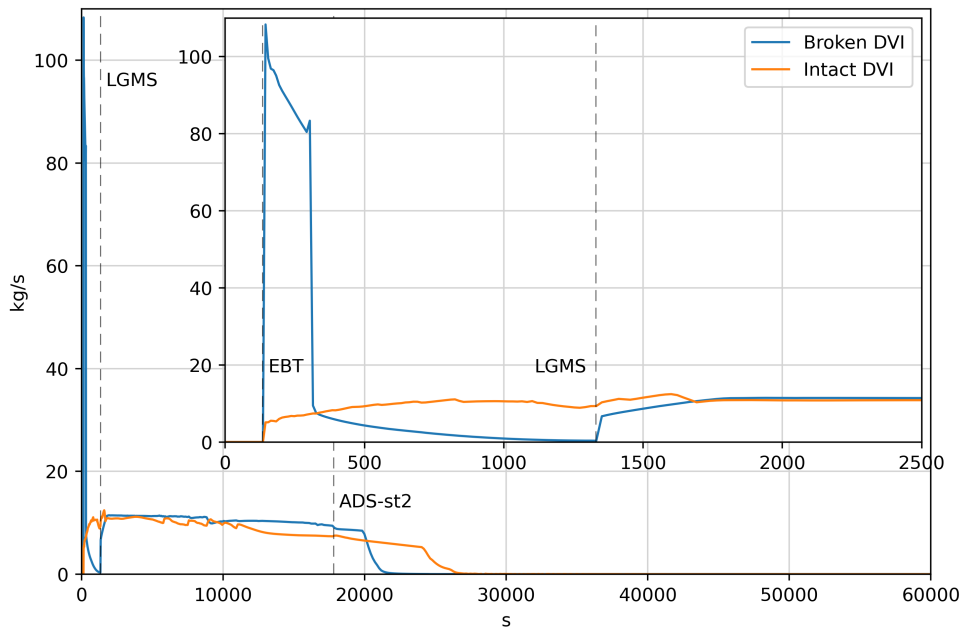


Figure 4.17: Mass flow rate through the broken DVI (to the RC) and the intact DVI (to the RPV).

of LGMS injection through the DVI lines; as expected in the passive mitigation strategy. The LGMS injection rate is similar within the two DVI lines (Fig. 4.17), and it lasts until 20600 s for the broken line and 25500 s for the intact line. In Fig. 4.19 it is reported the normalized water level inside PSS, LGMS, EBT tanks and inside RC. As can be inferred, most of the water filling the RC comes from the water dropped out of PSS vent-pipe. In the simulation the water level inside RC reaches the break level at around 4100 s. Following the LGMS injection, the RPV water level slowly increases again filling the core; until at around 9000 s a liquid natural circulation flow is re-established inside RPV, when the RPV water level reaches the RI-DC valves elevation (Fig. 4.19). A stable natural circulation regime is simulated inside the core until the end of the calculation. It is driven by the temperatures gap between RPV and RWST water (Fig. 4.15) and, despite the gap reduction during the sequence (and consequent reduction of EHRS heat removal), it keeps cooling the core up to the end of the simulation. The main predicted phenomena related to PSS, LGMS, RWST and EHRS here discussed are summarized in Table 4.3.

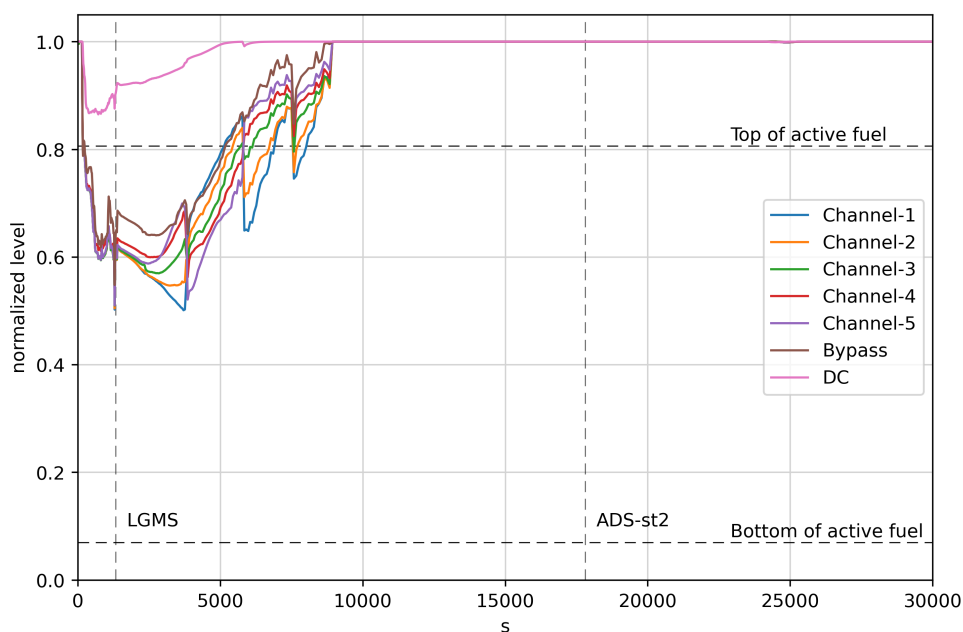


Figure 4.18: Normalized collapsed level inside the core channels (between upper and lower core plates elevations).

PhW-f

The valves of ADS Stage-2 are actuated at 17800 s and, due to the opening of the larger connection, RPV and containment get the same value of pressure. The pressure equalization of the two systems allows equalizing the water level between RPV and RC through the break connection. In the long-term cooling phase, a dynamic equilibrium is reached between RPV and RC and the break flow-rate becomes negative until the end of the transient. In this phase, the fuel is kept covered thanks to the break connection by the filled RC; and the temperature inside the core is kept constant at 401 K, as can be observed in Fig. 4.15. At around 48000 s the RWST water (at atmospheric pressure) reaches 100 °C and starts to boil increasing the heat transfer from the condenser tubes. During the long-term cooling the residual heat produced in the core is balanced by the power removed by the primary and secondary loops natural circulation through the EHRS, and by the heat losses from containment to the environment. During this phase there is still condensation of steam coming from RPV on the large surfaces of the DW liner, and the condensed water flows inside RC. Up to the end of the calculation, the reactor reaches a quasi - steady state regime. The main predicted phenomena related to RPV, RC and EHRS are summarized in Table 4.3.

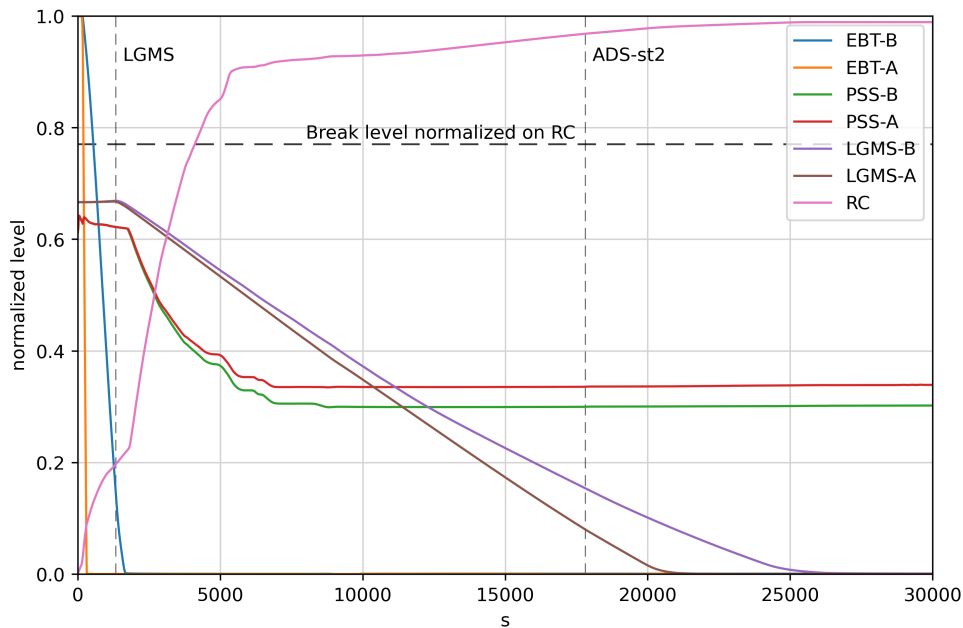


Figure 4.19: Normalized water level inside the tanks of PSS (1 and 2), LGMS (1 and 2), EBT (1 and 2), the RC and Break relative level in RC.

4.3.3 Conclusions and remarks

Main modelling simplifications adopted

Despite the fact that the IRIS model developed with ASTEC can be considered “generic” and, hence, it is not intended to make quantitative comparison with a reference sequence, but aimed to the investigation and qualitative identification of the phenomena predicted; some major modeling assumption and differences to the DBA reference sequence has to be underlined:

- First main simplification concerns the nodalization of EHRs: since the ASTEC model features only one EHRs loop (with a volumes weights of 4), this system has to be activated all at once (at the triggering of the S-signal). On the contrary, in the reference sequence the EHRs activation is expected in two steps, as described in Section 4.2.3. As a consequence, a slightly greater amount of power removed from RPV is expected in the first part of the ASTEC simulation. The simplification choice made is necessary to ensure acceptable calculation timing also in the case of long SA sequences.
- Another assumption that could have a quantitative effect in the code estimation of EHRs removal power is related to the modelling of helical-coil SGs,

which is realized by assuming 30% of additional exchange surface due to the lack of specific SG helical-coil model in the code.

- It is important to underline that in ASTEC simulation the time evolution curve of the decay heat at the core has been calculated by ISODOP on the base of the FPs inventory provided. The burnup assumed for the inventory should concern a quite conservative core power.
- One more modelling simplification is related to the evaluation of the heat-transfer between RC and the external structures of the bottom RPV and LP (ICARE structures): the heat transfer coefficient has been manually imposed on the base of the water level in RC, as it is described in Section 4.2.4.

Conclusions

One of the main challenging in modelling integral passive SMR with a modular code as ASTEC is the need to ensure the tight thermal-hydraulic coupling between all the reactor systems (RPV, containment, safety systems) on which the passive mitigation strategy is based. It implies a use of the code modules which is beyond the common requests for conventional LWR applications, in which the modules coupling has much simpler features and different modules are employed for separated parts of the reactor with more limited interactions.

The proposed ASTEC nodalization approach (described in Section 4.2.4) has been proven able to reproduce the expected phenomena involved in the complex passive mitigation strategy adopted by the IRIS design in the case of a 2-in break of a DVI. Within the adopted modelling scheme, the code has been qualitatively able to predict the expected main thermal-hydraulic phenomena driving the sequence. In particular, the simulation features the thermal-hydraulic coupling between containment, RPV and passive safety systems, which allows the success of the passive mitigation strategy leading to the RPV depressurization and core refill and cooling in safety conditions; the phenomena of direct interaction of hot gas and steam dumping inside the PSS pool limiting DW pressurization; the natural circulation taking place inside the RPV, EHRS loops, RWST tank and DW, that allows the passive removal of decay heat in safety conditions. The containment and PSS pressure inversion is also predicted by the code, allowing the prediction of the passive water injection in the RPV and in the RC.

In order to improve the current generic IRIS model, some new modelling features already implemented in the new version of ASTEC (V2.2.0), such as the possibility to more accurately estimate the heat-transfer between RPV and RC, should be adopted in the model.

The development of some new code modelling features, such as the introduction

of specific heat transfer models for helical-coil SG, could be very important to be able to assess accurate quantitative predictions of the phenomena characterizing a SMR passive mitigation strategy. Validation of thermal-hydraulic modules of ASTEC against experimental facility designed to characterize phenomena typical of passive safety systems and integral SMRs (as described in Chapter 2) is also a crucial step to be faced by the code.

4.4 ASTEC simulation of BDBA sequences on the generic IRIS model

The Fukushima accident showed to the international nuclear community that even in well designed and operated NPP, unexpected events could lead to beyond design scenarios and should never be underestimated. Despite the design of advanced SMRs being meant to be inherently safe (see Section 4.1), the investigation of accidental scenarios which can potentially lead to core melt (BDBA scenario) and the study of SA condition should not be excluded. Accordingly, independent features for preventing and mitigating a core melt accident have to be included at level 4 of Defence-in-Depth, together with the offsite emergency response at level-5.

Despite the probability of a beyond-design scenario is considered to be very low in passively cooled reactors, the application of SA codes to simulate BDBA and core degradation conditions in SMRs is an important step to find valuable outcomes regarding the current capability of the code in the simulation of the main core degradation phenomena in such designs. And, therefore, to plan further research programs and experimental activities for the improvement and validation of codes on the identified phenomenology specific of advanced designs. In addition, the simulation of the reactor in BDBA and SA can lead to valuable outcomes regarding the role played by each passive system in the mitigation strategy and insights for improvement of the current design to avoid core melt or to mitigate its consequences.

In the present section, the generic ASTEC model of the IRIS reactor has been used for the development of 4 BDBA sequences, by using as a reference scenario the DBA calculation presented in the previous section. The description of the simulations results and the following remarks and outcomes are addressed in the following.

4.4.1 Assumptions of BDBA sequences

Considering as a reference sequence the DBA described in the previous section, four different BDBA scenarios have been assumed by starting from the same initiator event: a 2-in double ended break of DVI line-A. In all the scenarios it is assumed the failure of selected passive safety systems, which would be activated by the opening of valves at specific set-points. Accordingly, despite passive systems work thanks to natural-driven forces, the activation of these systems is based on electric signals and the opening of valves that, as an extreme hypothesis, have been considered to fail.

The 4 assumed beyond-design scenarios are:

- *Failure of EBTs;*
- *Failure of EBTs and LGMS;*
- *Failure of EHRS and ADS st-1;*
- *Failure of EBTs, LGMS, EHRS and ADS.*

The activations of the safety systems considered available in a sequence are assumed to follow the same control logics of the reference DBA without any modification (see Table 4.2). The passive safety systems assumed to guarantee the operability in all the scenarios are those not activated by safety signals: PSS system (which consists in 2 suppression pools connected to the DW of containment by open vent-pipes); opening of the RI-DC valves (kept closed by the primary pumps delivery pressure, until the pumps coastdown).

Also the thermal-hydraulic coupling between RPV, containment and PSS can be considered as a passive mitigation strategy that is always available. As a further hypothesis, the steel spherical containment of the reactor is assumed to fail in case it overcome an internal pressure of 13.5 bar (design pressure of the IRIS containment). In case this condition is fulfilled, a large breach is assumed to open and to directly connect the top part of the DW to the environment, hence, assuring the containment depressurization to atmospheric pressure.

4.4.2 Results of BDBA simulations

The 4 calculations have been initiated by starting from the same steady-state conditions (described in Table 4.1); the opening of the 2-in break of DVI line-A is considered to take place at the SOT ($t = 0$ s). The main timings of the simulation results are summarized in Table 4.4 and the plots of the selected main FOMs have

been reported in Fig. 4.20–4.26 against the reference DBA results. A description of the main features of each simulated sequence is given in the following.

Event	Reference DBA	EBT failure	EBT, LGMS failure	EHRs, ADS-st1 failure	All failure
Break	0	0	0	0	0
High Containment P. set-point	29	29	29	29	29
Low PRZ P. set-point	134	134	134	302	302
EBT-B emptying	1650	-	-	2400	-
EBT-A emptying	320	-	-	580	-
Low ΔP RPV-Cont. set-point	1330	1375	1375	16905	26960
RC level at DVI level	4100	5200	5200	14900	74000
Low LGMS mass set-point	17800	18000	-	132150	-
LGMS-B emptying	25500	25600	-	155000	-
LGMS-A emptying	20600	21500	-	135000	-
RWST water boiling	48000	48000	55000	-	-
Cladding failure	-	-	-	7800	9170
Corium relocation in LP	-	-	-	91560	111600
Containment failure	-	-	-	133950	113050

Table 4.4: Timings (s) of main events in the 4 BDBA sequences.

EBTs failure scenario

From a phenomenological point of view, the assumption of EBTs injection failure does not result in a different scenario with respect to the reference DBA sequence. The lack of EBT cold water injection leads to a slight delay in the cooling and depressurization of the reactor. This can be inferred by Table 4.4, in which can be observed that all the timing following the low PRZ pressure set-point (failure of EBT intervention) takes place with some delay in this scenario with respect to the reference DBA. The only major difference is observed in the final water level in the RC (Fig. 4.21), which is slightly lower in this case due to the lack of EBTs injection.

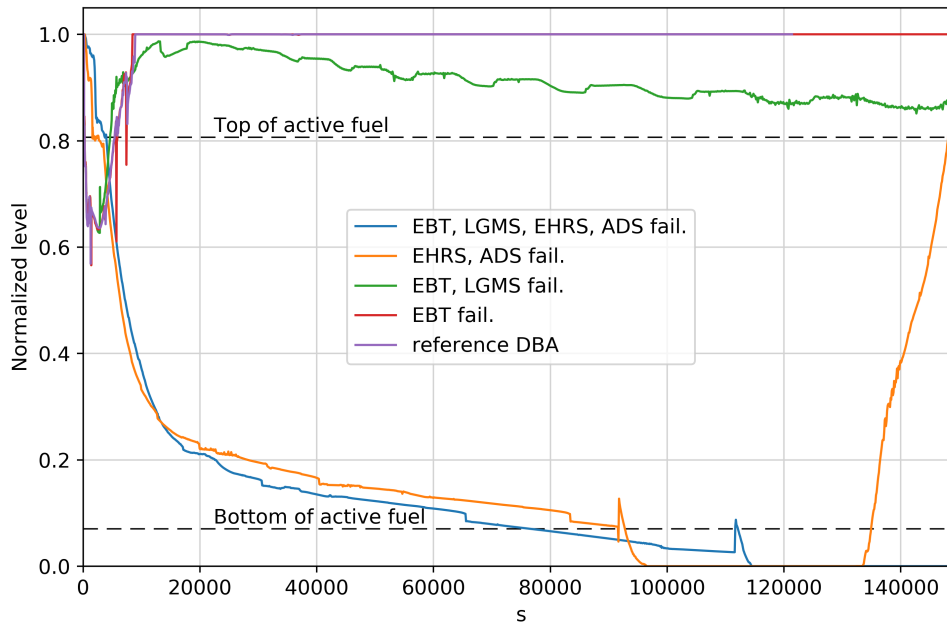


Figure 4.20: Normalized value of the average collapsed level in the core (upper and lower core plates elevations taken as reference).

EBTs and LGMS failure scenario

The scenario of EBTs and LGMS injections failure features a very similar phenomenological evolution to the previous scenario (EBTs failure) and to the reference DBA scenario. With respect to these two calculations, the present transient shows a very similar decrease of the averaged level in the core during the RPV depressurization, in Fig. 4.20; and a similar following core refill which prevents any core heat-up, as can be stated from the core output temperature of Fig. 4.25. Accordingly, the low differential pressure between containment and RPV (due to the RPV depressurization effect of the ADS st-1 openings and of the EHRS power removal) quickly mitigates the leak of coolant from the break. Despite the lack of EBT and LGMS injections, the remaining water in the RPV is sufficient to cover the active core and, hence, to remove the decay heat and prevent any core damages thanks to the action of the EHRS in natural circulation. As expected, the final core level (Fig. 4.21) is lower than the previous scenarios (DBA and EBTs failure) due to the lack of LGMS injection. At the end of the simulation (150000 s), the water level is above the active core elevation, despite keeping to slowly decrease due to the water evaporation.

A phenomenological difference, with respect to the *EBTs failure* and to the

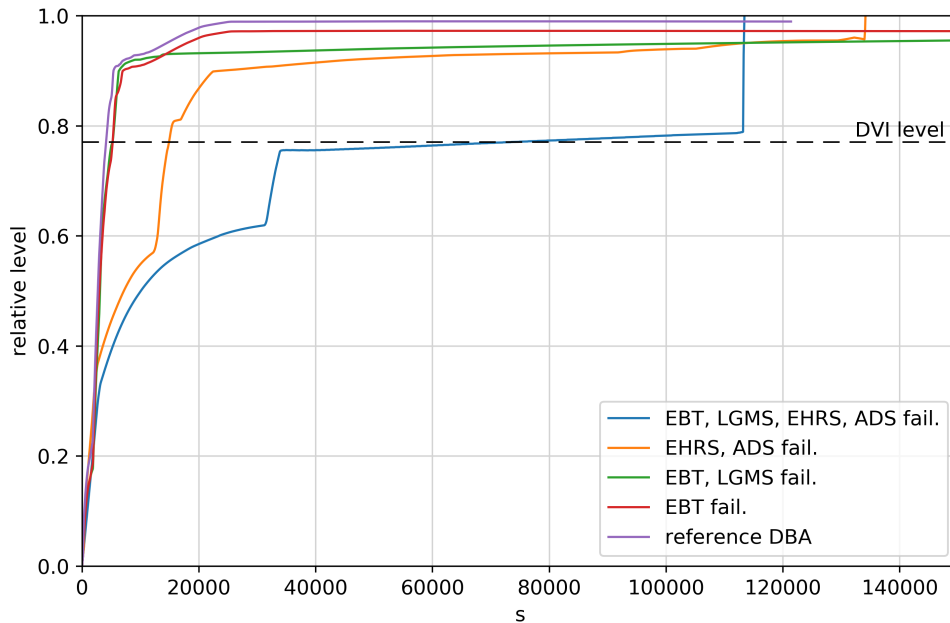


Figure 4.21: Normalized value of the water level in the RC, with respect to the RC total elevation.

reference DBA scenarios, is related to the coupling between RPV and containment. Indeed, despite the water level in the RC reaches and overcomes the DVI level with a very similar timing (Fig. 4.21, Table 4.4), the present transient does not feature a backward water flow through the break keeping the RPV water level at the same level as the RC (Fig. 4.22 and 4.20), as one could expect. The reason should be attributed to the lack of opening of ADS st-2, activated by “LGMS low water mass signal” never reached in this scenario (Table 4.4). The opening of these larger connections between PRZ and containment atmosphere allows the RPV and the containment atmospheres to match at the exact same pressure (as happens in reference DBA and EBTs failure scenarios). In the present scenario only ADS-st1 valves are opened; which, on the contrary, are smaller valves and connect the PRZ to the pool of the QT through a series of pipes. Therefore, a small overpressurization of RPV with respect to containment (of about 0.3 bar = 3 m of water head) is preserved if only these valves are opened. For this reason, no backward water flow through the break is simulated by the code in the present calculation.

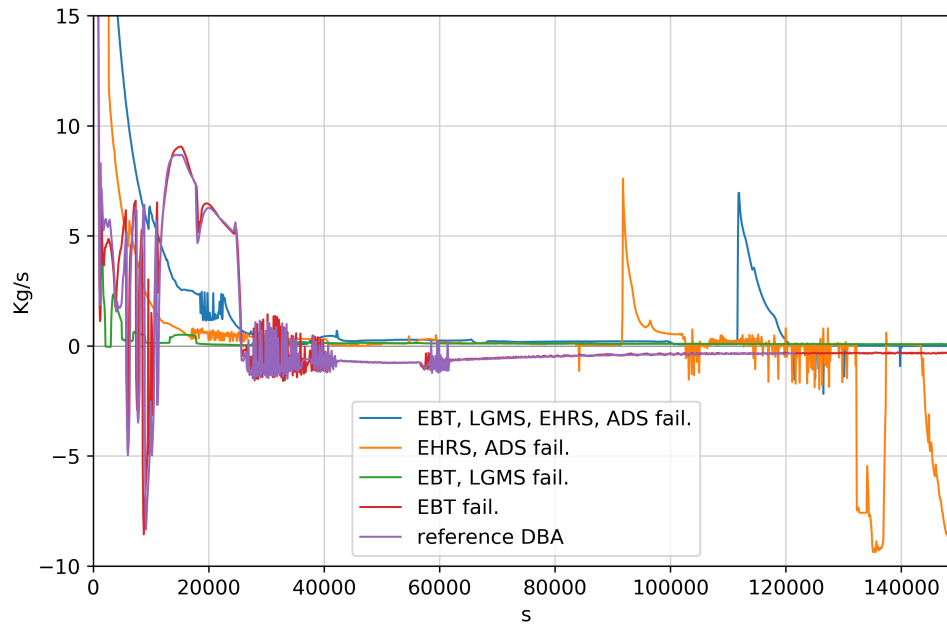


Figure 4.22: Mass flow rate through the brake (positive value is from RPV to containment).

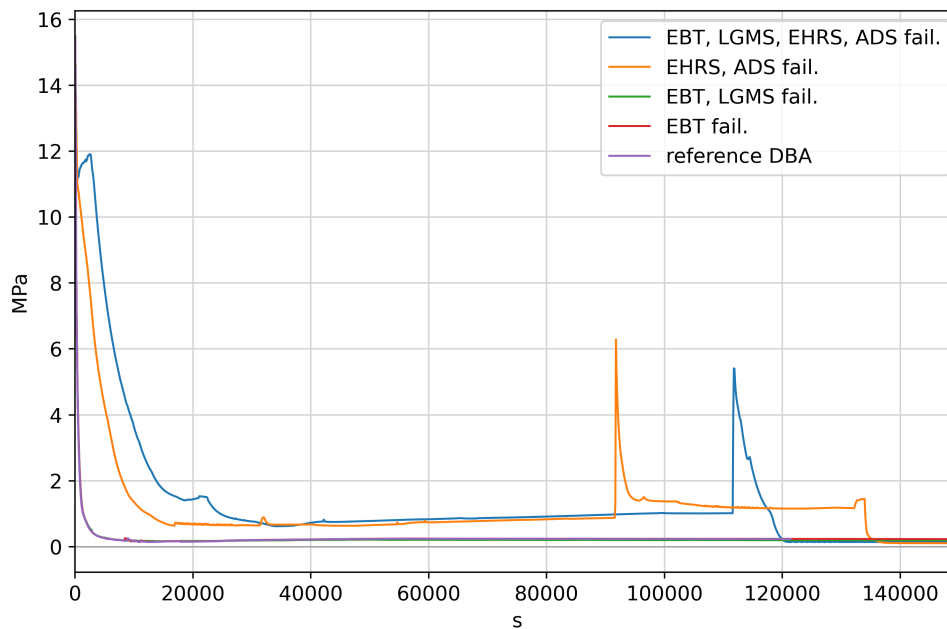


Figure 4.23: Primary system pressure (PRZ).

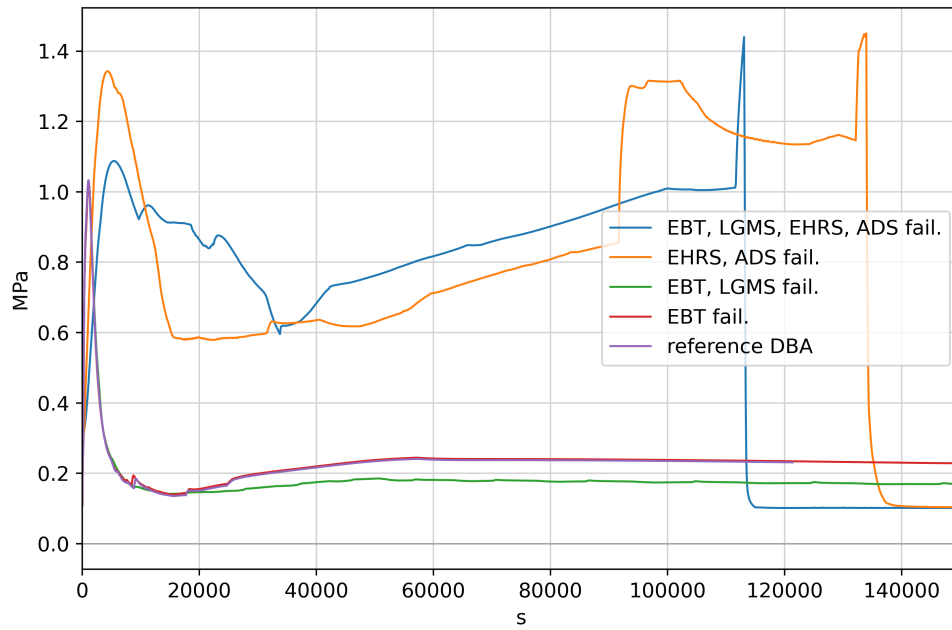


Figure 4.24: Containment pressure.

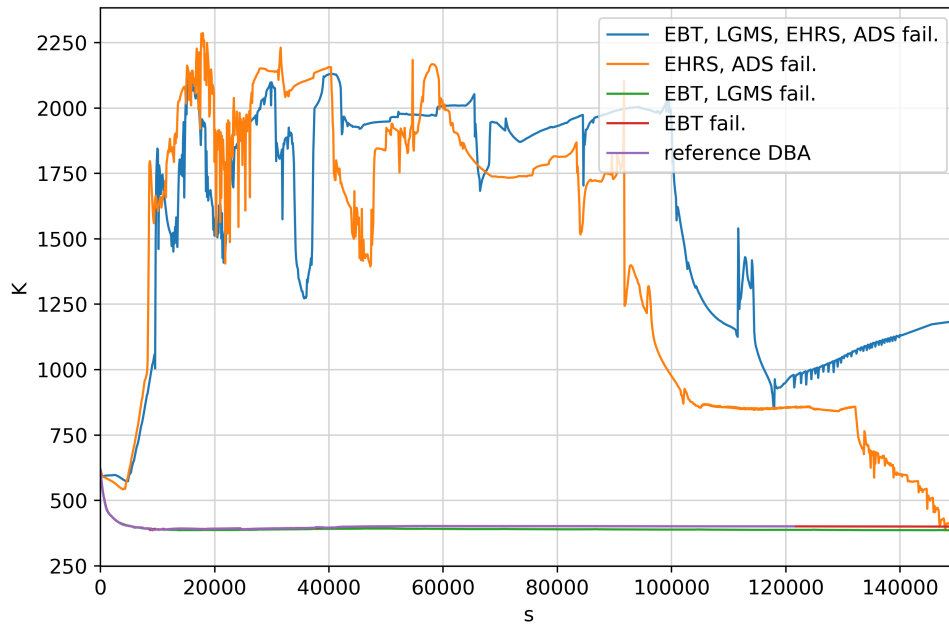


Figure 4.25: Core outlet temperature.

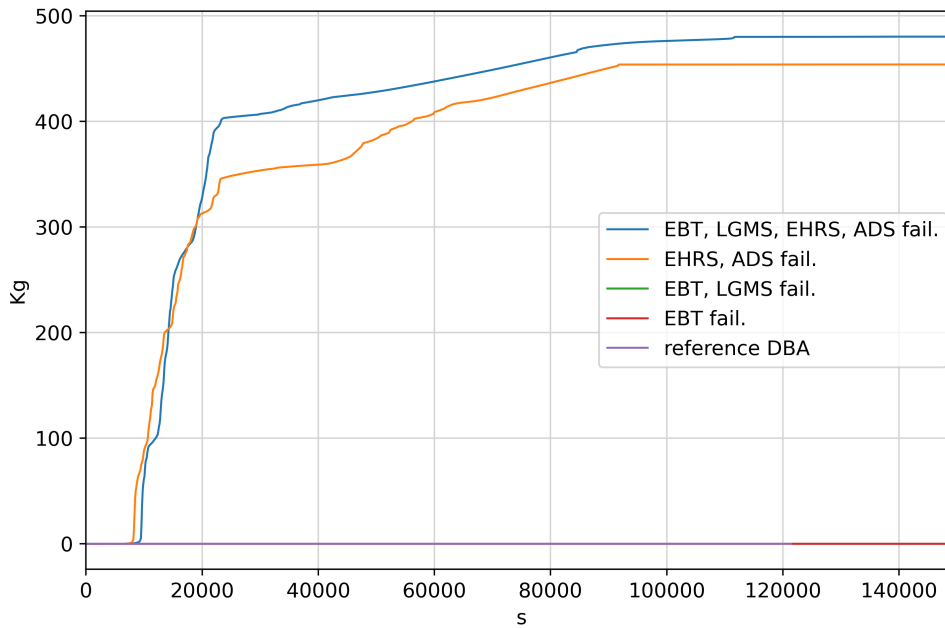


Figure 4.26: Total hydrogen mass produced.

EHTS and ADS st-1 failure scenario

A very different transient evolves in this case with regard to the previously described simulations. The lack of ADS-st1 opening and of EHTS heat removal leads the containment-RPV low differential pressure set-point ($\Delta P < 0.5$ bar) to be reached much later in the sequence (Table 4.4). As a consequence, the water leak through the break does not decrease soon enough to avoid the core uncovering in the first part of transient (0 - 10000 s). The impossibility to cool the uncovered core (despite the intact EBT injection) leads to the start of degradation at around 7800 s; the RPV–containment low DP-signal arrives at about 16905 s (Table 4.4), opening the LGMS valves.

During the core degradation, steam and incondensable gases produced and the lack of the EHTS cooling maintain the containment and the RPV pressurized between 6 and 9 bar, as can be observed in Fig. 4.23 and 4.24. The higher RPV pressure (with respect to the other systems) prevents any injection of LGMS water into RPV (through the intact DVI line); while a slow LGMS injection into the containment (through the broken DVI line) takes place. Also the RC water level, which has reached the break elevation at 14900 s, is not allowed to refill the core due to the RPV pressurization.

Core degradation advances until the bottom support plate failure and corium

relocation in the LP takes place at 128100 s. The vaporization of LP water causes a very high pressure peak in the RPV (about 63 bar), which is followed by a steep containment pressurization, up to around 13 bar; very close to the containment design pressure of 13.5 bar. After the slumping, the systems feature a stable phase with RPV pressure around 13 bar, during which the corium is retained in the LP externally cooled by the RC water. At 111600 s the low water mass in the LGMS tank-A triggers the “Low LGMS mass set-point”, opening the ADS st-2 valves. As a consequence (for the same reasons underlined in the previous case), the RC water is allowed to flow back through the break, interacting with the hot corium pool and, hence, producing overheated steam which quickly increases again the RPV and the containment pressure. In this case, the containment pressure reaches soon the containment design pressure determining its failure at 113050 s. The containment failure is followed by a fast depressurization of all the reactor systems to the atmospheric pressure and as expected by a large release of hydrogen, steam and FPs to the environment zone. The ASTEC visualization of the core degradation is reported in Fig. 4.27 for four timings during the core degradation sequence. As can be observed, the RC water keeps entering in the RPV through the break, completely filling the core. The final state of the reactor, at 150000 s, features the corium retained in the LH and submerge by water, as reported in Figure 20 showing the evolution of the core degradation along the sequence. The possibility of IVMR within this final configuration (internal and external core cooling) has to be investigated in a separate analysis. From a preliminary study, there seems to be promising possibilities to retain the corium in the LP by both internal and external cooling.

EBTs, LGMS, EHRS and ADS st-1 failure scenario

As can be inferred at first sight of Fig. 4.20-4.26, the present scenario features a similar phenomenological behavior to the one above described (failure of EHRS and ADS stage-1). Accordingly, both the scenarios feature the failure of the mitigation strategy and a SA sequence. The first phases of transient, before the onset of core oxidation, features some discrepancies with respect to the previous scenario: due to the lack of the EBTs cold water injection in RPV, the core temperature and primary pressure remain slightly higher; while, on the contrary, the containment pressure increase is much stronger in the previous scenario, where the water of the EBT connected to the broken DVI is flashed in the containment (EBTs are at the primary pressure) increasing the pressurization. The onset of core oxidation and degradation arrives within a similar timing in the two SA scenarios, as can be inferred by looking at Table 4.4 and at the hydrogen generation in Fig. 4.26. The

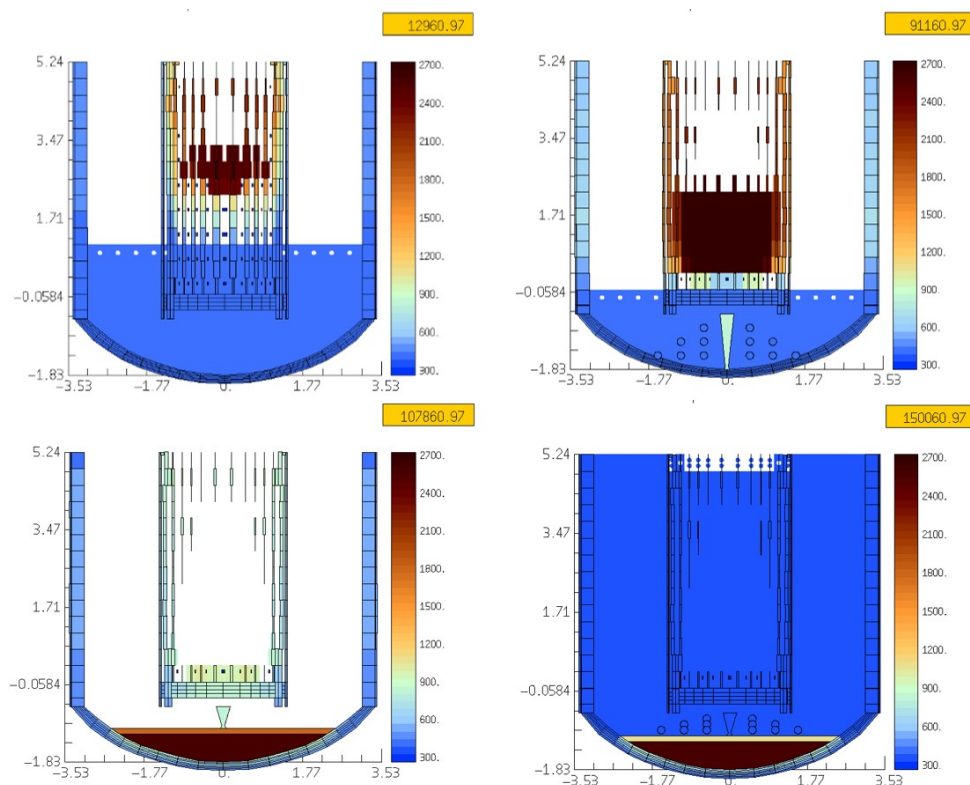


Figure 4.27: ASTEC - ICARE mask of core degradation evolution for the *ADS st-1* and *EHRS failure* scenario.

core degradation evolution of the present scenario features a very similar qualitative behavior to the previous one, as can be observed by looking at the hydrogen production (oxidation processes) and at the temperature evolution, in Fig. 4.25 and 4.26 respectively. The lower plate failure (and corium slumping in LP) arrives 20000 s later in this last scenario with respect to the previous one and a similar primary pressure peak is predicted by the code in the two scenarios (Fig. 4.23). Also the following containment pressurization features similar increase; with the major difference that, in the present scenario, due to the initial higher pressure, the containment reaches the failure pressure determining an earlier opening to the environment (about 21000 s earlier). After the containment failure, a very different behavior evolves in this simulation: the lack ADS-st2 valves opening on the PRZ head makes the RPV pressure to remain higher than the containment pressure along all the sequence (with a minimum over-pressurization value of 0.4 bar). As a consequence, a reverse flow through the break refilling the core is never predicted in this scenario. At the end of the sequence (150000 s), the corium is retained in the LP and the LH structures is cooled only by the external water in the RV (Fig.

4.28). It is evident that the possibility of IVMR retention within this configuration has a lower possibility to succeed.

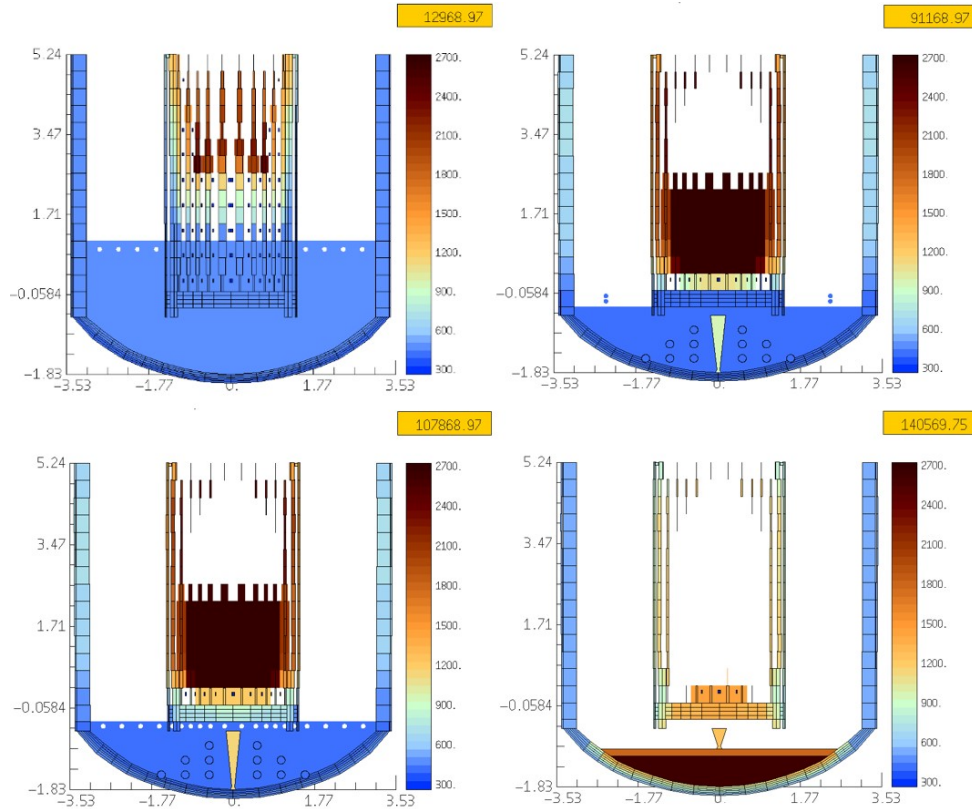


Figure 4.28: ASTEC - ICARE mask of core degradation evolution for the *EBTs*, *LGMS*, *EHRs* and *ADS st-1 failure* scenario.

4.4.3 Conclusions and remarks

The first main outcome of the 4 DBDA analysis is the different weight that each passive safety system has in the success of the mitigation strategy. The accident mitigation achieved in the first scenario (*EBTs* failure) and the partial mitigation of the second scenario (failure of *EBTs* and *LGMS*) show that a good safety margin is guaranteed by the passive mitigation strategy even in the case of multiple failures of the passive injection systems (*EBTs* and *LGMS*). Moreover, the comparison with the results of the following two failure scenarios (failure of *EHRs* and *ADS*; failure of *EBTs*, *LGMS*, *ADS*, *EHRs*), highlights as the two injection systems play a secondary role in the accident mitigation compared to the *EHRs* and the *ADS* systems. On the contrary, it seems clear that the role played by *EHRs* and *ADS* is

crucial for accident mitigation. In particular, the actuation of ADS st-1 and EHRS guarantees the depressurization of the primary system and the pressurization of containment (in safety conditions), anticipating the pressure equalization between the two systems which mitigates the leak of water from the RPV avoiding a complete core uncover. In addition, the containment pressures decreasing below the PSS pressure guarantees the RC flooding (from PSS vent-pipes) and the enhancement of LGMS injection.

Another important point to be highlighted is the effect played by the actuation of ADS st-2. Accordingly, one of the key features of the passive mitigation strategy is the filling of the RC above the break level, which would guarantee the refill of the reactor core (lower half of RPV) through the break. In the simulations it can be observed that this refill is expected to take place only in case ADS st-2 (connecting RPV head to containment) is open (EBTs failure scenario; EHRS, ADS st-1 failure scenario). If ADS st-2 valves are closed, indeed, the RPV remains pressurized and water cannot flow back through the break. In the reactor logic considered, ADS st-2 is actuated only upon reaching the “low LGMS water mass set-point”, which implies the actuation of the LGMS system. In view of considering in SMR designs also the possibility of BDBA and even SA (possibility of passive systems failure) and therefore adding some level of defense to these scenarios, it would seem appropriate to add some criteria for the opening of ADS st-2 in the control logic of the reactor.

Among the SA management actions which can be considered in SMRs, the IVMR strategy is one of the most promising if compared with large LWR. Accordingly, SMRs are characterized by a much lower total corium mass (lower initial decay power) and, as a consequence, for SMRs it is expected a general longer time interval from the SOT to the onset of IVMR. This can be observed also by comparing the two SA simulations studied in this chapter for a SMR with the SA simulation of Section 3.3 (SBO in a generic PWR 900 MWe): the corium slumping in the LP takes place in the order of 100000 s for the SMR and of 20000 s for PWR 900 MWe. The consequence is a further reduction of the decay heat before the beginning of IVMR. Besides these general remarks, two different IVMR configurations have been observed in the present SA scenarios for the general IRIS reactor (Fig. 4.27 and 4.28). The second one, regarding the *EBTs, LGMS, EHRS and ADS st-1 failure* scenario, is a traditional IVMR configuration in which most of decay-heat is removed by the external RC water thorough the LH structure and a corium stratification with strong focusing effect is present. The LH integrity and feasibility of corium retention within this configuration has to be investigated, but it has to be underlined that the focusing effect may challenge the integrity of LH. The second IVMR configuration is related to the *EHRS and ADS st-1 failure* scenario, and it

features a corium cooling from both the external water in RC and the internal water on the top of the corium pool, removing heat directly from the top of the metallic layer. The large heat removed by water from the top metallic layer mitigates the focusing effect and may prevent too high heat-flux to the LH structure. Deeper investigation is needed also for this IVRM feasibility; yet the refill of the RPV and realization of this second IVMR configuration is preferred as it presents much more promising possibilities for success.

The result of the simulations highlight also some potential critical points, related to the generic SMR design, that should be considered and investigated in more representative analysis. The first point is related to the actuation of the EBTs which, in some cases, ends up challenging the containment integrity. It is well highlighted in the *failure of EHRs and ADS* scenario, where the containment pressure reaches values very close to its maximum value at around 6000 s of transient due to the actuation of EBTs. Indeed, EBTs are pressurized at the RPV pressure and, once actuated, the tank connected to the broken DVI injects high-pressure water in the containment atmosphere, with a consequent water flashing and contribution to the containment pressure increasing. This consideration should be important for the development of further better management mitigation action taking into consideration the possibility of this drawback. Another important critical point that may characterize a SMR when considering SA (and which may also be applicable to other SMR designs) is highlighted in the evolution of the two core melt simulations. It is related to the small value of the ratio containment volume/reactor power, which may easily lead to the containment failure in the case of dynamic events during the SA evolution (s.a. due to corium slumping in LP, etc). This possibility should also be considered in the design of SA mitigation action in SMRs.

In general, the study highlights the possibility of several accidental sequences (including SA), due to the not operation (or partial operation) of passive systems, characterized by specific phenomena (e.g. IVMR with top water cooling, systems coupling during core degradation, etc.) not yet investigated. Such phenomenology derives from the coupling of the peculiarity of these reactors with the evolution of core degradation and needs to be thoroughly investigated. Regarding the ASTEC performances, it has been proved the capability of the code to simulate different accidental sequences in a SMR; yet, at the same time, the realization of new research programs and experimental activities to help the validation of code models dealing with the mentioned new phenomenology is necessary.

Bibliography

- [1] R. J. Budnitz, H.-H. Rogner, and A. Shihab-Eldin, “Expansion of nuclear power technology to new countries—SMRs, safety culture issues, and the need for an improved international safety regime,” *Energy policy*, vol. 119, pp. 535–544, 2018.
- [2] H. Subki, *Advances in Small Modular Reactor Technology Developments*. International Atomic Energy Agency (IAEA), 2020.
- [3] H Hidayatullah, S Susyadi, and M. H. Subki, “Design and technology development for small modular reactors—safety expectations, prospects and impediments of their deployment,” *Progress in Nuclear Energy*, vol. 79, pp. 127–135, 2015.
- [4] F. Mascari, B. G. Woods, K. F. Welter, f. D’Auria, A. Bersano, and P. Mac-cari, “Small modular reactors and insights on passive mitigation strategy modeling,” in *Proceedings of OECD/NEA/CSNI Specialists Meeting on Transient Thermal-hydraulics in Water Cooled Nuclear Reactors (SM-TH)*, CIEMAT, Madrid (Spain), 2021.
- [5] M. K. Rowinski, T. J. White, and J. Zhao, “Small and medium sized reactors (smr): A review of technology,” *Renewable and Sustainable Energy Reviews*, vol. 44, pp. 643–656, 2015.
- [6] R. H. Lasseter and P. Paigi, “Microgrid: A conceptual solution,” in *Proceedings of 2004 IEEE 35th Annual Power Electronics Specialists Conference (IEEE Cat. No. 04CH37551)*, IEEE, vol. 6, 2004, pp. 4285–4290.
- [7] M. R. Islam and H. A. Gabbar, “Study of small modular reactors in modern microgrids,” *International Transactions on Electrical Energy Systems*, vol. 25, no. 9, pp. 1943–1951, 2015.

- [8] D. Shropshire, A. Purvins, I. Papaioannou, and I. Maschio, “Benefits and cost implications from integrating small flexible nuclear reactors with off-shore wind farms in a virtual power plant,” *Energy Policy*, vol. 46, pp. 558–573, 2012.
- [9] P. Maccari, F. Mascari, S. Ederli, P. Meloni, and S. Manservigi, “ASTEC code DBA analysis of a passive mitigation strategy on a generic IRIS SMR,” *Annals of Nuclear Energy*, vol. 156, p. 108 194, 2021.
- [10] “Relevant thermal hydraulic aspects of advanced reactor design: Status Report,” Nuclear Energy Agency of the OECD (NEA), NEA/CSNI/R(96)22, 1996. https://inis.iaea.org/search/search.aspx?orig_q=RN:41025227.
- [11] “A state-of-the-art report on scaling in system thermal-hydraulics applications to nuclear reactor safety and design,” Nuclear Energy Agency of the OECD (NEA), NEA/CSNI/R(2016)14, 2016.
- [12] *Natural Circulation Phenomena and Modelling for Advanced Water Cooled Reactors*, ser. IAEA-TECDOC 1677. Vienna: International Atomic Energy Agency (IAEA), 2012, ISBN: 978-92-0-127410-6. <https://www.iaea.org/publications/8638/natural-circulation-phenomena-and-modelling-for-advanced-water-cooled-reactors>.
- [13] *Safety Related Terms for Advanced Nuclear Plants (Report of a Technical Committee Meeting, Vaesteras, Sweden, 30 May - 2 June 1988)*, ser. IAEA-TECDOC 626. Vienna: International Atomic Energy Agency (IAEA), 1991. <https://www.iaea.org/publications/882/safety-related-terms-for-advanced-nuclear-plants-report-of-a-technical-committee-meeting-vaesteras-sweden-30-may-2-june-1988>.
- [14] R. Ferri, A. Achilli, and S. Gandolfi, “PERSEO PROJECT Experimental Data Report, SIET 01 014 RP 02,” 2002.
- [15] F. Mascari, A. Bersano, R. Ferri, C. Lombardo, and L. Burgazzi, “Description of PERSEO Test N7, ENEA SICNUC-P000-029,” 2019.
- [16] F. Mascari, A. Bersano, F. Alcaro, *et al.*, “OECD/NEA/CSNI/WGAMA PERSEO benchmark: main outcomes and conclusions,” in *Proceedings of OECD/NEA/CSNI Specialists Meeting on Transient Thermal-hydraulics in Water Cooled Nuclear Reactors (SM-TH)*, CIEMAT, Madrid (Spain), Dec. 14-17, 2020.

- [17] *Evaluation of Advanced Thermohydraulic System Codes for Design and Safety Analysis of Integral Type Reactors*, ser. IAEA-TECDOC 1733. Vienna: International Atomic Energy Agency (IAEA), 2014, ISBN: 978-92-0-100314-0.
- [18] “TRACE v5.840 Theory Manual, 2013; User’s Manual Volume 1, Volume 2,” 2014.
- [19] F. Mascari, G. Vella, B. G. Woods, K. Welter, and F. D’Auria, “Analysis of primary/containment coupling phenomena characterizing the MASLWR design during a SBLOCA scenario,” in *Nuclear Power Plants*, InTech, 2012, pp. 203–233.
- [20] F. Mascari, F. De Rosa, B. G. Woods, K. Welter, G. Vella, and F. D’Auria, “Analysis of the OSU-MASLWR 001 and 002 Tests by using TRACE code,” NUREG/IA-0466, 2016.
- [21] F. Mascari, G. Vella, B. Woods, *et al.*, “Sensitivity analysis of the MASLWR helical coil steam generator using TRACE,” *Nuclear Engineering and Design*, vol. 241, no. 4, pp. 1137–1144, 2011.
- [22] F. Mascari, B. Woods, K. Welter, and F. D’Auria, “Validation Of The Trace Code Against Small Modular Integral Reactor Natural Circulation Phenomena,” in *Proceedings of NURETH-18*, Portland, USA, 2019.
- [23] P. Chatelard, “ASCOM project overview and description of work,” SARNET-ASCOM-COORDI-P1, 2018.
- [24] *NUGENIA TA-2 : ASCOM project (2018-2022)*. <https://snetp.eu/portfolio-items/ascom/>.
- [25] “IRIS International Reactor Innovative and Secure, IRIS Plant Overview,” October 17, 2002. <https://www.nrc.gov/docs/ML0336/ML033600086.pdf>.
- [26] M. Carelli, L. Conway, M. Dzodzo, *et al.*, “The SPES3 experimental facility design for the IRIS reactor simulation,” *Science and Technology of Nuclear Installations*, vol. 2009, 2009. DOI: <https://doi.org/10.1155/2009/579430>.
- [27] R. Ferri and C. Congiu, “Conceptual design of SPES3-IRIS facility,” Piacenza (Ita), SIET 01 334 RT 07 Rev.1, September 5th, 2008.
- [28] R. Ferri, F. Mascari, P. Meloni, and G. Vella, “TRACE and RELAP5 Codes for Beyond Design Accident Condition Simulation in the SPES3 Facility,” in *Proceedings of 20th International Conference on Nuclear Engineering and the ASME 2012 Power Conference. American Society of Mechanical Engineers Digital Collection*, 2012.

-
- [29] A. Achilli, C. Congiu, R. Ferri, *et al.*, “Spes3 facility relap5 sensitivity analyses on the containment system for design review,” *Science and Technology of Nuclear Installations*, vol. 2012, 2012.
- [30] R. Ferri, “SPES3-IRIS facility RELAP5 sensitivity analyses on the containment system for design review,” Piacenza (Ita), SIET 01 526 RT 09 Rev.0, 2010.
- [31] F. Castiglia, P. Chiovaro, M. Ciofalo, *et al.*, “TRACE input model for SPES3 facility,” Rep RdS/2010/62, 2010. https://iris.enea.it/retrieve/handle/20.500.12079/5419/671/NNFISS-LP2-015_rev_0.pdf.
- [32] “IRIS Plant Description Document, WCAP-16062-NP Revision 0, Westinghouse Non-Proprietary,” March 21, 2003. <https://www.nrc.gov/docs/ML0336/ML033600112.pdf>.
- [33] F. Mascari, F. De Rosa, M. Sangiorgi, and G. Bandini, “Analyses of an Unmitigated Station Blackout Transient in a Generic PWR-900 with ASTEC , MAAP and MELCOR Codes,” NUREG/IA-0515, 2019.
- [34] B. T. Rearden and M. A. Jessee, “Scale code system,” Oak Ridge National Lab.(ORNL), Oak Ridge, TN (United States), ORNL/TM-2005/39 Version 6.2.3, March 2018.
- [35] A. Annunziato, H. Glaeser, J. Lillington, P. Marsili, p. Renault, and A. Sjoberg, “CSNI integral test facility validation matrix for the assessment of thermal-hydraulic codes for LWR LOCA and transients,” Nuclear Energy Agency of the OECD (NEA), NEA/CSNI/R(96)17, 1996.

CHAPTER 5

Uncertainty Quantification analyses

Best-estimate thermal-hydraulic and SA codes have reached a high level of maturity in the last decades; however, several sources of uncertainty are inevitably present and affect the results of code simulations. This chapter starts with an introduction to the concept of uncertainty affecting code simulations and, afterward, it introduces a methodology developed with the aim of quantifying this uncertainty. The following Uncertainty Quantification (UQ) studies on ASTEC code simulations have been developed thanks to the coupling of the code with the Uncertainty & Sensitivity code RAVEN. The first application treated concerns the ASTEC simulation of the QUENCH test-6 experiment, which involves the simulation of early core degradation phenomena. This study aims at exploring the applicability of the UQ method to SA simulations, and the related challenges are identified and discussed in this Chapter. The following UQ study has been carried out on the DBA sequence of the generic IRIS model described in the previous chapter. The chapter concludes with the description and the application of a Limit Surface (LS) search algorithm as a useful tool in support of the UQ studies developed.

5.1 Uncertainty Quantification in deterministic code simulations

5.1.1 Introduction to Uncertainty Quantification methodology

BEPU approach

Thermal-hydraulics codes were once used in safety analyses of NPPs by following what is called a *conservative* approach: since the analysis has the purpose to demonstrate the safety state of the reactor under the investigated conditions, rather than investigating the most realistic situation (best-estimate), we might study a more unfavorable case, assuming that if this situation is safe then any real situation should be considered to be on the safe side [1][2]. In recent years, due to the improvement in codes models predictions and robustness, as well as in the computational power available, this conservative approach in the use of simulation system codes has been replaced by a *best-estimate* approach [3]. In a best-estimate analysis the practice is to investigate the real reactor accidental situation and to simulate it with the code as accurately as it is allowed by our knowledge. In this framework, it comes out crucial to supplement the result of the best-estimate analysis with an estimate of the uncertainty affecting the best-estimate result of the code. It can be the case where the result has to be compared with a given safety limit (e.g. cladding temperature, public exposure limit, etc.). In this case, best-estimate result can be increased by a reasonable error (uncertainty) and we can write:

$$x_{licensing} = x_{best-estimate} + uncertainty < x_{safety-limit} . \quad (5.1)$$

In other deterministic code analyses and applications, we might not have to compare the code results with some tolerance limits, for example in validations of code/model/input against experimental data; accuracy evaluation analyses; ST evaluations for Radiological Consequences, etc. Yet, also in this case, it could be very important to provide information regarding the uncertainty affecting the results of the best-estimate analysis, with the aim of estimating the confidence we can attribute to the best-estimate result. Best-estimate plus uncertainty analysis is generally called BEPU approach [4] and it is today largely used in the framework of thermal-hydraulic code application to nuclear safety. This approach is starting to be used also in the framework of SA code simulation, which may suffer of even larger results uncertainty due to the large number of complex phenomena that are involved. A large experience in applying UQ to safety analysis of level 1 to

3 has been developed in the past. Currently, new international research projects have started with the aim of establishing a consolidated approach for the analysis of uncertainties and sensitivities associated with SA analysis, e.g. the EU-MUSA project [5] and the CRP - I31033 of IAEA [6].

Sources of uncertainty to the code

Code predictions are affected by uncertainty deriving from several sources of uncertainty in input to the calculation. The limited lack of knowledge (input uncertainty) inputted to the code calculation is nonlinearly propagated through the simulation, and it ends up to a more or less wide spread of the code result (output uncertainty). For example, input uncertainty may come from errors on measured geometric values, modelling approximations, uncertainty in model parameters, etc. We can generally classify the sources of uncertainty in the following 5 categories, according to [4][7]:

- Code uncertainty (e.g. approximation in the conservative equation and in the closure models and correlations);
- Representation uncertainty (meshing and nodalization effect);
- Scaling (codes are in general validated against scaled down facilities);
- Plant uncertainty (e.g. initial and boundary conditions, plant geometric data);
- User effect.

Among these sources of uncertainty, some are related to inaccurate knowledge of data and maybe reduced to some extent with R&D efforts (commonly named epistemic uncertainty) [8]. In order to deal with it in our UQ analysis, an input uncertainty source can be parametrized and represented as input to the study by properly defining it on the base of three elements:

- Reference value;
- Range of variation;
- Probability Density Function (PDF) type.

The reference value of an input uncertain parameter is the expected value of the parameter and is the one to be used in the best-estimate calculation. Range of variation and PDF quantitatively describe the uncertainty related to the input parameter and express the corresponding state of knowledge.

Selection of Input Uncertain Parameters

The selection of the input uncertain parameter to be considered in an UQ analysis depends on the purpose of the analysis. A limited number of parameters related to

specific simulation features (e.g. to specific phenomenology, part of the system, type of input uncertainty) can be chosen in order to study the system response to the lack of knowledge related only to these specific input features. More comprehensive analyses can be developed by considering all the input uncertain parameters ranked as relevant to the simulation [9]. (that can be parameterized and then assessed with the chosen UQ methodology). And, therefore, this type of analysis would be closer to assess the overall output uncertainty affecting the calculation.

The evaluation of ranges and PDFs of the input uncertain parameters is a crucial and challenging task. Care has to be taken in the selection of suitable values in order to guarantee the right uncertainty assessment by the UA. For parameters related to physical code models, code manuals should be consulted to retrieve information on the error associated with the parameter and to choose the right range of variation whether available. For initial and boundary conditions parameters, information available from the plant or from the facility should be used. For material properties, the producer usually supplies information on the variability of relevant parameters. When any of this information is not available, data can be taken from experimental database or from previous UQ studies. When lacking of it, the use of expert judgment is recommended [9]. The selection of the PDF type and its features depends on the type of input parameter and its state of knowledge. Some comprehensive guidelines for the PDF selection are given in [10]. Specific and advanced methodologies have also been developed for this purpose [11], yet those will not be subject of this work of theses.

Classification of Uncertainty Quantification methods

Uncertainty analysis application to a deterministic code calculation has the main objective to assess the uncertainty affecting the results of the calculation and deriving from specific input sources. It has to deal with the identification and characterization of the relevant input uncertain parameters (input uncertainty) to the calculation, and with a methodology able to qualitatively quantify the global influence of the combination of the input uncertainties to the selected output parameters (output uncertainty). These main features are treated differently by different UQ methodologies [4]. In particular, UQ methods can be grouped in:

- a) Propagation of input uncertainties methodologies: after the identification of uncertain input parameters with specified ranges and probability distributions, uncertainty is evaluated by performing calculations by varying these parameters. The propagation of input uncertainties can be performed by either deterministic methods (e.g. AEA, EDF-Framatome) or probabilistic methods (e.g. CSAU, GRS, IPSN).

- b) Extrapolation of output uncertainties methodologies: uncertainty is obtained from the output uncertainty based on the comparison between calculation results and significant experimental data (e.g. UMAE).

The developed UQ analyses that will be argument of the present work of thesis can be classified as probabilistic *method of input uncertainties propagation* methodology. An exhaustive introduction to this method will be covered in the next section.

5.1.2 The propagation of input uncertainty probabilistic method

The approach used by the UQ method is based on the perturbation of the input state of the system within the domain of variation of the considered uncertain input parameters (described by PDF type and range), and the following analysis of the output response of the code to this variation by means of statistical tools [3][12]. The method is particularly suitable for codes application since, in this case, the procedure deals with running a number N of code simulations of the same sequence. In each simulation performed the value of all the selected input uncertain parameters is changed according to the estimation of the uncertainty affecting each parameter. In particular, values of the input parameters are sampled according to a scheme (Monte Carlo, Latin Hypercube, etc.) on the base of PDF and range of variation characterizing each parameter. The response of the code to the input variation, i.e. a set of N output values of the chosen FOMs, can be thus analyzed in statistical terms (mean, standard deviation, percentiles, etc.) as a vector of aleatory variables.

One of the main features of this methodology is that the number of code calculations needed does not depend on the number of selected input uncertain parameters; but it depends on the “probability content” and “confidence level” of the tolerance limits requested in the uncertainty assessment of the results [3]. The meaning of this sentence will be clarified in the following theoretical part, developed according to [2].

Theoretical basis: statistic of black-box model and Wilks confidence interval formula

Let’s consider a system as complex as a code model of a NPP. Such a system is described by input data (material and geometric properties; boundary conditions; etc.), and it enables us to calculate an output response in terms of physical parameters. Given the high complexity of such a system, we can consider it as a *black-box*

mapping the input random vector \vec{x} into an output vector $\vec{y}(t)$. Hence, we can write:

$$\vec{y}(t) = L(t)\vec{x} , \quad (5.2)$$

where $L(t)$ is a non-linear operator representing the code model.

In practical applications the link between input and output is very complicated and there is no way to find an analytical formula. Yet, we assume $L(t)$ to be deterministic and, hence, to map an input vector \vec{x}_i to one and only one output vector $\vec{y}_i(t)$. We consider the input vector to be a stochastic random variable, varying accordingly to a distribution which reflects the uncertainty of the input parameters and, consequently, the output parameters is also a random variable with an associated probability distribution function [2].

We call a state \vec{x}_0 nominal, if all the input parameters take their respective expectation value, i.e. $\vec{x}_0 = E[\vec{x}]$. The corresponding output will be $\vec{y}(t)_0 = L(t)\vec{x}_0$. We consider X to be the set of all possible values of \vec{x} due to the input variations around \vec{x}_0 , and Y to be the set of output $\vec{y}(t)$ given by the mapping through $L(t)$ of all the $\vec{x} \in X$. In the following, to simplify the time t will be taken as fixed and its notation omitted; the generalization is straightforward.

Assumed as known the input set of uncertain values X and the distribution of $\vec{y} \in X$, what we aim to do is to find a criterion to have enough information regarding the output set Y (output uncertainty) without going to compute the mapping of the whole input phase space X into Y . That in the case of a code, would mean to run an infinite number of calculations.

Before advancing in the statistical procedure we need to make some assumptions and, hence, to introduce the concept of *chaotic behavior*. Chaos, is usually defined in connection with evolution equations [2][13] and some of the definitions are easily transferable to our case. According to this analogy, if we are investigating a smooth curve in an input space and we consider its image in the output space, we can speak of a chaotic behavior when the output space results to be the union of disjoint sets. In other words, when an arbitrary smooth curve is mapped into an arbitrary curve, if in some points of the input set (bifurcation points \vec{x}_{bi}) the gradient assumes different values depending on the direction of approach to the point, that is:

$$\lim_{\delta\vec{x}_1 \rightarrow 0} f(x) \frac{\vec{y}(\vec{x}_{bi} + \delta\vec{x}_1) - \vec{y}(\vec{x}_{bi})}{|\delta\vec{x}_1|} \neq \lim_{\delta\vec{x}_2 \rightarrow 0} f(x) \frac{\vec{y}(\vec{x}_{bi} + \delta\vec{x}_2) - \vec{y}(\vec{x}_{bi})}{|\delta\vec{x}_2|} , \quad (5.3)$$

we can speak of chaos. It can be shown that when chaos is present, the input set X can be divided into disjoint subsets: $X = \bigcup_{j=1}^n X_j$. In this case the mapping operator $L(t)$ is the same and it is smooth in each subset X_i , but it varies when passing from X_i to X_j . It is possible to demonstrate that in this case the expectation

values of the output variables are linear combinations of the expectation values over the disjoint subsets X_i . This gives us hints on the detection of chaotic behavior in the framework of the black box model which, according to [2], appears when the following three conditions are simultaneously satisfied:

- a) Output average value considerably changes;
- b) Output variance suddenly increases considerably;
- c) Output variables tend to separate into disjoint groups.

In relation to the statistics of the *black-box* model for the determination of the *Wilks confidence interval formula*, we have to make the assumption that the mapping $L(t)$ representing our model does not show chaotic behavior.

As first simpler case, we consider one scalar output random variable y , and we assume its density function to be $g(y)$. If we carry out N runs with N fluctuating input $\{\vec{x}_1, \vec{x}_2, \dots, \vec{x}_N\} \in X$, we obtain a sample $\{y_1, y_2, \dots, y_N\}$ of the random variable y . Let's now construct two random functions $L(y_1, \dots, y_N)$ and $U(y_1, \dots, y_N)$ called upper and lower *tolerance limits*, such that:

$$\mathbb{P}\left\{\int_L^U g(y)dy > \gamma\right\} = \beta, \quad (5.4)$$

where \mathbb{P} has the meaning of probability. Equation (5.4) defines the probability β , that we call *confidence level*, such that the portion of the output distribution included in the *tolerance limits* L and U is greater than the number γ . Indeed, the value of the integral $\int_L^U g(y)dy$ is a random variable (and it is not a probability) measuring the portion of the output distribution $g(y)$ included in the interval $[L, U]$. We call *probability content* the value of the parameter γ limiting this portion. Both the values of γ and β are in the interval $[0, 1]$.

Our aim at this point is: having fixed γ and β , we want to determine the number of runs N , so that carrying out a sample of N input values $\{\vec{x}_1, \dots, \vec{x}_N\}$, we get $\{y_1, \dots, y_N\}$ from which we can determine an appropriate tolerance interval $[U, L]$. The pioneering work of setting *tolerance limits* when nothing is known about the density function $g(y)$, was done by Wilks [14][15]. Without going into details on the proof, we provide here a well-known Theorem useful in our purpose [2].

Theorem. *Let $\{y_1, \dots, y_N\}$ being N independent observations of the random output y . Suppose that nothing is known about the density function $g(y)$ except that it is continuous. Arrange the values of $\{y_1, \dots, y_N\}$ in increasing order and denote by $y(k)$ the k -th of these ordered values. Hence, in particular*

$$y(1) = \min_{1 \leq n \leq N} y_n, \quad y(N) = \max_{1 \leq n \leq N} y_n. \quad (5.5)$$

And by definition $y(0) = -\infty$ and $y(N + 1) = +\infty$. In this case for some positive $\gamma < 1$ and $\beta < 1$, there can be constructed two random functions $L(y_1, \dots, y_N)$ and $U(y_1, \dots, y_N)$ called tolerance limits, such that the probability that

$$\int_L^U g(y)dy > \gamma \quad (5.6)$$

holds and is equal to:

$$\beta = \sum_{j=0}^{s-r-1} \frac{N}{(N-j)} \gamma^j (1-\gamma)^{N-1}, \quad (5.7)$$

where $0 \leq r \leq s \leq N$, and $L = y(r)$, $U = y(s)$.

The proof this Theorem can be found in [2]. The *two-sided tolerance interval formula* can be get from equation (5.7) by selecting the tolerance limits $L = y(1)$ and $U = y(N)$. Therefore, by choosing $r = 1$ and $s = N$ we get:

$$\beta = 1 - \gamma^N - (N-1)(1-\gamma)\gamma^{N-1}. \quad (5.8)$$

Selected the desired values of γ and β , this equation can be solved with respect to N to find the size of the needed sample. Often we are interested only in the upper or in the lower tolerance limits, and by choosing $L = y(0) = -\infty$ and $U = y(N)$, that is $r = 0$ and $s = N$ in equation (5.7), we get the *one-sided tolerance limit* expression:

$$\beta = 1 - \gamma^N. \quad (5.9)$$

With a similar approach, the formula can be generalized in case we are interested in a confidence level for an output including p variables $y = [y_1, \dots, y_N]$. If either the outputs are statistically completely independent or we are interested in a *confidence level* β and a *probability content* γ for each of the output variable, we can apply the previous result. Otherwise, if we are interested in the joint probability β that, given γ , the integral

$$\int_{L_1}^{U_1} \cdots \int_{L_p}^{U_p} g(y_1, \dots, y_p) dy_1 \dots dy_p < \gamma, \quad (5.10)$$

holds (where $g(y_1, \dots, y_p)$ is the joint density distribution of the p outputs), we have to consider a higher order *Wilks formula*. With this purpose, a Theorem similar to the previous one can be proved in order to find the following *two-sided confidence interval expression* for p output [2]:

$$\beta = \sum_{j=0}^{N-2p} \frac{N}{(N-j)} \gamma^j (1-\gamma)^{N-1}. \quad (5.11)$$

And for the *one-sided tolerance limit*, in case of p output, we have [2]:

$$\beta = \sum_{j=0}^{N-p} \frac{N}{(N-j)} \gamma^j (1-\gamma)^{N-1}. \quad (5.12)$$

Application examples of the Wilks confidence interval formula

As a first example let's consider a UQ analysis in which we have a certain number of input uncertain parameters to the code calculation, and where the upper safety limit not to be exceeded in the sequence is represented by the peak cladding temperature. We may want to require a *confidence level* $\beta = 95\%$ and a *probability content* $\gamma = 95\%$, and therefore, from the *one-sided confidence interval formula* (5.9), we calculate that $N = 59$ calculations are needed. Therefore, by sampling the values of all the input parameters and executing 59 different simulations, we collect the highest temperature obtained as output. This value, representing the *upper tolerance interval*, gives us a probability of 95% (β) that it is higher than the 95 percentile (γ) of all the infinite calculations theoretically realizable by varying the input uncertain parameters within their uncertainty.

If we are interested in respecting the upper safety limits of two FOMs, let's say a maximum temperature and a maximum pressure, we can use the *one-sided formula* (5.12) and set $p = 2$ FOMs. We get that, for a *confidence level* $\beta = 95\%$ and a *probability content* $\gamma = 95\%$ to not exceed the two upper limits, the required number of calculations is $N = 93$.

In a different study, we could be interested in characterizing the output uncertainty of an output FOM to a simulation, as a result of selected input uncertain parameters; thus, without having safety limits to be respected. We can make use of the *two-sided confidence level*, by selecting for instance 98% of *confidence level* and 98% *probability content*, and getting $N = 289$ calculations needed. Collecting the simulation results we take the upper and the lower values of the FOM [$L(t)$, $U(t)$] as *tolerance intervals*, at each time step t . In this way, we have the 98% probability that, at each time step, the related interval includes at least a portion of 98% of all the possible output values distribution for this FOM. In this last case, the *two-sided confidence level formula* (5.8) provides us information on the statistical content of the band of results obtained in the UQ study, and this can be considered a quantification of the confidence we can attribute to the best-estimate result.

5.1.3 Sensitivity analysis

An important feature of the presented UQ method is the possibility to perform an additional sensitivity analysis. This study provides a measure of the importance of each input uncertain parameter in the generation of the output uncertainty. The sensitivity analysis quantifies and gives a ranking of the input uncertain parameters; hence, providing guidance as to where the main sources of uncertainty derive. It is an important step to improve the state of knowledge of the input in order to reduce most effectively the simulation uncertainty or to improve the modelling of the computer code [3]. In addition, this information can provide some insight regarding the physical phenomenology governing the sequence.

Sensitivity analysis is assessed thanks to the use of sensitivity parameters, which can be generally taken among *correlation coefficients* and *regression coefficients*. The sensitivity coefficients that are used in the present work are presented in the following.

Pearson correlation coefficient

The simple *Pearson correlation coefficient* between the random variables x and y , in N samples, is obtained by dividing the covariance of the two variables by the product of their standard deviations [16].

$$r = \frac{\sum_i^N (x_i - \hat{x})(y_i - \hat{y})}{\left[\sum_i^N (x_i - \hat{x})^2 \sum_i^N (y_i - \hat{y})^2 \right]^{1/2}} = \frac{cov(x, y)}{\sigma_x \sigma_y}, \quad (5.13)$$

where \hat{x} and \hat{y} represent the expected values (mean) of the random variables x and y . This coefficient provides a measure of the degree of linear correlation between the two random variables and its value lays in the interval $[-1, 1]$. If $r < 0$ the linear correlation is negative (an increment of x leads to a reduction in y); if $r = 0$ there is no linear correlation between the two variables; if $r > 0$ the linear correlation is positive (an increment of x leads to an increment of y). Result closer to -1 and 1 stands for stronger linear relationship between the variables.

Spearman rank correlation coefficient

The *Spearman correlation coefficient* can be defined as the *Pearson correlation coefficient* between the ranking of the two random variables x and y [16]. In this case, the coefficient provides a measure of the rank correlation or, in other words, it assess how well the relationship between the variables can be described as a monotonic function. Also in this case it is enclosed in $[-1, 1]$, where a negative

value stands for negative monotonic correlation; positive value stands for positive monotonic correlation. Results closer to -1 and 1 stand for a stronger monotonic correlation between variables than values closer to 0 .

For Pearson and Spearman correlation coefficients we can assume: for absolute value of the correlation coefficient higher than 0.5 the correlation can be classified as *significant*; between 0.2 and 0.5 the correlation can be considered *moderate*; otherwise, the correlation is assumed to be *low or absent* [7].

Linear regression coefficients

Regression analysis refers to a large collection of tools designed to make inferences concerning the structure of the model under consideration [8], and the simplest parametric regression methods are the *linear regression* models. These methods attempt to approximate an unknown relation, $y = f(x)$, by fitting the data available with a simplified expression:

$$\tilde{y} = y + \epsilon , \quad (5.14)$$

where \tilde{y} is the approximation of the dependent variable y and ϵ is the residual error. In linear regression models we assume the \tilde{y} to be a linear combination of the independent variable vector \vec{x} (vector of input parameters), that is

$$\tilde{y} = \vec{x}\vec{b} + b_0 , \quad (5.15)$$

where b_0 is the y-intercept and \vec{b} is the vector of *regression coefficients*. In general, the regression coefficient b_i is considered the sensitivity coefficient of the corresponding variable x_i .

A first simplest way to find the vector \vec{b} is to solve the problem of minimization of the residual sum of squares between the observed y and the targets predicted by the linear approximation \tilde{y} . Given a set of N observations $\{y_1, \dots, y_N\}$ associated with the set of N independent input vectors $\{\vec{x}_1, \dots, \vec{x}_N\}$, it is possible to solve a minimization problem of the form

$$\min_b \left(\|\vec{X}\vec{b} - \vec{y}\|_2^2 \right) = \min_b \left(\sum_{j=1}^N \|\vec{x}_j\vec{b} - y_j\|_2^2 \right) . \quad (5.16)$$

Where \vec{X} stands for the matrix of input values, having in each row the input vector \vec{x}_j at the observation j ; \vec{y} is the column vector of observations; $\|\cdot\|_2$ is the L^2 norm or *Euclidean norm*. In this case we consider the solution of the minimization problem \vec{b} , to be the coefficients of an *Ordinary Least Square regression* problem. Alternatives to this regression problem are obtained by adding *regularization* (or

penalization) terms to this problem with the aim of avoiding what is generally called *overfitting* of the model in the prediction of new data [17]. Most common examples of regularization of *Ordinary Least Square regression* problem, are the *Ridge Regression*, expressed by the minimization problem:

$$\min_b \left(\|\vec{\mathbf{X}}\vec{\mathbf{b}} - \vec{\mathbf{y}}\|_2^2 + \alpha \|\vec{\mathbf{b}}\|_2^2 \right), \quad (5.17)$$

and the *Lasso Regression*, expressed by the minimization:

$$\min_b \left(\|\vec{\mathbf{X}}\vec{\mathbf{b}} - \vec{\mathbf{y}}\|_2^2 + \alpha \|\vec{\mathbf{b}}\|_1 \right). \quad (5.18)$$

Where $\|\cdot\|_2$ and $\|\cdot\|_1$ represent respectively the L^2 and the L^1 norms. The *Ridge Regression*, by imposing a L^2 penalty on the size of the coefficients, makes the model to become more robust to collinearity, and it is recommended in scenarios where independent variables $\vec{\mathbf{x}}$ are highly correlated. The *Lasso Regression*, by the addition of L^1 penalty, has the effect to push a subset of the coefficients to become zero, suggesting that the influence of the corresponding x parameter may safely be neglected. In this sense, the *Lasso Regression* is useful as a “coefficients selection” by reducing to zero the coefficients related to the less important parameters [17]. The solution of the Lasso and the Ridge problems is generally found by means of iterative methods, such as *coordinate descent algorithm*; the optimal value of the α parameter for the regularization term of the linear model can be found by dedicated techniques, such as *Cross-Validation* [17].

Regression coefficients of a given output y are expressed in the unit of measure of the output variable over the unit of the related input variable x_i . As a consequence, sensitivity coefficients related to input variables representing different physical parameters are in general not comparable. A useful way to standardize the set of input vectors is the following standardization transformation [18]:

$$x_i^{st} = \frac{x_i - \hat{x}}{\sigma_{x_i}}. \quad (5.19)$$

In general, despite the *Wilks confidence formula* does not relate the number of runs with the number of input parameters, is important to remember that, to guarantee reliable sensitivity measures, the number of code calculations has to be much larger than the number of uncertain parameters [9]. Moreover, in a sensitivity study it is recommended to interrogate more than one sensitivity parameter to perform the analysis. The use of only one sensitivity parameter could lead to a wrong evaluation of the main sources of uncertainty.

5.1.4 Implementation of RAVEN – ASTEC coupling for UQ

In the present work of thesis, the applications of the *input uncertainty propagation method* for UQ analyses, performed on ASTEC code simulations, have been developed thanks to the coupling of ASTEC with the statistical tool RAVEN. This section covers a brief introduction to RAVEN and its coupling with ASTEC for UQ. Also, some details on the implementation of the codes coupling on a multi-core cluster to reduce the computational time have been provided.

Introduction to RAVEN

RAVEN [12][19] (Risk Analysis and Virtual ENvironment) is a platform that includes a large number of tools, models and algorithms for parametric and probabilistic analysis, developed by the Idaho National Laboratory (INL). It adopts an open-source code developed with Python, using an object-oriented approach: the development aims at a clear and modular organization in order to favor the user contribution (on the GitHub platform). Parallel calculations, for both standard and HPC systems, are fully integrated. RAVEN is designed to be coupled with simulation codes (e.g. RELAP, MELCOR, ASTEC) in order to perform: Classical and advanced statistical analyses; Parametric studies; LS determination; ML with Artificial Intelligence (AI) algorithms; Data mining with clustering techniques; Phase space optimization; Sampling with dynamic event trees.

The AI algorithms implemented in RAVEN can build Reduced Order Models (ROMs) that work as a statistical surrogate of the complex code. These can be used in parametric studies, UQ analyses and other applications with a strong reduction of the computational effort.

RAVEN - ASTEC coupling

Since RAVEN is an open-source software, the procedure for coupling it with a new code allows the creation of a new Python interface that is going to be embedded at runtime [19]. Following this approach, an appropriate Python interface has been developed for the coupling with ASTEC and added to the source code of RAVEN.

The instructions needed to perform the statistical analysis are imputed in RAVEN in form of a XML file. In case of UQ study has to be performed, the following information have to be provided in the XML input:

- Information regarding the current code calculation, s.a. path of code input-deck files, path of code executable and path of code output files;

- List of uncertain input parameters with their ranges and PDFs type;
- Information regarding the sampling of input values, s.a. sampling strategy to be used (Monte Carlo, Latin Hypercube, etc.), total number of code calculations N and number of calculations to be executed in parallel;
- List of output FOMs selected for the study and the desired statistical analyses to be performed on these, e.g. mean, STandard Deviation (STD), percentile, sensitivity coefficients).
- In case of implementation on a multi-node cluster, all the instructions for the communication with the HPC infrastructure (parallel protocol, nodes address file);

With the information above, RAVEN is able to drive the processes needed for the UQ study:

- It samples the values $\{\vec{x}_1, \dots, \vec{x}_N\}$ of the selected input parameters, according to the total number of calculation chosen N (by following the *Wilks formula*), and the sampling strategy selected;
- Creates a set of N different input-deck of the same sequence by using the sampled values;
- Launches the code simulations by following instructions on the number of parallel calculations and communicating with the computer infrastructure;
- Collects the results and, once all the calculations are terminated, it performs the statistical analysis

The ASTEC-RAVEN coupling workflow for UQ analysis is represented in Fig. 5.1.

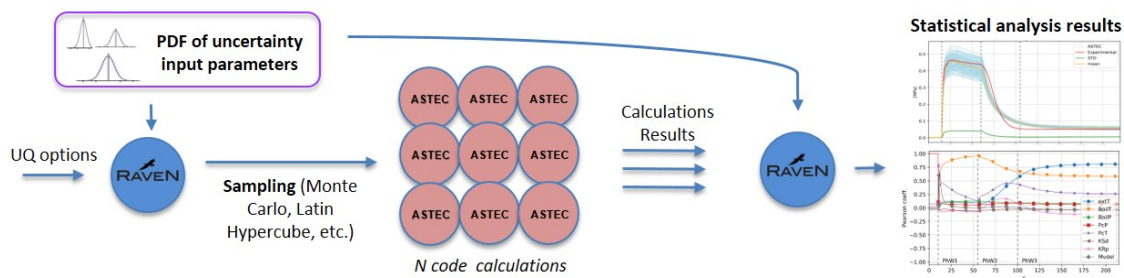


Figure 5.1: Scheme of ASTEC – RAVEN coupling workflow for UQ analysis.

As already underlined, the described UQ methodology is based on the running of a large number (*Wilks confidence interval formula*) of code calculations of the same sequence. Since a single transient simulation can require from hours to several days, it follows that performing several sequential calculations can become very time

demanding. The solution to this technological issue is the implementation of the analysis on a multi-core infrastructure (s.a. multi-nodes HPC) and running the simulations in parallel on the different available cores. In the following, a brief description of the RAVEN-ASTEC implementation on the ENEAGRID - CRESCO infrastructure has been assessed [20].

Implementation on CRESCO HPC

The CRESCO-6 cluster [21] provides a structures of 434 nodes and 48 CPU per node, for a total of 20832 cores connected by a 100 Gb/s Intel Omni-Path-based broadband and low latency network. The procedure for running multicore calculations is the submission of a *batch job* on a specific *queue*, specifying the number of cores requested. Once the CPUs are available, the system assigns one or more nodes on which are located the requested cores to run the calculation. RAVEN is capable of running MPI parallel processes and read the file containing the addresses of the assigned nodes provided by CRESCO. Each ASTEC calculation is a serial process running on one of the available cores of the CRESCO dual-CPU nodes. In order to run ASTEC on an HPC environment a license server is also required, so that it manages all the concurring executions up to the limits of the license.

5.2 BEPU analysis of the ASTEC simulation of QUENCH test-6

In the present section, the UQ method described in the previous chapter has been used in a BEPU analysis of ASTEC code simulation of an experimental test. The study is a benchmark exercise regarding the ASTEC (v2.2. beta) modelling and simulation of the experimental test-6 performed in the QUENCH facility of Karlsruhe Institut fur Technologie (KIT) [22]. A reference simulation has been carried out with the ASTEC model of the facility and the results have been analyzed against the experimental data. The following UQ analysis on the same sequence is aimed to characterize the uncertainty related to the code modelling of the sequence and, in particular, to the simulation of the main early core degradation phenomena governing the experiment. The activity has the purpose to validate the code models for early-degradation phenomena and hot core quenching, against experimental data and to find the main sources of uncertainty affecting the code simulation of this phenomena. It has been developed in the framework of the IAEA CRP - I31033 [6].

5.2.1 The QUENCH-6 experiment

QUENCH is an experimental facility hosted by KIT in the Karlsruhe Research Center to investigate the behavior of hot and pre-oxidized LWR fuel rods in quenching conditions. The QUENCH test-6 experiment was performed on 13 December 2000 and the set-up of the facility had the aim of studying the accident management measure of injecting water from the bottom of a hot core. This test has been used as an OECD - ISP (ISP-45) for blind and open calculations to assess the accuracy of severe accident codes [22].

Description of QUENCH-6 facility

The main component of the QUENCH facility is the test section which incorporates the bundle of test rods (Fig. 5.2). In test-6, the test section includes 21 fuel rod simulators surrounded by a Zircaloy shroud, a fiber insulation and an annular external cooling jacket made of stainless steel. 20 of the 21 fuel rod simulators are electrically heated over a length of 1024 mm, thanks to tungsten heaters in the center of the rods surrounded by ZrO_2 pellets and a Zr cladding. The unheated rod is placed at the center of the bundle and is filled only with ZrO_2 pellets. Above rods the heated zone there is no insulation and this region of the cooling jacket is cooled by a water flow, forcing the maximum axial temperature downward. 4 additional Zr rods (corner rods) are positioned at the corners of the bundle, helping to obtain a rather uniform radial temperature profile and hosting many of the instrumentation for the thermocouple. The upper and lower boundaries of the section are sealing plates and the rods are supported by spacer grids. Superheated steam from a steam generator mixed with argon enters from the bundle bottom and moves upwards along the bundle. The mix of gases with the hydrogen generated during the experiment exit from the bundle at the top end, where a mass spectrometer and other instrumentations are located. The quenching water can enter the test section through separate lines from the bottom of the bundle. A more detailed description of the QUENCH facility and of the arrangement for test-6 can be found in [22].

Description of QUENCH test-6 experiment

The experimental sequence can be divided in 3 main PhWs defined by the injections of coolant fluids and by the electrical power applied to the heated rods of the test bundle:

- 1) *Pre-oxidation PhW*: from the start of the sequence (0 s) up to 6011 s, when

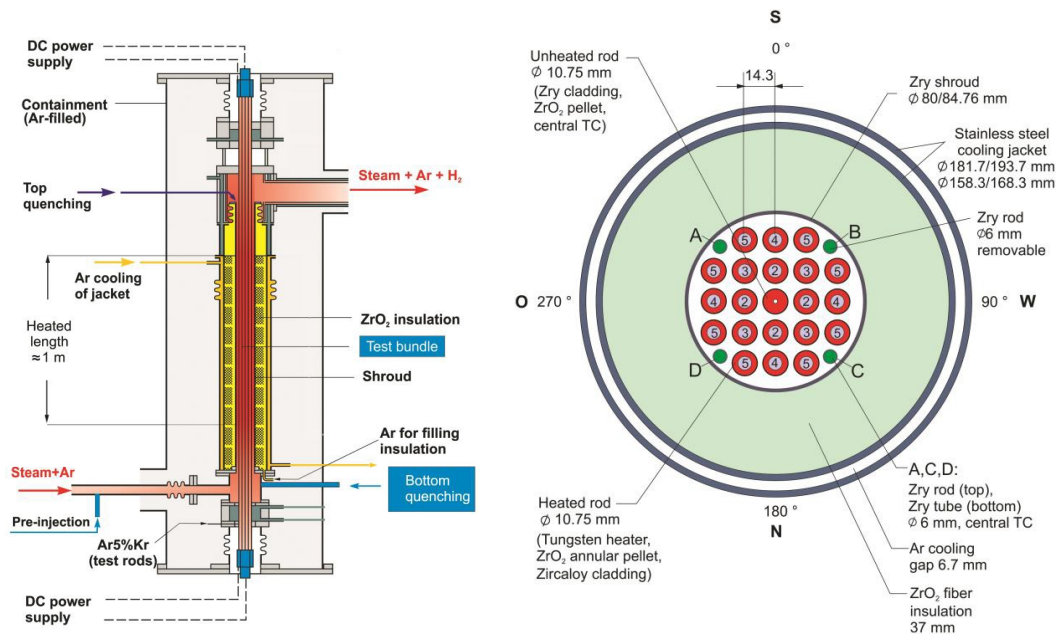


Figure 5.2: Schematic view of the QUENCH facility (Left); Section of the QUENCH-06 bundle (Right) [23]

the electric power applied in the heated up rods starts to be increased as a linear ramp.

- 2) *Heating-up PhW*: from the onset of the electric power increasing (6011 s) to the first injection of quenching water, at 7179 s
- 3) *Quenching PhW*: From the starting of pre injection water (7179 s) to the end of the calculation (9000 s).

Table 5.1 summarizes the timings of the main events characterizing the experiment.

5.2.2 ASTEC model of QUENCH-6

Geometry and model assumptions

The ASTEC - ICARE model of the test section is made of 2 axial channels, as represented in Fig. 5.3 - left. The central unheated rod and 8 inner heated rods belong to the inner fluid-channel (channel 1); the 12 external heated rods and the 4 Zr corner rods are defined inside the outer fluid channel (channel 2). The two fluid channels are confined by the Zr shroud structure, which is wrapped in the fiber insulation along the heated elevation and in the argon gap along the unheated upper length. Externally, the cooling jacket embeds all the other structures. The

Time (s)	Event	PhW
0	Start of test, bundle at $T \sim 870$ K	Pre-oxidation
30	Start of heating up to ~ 1473 K	Pre-oxidation
1965	Start of steady temperature oxidation at ~ 1473 K	Pre-oxidation
6011	Start of heat up phase	Heating-up
6620	Extraction of corner rod B from the bundle	Heating-up
~ 7200	Onset of temperature escalations and of significant H_2 production	Heating-up
7179	Argon injection moved to the upper plenum; shutoff of steam injection; start of pre-injection and quenching; rod failure in the experiment	Quenching
7180	Shroud failure in the experiment	Quenching
7205	Start of electric power reduction from 18.2 kW to 3.9 kW	Quenching
7215	Start of water main injection	Quenching
7221	Electric power at 3.9 kW	Quenching
7431	Electric power shutoff,	Quenching
7434	Main water at zero	Quenching
9000	End of the test	Quenching

Table 5.1: Timings of main events characterizing the test and relative PhW [22].

model includes also grid spacers and plates. Concerning the axial meshing (Fig. 5.3 - right), the bundle is divided into equal slices of 55 mm of height. All the elements are modelled with azimuthal symmetry. The ASTEC version used in this application is the v2.2 beta, with a 5-equations model for the thermal-hydraulic calculation.

Modelling of physical phenomena

The relevant physical phenomena related to the early in-vessel degradation phase and to the quenching have been considered in the ASTEC model of the bundle:

- Conduction heat-transfers within each element and between the different elements in contact; convection between each element facing the fluid channels (i.e. fuel rods, corner rods, grids, plates and shroud); radiation among fuel rods simulators, cladding, corner rods and the shroud.
- Oxidation of Zr components (rods cladding, corner rods, shroud, grids).
- Degradation and relocation of molten material along the rods and molten material oxidation.

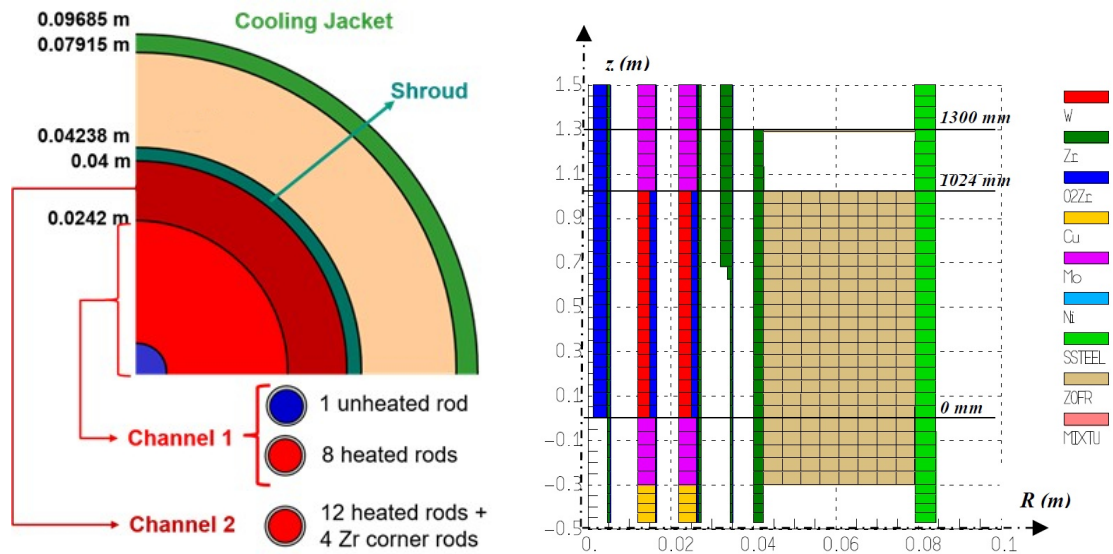


Figure 5.3: Radial view of the QUENCH model in ASTEC (left); Translation of the QUENCH model into the ASTEC computational together with the distribution of materials (right).

- Capture of steam into the fiber or in the argon gap after shroud failure is not considered.

Initial and boundary conditions

At the SOT ($t = 0$ s), the initial temperature distribution of the test section components (central rod, heated rods, corner rods, shrouds, plates, grids, etc.) is given as a function of the components elevation. Along the simulation, the time evolution matrix of the applied thermodynamic quantities (mass flow rate, pressure, temperature) related to the injections of coolant fluids (argon, steam and water injection) is taken from the recorded experiment and inputted to the code as a time-dependent boundary condition. Without detailed measurements available, the quenching water pre-injection (5 s of injection, at 370 K and 6 bar) has been defined to take place with a constant rate. The mass flow rates of all the fluids imposed along the test are reported in Fig. 5.4 - left. The boundary conditions applied to the channels top outlet is a constant pressure of 0.2 MPa. Regarding the time evolution of the electric power applied to the outer and the inner heated rods, the data have been taken from the experimental power and the distributions between the two rings is reported in Fig. 5.4 - right.

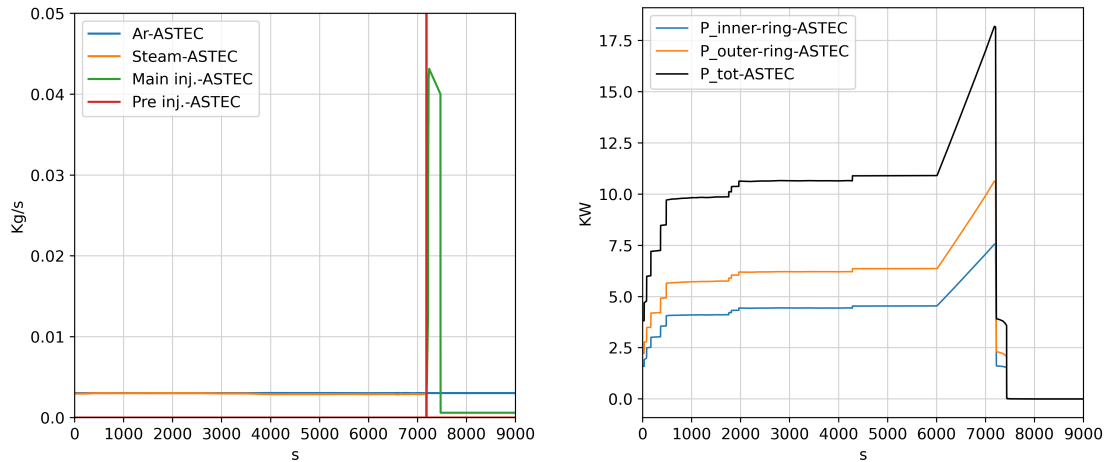


Figure 5.4: Mass flow rate of fluids injections (left) and electric power generated in the heated rods (right), considered as boundary conditions to the ASTEC simulation.

5.2.3 Results of reference simulation

The results of the ASTEC code simulation of QUENCH test-6 experiment have been analyzed against the experimental data, by focusing the attention on some relevant FOMs. In Fig. 5.5, 5.6 and 5.7, the temperature evolution of central unheated rod center; the temperatures of outer-ring heated rods cladding; and the temperature of shrouds are reported for the elevation of 950 mm along the sequence. For each component, the ASTEC result refers to the representative ICARE component; the experimental data are related to thermocouples located in one of the components. Unfortunately, some thermocouples fail during the transient and the related experimental data are lost. The H_2 cumulative mass and the H_2 mass production rate are respectively reported in Fig. 5.8 and 5.9, against the experimental observation.

Pre-Oxidation PhW

At the start of the experimental transient, the sources of argon and steam to the test section bottom inlet are activated (both of around 3 g/s). Up to around 2000 s, the structures temperatures are brought to a maximum value around 1473 K (reached at the elevation of the 950 mm), by applying the electric power steps increase registered in the experiment. In about 3000 s, the quasi-steady temperature conditions are reached and kept up to the end of the *pre-oxidation PhW*.

The reported temperatures of ASTEC (Fig. 5.5 - 5.7) feature in general, a very

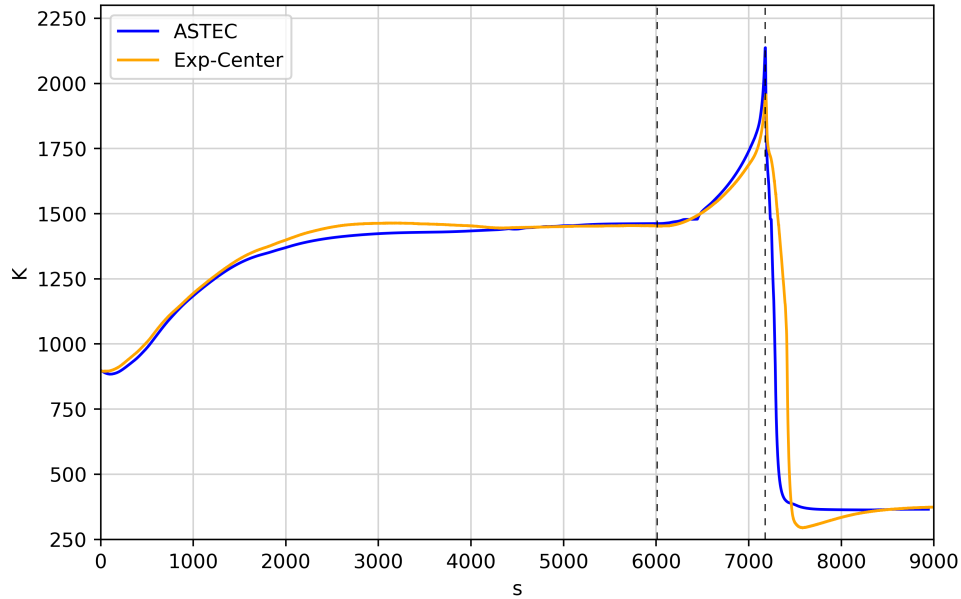


Figure 5.5: Central un-heated rod center temperature evolution from experimental data and from code simulation, at 950 mm of elevation.

good prediction of the experimental temperatures evolution during this PhW. From a quantitative point of view, the code seems to reach the steady temperature with some delay. The H_2 production rate (Fig. 5.9) features a first quasi-linear increase during the heat up of the bundle (0 - 2500 s); after about 2500 s, the production reaches a local peak before starting to decrease during the plateau of temperature. The H_2 rate decrease at constant temperature is due to the Zr oxidation kinetics: the reaction is governed by the Oxygen diffusion in the ZrO_2 layer, whose thicken increases along the phase. The ASTEC simulation shows the prediction of the described oxidation phenomena. However, the hydrogen production peak occurs approximately 200 s earlier and is 0.001 g/s lower for the code. The total hydrogen mass produced at the end of the *pre-oxidation PhW* (6010 s), is 18.5 g for the experimental case and 19.0 g for ASTEC (Fig. 5.8).

Heating-up PhW

The *heating-up PhW* starts at 6011 s with the linear increase (of 0.3 W/s per rod) of the electric power applied to the heated rods. In both the experimental and the ASTEC results, it can be observed (Fig. 5.5 - 5.7) that the temperatures start to increase after about 200 s from the onset of the *heating-up PhW* at a rate close to 0.32 K/s, which is kept constant between 1450 K and 1750 K. Reached

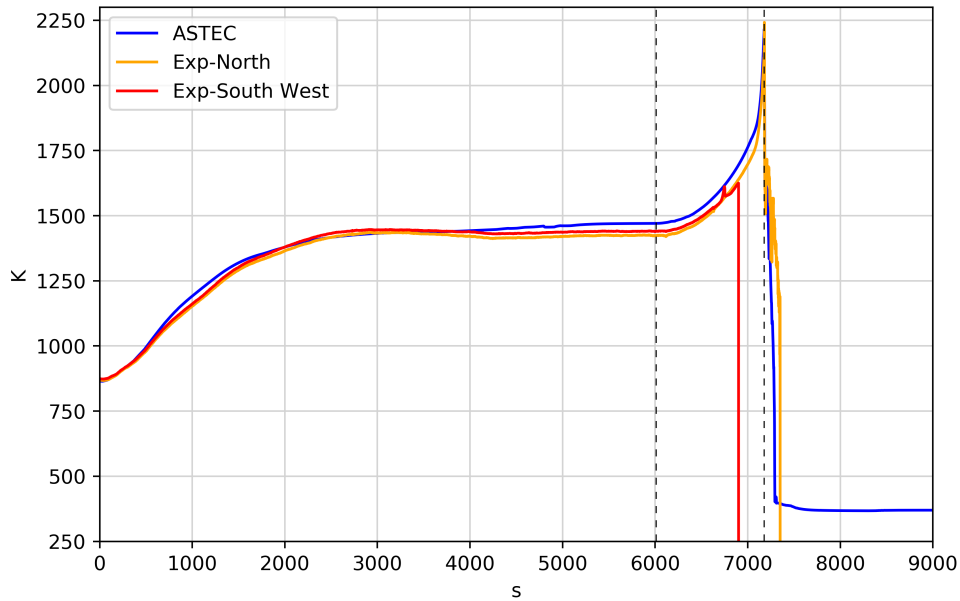


Figure 5.6: Outer-ring heated rod cladding temperature evolution from experimental data (north and south-west oriented thermocouples) and from code simulation, at 950 mm of elevation.

the temperature of 1770 K in the Zr components (at about 7100 s), the oxidation processes accelerate and a steep escalation of temperatures takes place (reaction runaway). This acceleration is best fitted by the code calculation in the outer-ring rods cladding temperature (Fig. 5.6) and slightly overestimated in the other components presented (central rod in Fig. 5.5 and shroud in Fig. 5.7).

The H_2 production rate is accurately predicted by the code up to the acceleration of the oxidation (about 7100 s). In the last 20 s of this PhW, ASTEC predicts a higher H_2 production, in agreement with the discussed temperature behavior. The peak of production rate in the code simulation is of 0.23 g/s, occurring almost at the quenching time (0.5 s later). From the experimental data, the H_2 production rate at quenching time is of 0.17 g/s; while the production peak, of 0.23 g/s, is registered to be 3 s later. It is important to underline that the experimental detection of the H_2 is expected to have up to 5 s of delay due to the locations of the mass spectrometer. The total hydrogen mass produced at the end of the *heating-up PhW* (7179 s), is slightly higher for the calculation (35 g) compared to the experiment (33 g).

At 6620 s of transient, one of the two corner rods is extracted in the experiment in order to analyze its oxidation state (Table 5.1). The ZrO_2 thickness profile of the ASTEC representative corner rod is shown against the experimental data in

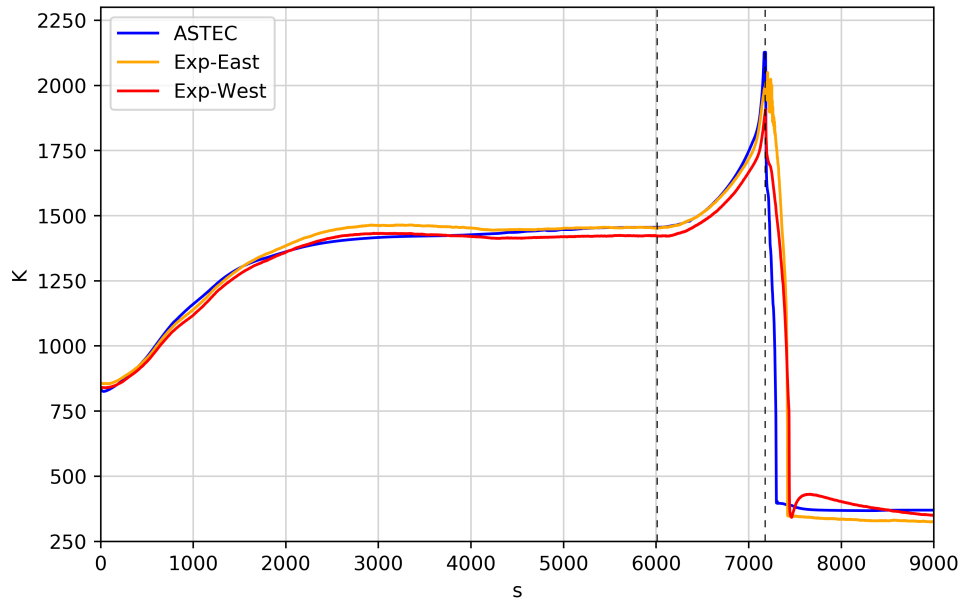


Figure 5.7: Shroud internal temperature evolution from experimental data and from code simulation, at 950 mm of elevation.

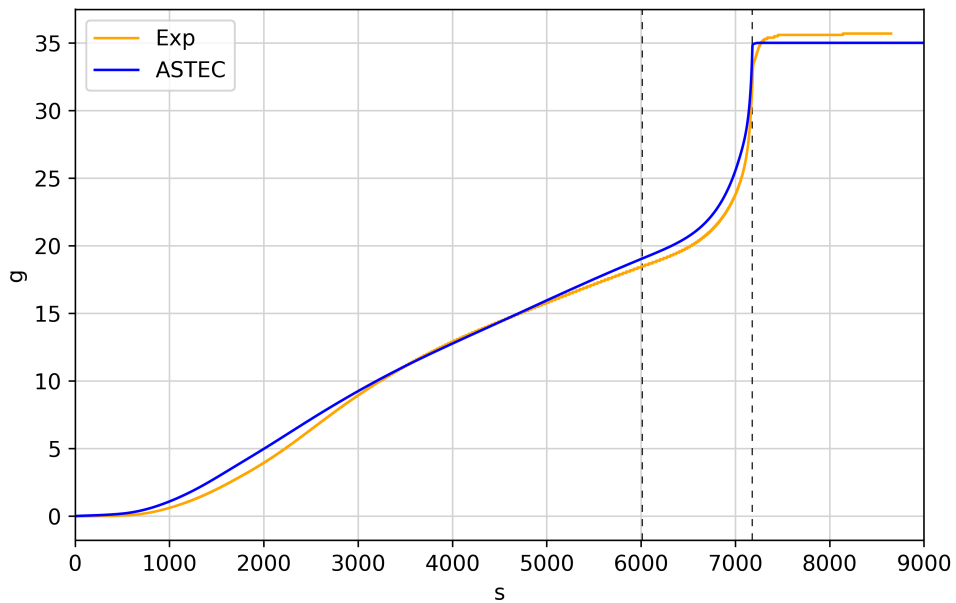


Figure 5.8: Hydrogen cumulated mass produced from experimental data and from code calculation.

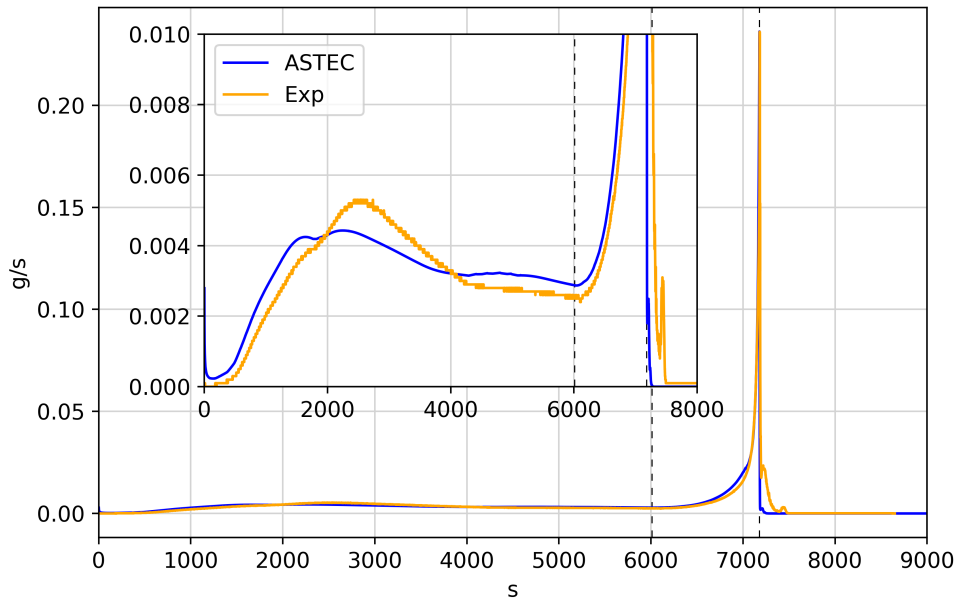


Figure 5.9: Hydrogen mass production rate from experimental data and from code calculation.

Fig. 5.10.

Quenching phase

At 7179 s the source of argon is moved to the upper inlet of the channels (above the bundle) and the source of steam is turned off. The quenching water (pre-injection) starts to enter from the section bottom inlet, and it lasts for 5 s. 26 s later, the electric power is reduced from 18.2 kW to 4.0 kW in 16 s; and at 7215 s the main water injection system starts to pump water in the bundle (Table 5.1). In the experimental test, shroud and some rods simulators feature a local failure, around the elevation of 950 mm, at the quenching timing. It determines a relocation of a limited mass of melted material without loss of system geometry [22].

In Fig. 5.11 and 5.12 it is shown the material compositions of the bundle components predicted by ASTEC at the quenching time. The code predicts the local melting of Zr in the corner rod and in the shroud, around the elevation of 950 mm (“MIXTU” material in yellow). Yet, the loss of integrity conditions set in the input are not reached in the simulation (due to ZrO and ZrO_2 solid layers). Neglecting the limited melt relocation and the limited internal cladding oxidation observed in the experiment, the ASTEC reference calculation features a components degradation phenomenology in good agreement with the experiment.

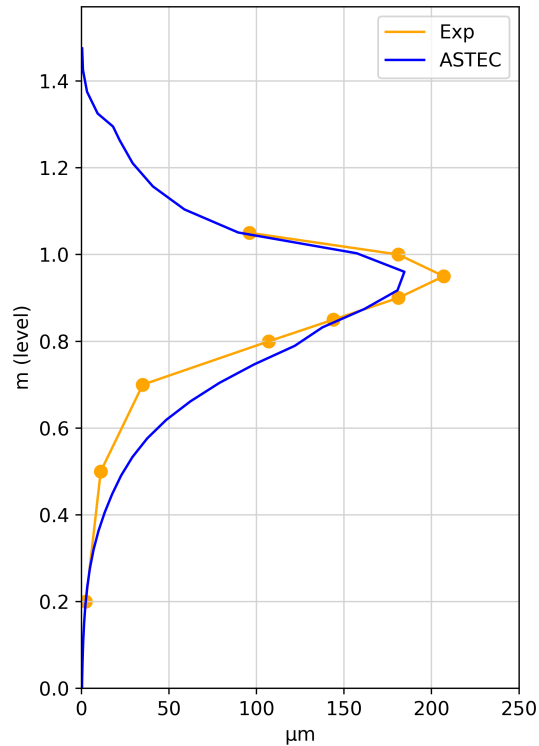


Figure 5.10: ZrO_2 outer layer thickness axial profile for the extracted corner rod at 6620 s.

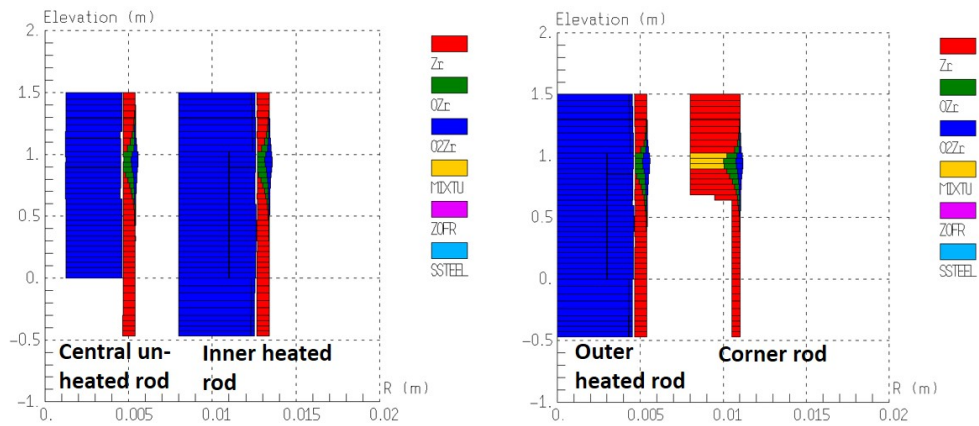


Figure 5.11: Materials in unheated rod and inner-ring heated rod (left); materials in outer-ring heated rod and cornered-rods (right), at 7179 s of ASTEC simulation.

The quick drop of temperature (quenching), due to the pre-injection water, is followed by a slight increase of the rods temperature between the end of the

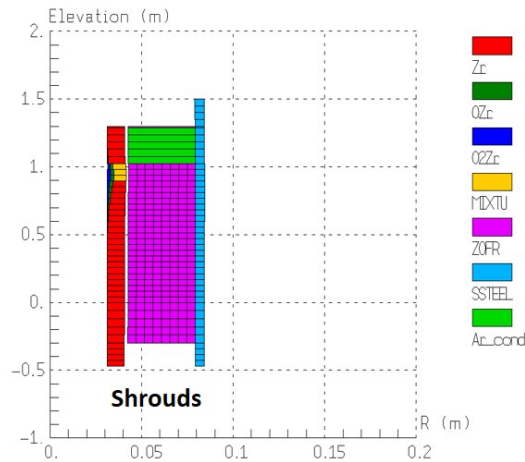


Figure 5.12: Materials in shrouds at 7179 s of ASTEC simulation.

pre-injection and the onset of the main injection. The second cooling (main water injection) leads to the saturation temperature at the system pressure. From a quantitative point of view, the code predicts with a good agreement the first temperatures drop; the second cooling is simulated to be faster than in the experimental data, leading to the final saturation temperature around 120 s earlier in the rods (Fig 5.5 and 5.6). Also, for the shroud (Fig. 5.7), ASTEC predicts a faster cooling, with the final temperature reached almost 150 s earlier. In agreement with the temperatures comparison, the calculated hydrogen production features a similar behavior and the production decrease is faster in the code than in the experiment. The total amount of H_2 produced, reported in Fig. 5.8, shows a mass slightly lower (of around 1 g) in the ASTEC simulation.

The ZrO_2 thickness profiles in the corner rods (not extracted) and in the shroud are shown in Fig. 5.13. The curves have been predicted with a good qualitative and quantitative agreement in the simulation. The different cooling behavior observed underlines some (minor) discrepancies in the prediction of the heat exchange between hot components and quenching water. Further studies will have the purpose to investigate if this discrepancy should to be attributed to the ASTEC thermal-hydraulics and convection heat-transfers or to the nodalization approach adopted.

5.2.4 Uncertainty Quantification analysis

Assumptions of the UQ analysis

The UQ analysis of the ASTEC simulation has been developed through the application of the Input uncertainty propagation method and the RAVEN-ASTEC

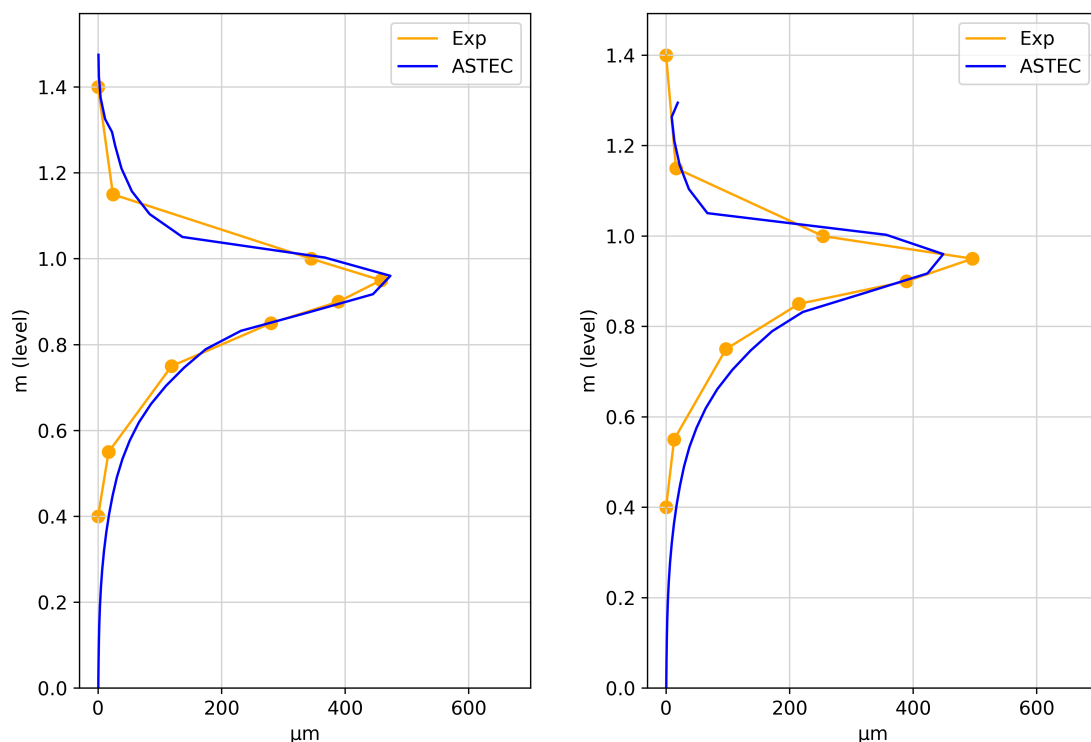


Figure 5.13: Axial profile of ZrO_2 thickness, averaged on not-extracted corner rods (left), and of shroud (right), at 9000 s.

coupling. The main uncertainties affecting the ASTEC simulation have been considered by selecting 23 input uncertain parameters in order to have a comprehensive assessment of the uncertainty inputted in the calculation. The uncertain parameters have been provided by KIT in the framework of the CRP **CRP-I31033** among the following types:

- Geometry of the test section;
- Initial and boundary conditions;
- Integrity criteria of the cladding;
- Physical models parameters related to convection heat transfer;
- Physical models parameters related to degraded material relocation.

Reference values, ranges and PDF types of the parameters have also been provided by KIT, as a result of a study from public references, parametric studies and expert judgment. 200 ASTEC calculations of the sequence have been performed by sampling the values of the input uncertain parameters. According to the *two-sided Wilks formula*, this sampling size guarantees a probability content of 97% within a

confidence level of at least 98%, for each FOM (a more conservative approach with respect to the usual used values of 95% - 95%). In Tables 5.2 and 5.3 has been reported the list of input uncertain parameters, with their ranges of variation and PDF types. The sampling strategy adopted is a *random Monte Carlo*; the chosen

Name	Parameter	Reference Value	Range	PDF type
RodP	Rod pitch (mm)	14.3	± 0.15	Uniform
FpDe	Fuel pellet simulator (ZrO_2) external diameter (mm)	9.15	± 0.02	Uniform
ClTh	Cladding thickness (mm)	0.725	$\pm 7.25e-3$	Uniform
ShDi	Internal diameter of Shroud (mm)	80.0	± 0.8	Uniform
ShTh	Thickness of Shroud (mm)	2.38	$\pm 23e-3$	Uniform
InsTh	Thickness of Insulator (mm)	37.0	± 0.37	Uniform
dtQuench	Timing of quench water injection (s)	7215.	$\pm 0.5\%$	Uniform
fmQuench	Quench water mass flow rate at the bundle inlet (kg/s)	$f(t)$ from experiment	$\pm 2\%$	Normal
fmAr	Argon mass flow rate at the bundle inlet (kg/s)	$f(t)$ from experiment	$\pm 2\%$	Normal
fmSteam	Steam mass flow rate at the bundle inlet (kg/s)	$f(t)$ from experiment	$\pm 2\%$	Normal
pres	Pressure at the bundle outlet (bar)	2.0	$\pm 2\%$	Normal
fpow	Electrical power (W)	$f(t)$ from experiment	$\pm 2\%$	Normal
fTquench	Quenching water temperature (K)	$f(t)$ from experiment	$\pm 2\%$	Normal
PGap	Fuel/Clad internal pressure (bar)	2.2	$\pm 2\%$	Normal

Table 5.2: Uncertain parameters of type: Geometry of the bundle; Initial and boundary conditions.

output FOMs for the UQ analysis are: H_2 production rate; Temperature of central unheated rod center at the elevation of 950 mm; profile of corner rod ZrO_2 thickens at extraction time (6620 s).

Results of UQ analysis

The 200 calculations of the UQ have been successfully completed. The uncertainty band of the hydrogen production rate (result of the 200 simulations), has been reported in Fig. 5.14, against the reference value of ASTEC and the Experimental data. In the figure, it can be observed that the code result uncertainty (in terms of

Name	Parameter	Reference Value	Range	PDF type
ThkFail	Threshold thickness for ZrO_2 layer failure (μm)	300.0	$\pm 10\%$	Uniform
TempFail	Failure temperature of the ZrO_2 layer (K)	2374.	$\pm 5\%$	Uniform
HeatRani	Rod anisotropic factor for Radiative H.T.	0.5	$\pm 10\%$	Uniform
HeatSani	Shroud anisotropic factor for Radiative H.T.	0.15	$\pm 10\%$	Uniform
DropHd	Heat transfer coefficient due to droplet projection	100.	$\pm 5\%$	Uniform
DropZd	Height above the quench front concerned by droplet projection	0.8	$\pm 5\%$	Uniform
DropThr	Threshold void fraction to allow exchange with liquid droplets	0.999	0.99 - 0.999	Uniform
MovKsmx	Max. value of the ratio permeability/viscosity of degraded material	0.1	$\pm 5\%$	Uniform
MovMliq	Min. liquid fraction allowing the material relocation %	0.0	0.0 - 5 %	Uniform

Table 5.3: Uncertain parameters of type: Integrity criteria of cladding; Radiative H.T.; Convection H.T.; Material relocation parameters [24].

the dispersion band width) is relatively low during the *pre-oxidation PhW* and the first part of *heating-up PhW*. Reached the acceleration of the oxidation processes (at around 7050 s), the results feature a quite large spread of the simulated H_2 production rates, up to reach peaks of 3 times the magnitude of the reference value. Following the onset of the quenching injection, the width of the dispersion band rapidly reduces again.

Despite the H_2 production reaches very high peaks, only a few calculations (less than 10 over 200) feature peaks which are far from the average of the calculated values. In addition, it is important to underline that by considering up to 5 s of delay for the experimental H_2 detection, the experimental data is always enclosed in the dispersion band; except for the 150 s after the quenching, in which the calculated drop in hydrogen production is faster than in the experimental one and none of the calculations is able to capture the experimental slower reduction. The behavior of the H_2 production uncertainty along time can be well assessed by Fig. 5.15, reporting the STD of the FOM (error bars) around the mean value, from 7000

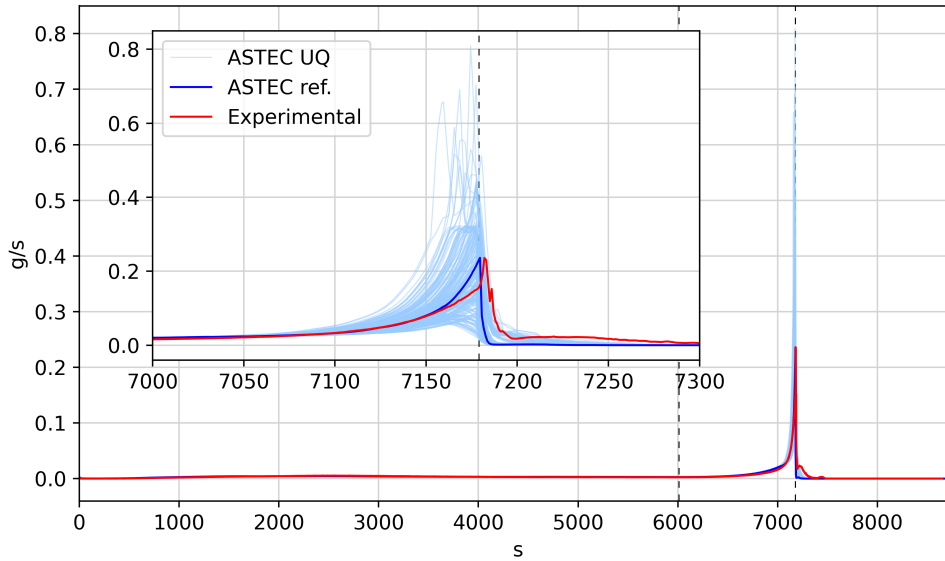


Figure 5.14: Dispersion band of instantaneous H_2 production, against experimental data.

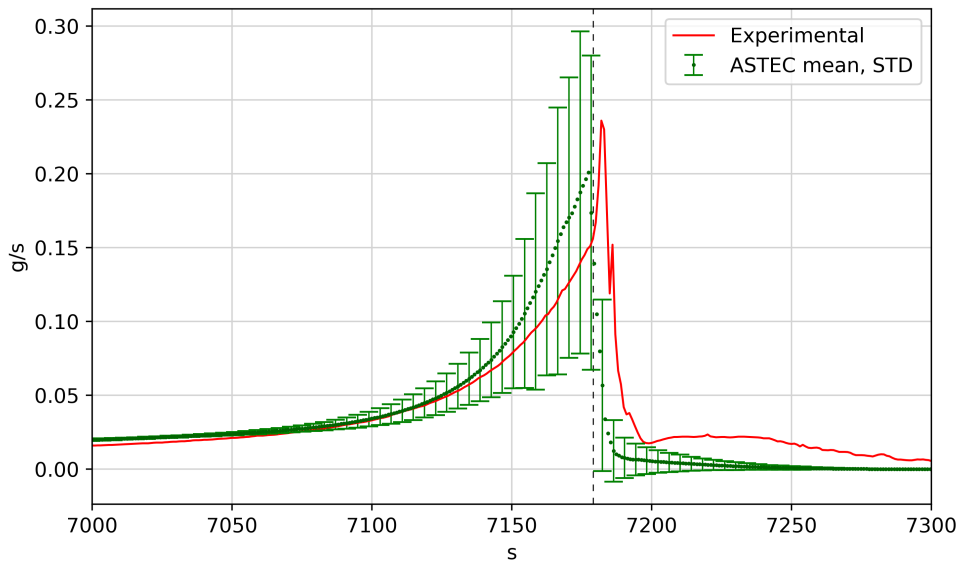


Figure 5.15: Mean value and STD of H_2 production rate against experimental data, from 7000 to 7300 s.

to 7300 s. It can be observed that the reported STD features a fast increase during the oxidation acceleration (7050 s) and a fast reduction after quenching.

Important remarks can be inferred by looking at Fig. 5.16, reporting the final

rods material composition for 2 calculations of the 200, taken from the extremes of the H_2 production rate (lowest heating-up to the left and highest heating-up to the right): different degradation phenomenology has been predicted in the reported cases: the scenario to the left features no melting of materials; the one to the right features a localized melting and relocation of material in the meshes around the height of 950 mm. The reference scenario, in Fig. 5.11, is something in between, as well as the behavior of the rods observed in the experiment.

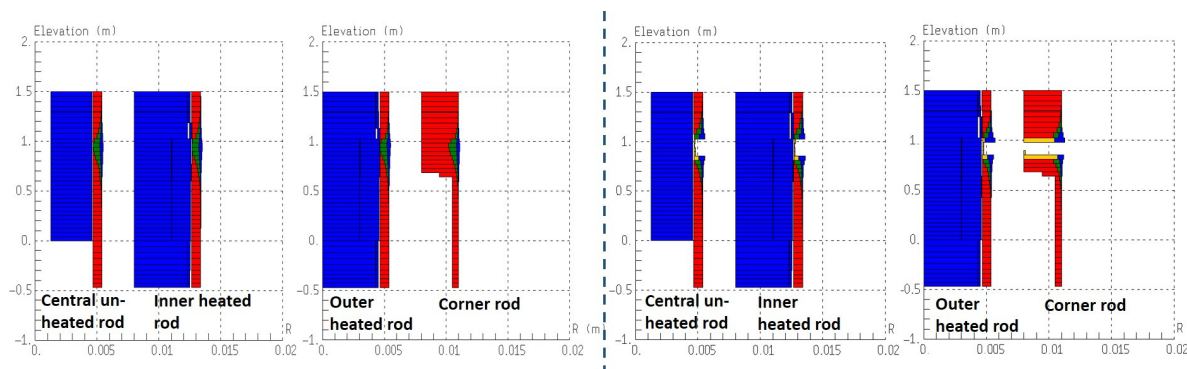


Figure 5.16: Final components materials in cases of lowest (left) and highest (right) heating-up.

Another FOM analyzed, taking into account the simulated oxidation evolution in the components, is the ZrO_2 thickness profile. Fig 5.17 shows the uncertainty band of the ZrO_2 thickness profile in the representative corner rods of ASTEC, at 6620 s of simulation (extraction of the corner rod), against the reference calculated value and the experimental profile.

It can be observed that the uncertainty of the FOM increases with the increase in the reference thickness. The maximum width of uncertainty band, of around $55 \mu m$, is reached nearby the elevation of 950 mm. The experimental data is not enclosed in the band for levels lower than 800 mm, showing a slight overestimation of the oxidation for these levels of the bundle.

The following analyzed FOM is the internal temperature of the central (un-heated) rod simulator, at the elevation of 950 mm. The temperature is strongly correlated to the oxidation rate and hydrogen production phenomena. However, this parameter contains more “local” information with respect to the H_2 production rate and to the Oxidation profile, which represents integral parameters over volume and over time, respectively. The integral nature of such FOMs makes that they contain more information, but also that the uncertainty (error) accounted is summed over the domain of integration. The uncertainty band of the internal

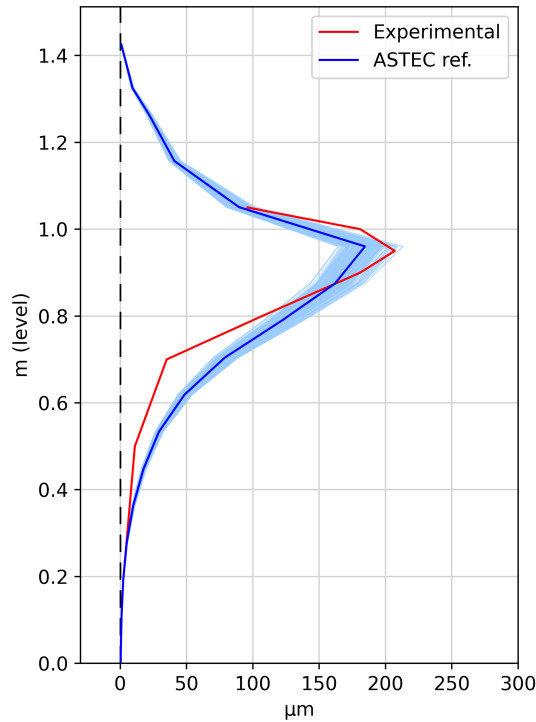


Figure 5.17: Dispersion band of ZrO_2 profile in the ASTEC representative corner rod against experimental ZrO_2 profile in the extracted corner rod, at 6620 s.

central-rod temperature, at 950 mm of elevation, is reported in Fig. 5.18 against the reference and the experimental data.

In this case, the spread of results is less relevant along the sequence, until the quenching injection. Some more observations regarding the uncertainty evolution can be inferred by plotting the mean value and the STD between 6500 and 8500 s of transient (Fig. 5.19). The uncertainty evolution along time (in terms of STD and width of uncertainty band) of the central rod temperature (Fig 5.18 and 5.19) behaves differently from the H_2 production rate (Fig 5.14 and 5.19): it features a first minor increase during the oxidation acceleration and heat-up of the bundle; yet, the main increase of STD (and uncertainty band width) can be observed after the onset of quenching, reaching a maximum value at around 7350 s during the cooling of the bundle. Fig 5.18 shows that the experimental temperature is not included in the uncertainty band during the temperature decrease. This discrepancy underlines the code difficulties in capturing the temperatures decrease observed in the previous section.

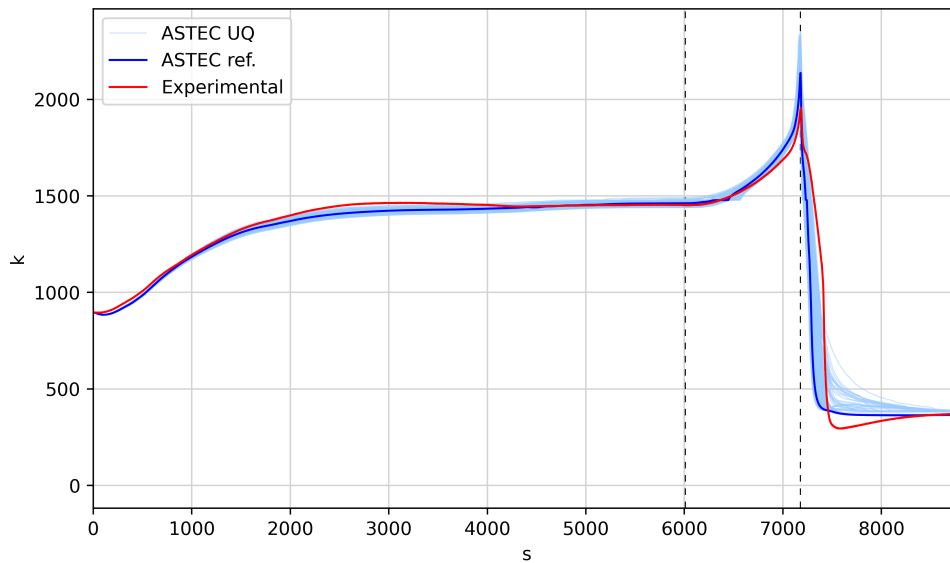


Figure 5.18: Dispersion band of internal temperature of central rod simulator, at the elevation of 950 mm, against experimental data.

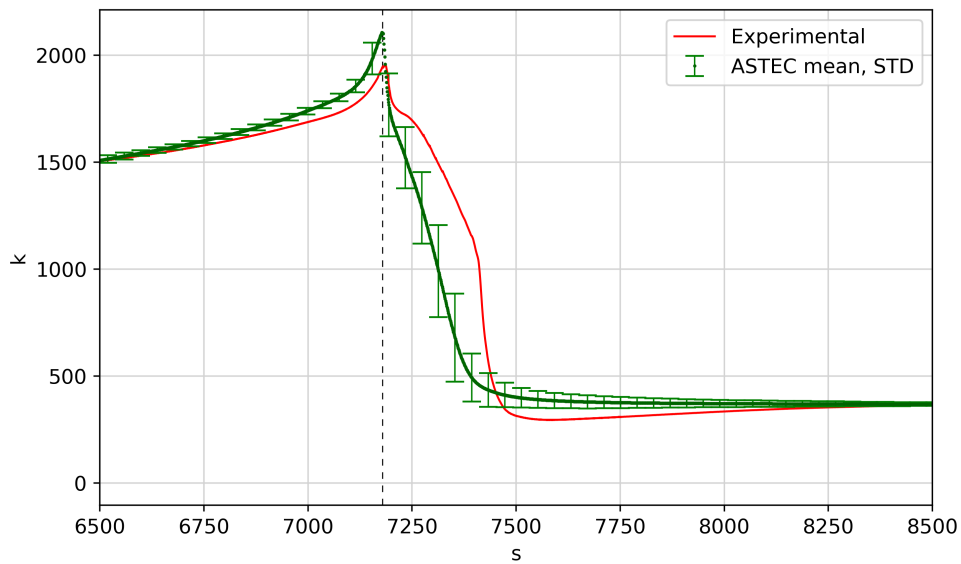


Figure 5.19: Mean value and STD of internal temperature of central rod simulator against experimental data, from 6500 to 8500 s.

Results of sensitivity analysis

The sensitivity of the 23 input uncertain parameters with respect to the 3 output FOMs used in the last section has been analyzed with the use of the *Pearson* and *Spearman response correlation* coefficients and by calculating the coefficients of a *Lasso regression* (optimized with a 5-fold Cross-Validation). To simplify the results of the sensitivity analysis, the plots of the Pearson coefficients have not been presented in the following, but in all the cases the Pearson values are very close to the values of Spearman coefficients.

Fig. 5.20 and 5.21 show the evolution of Spearman coefficients along the sequence for the H_2 production rate, and Fig. 5.22 and 5.23 present the same data for the Lasso regression coefficients. In the plots, have been reported the timings dividing the 3 PhW with vertical dashed lines.

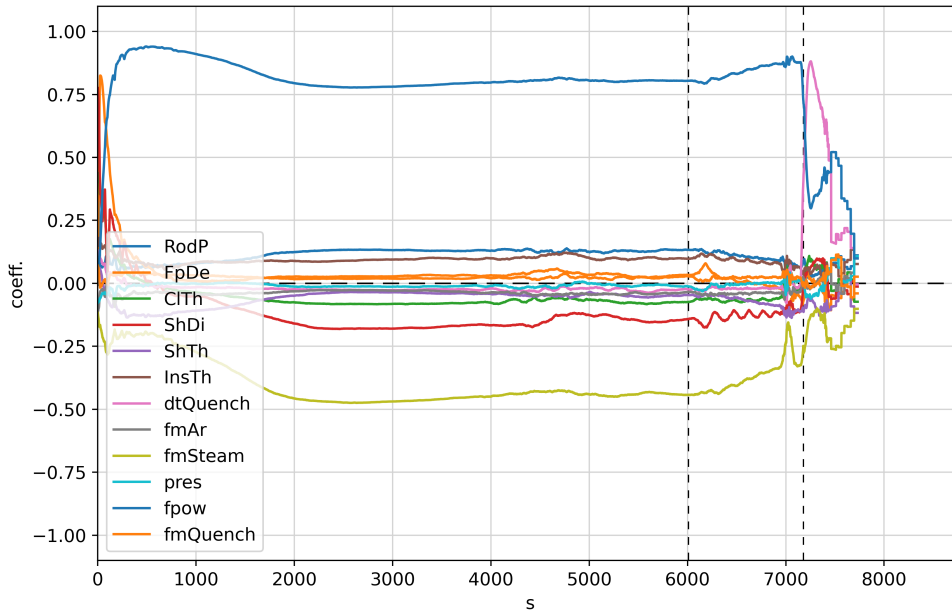


Figure 5.20: Spearman correlation coefficients related to H_2 production rate (geometric and boundary conditions parameters).

The coefficients reported capture a significant positive sensitivity of the FOM with the *power in the bundle* and a moderate negative sensitivity with the *steam mass flow rate*, along the *pre-oxidation* and *heating-up PhWs*. The first 500 s of simulation are characterized by different correlations, but these values can be considered of minor importance considering the low H_2 production and the consequent low value of absolute uncertainty in this phase. During the last part of *heating-up*

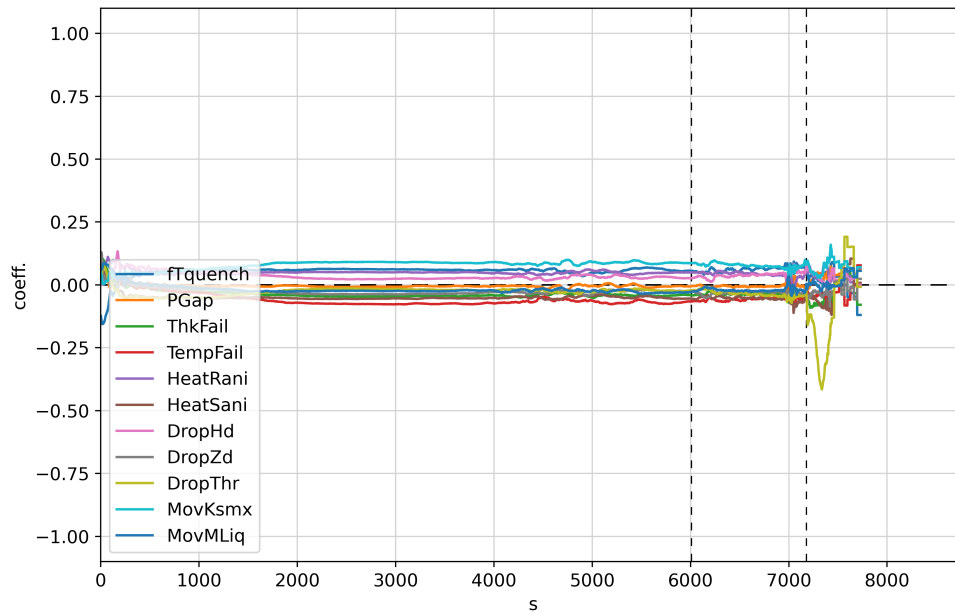


Figure 5.21: Spearman correlation coefficients related to H_2 production rate (cladding integrity criteria and physical models parameters).

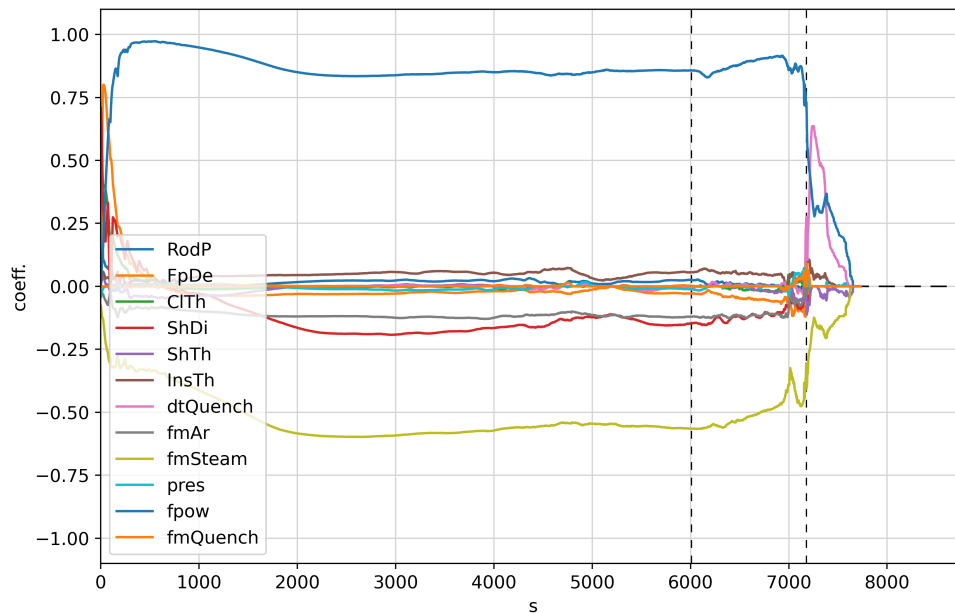


Figure 5.22: Coefficients of Lasso regression related to H_2 production rate (geometric and boundary conditions parameters).

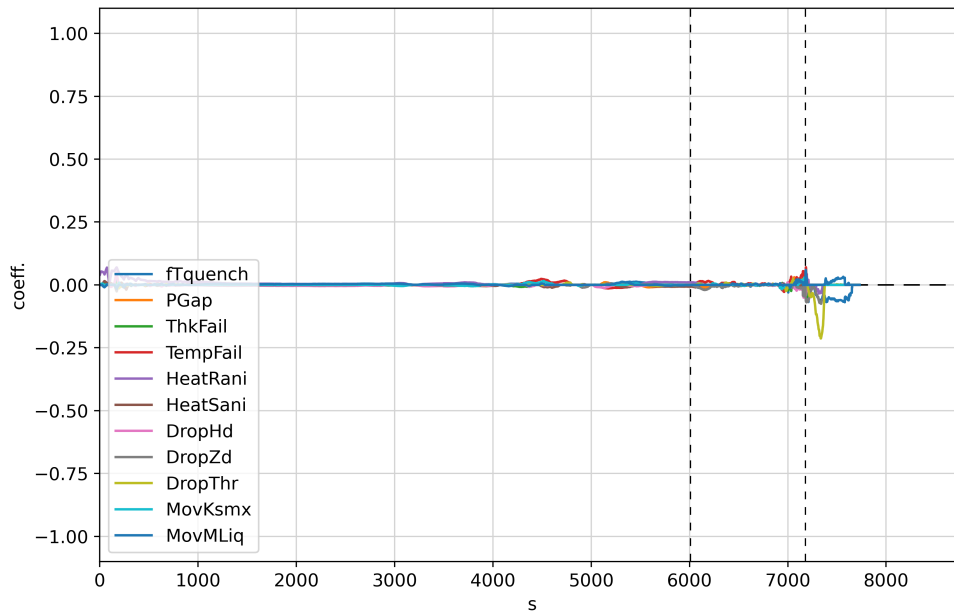


Figure 5.23: Coefficients of Lasso regression related to H_2 production rate (cladding integrity criteria and physical models parameters).

PhWs (after 7050 s), characterized by the acceleration of oxidation and large spread of the FOM, the main uncertainty source seems to be the *power in the bundle* with a positive relevant sensitivity. After the injection of quenching water, the situation changes and the sensitivity of the *power in the bundle* and of the *steam mass flow rate* respectively reduces to moderate and low values. At this point, around 100 s after the reference quenching timing, both the Spearman and the Lasso sensitivity coefficients of the Instant of quench injection increases to reach a peak of significant value.

The Spearman and the Lasso coefficients, related to the ZrO_2 thickness of the corner rod at 6620 s, are reported in Fig. 5.24 and 5.25 as a function of the elevation of the bundle. The sensitivity coefficients related to the ZrO_2 profile capture a significant positive correlation with the electrical power along all the elevation, and a significant negative correlation with the steam mass flow rate for elevation lower than 1300 mm. The shroud internal diameter features a moderate negative correlation with the FOM at the bundle elevations presenting low oxidation thickens (above 1300 mm and below 500 mm). The elevations presenting the largest uncertainty (around 950 mm) are characterized by a significant sensitivity only with the first two mentioned input uncertain parameters.

Fig. 5.26 - 5.29 show the Spearman and Lasso coefficients related to the Tem-

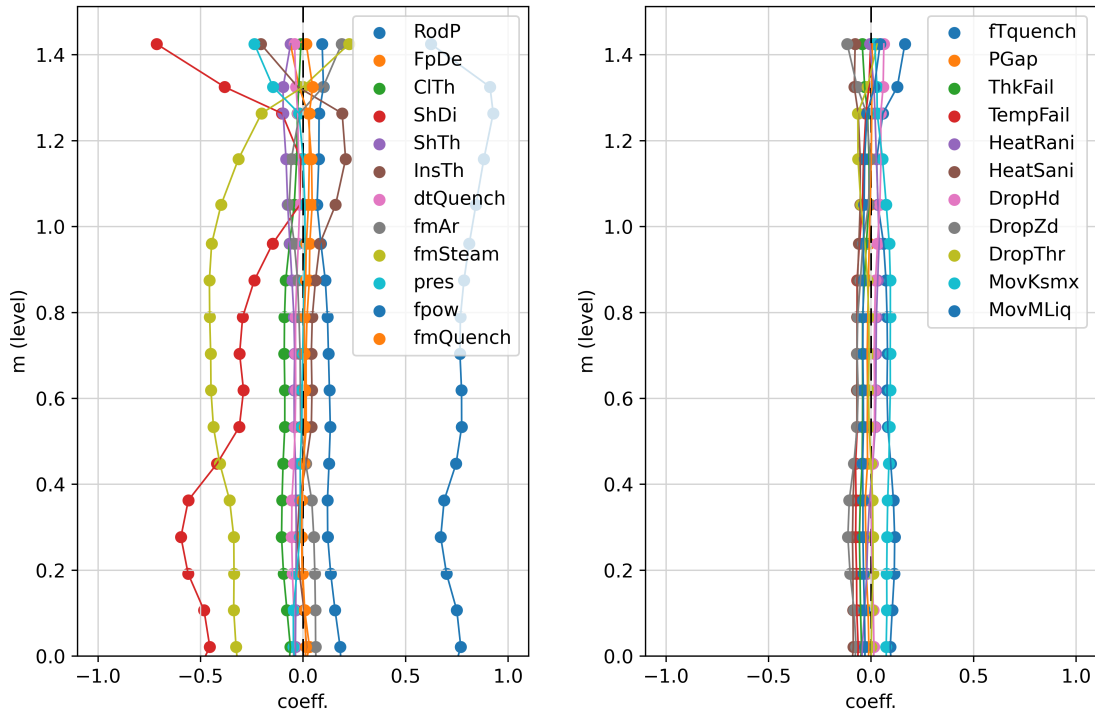


Figure 5.24: Spearman correlation coefficients related to the corner rod ZrO_2 thickens, at 6620 s, for geometric and boundary conditions parameters (left), and for cladding integrity criteria and physical models parameters (right).

perature FOM presented in the previous section (central temperature of central rod at 950 mm). Along the first two PhWs and until quenching, the sensitivity of the temperature is mainly governed by the *electrical power* and the *steam flow rate*. After the onset of quenching injection, as observed for the H_2 production uncertainty, the temperature features a moderate positive sensitivity with the *time of water injection*. In addition to this correlation, both the coefficients also capture a peak of significant negative sensitivity (around 150 s after quenching) with the input parameter of *threshold void fraction to allow exchange with liquid droplets*. During the *quenching PhW* the *electrical power* and the *steam flow rate* show a moderate sensitivity with the FOM.

5.2.5 Conclusions

The benchmark exercise on the ASTEC code simulation of QUENCH test-6 experiment, developed in the framework of IAEA CRP - I31033, is among the first applications of UQ analysis to SA code for studying the uncertainty related to the

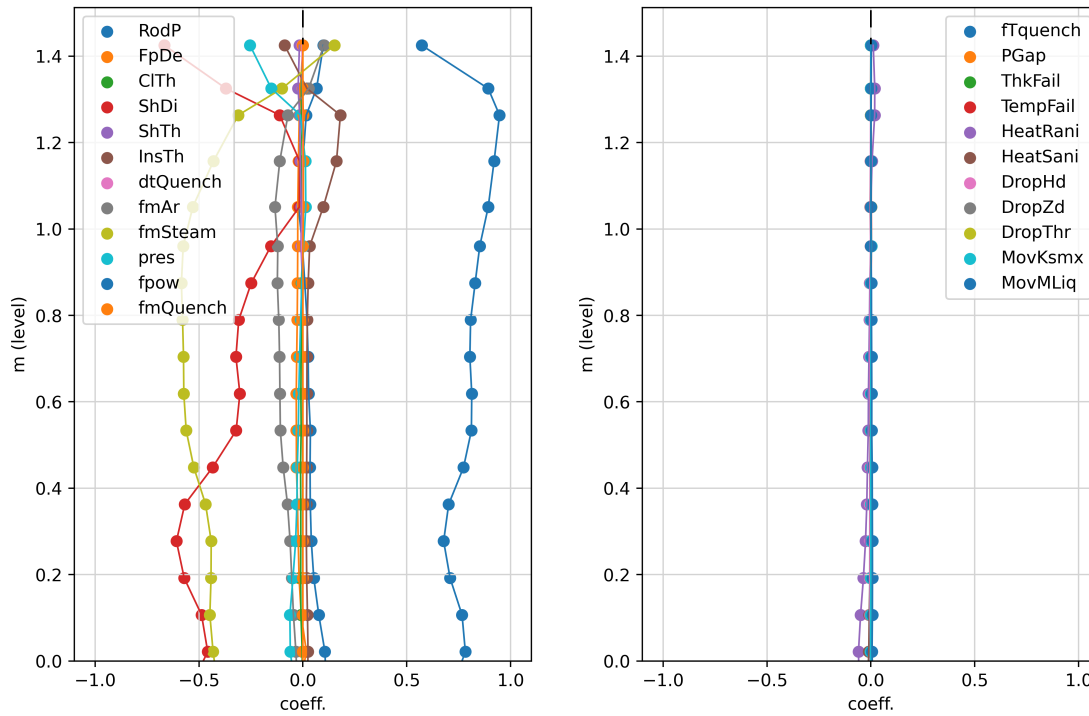


Figure 5.25: Coefficients of Lasso regression related to the corner rod ZrO_2 thickens, at 6620 s, for geometric and boundary conditions parameters (left), and for cladding integrity criteria and physical models parameters (right).

simulation of core-melt phenomena in LWR. Objective of the study is the evaluation of the code capability to simulate the main phenomena involved in the experimental transient and the characterization of the uncertainty affecting the related code models. In addition, this benchmark exercise has been used with the aim of testing the applicability of the UQ methodology on SA phenomena simulations.

Lessons learned and recommendations on the use of the BEPU methodology

The methodology used in the study follows a BEPU approach: Best-Estimate simulation + UQ analysis. The direct comparison of the reference best-estimate simulation against the experimental data is a first step in the qualitative and quantitative evaluation of the code prediction accuracy. It helps in the identification of the main physical phenomena governing the sequence, and in the selection of those phenomena which are not well assessed in the simulation and that need further investigation. In the CRP - I31033, this operation has been followed by the application of a *quan-*

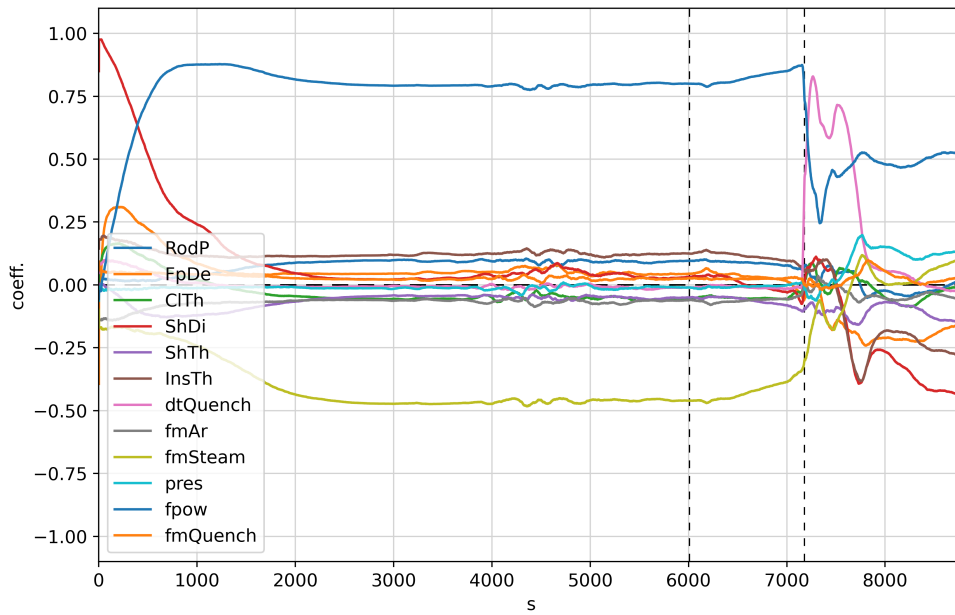


Figure 5.26: Spearman correlation coefficients related to central temperature of central rod at 950 mm (geometric and boundary conditions parameters).

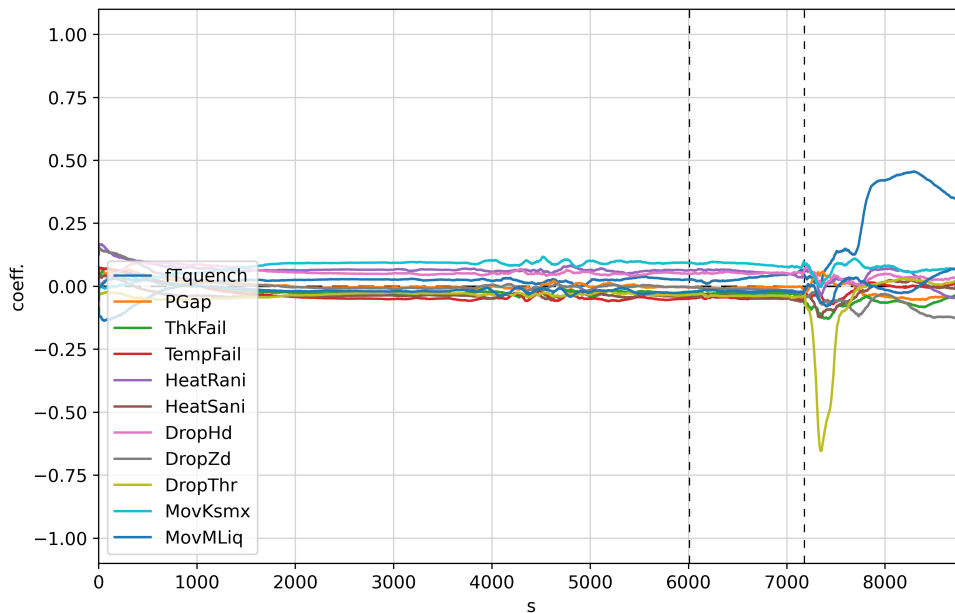


Figure 5.27: Spearman correlation coefficients related to central temperature of central rod at 950 mm (cladding integrity criteria and physical models parameters).

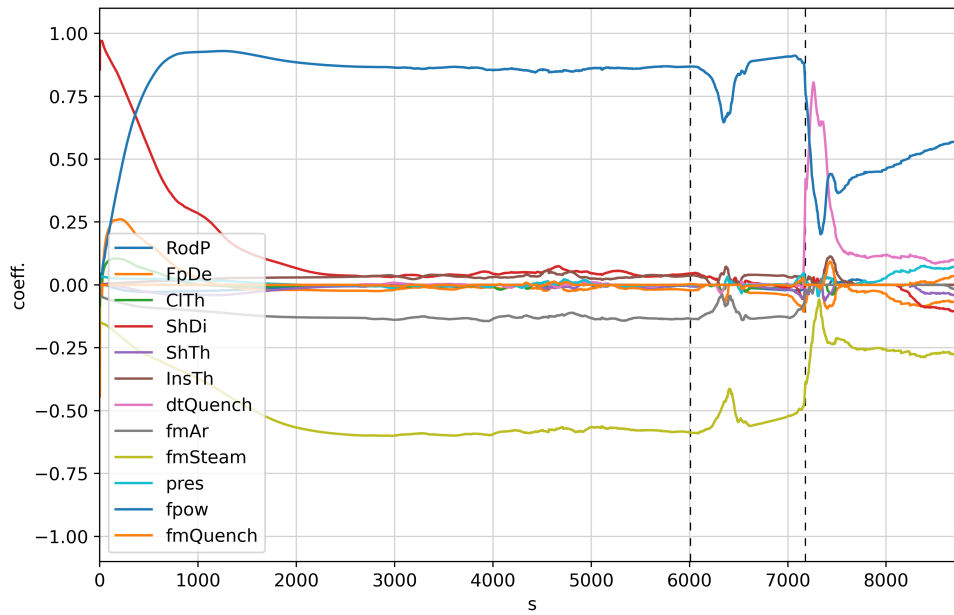


Figure 5.28: Coefficients of Lasso regression related to central temperature of central rod at 950 mm (geometric and boundary conditions parameters).

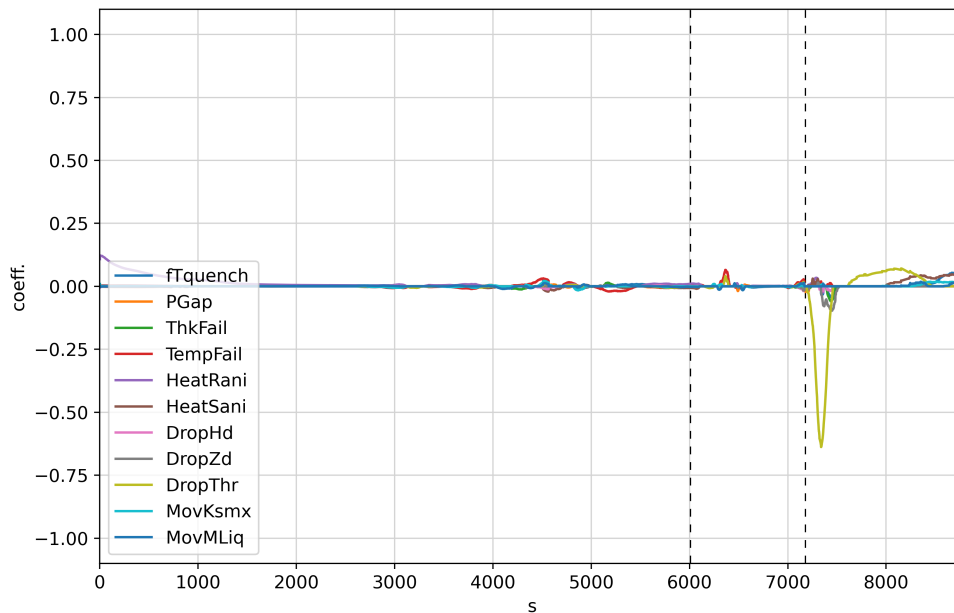


Figure 5.29: Coefficients of Lasso regression related to central temperature of central rod at 950 mm (cladding integrity criteria and physical models parameters).

titative accuracy evaluation method (FFTBM method [25]) aimed at providing a quantitative measure of the code prediction accuracy (see Section 3.1.2). The UQ analysis completes the study by providing information regarding the uncertainty affecting the code prediction and, thanks to the sensitivity analysis, it is possible to estimate the contribution of each input parameter in the uncertainty propagation to the results. Using the *Propagation of input uncertainty method*, the statistical confidence in the UQ results is not affected by the number of input parameters, and it is an advantage in case this number is large like in the present study.

Care should be taken in the use of the *Wilks confidence level formula*: it can be done only under the hypothesis presented in Section 5.1.2. Code failures should be avoided when possible. Otherwise, the failures should be very limited in number [9]. In addition, in case of bifurcation of the output domain of a FOM the *Wilks formula* statistics may not hold for this FOM [2]. This point is discussed in the next Section and a proposed solution to this issue is assessed in the last Section of this Chapter.

In addition, in the selection of the FOMs for the UQ, it is important to consider that integral parameters contain integral information and take into account for the uncertainty summed along the domain of integration. For this reason, in order to address more exhaustive analyses, it results important to consider different integral FOMs over different domains of integration (time, volume, etc.), but also to add localized parameters.

Conclusions of the reference simulation analysis against the experimental data

The direct comparison of the reference simulation against the experimental data exhibits a good qualitative and quantitative prediction of the phenomena governing the *pre-oxidation PhW* by the code.

During the *heating-up PhW*, the ASTEC prediction can also be classified as very good; the only observed discrepancy with the experimental data regards the simulation of a slight faster heat-up of some components (e.g. corner rod, shroud), during the phenomenon of *Zr* oxidation runaway. The *ZrO₂* thickness profiles of the extracted corner rod is qualitatively well assessed by the code.

The accuracy in the prediction of the *quenching PhW* can be classified as good. There are yet some discrepancies in the assessment of the quenching heat exchange and the following temperature drop, which in some components is predicted by ASTEC to be faster, leading to an earlier stop of the oxidation processes. It may be due to a slight overestimation of convection heat-transfer simulated by ASTEC, but also to the modelling assumptions adopted in the nodalization. Further studies

and sensitivity analysis should be conducted on this point.

An important qualitative observation is that ASTEC captures the local melting of materials around the most heated-up level, without a loss of integrity and relocation of melted. This is consistent with what is observed in the post-experiment analysis of the bundle, in which rods and shroud feature a localized melting without a major loss of system geometry. The code prediction of the total hydrogen mass production is only 1 g lower than the experimental, over a total of 36 g. This proves a good evaluation of the global Zr oxidation.

Conclusions of the UQ analysis

By analyzing the results of the 200 calculations it is possible to characterize the uncertainty of the selected FOMs as a result of the input uncertain parameters variation. The uncertainty of H_2 production rate is characterized by a large spread of results starting at the onset of Zr oxidation acceleration and rapidly reducing after the onset of quenching. This behavior can be expected considering the non-linear escalation of oxidation, for temperatures higher than about 1770 K, leading to a spread of the results. Yet, as already underlined, the quite large width of the uncertainty band characterizing this parameter can also be attributed to its integral nature, taking into account the total oxidation uncertainty integrated over the system volume.

Some different behavior characterizes the time evolution of uncertainty affecting the central rod temperature (at 950 mm level). This FOM suffers from uncertainty increasing mainly during the quenching of the system. Moreover, the behavior of the uncertainty band of this FOM, which does not enclose the experimental curve during quenching, confirms some code difficulty in the prediction of the heat exchange during this phenomenon. In agreement with the results of H_2 production, the bands of ZrO_2 thickness profile at 6620 s of transient presents a moderate uncertainty which increases nearby the most heated up elevation of 950 mm.

Another crucial reason that may lead to the general uncertainty spread can be attributed to the fact that the reference simulation (as well as the experiment) is on the edge of changing in a core degradation phenomenology. In the reference simulation, indeed, the conditions for components loss of integrity and material relocation have not been met. Yet, at the onset of *quenching PhW*, such conditions are very close to being reached by several components at 950 mm of elevation. As a consequence, many of the 200 uncertainty simulations incur in a different phenomenology than the one observed in the reference scenario. Failure of structures leads also to further oxidation and H_2 production since also the internal surfaces get available for Zr oxidation.

Several SA code models and phenomena have often to deal with non-linear law (e.g. oxidation runaway, etc.) and edge-effects (e.g. components failures and corium slumping), which in some cases may determine a spread in the results uncertainty, or even some issues in the application of the UQ methodology. This point is deeper discussed in the following Section.

5.3 Discussion on the applicability of the UQ method to SA

5.3.1 Considerations on core degradation phenomena and UQ

The UQ study on the ASTEC simulation of QUENCH-6 experiment has been crucial to explore the applicability of the described UQ methodology to SA simulations. With this regard, this simplified sequence (with respect to a SA plant application) has been useful to identify and discuss some challenges that may occur when dealing with SA phenomena and UQ. Accordingly, core degradation is characterized by *non-linear law phenomena* (e.g. oxidation, quenching cooling) and by *edge-effect phenomena* taking place only upon achievement of specific physical conditions (e.g. components failures; corium relocation and slumping). This makes code modelling of core degradation a very challenging task and, in addition, it adds some challenges in the assessment of UQ studies.

The *Non-linear law phenomena* observed in the previous UQ study, e.g. H_2 production rate during the oxidation run-away and rods temperature decreasing during quenching, have the main effect to increase the propagation of the input uncertainty to the simulation results. This effect could be expected and is well assessed by the UQ methodology used.

Regarding *edge-effect phenomena*, multiple cases are expected to take place along a complete SA sequence in a plant application. Yet, the simplified scenario represented by the QUENCH-6 experiment gives us the advantage to limit the edge-effect phenomena to the loss of integrity condition of the Zr components and, therefore, it can be used to drive some important remarks on this point. The first remark is that, as for *non-linear law phenomena*, *edge-effects* may increase the propagation of the input uncertainty to the results, e.g. cladding failure means more Zr surface available for oxidation and, hence, a further increase of H_2 production and of temperatures. Yet, there are also additional aspects that should be underlined:

According to [2], in Section 5.1.2 it has been discussed as one of the *Wilks for-*

mula assumptions is that the mapping $L(t)$ (representing the input-output transformation done by the code model) does not show *chaotic behavior*. In the same Section, it is added that *chaos* can be considered to take place when there is a sudden change in mean and variance of the FOM, and when it tends to separate into disjoint sets. It is clear that this situation can often occur when dealing with UQ of SA simulations due to *edge-effect phenomena* and, in such cases, the statistics of *Wilks formula* might not hold for some FOMs. As an example, it is here reported in Fig. 5.30 the ZrO_2 profile in internal and external heated rods cladding, at calculation end, for the UQ study on QUENCH-6 presented in Section 5.2.

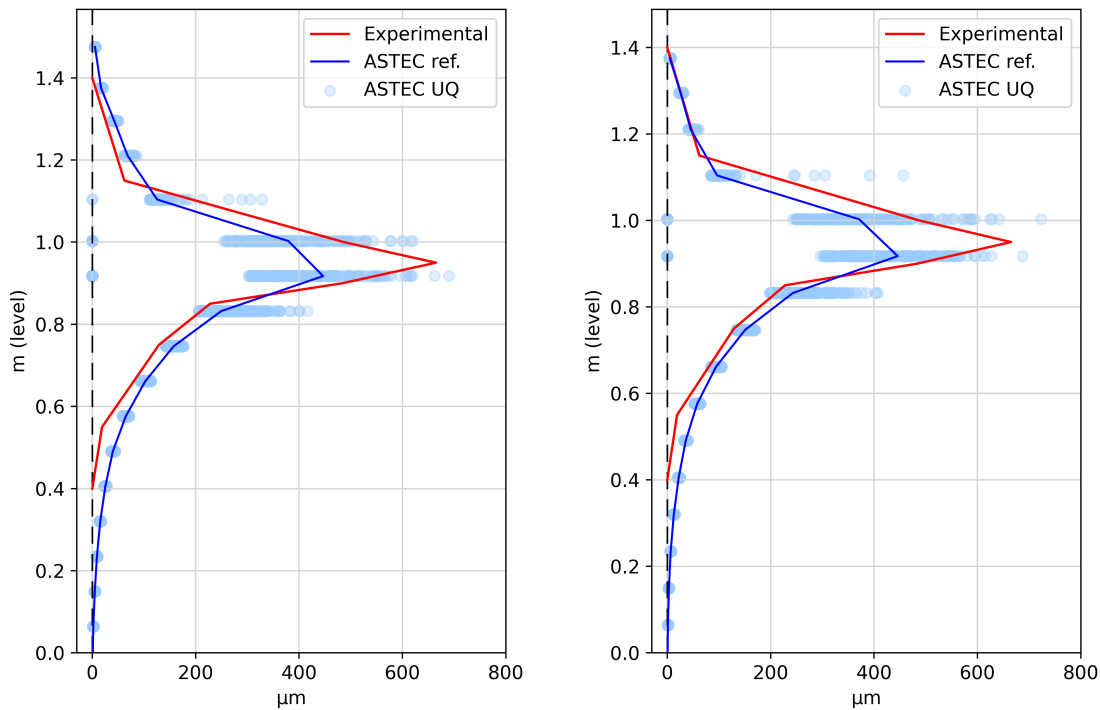


Figure 5.30: Dispersion band of ZrO_2 profile in the cladding of internal-ring heated-rod (left) and of external-ring heated-rod (right) at calculation end, against experimental data.

From Fig. 5.30, it can be observed that at elevations between 80 and 120 mm some of the UQ simulations feature a value of 0 for the ZrO_2 thickness. This is due to the achievement of the loss of integrity conditions of cladding that, as a consequence, relocates in other core regions. It is clear that the hypotheses of *Wilks formula* cannot be respected for this FOM (bifurcation of the output domain into disjoint sets). It means that, for the considered FOM manifesting bifurcations, we cannot know the statistical content (in terms of *confidence level* β and *probability*

content γ) of the uncertainty band obtained. Yet, we can at most assess a qualitative description of the band behavior.

With regard to the example presented in Fig. 5.30, it may result very useful to find the conditions (in terms of the value of input uncertain parameters) for which the simulation features a cladding loss of integrity and to be able to separate these from the intact cladding cases. A proposed solution to this problem is described in the last Section (5.5) of this Chapter.

5.3.2 Challenges of UQ analysis to SA in plant applications

The QUENCH-6 experiment and the ASTEC simulation of this test represent, under several points of view, a simplified situation with respect to a complete SA plant application. First of all, in this sequence are expected to take place a limited number of early core degradation phenomena (*Zr* structures oxidation, cladding failure and limited relocation); the facility features a geometry representing a simplified reactor core, neglecting the coupling with other plant systems; the sequence is limited to 9000 s of calculation; etc. As a consequence, it was possible to use the simulation of this sequence to test the UQ methodology and draw the above mentioned remarks.

In a complete SA sequence simulation at plant-level (e.g. the SBO simulation in Section 3.3 or the two SA simulations presented in Section 4.4), the application of the UQ method, described in Section 5.1.2, could present some main challenges that have been listed and discussed in the following:

- a) The calculation time of a single SA simulation in a plant application can last up to 2 weeks, or even longer. This makes that the feasibility of multiple simulations for the UQ study is often beyond the capability of the computational resources available, even considering the availability of large HPC whose use is often limited up to a maximum number of hours per *batch job* by the management system of the *queues*.
- b) SA plant simulations often suffer of high probability of failure, e.g. due to numerical problems. In the case of a single simulation failure, this issue can be easily overcome by an expert code user. However, when dealing with UQ analysis, it is possible to run into multiple simulations failures and it becomes nearly impossible to ensure the success of all the calculations at first or to correct all the failed simulations without changing them. In order to respect the statistics of *Wilks Formula*, it should be guaranteed that failures are very limited in number [9] and randomly distributed in the input phase space. It is clear that in real applications it is very difficult also to respect such conditions.

- c) In a code simulation of an entire SA in a NPP, many of the SA phenomena involved can potentially feature an *edge-effect*, leading to a phenomenological bifurcation under the application of the UQ method. Besides the inapplicability of the *Wilks formula* for most of the output FOMs, the effect of several sequential bifurcations taking place along the sequence, combined with the acceleration of processes due to *non-linear law phenomena*, would result in a general multiple and chaotic separation of the results. This means the impossibility to make a comparison between the simulations for a FOM at a specific time point, since different phenomena would have occurred in each simulation at this point. The possibility to split the simulations into sets on the basis of the phenomenology that occurred (as proposed for the QUENCH-6 simulation) would be possible only in the case of very limited *edge effect phenomena* and consequent FOM separations. As an example of this issue, in Fig. 5.31 it is reported the Cs-137 % mass fraction emitted from fuel in a loss of cooling accident occurring in a Spent Fuel Pool [26]. In the preliminary UQ study 36 calculations of the same SA have been executed by varying the input uncertain parameters. The calculations have been stopped at around 443800 s of simulation, after the beginning of core degradation. In the figure, it is possible to observe the multiple bifurcations occurring in the FP emission, that lead the FOM to divide first into 3 main groups and then, after 440000 s, in even more. The example reported is an extreme case of FOMs chaotic behavior; in other scenarios, the bifurcations could be few or even more, depending on the phenomena involved in the sequence, on the code model stability and on the considered input parameters variations.
- d) Multiple *non-linear law phenomena* and *edge-effects phenomena* make the relationship between input and output FOMs variations strongly non-linear. As a consequence, under these conditions, it becomes almost impossible to capture any sensibility and correlation between input and output variations by using the sensibility coefficients presented in Section 5.1.3.

Point a) of the listed possible issues is the main technological challenge precluding the application of the UQ method to the SA sequences on the generic IRIS reactor presented in Section 4.4. Indeed, as has been already mentioned in this Section, the lower power and consequent lower decay-heat of SMRs make the SA sequence become longer as compared to a SA in conventional size reactors and, as a consequence, the computational cost of such simulation also increases. With respect to SA scenarios on the generic IRIS of Section 4.4, the two calculations were stopped at a simulations time of 150000 s, which correspond to several days of real

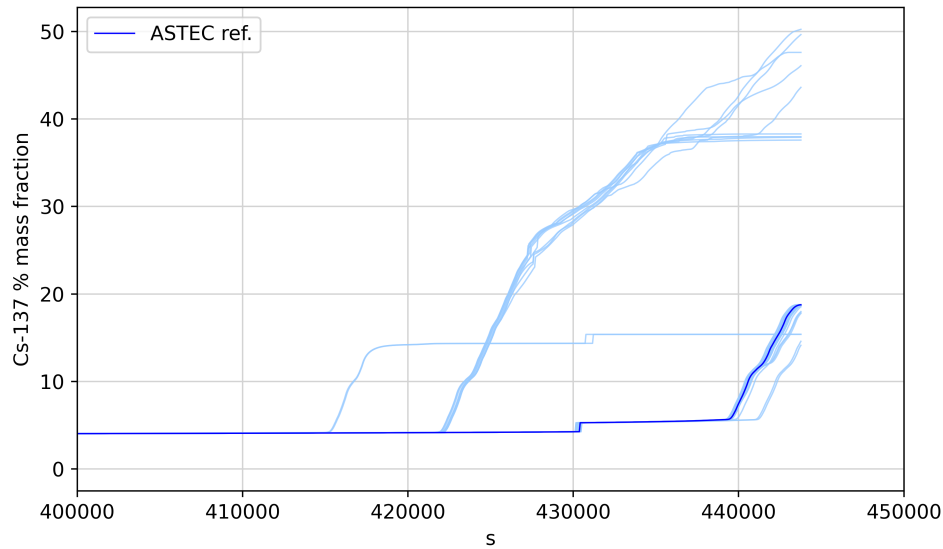


Figure 5.31: Cs-137 % mass fraction emitted from degrading fuel of a Spent Fuel Pool, in 36 calculations for a preliminary UQ analysis.

calculation. In a UQ study, this time can easily increase to more than a week in the case that one or more simulations encounter numerical problems of convergence. It comes out that the possibility to develop a comprehensive UQ analysis of this type of sequence is limited by the computational resources available.

5.3.3 Conclusions ad remarks

The UQ study on the ASTEC simulation of QUENCH-6 experiment offers a simplified case to explore the applicability of the described UQ methodology to SA simulations. It comes out that core degradation is characterized by two types of phenomena mainly influencing the application of UQ: *non-linear law phenomena* have the main effect to spread the results and increase output uncertainty; *edge-effect phenomena* may cause bifurcations of the FOMs, increasing uncertainty and creating chaotic behavior of the results.

For the simplified case of the QUENCH-6 application, the uncertainty of the chosen FOMs is well assessed by the UQ methodology. However, the obtained bifurcation of phenomena (loss of integrity condition of Zr components) prevents the application of the method whether considering some FOMs, s.a. the ZrO_2 thickness profile at calculation end (Fig. 5.30). Nevertheless, it has been possible to propose a solution to the obtained bifurcation of phenomena and the application is described in Section 5.5 of the present work of thesis.

Regarding UQ studies of complete SA scenarios at plant-level, some challenges often occur in the application of the method. The issues identified and described might or might not be present in a UQ application, mainly depending on the chosen reference sequence and on the input uncertain parameters selected. In general, these challenges open to the study and development of new UQ methodologies or to the modification and improvement of the already used.

Due to the too long computational times and the realization of some code failures (points a and b of the listed challenges), the UQ method has not been yet applied to SA sequences on the generic IRIS reactor. Nevertheless, the next Section of this Chapter deals with a UQ application to the DBA sequence of the generic IRIS described in Chapter 4.

5.4 UQ analysis of ASTEC simulation of DBA sequence in a generic IRIS reactor

The present section deals with the application of the UQ methodology to the ASTEC simulation of the DBA transient in the generic IRIS presented in Section 4.3. The study is aimed at characterizing the uncertainty affecting the main safety FOMs of the reactor as a consequence of the uncertainty inputted through selected relevant input uncertain parameters. In addition, the study provides valuable information regarding the ASTEC simulation thermal-hydraulics and characterizing the role played by the passive safety systems in the mitigation strategy.

The analysis has been carried out with the last released code version ASTEC v2.2.0, and implementing the *6-equation model* of CESAR for the 2-phase flow. The reference calculation of the DBA sequence features only minor discrepancies with respect to the sequence described in Section 4.3 (using the *5-equation model*) and an additional description of the DBA simulation results is not necessary.

5.4.1 Uncertainty Quantification analysis

Assumptions of the UQ analysis

The present study is not aimed to be a comprehensive analysis of the code simulation uncertainty, but to study the effect of selected main uncertainty sources affecting the natural-driven phenomena driving the operation of passive safety systems in the DBA sequence. Thus, a total of 7 uncertain input parameters have been selected, and the respective PDFs and ranges of variation have been derived from previous studies (such as [9][18]) from literature (ASTEC manuals, etc.) or by

expert judgment by following a conservative approach. The list of input uncertain parameters, with their ranges of variation and PDF types, is reported in Table 5.4. The cladding maximum temperature and the DW pressure have been selected as

Parameter	Name	Range	PDF type	Reference
Power of decay heat	FpPow	$[\pm 8 \text{ \%}]$	normal	[19]
Friction form loss in PRZ surge line	KPrz	$[0.5 - 2.]$	normal	[19]
Heat-transfer surface of EHRS – RWST exchanger	SEhrs	$[\pm 25 \text{ \%}]$	uniform	[20]
RWST initial temperature & environment temperature	TEnv	$[10 - 30 \text{ }^\circ\text{C}]$	uniform	Expert Judg.
Friction coeff. in subcritical condition of break connection	KfBrk	$[\pm 30 \text{ \%}]$	uniform	Expert Judg., [11]
Friction form loss coefficient at DVI outlet	KDvi	$[\pm 100 \text{ \%}]$	uniform	Expert Judg.
Initial water level in LGMS tanks	LLgms	$[\pm 10 \text{ cm}]$	uniform	[19]

Table 5.4: list of input uncertain parameters, range of variation and PDF type for UQ analysis.

safety output FOMs for the analysis. Both the parameters have a maximum safety limit, respectively of $1204 \text{ }^\circ\text{C}$ and 13.5 bar . A minimum of 92 calculations has been chosen in order to ensure $\gamma = 95\%$ and $\beta = 95\%$, according to the *one-sided Wilks formula* for $p = 2$ FOMs. 100 calculations have been launched to take into account possible code failures.

Results of UQ analysis

All the 100 calculations of the UQ have been completed without failures. The uncertainty of the DW pressure has been described in terms of uncertainty band by plotting the results of all the simulations in Fig. 5.32. The value of the reference simulation pressure is also reported in the figure in blue and the maximum calculated value in the UQ analysis (upper side) is plotted in red.

The safety condition of the DW pressure has been satisfied all along the sequence and the maximum value of pressure has been registered at around 1050 s and is of 11.7 bar . The maximum uncertainty of the FOM (of 1.2 bar), in terms of band width, is also reached at the same time. The same plot has been reported in Fig. 5.33 for the maximum cladding temperature. Also in this case, the safety criterion of the maximum cladding temperature is always satisfied all along the

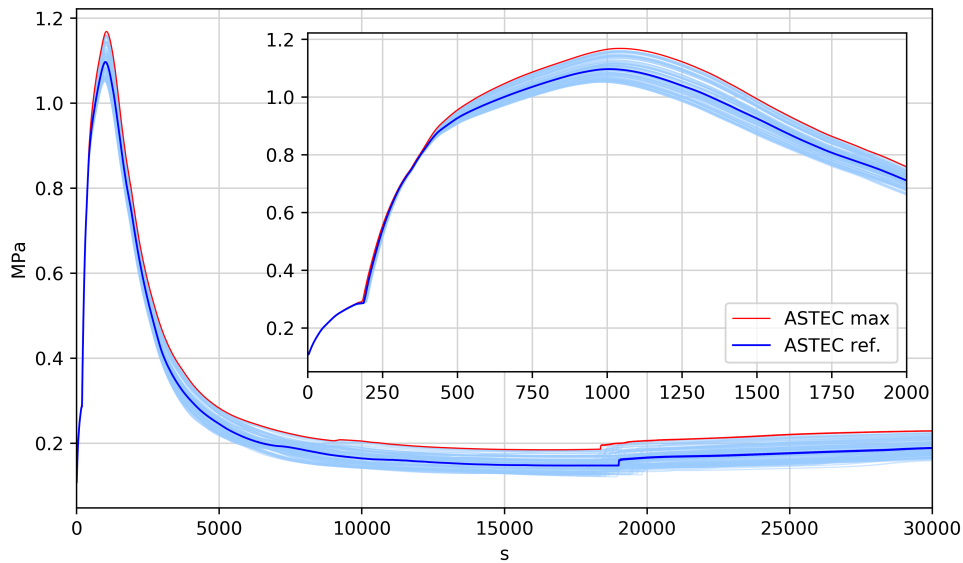


Figure 5.32: Dispersion band of DW pressure, against reference value data and upper bound.

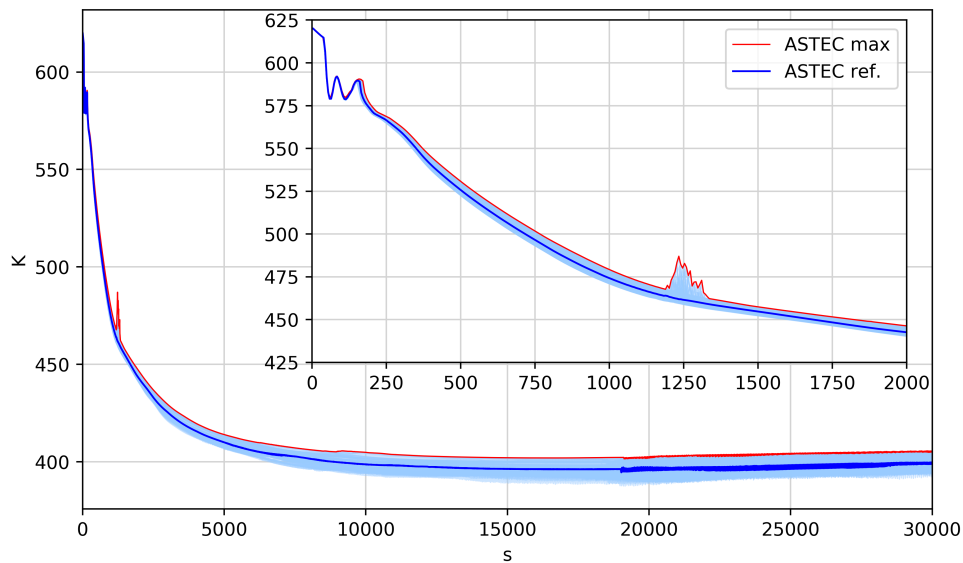


Figure 5.33: Dispersion band of maximum cladding temperature, against reference value and upper bound.

sequence. The maximum cladding temperature registered is the nominal condition temperature, at the onset of the transient ($t = 0$ s). Yet, differently from the reference calculation, whose temperature features a quasi-monotonic decreasing curve

(after the first oscillations), some of the UQ calculations are characterized by local temperature peaks at around 1250 s. The uncertainty band features the maximum width of 28 K at this point of the sequence. From a preliminary investigation, the local temperature peaks seem to be due to instabilities in the RPV natural circulation leading to a temporary decrease of the collapsed level in the core. This observation opens to future investigations of this phenomenon, whose study can be important in terms of safety of the system.

Results of sensitivity analysis

The sensitivity assessment of each input uncertain parameter with respect to the two FOMs has been developed using the Spearman, Pearson and Lasso regression coefficients. Fig. 5.34 and 5.35 report respectively the Spearman and the Lasso coefficients, related to the DW pressure. The plots also show the maximum calculated value of pressure in black dashed lines. The plot of Pearson coefficient has been omitted since in all cases its value is very close to Spearman.

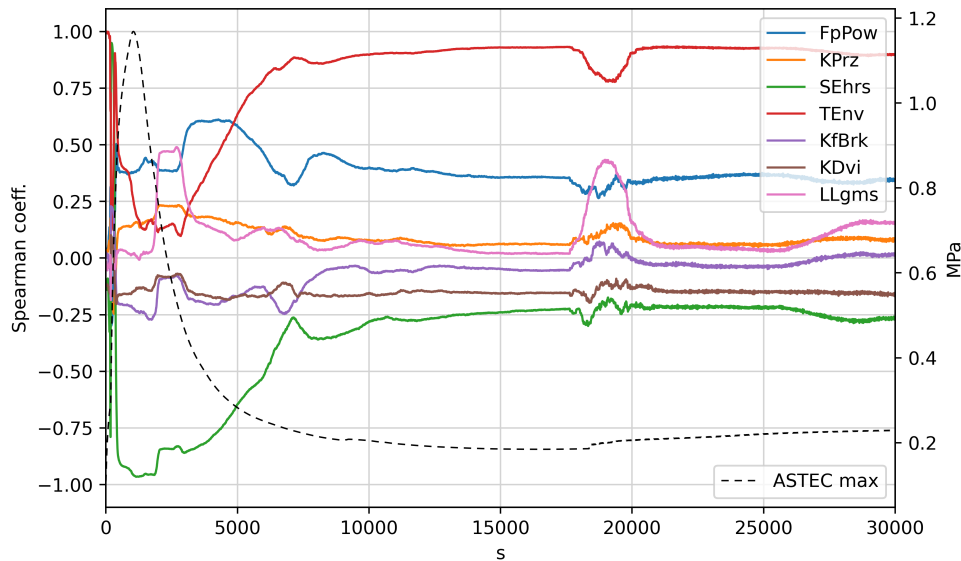


Figure 5.34: Spearman coefficients related to DW pressure, against maximum calculated DW pressure.

From the values of the sensitivity coefficients can be observed that, during the DW pressurization the input parameters dominating the FOM uncertainty are Fp - Pow , $Tend$ and $SEhrs$. During the DW depressurization, the sensitivity of the $TEnv$ parameter drops to low values, while there is an increase to moderate values of the

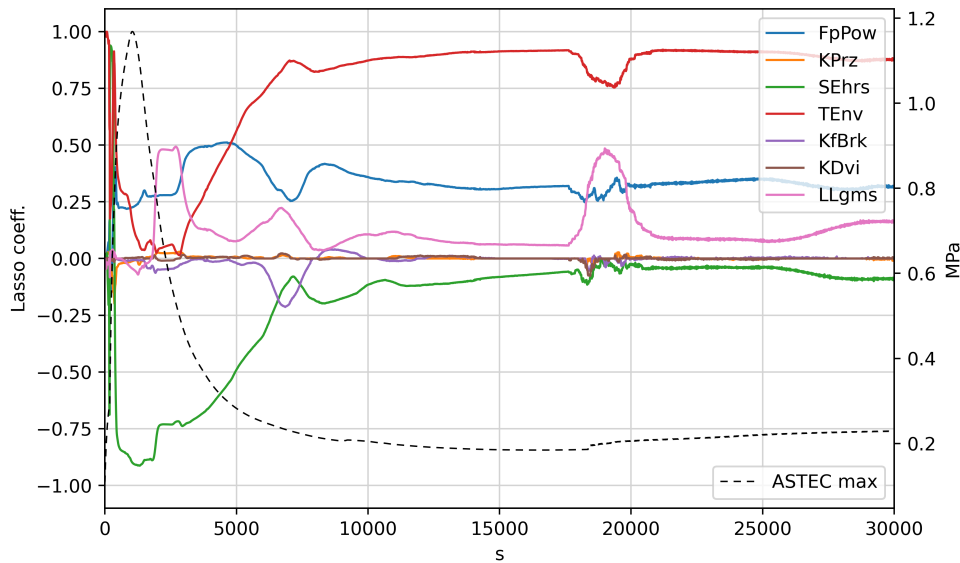


Figure 5.35: Lasso coefficients related to DW pressure, against maximum calculated DW pressure.

LLgms sensitivity. As one can expect, after 6000 s of transient, the parameter dominating the FOM uncertainty is the *TEnv* parameter, highlighting the dominant effect of the external temperature which contributes to the DW depressurization in the last part of the sequence by means of the DW walls heat-losses. It is important to underline that in terms of safety of the system, the most important sources of uncertainty can be considered those contributing to the uncertainty of the DW pressure at around 1050 s, characterized by the maximum value of pressure and the maximum band width (Fig. 5.34). It can be observed that the main source of uncertainty at this point is *SEhrs* parameter; though a moderate sensitivity is also captured with *TEnv* and *FpPower* parameters. A main outcome of this result is the central role played by the EHR system in the DW depressurization and, in particular, the main effect of the heat-transfer of EHR – RWST pipes.

In Fig. 5.36 and 5.37 are reported the same sensitivity coefficients for the maximum cladding temperature, against the maximum calculated value of cladding temperature (black dashed line).

At the very beginning of the sequence, during the initial temperature oscillations (0 – 250 s), the FOM is characterized by a significant sensitivity with the three parameters: *FpPow*, *SEhrs* and *TEnv*. During the following temperature decreasing phase (250 – 6000 s), the *FpPow* sensitivity remains moderate and positive; the *TEnv* sensitivity decreases to low values and the *LLgms* sensitivity increases to

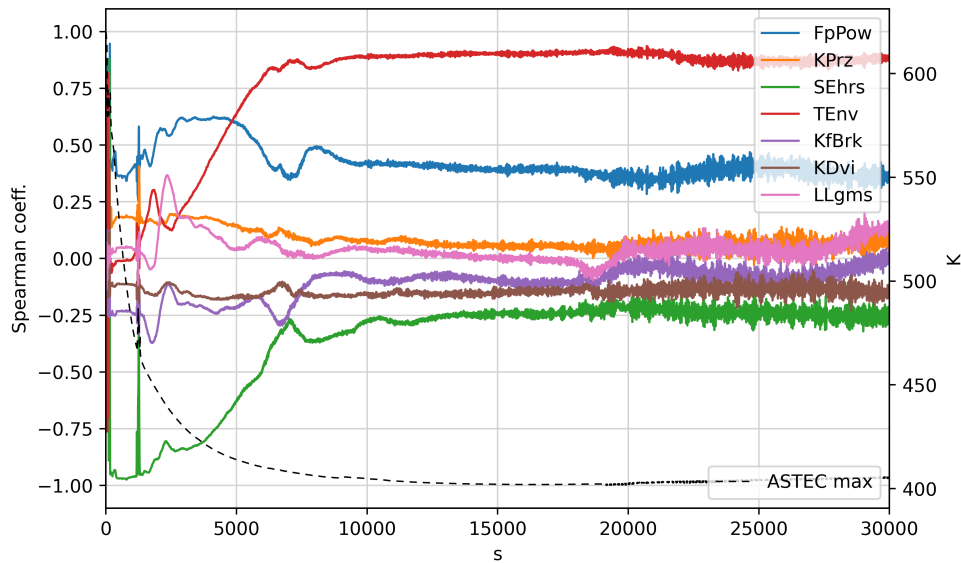


Figure 5.36: Spearman coefficients related to cladding maximum temperature, against maximum calculated DW pressure.

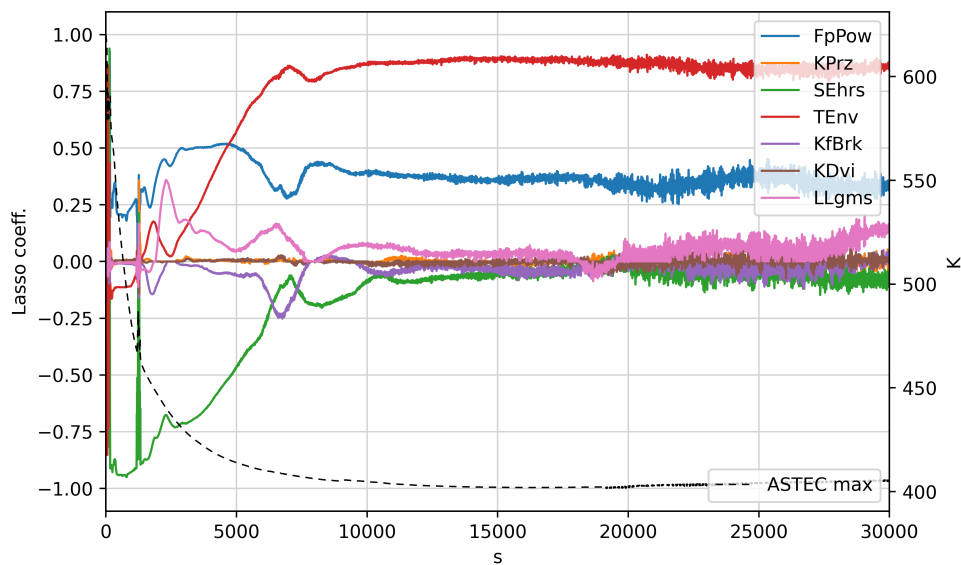


Figure 5.37: Lasso coefficients related to cladding maximum temperature, against maximum calculated DW pressure.

moderate negative values. As observed for the previous FOM, in the last part of the sequence (after 6000 s) the uncertainty is dominated by the $TEnv$ parameter.

In this case, it is important to point the attention to the time of the local

temperature peaks (around 1250 s) in which there is a local change in the sensitivity predicted: the sensitivity of $SEhrs$ drops to low values, while there is an increase in the sensitivities of $FpPower$ and of $KPrz$, that reach positive moderate values. This local change in the sensitivity parameters gives some insight regarding the natural-circulation phenomena leading to the local temperatures peaks. An important outcome is that these phenomena are not strongly influenced by the action of the EHRS system, as it is the rest of the temperature decreasing phase; but other features, such as the thermal-hydraulic coupling between DW and RPV may play an important role in this phenomenon.

5.4.2 Conclusions

The UQ analysis developed on the ASTEC v2.2.0 simulation of the IRIS DBA sequence (described in Section 4.3) has the objective to study the uncertainty propagation of 7 selected uncertainty sources mainly affecting the natural-driven phenomena driving the passive safety systems operation, in terms of safety condition of the reactor. The analysis also provides useful information on the robustness of the code model to the inputted uncertainties, and it is useful to further investigate the code capability to simulate the phenomena characterizing advanced SMR. With this regard, the first important outcome of the study is that all the 100 calculations performed feature the same expected phenomenological evolution of the DBA sequence, without major FOMs dispersion or bifurcations. In addition, the safety criteria for the two FOMs have been satisfied all along the transient with an adequate safety margin.

The highest value reached by the DW pressure along the transient matches the maximum spread of uncertainty at 1050 s; it follows that this timing should be considered the most challenging in terms of safety of this FOM. At this point, according to the adopted sensitivity coefficients, the major source of uncertainty influencing the DW pressure is the $SEhrs$ parameter (*Heat-transfer surface of EHRS – RWST pipes*). Besides highlighting a need to reduce the uncertainty inputted through this parameter, this result also underlines the central role played by the EHRS system in the limitation of dangerous containment pressurization. A moderate sensitivity is also captured with the $TEnv$ (*environment temperature and RWST initial temperature*) and $FpPower$ (*power of decay heat*) parameters at around this timing.

The maximum cladding temperature features a quasi-monotonic decreasing behavior in all the simulations; with the exception of local peaks, taking place at around 1250 s, only in a part of these. The maximum uncertainty spread of this FOM is registered at this point, in which the main contribution derives from the $FpPow$ (*power of decay heat*) and the $KPrz$ (*Friction form loss in PRZ surge line*) param-

eters. The observation of RPV natural circulation instability in some calculations, leading to the local peaks of temperature, is important to open to further studies on the origin of this phenomenon. Also for this FOM, another main source of uncertainty along the sequence is due to $TEnv$.

The result of this study also highlights the as taking simple but important plant precautions such as limiting the water temperature of RWST and the external temperature to the DW surface (external DW spray are also considered in the IRIS design but have not been simulated), would result in an increase of the inherent safety of this kind of reactor.

5.5 Application of the automatic Limit Surface Search Method

The increasing development of HPC along with the development of ML algorithms [17] are introducing new opportunities for nuclear safety analysis. These new technologies are allowing the efficient parallel run of several calculations and the automatic processing and inquiring of the resulting large datasets [27]. The present section presents some applications of the *Limit Surface (LS) search method* to ASTEC code analysis. This automatic method relies on the use of a ML algorithm for the generation of a surrogate model of the code simulation. The LS scheme is implemented in the RAVEN code and has been used thanks to the RAVEN – ASTEC coupling presented in Section 5.1.4, with the elaboration of a specific XML input file to RAVEN [12].

The LS search is an advanced method that can be used as support to UQ and safety analysis, and the two examples provided in this Section are aimed at showing two possible different applications. The first case deals with a phenomenological change between the simulations of a UQ (as often happens in the case of SA), and the method is used to find the input conditions leading to different simulation phenomenology. In the second example, the method is applied for the estimation of the input values leading to the safe and the unsafe conditions of the system.

5.5.1 Limit Surface Search

Theory of Limit Surface

As done in Section 5.1.2, let's consider again the dynamic system (representing the code) described by the deterministic non-linear transformation $L(t)$ of the input N -dimensions input aleatory vector \vec{x} ; with X its domain (set of all possible values

of \vec{x} in the N-dimensions phase space):

$$\vec{y} = L(t)\vec{x} . \quad (5.20)$$

We introduce the *goal function* C to be a binary function that, based on the response of the system, can assume the value 0 (e.g., system success) or 1 (e.g., system failure)

$$C(\vec{y}) = C(\vec{x}, t) . \quad (5.21)$$

Without loss of generality, let's assume that C does not depend on time, e.g.

$$C(\vec{y}) = C(\vec{x}) = \int_{t_0}^{t_{end}} C(\vec{x}, t) . \quad (5.22)$$

It is possible to identify the region of the input domain X leading to a specific outcome of the goal function. For example, we can define the failure region X_F as the subdomain of X where $C = 1$, and the success region X_C as its complementary:

$$X_F = \{\forall \vec{x} \mid C(\vec{x}) = 1\} ; X_C = \{\forall \vec{x} \mid C(\vec{x}) = 0\} , \quad (5.23)$$

where $X_F \cup X_C = X$. We call LS the boundary surface in the N-D space, separating X_F from X_C . If $g(\vec{x})$ is the density function of the random input vector \vec{x} , the failure probability of the system \mathbb{P}_F will be:

$$\mathbb{P}_F = \int_X C(\vec{x})g(\vec{x})d\vec{x} = \int_{X_F+X_C} C(\vec{x})g(\vec{x})d\vec{x} = \int_{X_F} g(\vec{x})d\vec{x} . \quad (5.24)$$

In other words, the system failure probability is equivalent to the probability of the system being in the input subdomain that leads to a failure pattern. This probability is equal to the probability-weighted hyper-volume that is bounded by the LS.

Limit Surface Search Algorithm

Once defined the concept of LS through a binary goal function C , we can move to the description of the algorithm used by RAVEN for the problem of LS identification. Ideally, to identify the real location of the LS, the evaluation of the system response is needed to be known in the full input domain of uncertainty X ; which would mean an infinite number of calculations given by all the combinations of input parameters. Obviously, this is not a feasible approach, and a more reasonable approximation could be to locate the LS on a Cartesian N-D grid defined in the input uncertain domain. With this approach, the location of the LS is not exactly determined but

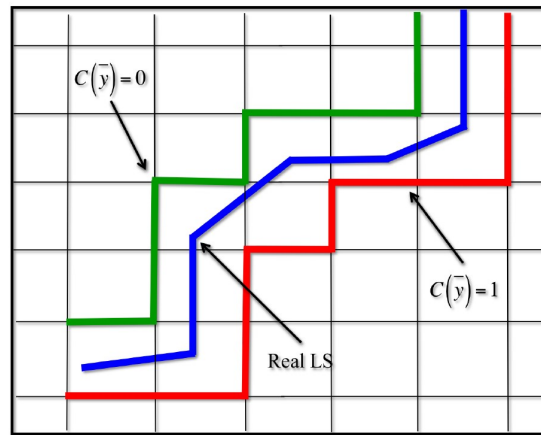


Figure 5.38: Transition of the goal function C on a 2-D Cartesian grid in the input domain [12].

rather bounded: it determines the set of grid nodes between which the transition 0 - 1 of the goal function takes place [12], Fig 5.38.

Even with this approximation, the identification of the LS location would require to perform a code computation for each node in the N-D grid. That, for a good grid resolution and for input dimension N higher than 2, would mean a too high computational effort. For this reason, the process needs to be accelerated by means of a predicting method that can be set up thanks to a *supervised ML algorithm* of type classifier (taking only integer output, e.g. 0 - 1).

This approach is commonly called to be an active learning process and it is based on the training of a Reduced Order Model (ROM) of the code learning to predict the outcome of the goal function $C(\vec{x})$ by using the values of the already performed calculations as training set. In the LS research algorithm, the prediction of the trained ROM is combined with criteria to choose the next nodes in the N-D grid that needs to be explored using the code in order to efficiently improve the knowledge of LS location. The iterative process is repeated until the prediction of the ML algorithm does not improve by further increasing the training set (under a particular metric). In more detail, the iterative algorithm can be summarized as in Fig. 5.39, according to [12].

With respect to the scheme in Fig. 5.39, there is an additional requirement to end the iterative process: the convergence has to be reached a certain number (user selected) of consecutive iterations. The reason for this choice is determined by the attempt to mitigate the effect of the creation of non-linear bias in the search; e.g. the algorithm might focus too much on a certain region of the LS while putting too few points in other zones and, hence, completely hiding undiscovered parts of the

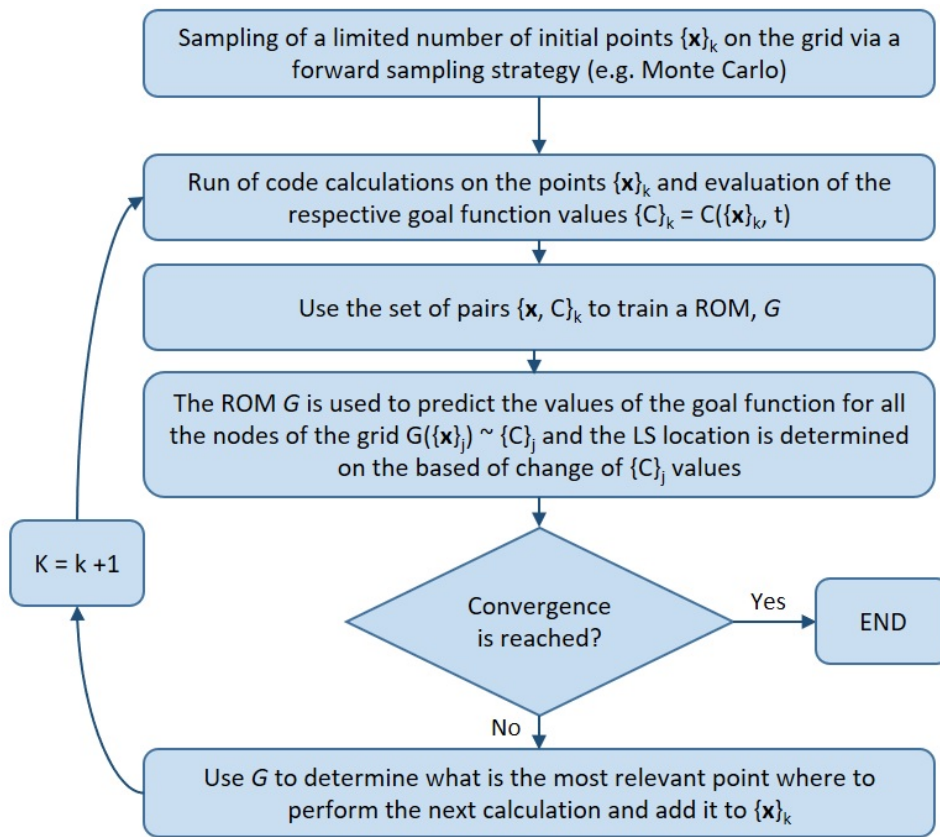


Figure 5.39: Iterative scheme of the LS Search algorithm of RAVEN.

LS. Regarding the strategy for the choice of the following nodes to be investigated at the end of an iteration, the method employs a metric based on the distance between the performed evaluations and the predicted LS (at the current iteration). In particular, the points on the LS are ranked on the basis of the distance from the closest explored point (the larger is the distance the higher is the score for the candidate point), and based on the persistence (the larger is the number of time the prediction of the goal function for that point has changed, the higher is the score). This approach created a queue of candidate points that can be used in the case of multiple calculations performed in parallel.

The ML algorithm that will be used in the following application of the LS Search Method is a *Support Vector Machine* (SVM) algorithm for binary classification, with a “rbf” (exponential) type kernel. The SVM is a robust supervised ML method that aims at determining the optimal separation hyperplane between data sets having different labels and it shows the best performance in binary classification problems. The ML classification method implemented in RAVEN is based on the Python

Scikit-learn library [28]. More information regarding SVM can be found in [29][17]. Yet, many other supervised ML algorithms for binary classification can be used in the present method to train the code ROM (s.a. Decision Trees, Neighbor class). Furthermore, the RAVEN algorithm for LS search improves the loop presented in Fig. 5.39 by adding the possibility to accelerate the process by means of an *adaptive refined multi-grid* approach [12].

5.5.2 LS search of change in SA degradation phenomenology

Motivations

The LS research method can be very useful as support to a UQ analysis for several purposes. In Section 5.1.2, it has been observed as a change in the phenomenology simulated may occur across different calculations performed for a UQ analysis. In Section 5.3 we have called this issue an *edge-effect phenomenon* and discussed that it can frequently occur in UQ applications to SA simulations. With regard to this point, it has been also underlined that, according to [2], the assumptions of the *Wilks formula* are not respected for those FOMs showing bifurcations (*chaotic behavior*), e.g. for the examples shown in Fig. 5.30 and 5.31.

Concerning the phenomenological bifurcation encountered in the UQ analysis of the ASTEC simulation of QUENCH-6 experiment (represented in Fig. 5.30), a proposed solution could be to split a priori the simulations that feature a cladding loss of integrity to those that feature always intact structures. In this way, it would be possible to apply a UQ analysis only to one of the two cases, by investigating only the input sub-domain leading to the phenomenon of interest. In other words, we may want to find the conditions (in terms of the value of input uncertain parameters) for which the simulations evolve to one of the two phenomenologies and to be able to separate these from the other phenomenology, that it turns out to be a LS search problem.

Set up of LS Search problem

With respect to the LS search method described in the previous section, in the present application it is possible to consider as binary goal function C the final state of cladding: we set $C = 1$ for intact cladding at calculation end; $C = 0$ for failed cladding at calculation end. As described, the LS method can be applied to problems with multiple input parameters; yet, in order to further reduce the computational effort, we will apply the method limiting the number of input parameters

to the most relevant to our goal function. With this purpose, the results of the 200 calculations performed for the UQ analysis on the QUENCH test-6 simulation have been used to calculate the Spearman correlation coefficients between the chosen goal function and the 23 input parameters. The coefficients are reported in Fig 5.40.

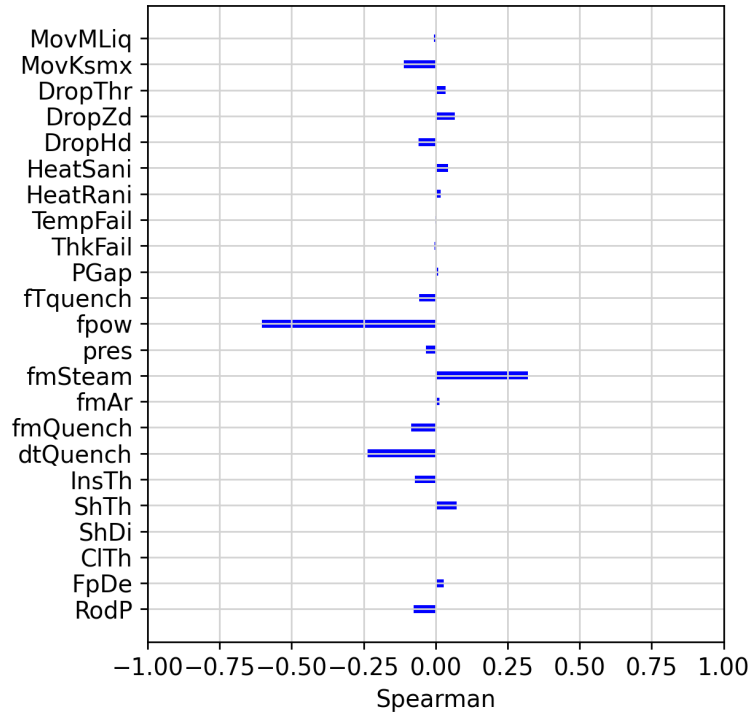


Figure 5.40: Spearman coefficients between the goal function C and the 23 input parameters to the UQ analysis.

The Spearman coefficients capture a relevant correlation (negative) with the *electric power* parameter; a relevant correlation (positive) with the *steam mass flow rate*; and a moderate-low correlation (negative) with the *timing of quench water injection*. The correlation with the other input uncertain parameters is low or negligible. As a result of this analysis, only the two main input uncertain parameters have been chosen to be used as input to the present LS search problem. Therefore, the input domain of the LS search has been considered to be the 2-D phase space generated by the domains of the two input parameters: *electric power* and *steam mass flow rate*, described by PDFs type and ranges reported in Tables 5.2 and 5.3.

The LS search method described in the previous section has been applied by using a SVM algorithm for the trained ROM; the number of parallel calculations

is 10 and the number of consecutive converging loops to determine the end of the search process has been selected to be 8. The *adaptive multi-grid* approach for the process acceleration has been activated.

Results of LS Search

The LS search algorithm stops (8 consecutive converging loops) at the total number of 180 calculations. Fig. 5.41 shows the results of the LS search problem: each point is a calculation in the 2-D input domain and the relative value of the output goal function is expressed with colors (purple for failed and yellow for intact cladding). The values of the input parameters on the two axes have been normalized on their reference values.

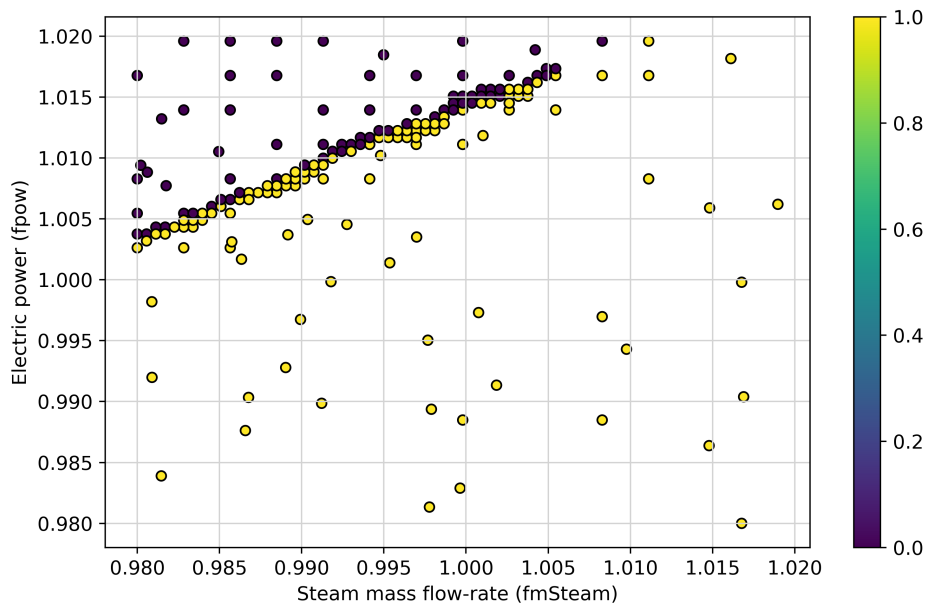


Figure 5.41: Calculations executed in the LS search in terms of input values (normalized) and corresponding goal function value (yellow for intact and purple for failed cladding).

It can be observed that the plot delimitates a line (LS) dividing the input domain in two zones for the 2 possible values of the goal function. The LS can be approximated as a straight line crossing the x -axis in at about 1.01 and the y -axis at about 1.003. Calculations whose value of the two input parameters is located above the LS will result in the failure of cladding; calculations having input value located below the LS will have final intact structures. Therefore, it results that for Steam mass flow rater value (normalized) higher than about 1.01, the cladding will

always be intact, no matter the value assumed by the fuel electric power (within its input range).

Certainly, for points too close to the LS the goal function result will not be known with good confidence. The higher the resolution of the LS is needed and the higher the grid refinement and the final number of calculations will be. Without doubts the implemented algorithm allows to have a very good estimation of the LS position by using a limited number of calculations; the same number of calculations within a random sampling approach will result in a very bad delimitation of the LS.

In Fig. 5.42 the same plot has been reported, where the color of the points in this case stands for the order of execution of the calculation in the LS search. Fig.

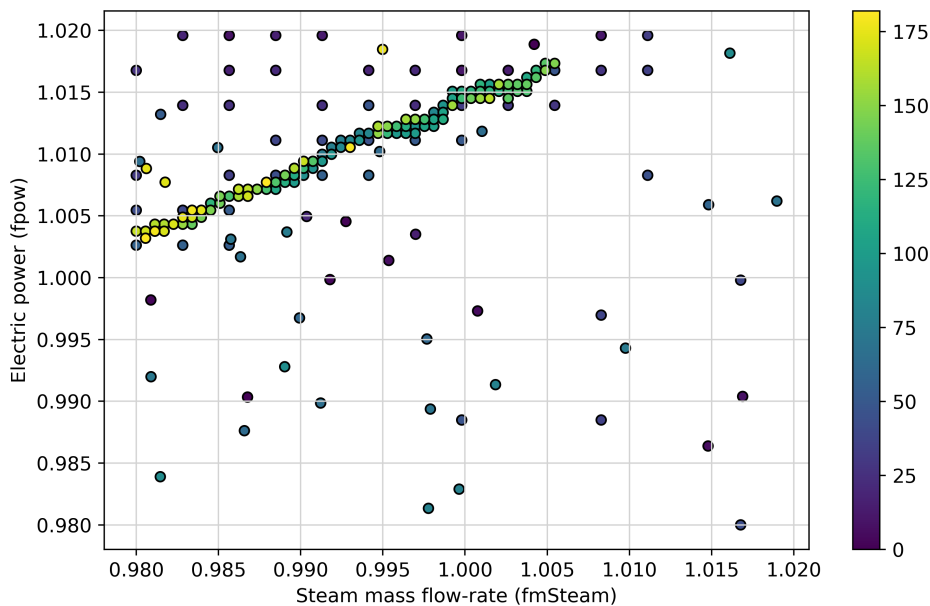


Figure 5.42: Calculations executed in the LS search in terms of input values (normalized) and corresponding order of execution in a color scale.

5.42 shows as the first calculations (dark color) are randomly distributed in the input domain; while advancing, the following calculations converge on the LS line.

Conclusion and remarks

The work described wants to highlight as the LS Search method can be a particularly useful tool in support of UQ analyses involving the simulation of core degradation phenomena and evolving to a phenomenological bifurcation. Accordingly, in case the statistics of *Wilks formula* do not hold across the entire input domain due to

the bifurcation of a FOM, the method can be used to identify the subsets of the input domain evolving to different phenomena. The proposed solution deals with the identification of the different input sub-domains, by drawing the LS surface of separation with the LS search method. In this way, the two input domains can be used in separated UQ analyses.

Besides this possibility, the information obtained by the LS line, in terms of combinations of the two input parameters resulting in the failure or not of cladding structures, is a very important additional result to be included in the outcomes of the UQ analysis conducted on the ASTEC simulation of QUENCH test-6. The approximated knowledge of the LS line allows to estimate the probability of components failure (or not-failure) by using equation (5.24).

5.5.3 LS Search of safety conditions

Another more common application of the LS search method is the identification of the boundary between the safe and the unsafe conditions of a system. The safety conditions of NPP during an accidental transient is usually identified by a physical output parameter describing the state of the reactor (e.g. cladding maximum temperature, water level in core, containment pressure) having either an upper or a lower safety limit. The LS boundary has to be identified in the input domain of variation of N input parameters (e.g. input uncertain parameters in case the of a UQ analysis), and the results of the research will be the surface dividing the N -D input domain into a safe zone (leading to a safety result) and an unsafe zone (leading to unsafe conditions).

The aim of this section is to provide an example of this LS application: with respect to the UQ analysis presented in Section 5.4, we can set a safety limit to the containment pressure of the IRIS reactor and look for the input safety conditions respecting this limit along the DBA sequence.

Set up of LS Search problem

Considering the UQ study on the DBA simulation of ASTEC on the generic IRIS reactor (described in Section 5.4), the goal function of the LS search problem can be defined by considering the output DW pressure as safety parameter. As discussed, the design pressure of the IRIS containment is 13.5 bar and this value is never reached in the UQ analysis (Fig. 5.32). For this reason, in order to apply the LS search method, it is necessary to assume a more restrictive safety condition to be respected by the DW pressure.

As an example, a safety margin of 2.5 bar from the DW design pressure has

been chosen and, as a consequence, the new safety limit to be respected is of 11 bar, and it falls inside the uncertainty band obtained in the UQ analysis (Fig. 5.43). With this assumption, we can set up a binary goal function $C(P_{max})$ based on the maximum value of DW pressure registered during the simulation, i.e. $C = 1$ for $P_{max} > 11$ bar; $C = 0$ for $P_{max} < 11$ bar.

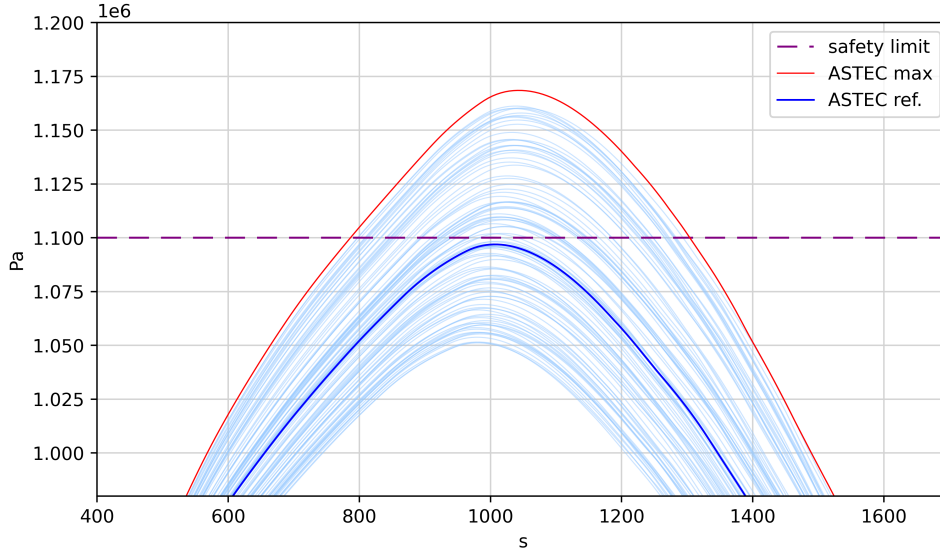


Figure 5.43: Maximum values of DW pressure dispersion obtained in the UQ analysis, and new safety limit of 11 bar.

In the same way as done for the previous case, the input parameters considered can be chosen among the main input uncertain parameters influencing the value of the goal function, i.e. of the maximum DW pressure. From the results of the sensitivity analysis conducted in Section 5.4 (Fig. 5.34 and 5.35), we have observed that the main parameters influencing the DW pressure at about 1050 s (maximum pressure) are the *decay heat power factor* ($FpPower$) and the *heat-transfer surface of EHRS – RWST exchanger* ($SEhrs$). In the present problem, these 2 parameters within their uncertain domains (in terms of PDF type and range) have been chosen as input to the LS search method.

Also in this case, the algorithm chosen to train a ROM is a SVM; the number of parallel calculations is 10 and the number of consecutive converging loops to determine the end of the search process has been selected to be 8. The *adaptive multi-grid* approach for the process acceleration has been activated. In addition, it has to be underlined that, for the present application, it is not needed to carry out the DBA calculations of ASTEC until the final time of 30000 s. Yet, it is only

necessary to get through the maximum pressure time of 1050 s, with a consequent large reduction of computational cost.

Results of LS Search

The LS search algorithm stops (8 consecutive converging loops) at 230 simulations. In Fig. 5.44 it is reported the results of the LS search problem in terms of calculations executed in the 2-D input domain. The maximum DP pressure reached in each simulation is reported on a scale of color.

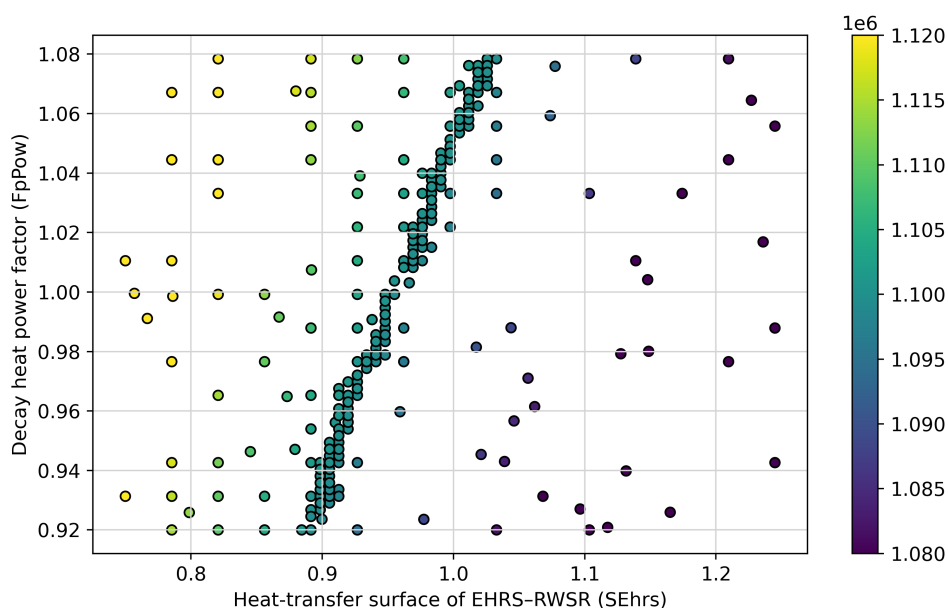


Figure 5.44: Calculations executed in the LS search in terms of input values (normalized) and corresponding value of output P_{max} in a color scale.

The diagonal line, drawn down by the algorithm at convergence, represents the combination of the two input variables where the maximum calculated DW pressure along the sequence is $P_{max} \sim 11$ bar. On the left of the line we have input values for that $P_{max} > 11$ bar (unsafe conditions); on the right of the line we have input values for that $P_{max} < 11$ bar (safe conditions). In agreement with the sensitivity analysis in Section 5.4 (Fig. 5.34 and 5.35), the slope of the LS line in Fig. 5.44 proves that the output FOM is mainly influenced by the input value of the $SEhrs$ parameter. Accordingly, for $SEhrs < 0.89$ we have $P_{max} > 11$ bar for any value of $FpPow$; for $SEhrs > 1.03$ we have $P_{max} < 11$ bar for any value of $FpPow$.

The convergence evolution of the algorithm is well described by the scatter-plot in Fig. 5.45, reporting the maximum DW pressure on the y -axis and the submission

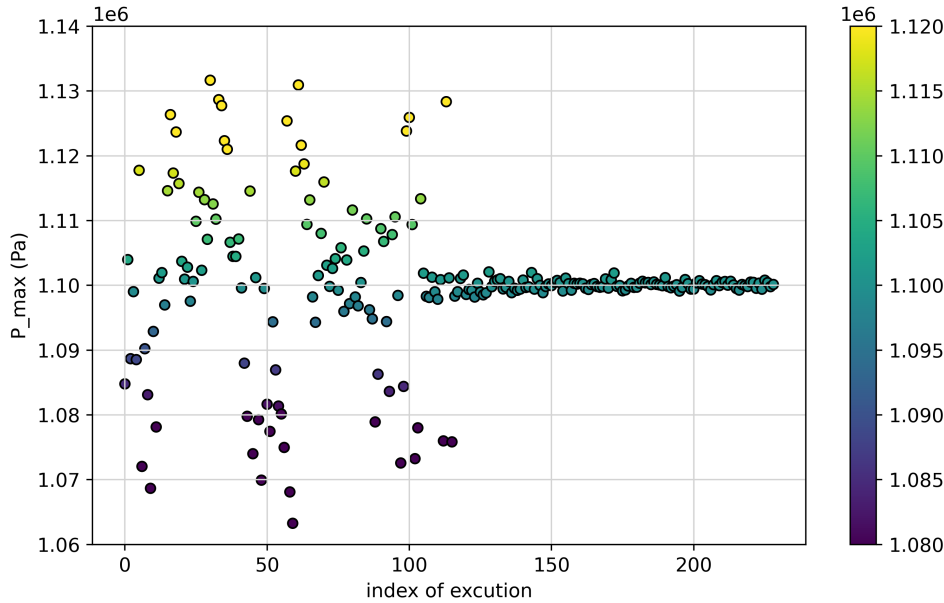


Figure 5.45: Calculations executed in the LS search in terms of submission index and output P_{max} .

number of the calculation on the x -axis. It can be observed that the algorithm has first to find the location of the limit pressure line and then to persist on it in order to draw down the whole line in the input domain.

Conclusions and remarks

The work described has the objective to underline as, in case of UQ analysis resulting in the crossing of the safety limit by the output uncertainty band, the LS search method can be used to identify the boundary between safe and unsafe conditions in the input domain. In this case, as a result of the LS search, important details are provided on where and how to improve the input parameter knowledge in order to reduce the safety margin and avoid exceeding the safety limit. Also in this case, it is clear that the location of the LS line is known within good confidence and that in order to improve the knowledge of its location more calculations are needed. It is also clear that with a random sampling of the same number of calculations the confidence with which the LS line is known would be much poorer. The approximated knowledge of the LS line in the input domain allows to estimate the probability of the system to be in the safe side (or in the unsafe side) by using equation (5.24).

Bibliography

- [1] *Status and Evaluation of Severe Accident Simulation Codes for Water Cooled Reactors*, ser. IAEA-TECDOC 1872. Vienna: International Atomic Energy Agency (IAEA), 2019, ISBN: 978-92-0-102919-5.
- [2] A. Guba, M. Makai, and L. Pál, “Statistical aspects of best estimate method—i,” *Reliability engineering & system safety*, vol. 80, no. 3, pp. 217–232, 2003.
- [3] H. Glaeser, “Grs method for uncertainty and sensitivity evaluation of code results and applications,” *Science and Technology of Nuclear Installations*, vol. 2008, 2008.
- [4] F. S. D’Auria, H. Glaeser, S. Lee, J. Miák, M. Modro, and R. Schultz, *Best Estimate Safety Analysis for Nuclear Power Plants: Uncertainty Evaluation. IAEA Safety Report Series*. International Atomic Energy Agency (IAEA), 2008, vol. 52.
- [5] <https://musa-h2020.eu/>.
- [6] <https://www.iaea.org/projects/crp/i31033>.
- [7] A. Bersano, F. Mascari, M. T. Porfiri, P. Maccari, and C. Bertani, “Ingress of coolant event simulation with trace code with accuracy evaluation and coupled dakota uncertainty analysis,” *Fusion Engineering and Design*, vol. 159, p. 111 944, 2020.
- [8] B. Foad, M. Hassan, and T. Takeda, “Uncertainty & sensitivity analyses for loca simulation of phebus experiment fpt-1 using a modified sunset code,” *Annals of Nuclear Energy*, vol. 144, p. 107 575, 2020.
- [9] M. Perez, F. Reventos, L. Batet, *et al.*, “Uncertainty and sensitivity analysis of a LBLOCA in a PWR Nuclear Power Plant: Results of the Phase V of the BEMUSE programme,” *Nuclear Engineering and Design*, vol. 241, no. 10, pp. 4206–4222, 2011.

-
- [10] M. Stephens, B. Goodwin, and T. Andres, “Deriving parameter probability density functions,” *Reliability Engineering & System Safety*, vol. 42, no. 2-3, pp. 271–291, 1993.
- [11] G. Roma, F. Di Maio, A. Bersano, *et al.*, “A bayesian framework of inverse uncertainty quantification with principal component analysis and kriging for the reliability analysis of passive safety systems,” *Nuclear Engineering and Design*, vol. 379, p. 111 230, 2021.
- [12] A. Alfonsi, C. Rabiti, D. Mandelli, *et al.*, “RAVEN theory manual,” Idaho National Lab.(INL), Idaho Falls, ID (United States), INL/EXT-16-38178, April 2020.
- [13] D. H. Sattinger, *Group theoretic methods in bifurcation theory*. Springer, 2006, vol. 762.
- [14] S. S. Wilks, *Mathematical statistics*, 1962.
- [15] S. S. Wilks, “Determination of sample sizes for setting tolerance limits,” *The Annals of Mathematical Statistics*, vol. 12, no. 1, pp. 91–96, 1941.
- [16] G. L. Shevlyakov and H. Oja, *Robust correlation: Theory and applications*. John Wiley & Sons, 2016, vol. 3.
- [17] I. Goodfellow, Y. Bengio, and A. Courville, *Deep learning*. MIT press, 2016.
- [18] F. Alcaro, A. Bersano, C. Bertani, and F. Mascari, “BEPU analysis of a passive decay heat removal system with RELAP5/MOD3.3 and RELAP5-3D,” *Progress in Nuclear Energy*, vol. 136, p. 103 724, 2021.
- [19] C. Rabiti, A. Alfonsi, J. J. Cogliati, and D. Mandelli, “RAVEN User Manual,” Idaho National Lab.(INL), Idaho Falls, ID (United States), INL/EXT-15-34123, April 2017.
- [20] P. Maccari, M. Massone, A. Bersano, F. Mascari, A. Cervone, and S. Manservigi, “Astec-raven coupling for uncertainty analysis of an ingress of coolant event in fusion plants,” *Fusion Engineering and Design*, vol. 169, p. 112 442, 2021.
- [21] F. Iannone, F. Ambrosino, G. Bracco, *et al.*, “CRESCO ENEA HPC clusters: a working example of a multifabric GPFS Spectrum Scale layout,” in *2019 International Conference on High Performance Computing & Simulation (HPCS)*, IEEE, 2019, pp. 1051–1052. DOI: [10.1109/HPCS48598.2019.9188135](https://doi.org/10.1109/HPCS48598.2019.9188135).
- [22] L. Sepold, W. Hering, C. Homann, *et al.*, “Experimental and computational results of the QUENCH-06 test (OECD ISP-45),” Forschungszentrum Karlsruhe GmbH Technik und Umwelt (Germany), FZKA-6664, 2004.

- [23] J Stuckert, A. Boldyrev, and A Miassoedov, “Experimental and computational results of the QUENCH-08 experiment (reference to QUENCH-07),” Forschungszentrum Karlsruhe GmbH Technik und Umwelt (Germany), FZKA-6970, 2005.
- [24] F. Gabrielli and V. Sánchez-Espinoza, “Uncertainty and Sensitivity Analysis by means of ASTEC/URANIE Platform of the QUENCH-08 Experiment,” in *Proceedings of the 24th Int. QUENCH Workshop*, Forschungszentrum Karlsruhe GmbH Technik und Umwelt (Germany), November 13-15, 2018. DOI: <https://doi.org/10.5445/IR/1000088229>.
- [25] A. Prošek, M. Leskovar, and B. Mavko, “Quantitative assessment with improved fast fourier transform based method by signal mirroring,” *Nuclear engineering and design*, vol. 238, no. 10, pp. 2668–2677, 2008.
- [26] A. Guglielmelli, S. Ederli, F. Mascari, F. Rocchi, and P. Maccari, “Coupling of ASTEC 2.1.1.6 and RASCAL 4.3 Codes to Evaluate the Source Term and the radiological Consequences of a Loss-of-Cooling Accident at a Spent Fuel Pool,” in *Proceedings of 29th International Conference Nuclear Energy for New Europe - NENE 2020*, Portoroz, Slovenia, 2020.
- [27] C Parisi, A Alfonsi, D Mandelli, and C Rabiti, “AUTOMATIC LIMIT SURFACE SEARCH FOR PWR TRANSIENTS BY RELAP5-3D/RAVEN CODES,” Idaho National Lab.(INL), Idaho Falls, ID (United States), INL/CON-18-45361-Rev000, 2018.
- [28] <https://scikit-learn.org/stable/>.
- [29] W. S. Noble, “What is a support vector machine?” *Nature biotechnology*, vol. 24, no. 12, pp. 1565–1567, 2006.

CHAPTER 6

Conclusions

In the framework of the NUGENIA TA-2 ASCOM collaborative project, an application of ASTEC code to advanced SMR has been developed. It concerns the development of an ASTEC model of an integral PWR facing passive safety systems. The reactor chosen is a generic design based on the IRIS advanced features. The generic SMR model, developed with the code ASTEC V2, has to be able to assess the specific natural-driven thermal-hydraulic phenomena of advanced integral SMR and of their passive safety systems. In addition, the model should contain all the ASTEC features needed to simulate the development of a core-melt accident. The activity has been developed in the framework of the present Ph.D. and can be considered a first step in the code assessment for advanced SMR design.

The description of the ASTEC nodalization approach used in the realization of the generic IRIS input-deck has been treated in Chapter 4. It underlines the limitations found in the code modules, describes the solutions and the assumptions adopted; therefore, providing some code-user guidelines to be followed for the modeling of passive systems and facing with integral SMR.

The main outcome of the DBA sequence simulation (2-in break of a DVI) is that, with the considered nodalization approach, the code can reproduce the expected thermal-hydraulic phenomena involved in the complex passive mitigation strategy adopted by the IRIS design. Moreover, the work has been important to underline that one of the main challenges in modeling integral passive SMR with a modular code as ASTEC is the need to ensure the tight thermal-hydraulic coupling between all the reactor systems (RPV, containment, safety systems) on which the passive mitigation strategy is based.

To improve the current generic IRIS model, some new modeling features already available in the new version of ASTEC (v2.2.0), such as the possibility to accurately

estimate the heat transfer between RPV and RC, should be implemented in the input-deck. The study also suggests the development of some new code modeling features, such as specific heat-transfer models for helical-coil SG. The validation of thermal-hydraulic modules of ASTEC against experimental facilities and tests designed to characterize phenomena typical of passive safety systems and integral SMRs (e.g. PERSEO, OSU-MASLWR DOE tests) is also a crucial step to be faced by the code.

The following simulation of the 4 BDBAs explores the applicability of SA codes to SMR beyond design conditions and proves the capability of the IRIS generic model to be used in SA. By the comparison of the 4 simulations results, the first main outcome is the different weight of each passive safety system in the success of the mitigation strategy: the two passive injection systems (LGMS, EBTSs) play a secondary role in the accident mitigation compared to the EHRS and the ADS, whose intervention is crucial for the success of the accident mitigation. The main role played by the ADS-st2 in the core refill through the RC water has been also highlighted. In the two SA scenarios, different configurations of IVMR with different features have been observed; in both cases, the IVMR strategy should be proved feasible. These results can be relevant for the planning of better management mitigation strategies and passive safety systems development. In addition, the new phenomenology deriving from the coupling of SMRs peculiarity with core degradation evolution needs to be thoroughly investigated in future research programs and experimental activities.

The evaluation of the uncertainty affecting the result of simulation codes is an important task, necessary to quantify the confidence that should be attributed to the simulation result. In Chapter 5 of the present work of thesis, the probabilistic *method of input uncertainty propagation* has been described along with the implementation of the method through the RAVEN - ASTEC coupling for UQ analysis on ASTEC code simulations.

In the framework of IAEA CRP - I31033, a BEPU analysis of the ASTEC simulation of the QUENCH test-6 experiment has been developed. The comprehensive study is aimed at evaluating the code capability to simulate the main phenomena involved in the experimental transient and at characterizing the uncertainty affecting the related code models. The first outcome of the benchmark has been the characterization of the methodology adopted: the direct comparison of the simulation against the experimental data is the first step for a qualitative and quantitative evaluation of the code prediction accuracy; the following UQ analysis completes the study by providing information regarding the uncertainty affecting the code prediction, estimate the contribution of each input parameters.

The direct comparison of the reference simulation against the experimental data has shown good prediction of the phenomena governing the *pre-oxidation* and the *heating-up PhWs* of the sequence. The accuracy in the prediction of the *quenching PhW* can be classified as good. Some discrepancy has been observed in the prediction of the heat exchange during quenching. An important qualitative observation is that ASTEC predicts the local melting of materials around the most heated-up level without a loss of integrity of the components and this is consistent with the post-experiment analysis of the bundle.

Regarding the UQ analysis, the spread of the uncertainty in H_2 production rate, at the *Zr* oxidation acceleration, can be expected considering the non-linearity of the phenomenon. Some different behavior characterizes the uncertainty evolution of the central rod temperature (at 950 mm level), which suffers from a minor uncertainty increase, mainly during quenching. A crucial reason leading to a general uncertainty spread is the fact that the reference simulation (as well as the experiment) is on the edge of changing in a core degradation phenomenology. As a consequence, phenomenological bifurcations take place in the UQ study and part of the 200 simulations incurs in the failure of *Zr* structures, leading to further oxidation.

The UQ study on the QUENCH-6 simulation represents an important step in the exploration of the UQ method applicability to SA simulations. It highlighted two aspects mainly affecting UQ application to SA: *non-linear law phenomena* have the main effect to increase the output uncertainty; *edge-effect phenomena* may cause a bifurcation of the FOMs, increasing uncertainty and creating a chaotic behavior of the results. In addition, the main challenges that might be faced in the application of the UQ method in a complete SA sequence at the plant level have been discussed.

The UQ analysis developed on the ASTEC v2.2.0 simulation of the IRIS DBA sequence has the purpose to study the uncertainty propagation of 7 selected uncertainty sources mainly affecting the natural-driven phenomena characterizing the passive safety systems operation. The first outcome of the study is that all the calculations performed feature the same expected phenomenological evolution of the DBA sequence, without major FOMs dispersion or bifurcations. In addition, the safety criteria for the two FOMs have been satisfied all along with the transient. This result underlines the robustness of the ASTEC V2.2 code and of the reactor model developed. The highest value reached by the DW pressure along the transient matches its maximum spread of uncertainty. At this timing, considered the most challenging in terms of safety of this FOM, the major source of uncertainty is the *Heat-transfer surface of EHRS – RWST pipes*. Besides highlighting a need to reduce the uncertainty deriving from this parameter, this result underlines the central role played by the EHRS system in the limitation of dangerous containment

pressurization. The maximum cladding temperature features a quasi-monotonic decreasing behavior except for local peaks only in a part of the 100 simulations. At this point, the main uncertainty contribution derives from the power of decay heat and the Friction form loss in PRZ surge line parameters. The observation of RPV natural circulation instability in some calculations, leading to the local peaks of temperature, is important to open to further studies on the origin of this phenomenon. The study has been also important to highlight as taking simple plant precautions, such as limiting the water temperature of RWST or the external temperature to the DW, would result in an increase of the inherent safety of this kind of the reactor.

In the last Section of Chapter 5, it has been presented an advanced methodology as support to UQ and safety studies. In the first application reported, the LS search method has been proposed as a solution to a UQ analysis presenting a FOM bifurcation deriving from an *edge-effect* in a degradation phenomenon. Accordingly, in this case, the hypothesis for the statistics of the *Wilks confidence interval formula* cannot be respected. In the study, the boundary between the two input sub-domains, driving the simulation to different phenomenological evolution, has been estimated using the LS search method.

In the second application, the iterative method is proposed as support to a UQ analysis resulting in the crossing of the safety limit of FOM. The LS search method can be used to identify the boundary between safety and unsafety conditions in the input domain. In this case, important information is provided by the estimated LS surface on where and how to improve the input parameter knowledge to reduce the safety margin and avoid exceeding safety limits.